THE UNIVERSITY *of* EDINBURGH

Analysis of P-wave seismic response for fracture detection: modelling and case studies

Yungui Xu

Thesis submitted for the degree of
Doctor of Philosophy

School of Geoscience

University of Edinburgh

2011

Declaration

I declare that this thesis has been composed solely by myself and that it has not been submitted, either in whole or in part, in any previous application for a degree. Except where otherwise acknowledged, the work presented is entirely my own.

Yungui Xu

November 2011

Abstract

This thesis addresses a few specific issues in the use of wide azimuth P-wave seismic data for fracture detection based on numerical modelling and real data. These issues include the seismic response of discrete fractures, the effects of anticline and uncertainties in real data analysis. For this, I implemented the finite difference scheme for modelling the seismic response in 3D fractured media; appropriate approaches are then selected to study discrete fracture models and the effect of the anticline with 3D seismic modelling, followed by an integrate real case study.

Finite difference (FD) is widely used in seismic modelling. There are three FD schemes described in this thesis, the standard staggered grid (SSG), the rotated staggered grid (RSG), and the diamond staggered grid (DSG). Both qualitative and quantitative comparison has been made to reveal their capability in modelling 3D fractured media. The SSG has shown best performance for anisotropic media with orthorhombic symmetry or higher symmetry system. For lower anisotropy symmetry, the DSG is preferred than the RSG in terms of computation efficiency. A new solution to the diamond grid issue is developed which can simplify the DSG implementation, and an optimized workflow is proposed to simulate large 3D fractured models. The SSG scheme is implemented in three dimensions and it provides a useful tool for various practical modelling studies.

With the above tool, two modelling studies have been carried out, on the effects of the discrete fractures and of the presence of anticline: the Discrete Fracture Model (DFM) study provides many insights into seismic response of discrete fracture and the link between the discrete fractures and aligned micro cracks, as well as the features in scattering waves. The modelling results demonstrate that, P-wave seismic anisotropy increases with the decrease of discrete fracture spacing, and different

spacing leads to different patterns in scattering waves. The study also reveals the azimuthal AVO variation on the top of discrete fracture layer, which is similar to that we find in homogenous anisotropic media. The study of the anticline structure with vertical fractures, which is built with the parameters from a real case, is to assess the anticline structure effect on fracture parameter inversion based on the Singular Value Decomposition (SVD) method. The fracture density can be resolved accurately at the top of the anticline, whilst that on the flanks tends to be over-estimated. The results also indicate that the SVD method is a reliable approach for directly estimating the fracture density.

P-wave azimuthal attributes are commonly employed to invert fracture density and orientation. Many factors may affect the accuracy of the inversion results. The integrated study in this thesis shows that azimuthal coverage, offset-depth ratio, data quality and geological structures all affect the final prediction, and different attributes shows different sensitivities to these factors. Furthermore, the combined analysis of both geological observation and pre- and post-stack seismic attributes can reduce the uncertainties for fracture detection.

Acknowledgements

The past four years of my PhD study in Edinburgh come with a lot of gratitude to colleagues, friends and families. Without them my PhD work couldn't have come to a successful end.

First of all, I would like to express my great gratitude to my supervisor Professor Xiang-Yang Li for his academic guidance throughout the four years of my research work. He and his family also help me and my wife by sharing a lot of wonderful experience, which made us have an enjoyable life in Scotland.

I am very grateful to Dr. Hengchang Dai for his professional supportsparticularly in seismic data processing and for his brilliant computational ideas. I would also like to thank Dai's wife, Ying Zhou for her helpful tips on looking after my two sons, so I could have more time for my PhD work.

From Dr. Mark Chapman, I have got a lot of valuable advice on rock physics and thesis writing. Also I had shared a lot of beer time with him in the King's Buildings House of the university campus. Many thanks to him.

I wish to thank my second supervisor in Edinburgh University Professor Ian Main for his advice on writing quality scientific papers and giving good presentations. He took a lot of times to revise my thesis chapters as well, and gave me valuable suggestions to refine the thesis structure and content.

I would like to thank Dr. David Booth for helping me proofread each paragraph of my thesis. Actually, many of my research meeting abstracts or reports are corrected with his help in the last four years and his professional feedbacks are very valuable for my later writing

My PhD project is supported by Edinburgh Anisotropy Project (EAP) of the British Geological Survey (BGS). Many thanks to EAP and its sponsors. I also wish to thank the BGS IT team, especially Brian Bainbridge, Steve Love, and Jane Roberson for their time-and-time-again help on computer problems.

Special thanks to TOTAL E&P UK for sponsoring my internship last year and many thanks to Gabriel Chao and other staff in TOTAL for their discussions and suggestions on my intern work.

I was pretty lucky to have so many lab mates, Zhongping Qian, Chuntao Zhang, Tieqian Zhang, Isabel Varela, Adam Wison, Martin Ekanem, Anish Varghese, Weilin Liu, Zhiqi Guo, Xiaoyang Wu, Shuangquan Chen, Feng Zhang, Song Hou and Heather Nichoson. Thank you all for sharing a lot of fun and wonderful ideas. This memory is unforgettable. Particularly, I have to mention Martin Ekanem helped me a lot on languages and sharing life experience in the past years. Special thanks to him. I also thank Lifeng Wang and other friends in Edinburgh and UK for their help and advice.

I would like to give big thanks to my wife, Li He for her patience and supports during the past years. Without her, I could’nt have finished my PhD. I truely thank my parents for their all-along care and support. Two junior, my two sons, Suchen Xu and Sufan Xu, bring me much enjoyable time, thank you both too.

To my family

List of Abbreviations

AVO	Amplitude Variation with Offset
AVOA	Amplitude Variation with Offset and Azimuth
CDP	Common Depth Point
CMP	Common Middle Point
CWT	Continuous Wavelet Transform
DFM	Discrete Fracture Model
DSG	Diamond Staggered Grid
FC	Fracture Corridor
FD	Finite Difference
HTI	Transverse Isotropy with Horizontal axis of symmetry
LS	Lebedev Scheme
NMO	Normal MoveOut
P-wave	Compressional wave (Primary wave)
PS-wave	Converted wave with down-going P-wave and up-going S-wave
RSG	Rotated Staggered Grid
S-wave	Shear wave
SSG	Standard Staggered Grid
SVD	Single Value Decomposition
TI	Transverse Isotropy
TTI	Transverse Isotropy with Tilted axis of symmetry
VTI	Transverse Isotropy with Vertical axis of symmetry
WFT	Windowed Fourier Transform

List of Symbols

qS1	Quasi fast shear wave
qS2	Quasi slow shear wave
qP	Quasi compressional wave
Q	seismic Quality factor
δ	Thomsen parameter related to wave front ellipticity
Z_N	Normal compliance component
Z_T	Tangential compliance component
ρ	Medium density
δ_{ik}	Kroneker's symbol
λ	Lame's constant
μ	Shear modulus
v_p	P-wave velocity in isotropic medium
v_s	S-wave velocity in isotropic medium
α	P-wave velocity along symmetry axis
ε	Thomsen parameter for P-wave anisotropy
β	S-wave velocity along symmetry axis
γ	Thomsen parameter for S-wave anisotropy

List of Figures

List of Tables

Table of Content

1 Chapter 1 Introduction

This chapter provides an introductory overview of the thesis as a whole. First I describe the basic theoretical background of fracture characterization, seismic modelling in fractured media, and fracture detection with P-wave data. This is presented in the following section, the aim being to summarise the motivations and objectives of this work in an appropriate context. The section also contains a brief summary of the outcomes. This is followed by three sections which summarise the thesis structure, the software and datasets used, and the work programme.

1.1 Motivations, objectives and outcomes

1.1.1 Background and context

The study of fractures and fracture networks in subsurface has been active for the past three decades, motivated strongly by the problems addressed in fractured

reservoir exploration and characterization. This is crucial both for discovering new reserves of oil and gas and for optimizing hydrocarbon production. Ultimately it is needed to meet increasing global energy demand. Most reservoirs, particularly those formed in carbonate rocks that contain most of the remaining oil and gas, are naturally fractured or contain a wide range of fractures, from microscopic fissures to kilometre-length meter-wide fracture swaths or fracture corridors. Fractured reservoirs are considered to be extremely challenging in terms of accurate fracture prediction due to their complexity and heterogeneity. Fractures may create porous storage or a highly permeable pathway (a leakage pathway in some cases) in reservoirs, which greatly impacts hydrocarbon concentration and migration.

Fracture properties can be examined directly in surface outcrops and in boreholes with appropriate logging tools. Fracture investigation in surface outcrops can help to understand geological process within a whole region, in particular how fractures develop and evolve over their history. Sometimes observations of surface fractures may also provide insight into the actual fracture distribution in the subsurface, but this is subject to large uncertainty. On the other hand, image logs provide a direct description fractures that intersect the borehole wall. Logging interpretation information is very valuable, and provides useful references for calibrating seismic cross-well sections. However, outcrop observation is not directly linked to fracture networks in subsurface, and logging interpretation for fractures is only valid in the immediate vicinity of borehole locations. Logging is also extremely expensive means of exploring the subsurface, given the costs of drilling to depths of a few km.

Given the problems with both means of direct observation, it is much more common to use remotely sensed seismic data to characterize fractures or fracture networks, sometimes calibrated against or used to interpolate between sites of direct observation. Seismic data is widely available and also samples the appropriate depths under in-situ conditions. Early efforts in the 1980s, for example by Crampin (1981, 1983, 1985) were made to reveal the mechanism and principles by which seismic waves were affected by fractures in the Earth’s crust, as well as to develop some practical seismic methods for fracture prediction. Critically, at reservoir depth, fractures tend to align vertically due to the large vertical compressional stress

associated with the gravitational field. This result holds when the vertical overburden pressure exceeds one of the two principal components of horizontal compressional stress, and is consistent with geological observation of fracture sets exhumed from depth, as well as mechanical inference (Anderson, 1942).

A key result of these early studies was the discovery of the phenomenon of shear wave splitting caused by the mechanical anisotropy introduced by aligned vertical fractures. This is important because it provided a method which could be used as a sensitive indicator of the degree of micro-fracturing and the state of in-situ stress. Some other efforts (e.g. Hudson, 1980 and 1981; Schoenberg, 1980; Schoenberg and Douma, 1988; Liu et al., 2000; Chapman, 2003) have built a series of theoretical links (known as anisotropic equivalent medium theories) between fractured rock properties and seismic behaviour. Based on these theories, seismic signatures, for example, S-wave splitting, seen either in the direct S-wave or the mode-converted PS-wave, and azimuthal variation in P-wave seismic attributes, can be used to infer fracture information based on such equivalent medium theories.

There have been two major trends since this early work. The first involves the development of better equivalent medium theories for anisotropic media, which now account for a wider range of properties of fractured rocks and their effect on seismic waves. The second focuses on inversion algorithm development and applications, being applied to invert for fracture parameters in subsurface from seismic data. Though many efforts have been made to reveal the mechanism and principles in fractured reservoir exploration and characterization, many problems remain unsolved.

Different anisotropic equivalent medium theories interpret fractures in different ways based on the scale of fractures involved. Two types of fractured media are often discussed in fracture characterization: homogenous fractured media (e.g. Hudson, 1980 and 1981) and discrete fracture media (e.g. Schoenberg, 1980). These two types of model for fractured media are complementary, and can be combined with models that account for multiple fracture sets or thin bed layering to produce more complex but more realistic models of fractured media. The task of fracture prediction in the Earth's crust needs more understanding of seismic response from models that

account for such realistic media, so as to extract more useful information from seismic data acquired from fractured targets.

Seismic modelling is a widely-used means of simulating the seismic response from Earth models with given parameters and also of evaluating the medium parameter inversion process from real field data. Two approaches are normally considered to investigate the effectiveness of such modelling and inversion processes: physical modelling and numerical modelling. Physical modelling is done by scaling the problem to appropriate frequencies applicable to a physical model for the Earth that is constructed and can be tested in a laboratory as a small-scale experiment. Otherwise it has similar characteristics to those of field acquisition, and the results are valuable for interpreting results obtained in real reservoir rocks that share similar geological features at the field scale. However, it is difficult to construct reliable physical models in a synthetic analogue material, particularly for aligned fractures, and the models that can be built for such laboratory simulation are usually too simple. On the other hand numerical modelling, either in 2D or 3D, provides a more generic and flexible solution.

1.1.2 Motivation and objectives

Numerical modelling solves seismic wave propagation mathematically, and has no restrictions in model construction, medium property variation, source type, and acquisition geometry. To date, most work on fracture studies based on numerical modelling is conducted in two dimensions. Work in three dimensions is very limited due primarily to the practical complexity in implementing fully 3D models numerically. This may involve developing new algorithms or selecting appropriate algorithms, optimizing and improving existing methods, accelerating computation and designing specific fractured models. However, real data is acquired in three dimensions, and fracture characterization or property inversion also involves studying variation of seismic azimuthal attributes in three dimensions. If we can promptly and accurately model the seismic response of 3D fractured media, it will undoubtedly extend our ability in fracture prediction and characterization. Therefore,

it is very necessary to overcome the complexities and practical difficulties involved in modelling 3D fractured media. Accordingly the first objective in this thesis was to construct such a model. This involved comparing different numerical schemes, selecting an appropriate modelling scheme, and choosing possible ways to accelerate the necessary computation.

Numerical modelling studies of discrete fracture media are rare because it is often assumed (as in effective medium theories for example) that the scale of seismic wave is much larger than that of fractures. In this case the seismic response from individual fractures does not have an easily identifiable effect on the wavefield. However, when fracture spacing and length are comparable with the scale of seismic waves, the seismic response from individual fractures can be explicitly observable. A practical case representation of discrete fracture media is fracture corridors (Singh et al., 2008). Most of the major efforts in existing studies of discrete fracture media are based 2D numerical modelling (Nihei et al., 2002; Vlastos, 2003; Worthington, 2007a; Rao and Wang, 2009). They focus on analyzing signatures in wave snapshots or related fracture inversion algorithms. However, they usually don't consider the effects of fractures on seismic attributes such as anisotropy, azimuthal attributes, and attenuation, all of which are critical for interpreting real data from case studies in fractured reservoirs. Therefore, my second major objective was to use the 3D numerical model I constructed to investigate such practical aspects of wave propagation in fractured, heterogeneous media.

Using P-wave data to detect fractures is considered as a more economic (acquisition with low cost) way compared with using multi-component data; also P-wave data have higher signal quality and vertical resolution. In a conventional routine, a number of P-wave seismic attributes, such as amplitude, velocity, travel time and AVO gradient are extracted from wide-azimuth datasets, and the degree of azimuthal variation is considered to be associated with fracture density and orientation. Normally the ellipse fit method is applied on such variation and finds fracture density and orientation. However, a group of factors may affect the final fracture parameter prediction, which may include azimuth coverage, offset-depth ratio, data quality, anisotropy in overburden layers and geological structures. Moreover, fracture

prediction from different attributes shows different sensitivities to these factors. Much work has been done to study some of these factors. For example, Qian (2009) conducted a thorough analysis of offset depth ratio on the fracture detection with P-wave and converted PS-waves, as well as the effect of data quality and attribute sensitivity on fracture prediction results. The effect of some other factors on fracture prediction needs further examination. Any finding of the effect of such factors on fracture prediction will surely help us to understand the application scope of fracture prediction with such seismic attributes. Also, numerical modelling with more realistic fracture models (for example explicitly considering geological structures in models) will reduce uncertainties when a similar inversion process is applied with field data. Therefore, the third objective here is to study the effect of more realistic Earth models and their effect on seismic attributes on the inversion process based on 3D numerical modelling and analysis of real data.

1.1.3 Outcomes

In achieving the aims of section 1.1.2 I first developed a fully functioning Finite Difference modelling tool for modelling seismic wave in 3D fractured media, and validated this in comparison with solutions obtained by the reflectivity method for simple models of anisotropic media. The model was based on a previous 2D model developed by Vlastos et al. (2003 and 2005), also at Edinburgh, and whose source code was made available to me near the start of the project. I then extended it to analyze the seismic response of model media containing discrete fractures in three dimensions. The synthetic seismograms and wavefield snapshots of the output of the numerical model illustrate various seismic characteristic signatures in the P-wave anisotropy, the scattering pattern, the azimuthal variation in AVO, and the resulting spectra and seismic attenuation. The snapshots illustrate the 3D effects in space at a given time, and the synthetic seismograms the wave properties at various points in that space. The latter can be compared to real seismic data. Also, I applied the model to analyze the issues in the process of fracture property inversion when geological structures are present. This was followed by a case study for fracture prediction with

seismic azimuthal attributes. The results indicate such characteristic signatures in P-wave can be used to diagnose fractures or fracture networks, and reveal the possible factors that may influence our inversion process for fracture properties.

1.2 Thesis structure

There are two principal topics in this thesis: (1) modelling fractured media and (2) fracture characterization with P-wave data. The first predicts the seismic response of various models of fractured media, based at the elementary scale on different equivalent medium theories, but modelling the effect of discrete fractures explicitly on larger scales. The second topic is studied by analysing the synthetic datasets produced (snapshots and seismograms), and comparing these with field data. The thesis structure and the chapter content is summarised below and illustrated schematically in Figure 1.1.

I start this thesis with a detailed review of the existing theoretical basis for this PhD work in Chapter 2, which include seismic anisotropy, equivalent medium theories, and fracture characterization with seismic anisotropy. Seismic anisotropy is defined here as a directional variation in seismic attributes. Seismic anisotropy in velocity can help to understand the seismic signatures in the thin layer formation, and azimuthal variation in seismic attributes can reveal the concentration of vertically aligned micro-cracks or fractures. Equivalent medium theories account for various Earth's rocks in seismic ways, which make it possible to invert rock properties from the seismic response, including seismic anisotropy. In practical geophysical exploration, fractured reservoir characterization with seismic anisotropy is a big current topic, and many approaches can be considered in terms of three body waves, P-wave, S-wave and the converted PS-wave. The azimuthal variation in seismic attributes of these waves, such as amplitude, velocity, travel time, attenuation and so on, can be used to infer the properties of fractures in subsurface reservoirs.

In Chapter 3, I focus on the comparison and implementation of different algorithms for Finite Difference (FD) seismic modelling. Three major FD staggered grid

schemes are discussed, the standard staggered grid (SSG), the rotated staggered grid (RSG), and the diamond staggered grid (DSG). The comparison reveals their relative suitability in modelling fractured media. Based on the issue addressed with the DSG scheme, I propose a new solution, which merges two staggered grid into one for a simplified implementation. Meanwhile, I introduce an optimized modelling workflow to deal with large 3D models, in which modelling parameters are separated in a reasonable way during modelling for efficiency of computational time. Finally, I implement the 3D FD SSG scheme, the example result of which is validated by the reflectivity method. The implementation is used as a practical tool for the seismic modelling in several 3D fractured models in Chapter 4 and 5.

In Chapter 4, I have analyzed a series of wave phenomena in the Discrete Fracture Model (DFM). Two numerical studies are carried out using the 3D modelling tool developed in Chapter 3. I observe some unique wave phenomena by modelling 3D DFMs. The result of the first study demonstrates the relation between discrete fracture spacing and P-wave seismic anisotropy, as well as the unique scattering patterns in different models. The second reveals the similar features in azimuthal AVO of the DFMs as those in homogenous fractured models. The obtained spectra and attenuation from the DFMs show azimuthal discontinuities.

Chapter 5 studies the effect of the anticline structure on fracture parameter inversion based on 3D numerical modelling. I use the Singular Value Decomposition (SVD) method to invert the fracture density. Three 3D models are considered for comparison. Modelling parameters are based on an existing real case study. I apply the conventional data processing on the three datasets, aiming to exact the reflection coefficients for each CDP gathers for the SVD analysis. The result shows the anticline structure has nearly no effect on the top of the structure where it is relatively flat, but the inverted fracture density is over-estimated at the two flanks. The result also proves the SVD method is a reliable method for directly inverting fracture density.

In Chapter 6, I perform an integrated study of fracture detection with P-wave data from Nanyishan Oil Field. Both post-stack and pre-stack data are considered. The study area is dominated by a major SE-NW anticline structure and the target layer is

a fractured tight gas reservoir. I first examine two post-stack seismic attributes, reflection strength and frequency content from the Continue Wavelet Transform. The two attributes confirm possible high fracture density in two prospective zones. Next I use two pre-stack seismic attributes, azimuthal amplitude and traveltime, to predict the fracture distribution across the survey. The result from amplitude analysis reveals high fracture density on the top of the anticline, which is consistent with the outcrop observation at exposed analogue anticlines, but also with well interpretation at the same reservoir. In contrast to these attributes, which produce a robust interpretation, the travel times are strongly influenced by the structure of the anticline itself, and any interpretation of the fracture properties is not reliable. Finally, I compare the anticline effect on the results in Chapter 5 and Chapter 6.

Chapter 7 summarizes the thesis conclusions and provides an overview of avenues to explore in future work, after an appropriate discussion of the relevant results of the thesis as a whole.

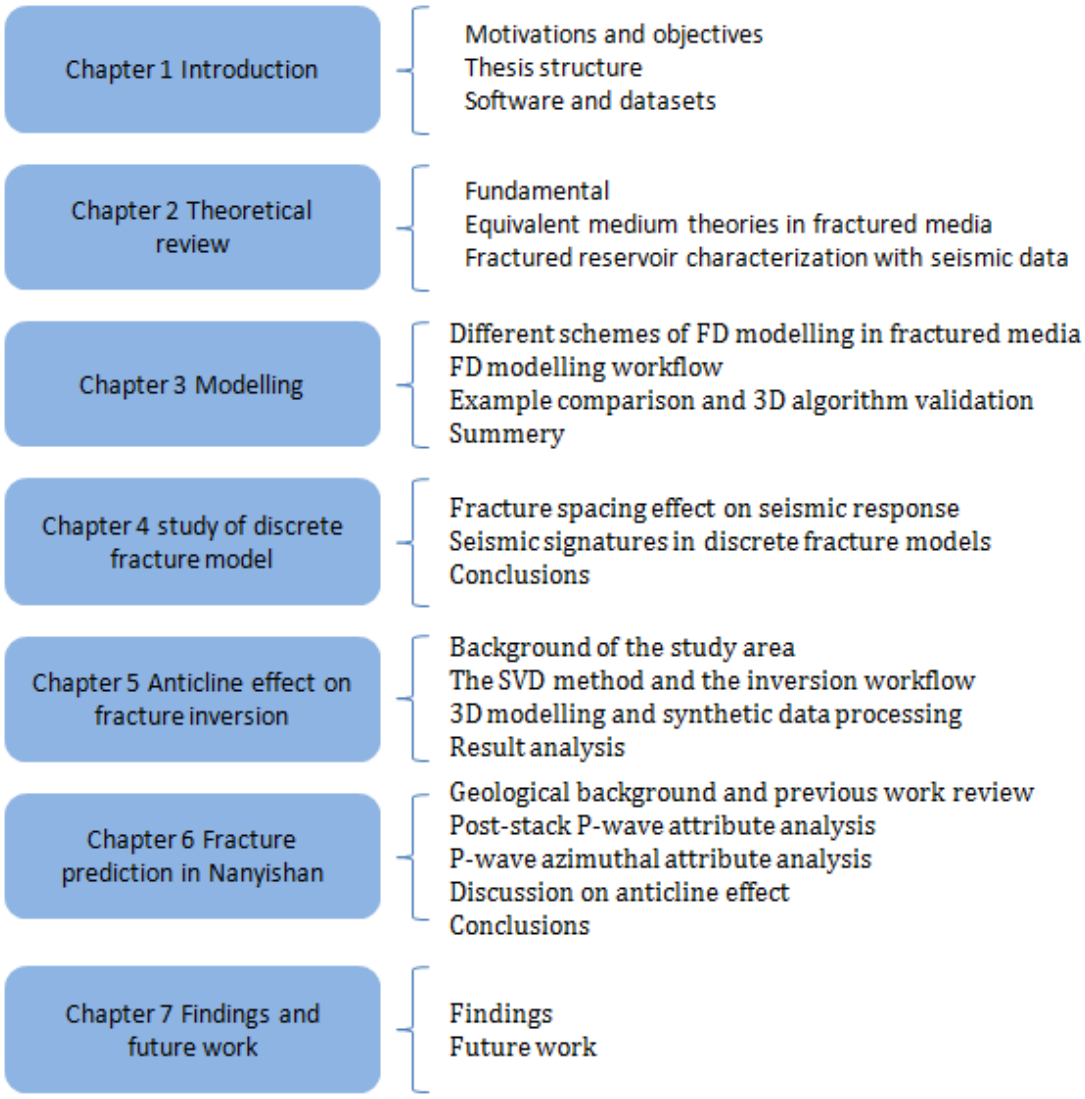

Figure 1.1: Thesis structure and chapter content

1.3 Software and Datasets

1.3.1 Software

Here I list all the software that I use in this work:

- **Seismic Unix** (SU) is an open source package for seismic data processing. Currently anyone can donate new codes to enhance the processing functions in return for access. I use it for two major purposes through all my work in

this thesis, seismic trace manipulation and seismic data visualization. Particularly, the modules to calculate pre-stack P-wave attributes in Chapter 6 were developed by Edinburgh Anisotropy Project, which are integrated with Seismic Unix to provide extra functions.

- **Wave Unix** (WU) is the software package I developed in Chapter 3 for seismic modelling in 2D/3D fractured media. Use of this code is free for Edinburgh Anisotropy Project (EAP) staff, students and sponsors. I use it for generating datasets based on various fractured models in Chapter 3, Chapter 4 and Chapter 5. It also includes the functions, data sort, CDP binning and fractured model building.
- **Rock Unix** (RU) is the rock physics software package developed by EAP. Use of this code is free for Edinburgh Anisotropy Project (EAP) staff, students and sponsors. I use it for the calculation of reflection coefficients and of seismic velocities in Chapter 5.
- **ANISEIS** is a commercial package of modelling seismic response in stratified anisotropic media based on the reflectivity method. I use it to generate two seismic sections to validate the results from Wave Unix in Chapter 3.
- **CXtools** is a PS-wave processing package developed by Edinburgh Anisotropy Project (EAP). It is free to members in EAP and its sponsors. I use it for P-wave data geometry setting and P-wave velocity analysis in Chapter 5.
- **Matlab** is commercial software for mathematical calculation, signal analysis, and 2D/3D visualization. I use it for the SVD decomposition in Chapter 6 and general result visualization.
- **CorelDRAW** is commercial software for general graphic design. I use it for displaying the fracture density prediction in Chapter 6.
- **Geoscope** is commercial software for seismic data interpretation. I use it for P-wave post-stack attribute calculation and visualization in Chapter 6.

1.3.2 Datasets

Five datasets are used in this project. Three synthetic datasets are generated from Wave Unix and one from the commercial software ANISEIS. One field data set is analysed from Nanyishan Oil Field in the north west of China.

- **Synthetic dataset 1**: The first dataset is generated from Wave Unix in Chapter 3 for a three layer HTI model.
- **Synthetic dataset 2**: This dataset is generated from ANISEIS in Chapter 3 for validating the implementation of the finite different modelling.
- **Synthetic dataset 3**: This dataset is generated from Wave Unix in Chapter 4 for analyzing seismic response in 3D discrete fractured model.
- **Synthetic dataset 4**: The dataset is generated from Wave Unix in Chapter 5 for studying the effect of anticline on fracture property inversion.
- **Nanyishan field data**: This P-wave dataset was acquired in Nanyishan Oil Field by China National Petroleum Company (CNPC) in 2006-2007. The dataset is around 400GB. The conventional data processing had already been done by the company, but they hadn't taken the full azimuth aspect into account in fracture prediction. I use the data kindly provided by CNPC in Chapter 6 for such an integrated study of fracture prediction based on the pre-stack and post-stack data.

1.4 Work programme

This PhD project was carried out in the three and a half years since September 2007 excluding a 4-month suspension where I gained work experience as an intern in Marathon Oil. Table 1.1 illustrates the work programme and timetable for reference.

Project progress	Content	Term (3.5 years)
Literature review	Review the theories in seismic anisotropy, anisotropy equivalent medium theories in fractured media, fracture reservoir characterization with seismic data, seismic modelling in 2D/3D fractured media with the Pseudo Spectra method (PS) and the Finite Difference (FD) methods.	6 Months
Seismic modelling in fractured media	• Examine the existing 2D fracture modelling by Vlastos (2005) • Describe and analyse three major schemes for seismic modelling of 3D fractured media using the FD method; • Propose a modified scheme to simplify the implementation of Diamond Staggered Grid (DSG) scheme; • Introduce an optimal 3D FD implementation • Implement FD modelling in 3D fractured media.	12 Months
Modelling seismic response based on Discrete Fracture Model (DFM)	• Study the effect of fracture spacing on P-wave anisotropy and scattering in DFMs • Study the seismic characteristics in DFMs with the presence of multiple sets of discrete fractures	6 Months
Geological structure effect on fracture property inversion with the SVD method	• Survey parameter investigation and modelling design • Preliminary test with seismic modelling on the effect of the anticline structure • Seismic modelling based on the simplified structural models • Seismic data processing • Fracture density inversion based on the SVD method	5 Months (including 3 month intern work in Total E&P)
A integrated study of fracture detection with P-wave data	• Survey parameter investigation • post-stack P-wave attribute analysis and fracture prediction • Data preparation and processing for pre-stack P-wave data analysis • pre-stack P-wave attribute analysis and fracture prediction • Anticline effect analysis	7 Months
Writing the thesis	7 chapters to detail this PhD project	6 Months

Table 1.1: Summary chart of the work programme.

2 Chapter 2 Review of seismic anisotropy

In this chapter I give an overview of the basic theories involved in my PhD, including wave propagation in anisotropic media, anisotropic symmetry systems, equivalent medium theories in fractured media, and fracture characterization with seismic anisotropy. When seismic wave propagates in certain natural rocks, it tends to show directional dependence in its attributes. A typical rock example is those containing aligned fractures. In order to reveal the intrinsic mechanism of seismic behaviour in such rocks, various equivalent media theories have been developed, based on which it is possible to characterize fractured rocks using seismic data. This chapter intends to cover many of these related aspects. In the later chapters, I may review some specific theoretical backgrounds that are related to the topics under study.

2.1 Fundamental

2.1.1 Seismic anisotropy

Seismic wave propagation in Earth's rocks is a complex subject involving various media, mineral inclusions, fluid flows, geological structures, and even surrounding stresses and underground temperatures, and hence it goes far beyond the most common assumption that Earth models are composed of horizontal elastic isotropic layers. Seismic anisotropy, as one of the seismic phenomena to reflect one aspect of that complexity, is known as the directional dependence of seismic attributes. One of the most often discussed seismic attributes is seismic velocity, which is dependent on the direction of wave propagation in an anisotropic medium. But the seismic attributes are not only limited to seismic velocity, and they also include seismic amplitude, seismic polarization, travel time etc.

Of all the categories of seismic anisotropy in geophysical exploration, two types of seismic anisotropy are very common: transverse isotropy with vertical symmetric axis (VTI), and transverse isotropy with horizontal axis (HTI). A thin-layer sedimentary sequence in the Earth's crust may produce layer-induced anisotropy, which intrinsically may have the same seismic behaviour as that of a equivalent homogenous VTI medium, provided that the seismic wavelength is long enough compared to the thickness of each layer in the sequence (Backus, 1962; Schoenberg and Muir, 1989). This 'equivalent medium' concept can be very useful for estimating seismic attributes in thinly layered media, such as seismic velocity.

Fractures or small cracks, at reservoir depth under large compressive stress, tend to preferentially align within vertical planes, which may yield aligned crack induced anisotropy, known as azimuthal anisotropy (Crampin, 1981, 1983 and 1985). This is equivalent to a homogeneous HTI medium based on the assumption that the scale of the cracks or fractures is much smaller than the wavelength of the probing wave. The references cited above reveal the significant links between seismic behaviour and fractured rock properties, such as fracture density and aligned direction, which can be used as an important tool to characterize fractured reservoir.

Some other representations of seismic anisotropy in the Earth's crust (e.g., orthorhombic, monoclinic) can be considered as the derivatives of VTI, or HTI or their combination under geometrical transformation or rotation. Take an example, aligned vertical fractures may develop in thin layered formations after geological process over their history, possibly resulting in equivalent orthorhombic media.

There is another geophysical concept, *heterogeneity*, which is closely related to anisotropy. A medium is *anisotropic* if its properties, when measured at the same location, change with direction; a medium is *heterogeneous* if its properties, when measured in the same direction, change with location (modified from Winterstein, 1990). The wavelength scale of the seismic wave used to probe a material is crucial to the concept of heterogeneity and anisotropy. A heterogeneous material may be treated as homogeneous on the scale of the wavelengths used to probe it. A heterogeneous medium may be anisotropic on the assumption that the scale of the wavelength is comparable to or much larger than that of the heterogeneity. For example, a material which consist of many horizontal homogeneous layers (each of them, as a single material, has different medium properties), is heterogeneous if the wavelength is less than the thickness of each layer; however, it may still be homogeneously anisotropic if the thickness of each layer is much smaller than the wavelength.

2.1.2 Wave propagation in anisotropic media

Before going to the details of wave propagation in anisotropic media, it is necessary to discuss the basic term 'tensor'. A tensor is defined as a multidimensional array that satisfies the general coordinate transformation law for right-hand rectangular coordinate system (Marion and Thornton, 1995), which can be expressed as follows (Mavko et al., 2009, pp. 19),

$$M'_{ABCD\dots} = \beta_{Aa}\beta_{Bb}\beta_{Cc}\beta_{Dd}\dots M_{abcd\dots} \tag{2.1}$$

where β_{Aa} is defined as the direction cosine of the angle between 'A'-axis in the new coordinate system and 'a'-axis in the old one, similar with the other β. $M_{abcd\dots}$ is the

tensor before the transformation, $M'_{ABCD\ldots}$ being the tensor after the transformation. Summation over the subscripts '*AaBbCcDd*…' is assumed.

In anisotropic media, the stiffness tensor c satisfies the same transformation law as follows,

$$c'_{ijkl} = \beta_{ip}\beta_{jq}\beta_{kr}\beta_{ls}c_{pqkl} \tag{2.2}$$

In order to understand how seismic waves propagate in elastic anisotropic media, a simplified derivation of wave equation in an elastic medium is carried out in this section based on Hooke's law and Newton's second law.

A general medium in discussion is considered to be linear elastic and anisotropic. Hooke's law for such a medium indicates that there is a linear relationship between the stress σ and the strain ε, which is expressed by,

$$\sigma_{i,j} = c_{ijkl}\varepsilon_{kl} \tag{2.3}$$

where c_{ijkl} is the four-rank elastic stiffness tensor and summation over the indices kl is assumed. The tensor has a total of 81 elements which can be merged into 21 independent elements due to the symmetric relation between six stresses and six strains, (Mavko et al., 2009, pp. 23),

$$c_{ijkl} = c_{jikl} = c_{ijlk} = c_{jilk} \tag{2.4}$$

and the existence of unique strain energy potential requires,

$$c_{ijkl} = c_{klij} \tag{2.5}$$

Stiffness tensor can be simplified by introducing the so-called abbreviated Voigt notation, which reveals the following conversion of the pair subscripts $ji(kl)$ in Hooke's law into the single subscript *I(J)* as follows (Mavko et al., 2009, pp. 25),

$$\begin{gathered} ij(kl) \rightarrow I(J) \\ 11 \rightarrow 1 \\ 22 \rightarrow 2 \\ 33 \rightarrow 3 \\ 23(32) \rightarrow 4 \\ 13(31) \rightarrow 5 \\ 12(21) \rightarrow 6 \end{gathered} \tag{2.6}$$

Therefore equation (2.3) can be written in a very convenient way

$$\begin{Bmatrix}\sigma_1\\ \sigma_2\\ \sigma_3\\ \sigma_4\\ \sigma_5\\ \sigma_6\end{Bmatrix} = \begin{Bmatrix} c_{11} & c_{12} & c_{13} & c_{14} & c_{15} & c_{16}\\ c_{12} & c_{22} & c_{23} & c_{24} & c_{25} & c_{26}\\ c_{13} & c_{23} & c_{33} & c_{34} & c_{35} & c_{36}\\ c_{14} & c_{24} & c_{34} & c_{44} & c_{45} & c_{46}\\ c_{15} & c_{25} & c_{35} & c_{45} & c_{55} & c_{56}\\ c_{16} & c_{26} & c_{36} & c_{46} & c_{56} & c_{66}\end{Bmatrix} \begin{Bmatrix}\varepsilon_{11}\\ \varepsilon_{22}\\ \varepsilon_{33}\\ 2\varepsilon_{23}\\ 2\varepsilon_{13}\\ 2\varepsilon_{12}\end{Bmatrix} \tag{2.7}$$

The stiffness matrix in equation (2.7) contains 21 elastic medium parameters (21 elements mentioned before), which are independent in a general anisotropic medium. However, in most cases, most elements in the stiffness matrix are zeros. Generally speaking, more zeros in the matrix imply a corresponding medium with a higher intrinsic elastic symmetry system. We will discuss this in section 2.1.3. After using the Voigt notation, the general coordinate transformation law is no longer valid for the two-rank stiffness matrix. However, the matrix can be transformed based on the Bond transformation matrix M (Auld, 1990),

$$[C'] = [M][C][M]^T \tag{2.8}$$

where C' and C are the new and old stiffness matrix respectively, and M^T are the transpose of the Bond transformation matrix. The Bond transformation matrix holds this form (Mavko et al., 2009, pp. 20),

$$M = \begin{Bmatrix} \beta_{11}^2 & \beta_{12}^2 & \beta_{13}^2 & 2\beta_{12}\beta_{13} & 2\beta_{13}\beta_{11} & 2\beta_{11}\beta_{12}\\ \beta_{21}^2 & \beta_{22}^2 & \beta_{23}^2 & 2\beta_{22}\beta_{23} & 2\beta_{23}\beta_{21} & 2\beta_{21}\beta_{22}\\ \beta_{31}^2 & \beta_{32}^2 & \beta_{33}^2 & 2\beta_{32}\beta_{33} & 2\beta_{33}\beta_{31} & 2\beta_{31}\beta_{32}\\ \beta_{21}\beta_{31} & \beta_{22}\beta_{32} & \beta_{23}\beta_{33} & \beta_{22}\beta_{33}+\beta_{23}\beta_{32} & \beta_{21}\beta_{33}+\beta_{23}\beta_{31} & \beta_{22}\beta_{31}+\beta_{21}\beta_{32}\\ \beta_{31}\beta_{11} & \beta_{32}\beta_{12} & \beta_{33}\beta_{13} & \beta_{12}\beta_{33}+\beta_{13}\beta_{32} & \beta_{11}\beta_{33}+\beta_{13}\beta_{31} & \beta_{11}\beta_{32}+\beta_{12}\beta_{31}\\ \beta_{11}\beta_{21} & \beta_{12}\beta_{22} & \beta_{13}\beta_{23} & \beta_{22}\beta_{13}+\beta_{12}\beta_{23} & \beta_{11}\beta_{23}+\beta_{13}\beta_{21} & \beta_{22}\beta_{11}+\beta_{12}\beta_{21}\end{Bmatrix} \tag{2.9}$$

Equations (2.8) and (2.9) are very convenient to perform the coordinate transformation when two-rank stiffness matrix is considered.

In a general anisotropic medium, the definition of strain vectors can be written as,

$$\varepsilon_{ij} = \frac{1}{2}\left\{\frac{\partial u_i}{\partial x_j} + \frac{\partial u_j}{\partial x_i}\right\} = \frac{1}{2}\{u_{i,j} + u_{j,i}\} \qquad i,j = 1,2,3 \tag{2.10}$$

where i,j are the indices of the Cartesian axes 1, 2 and 3, and $u_{i,j}$ is the spatial derivative of the ith components of displacement with respect to the index j. ρ is the

medium density. Merging equations (2.3) and (2.10) and the equation of Newton's second law yields the general anisotropic elastic wave equation,

$$\rho\ddot{u}_i - c_{ijkl}u_{k,jl} = 0 \qquad i,j,k,l = 1,2,3 \tag{2.11}$$

where we assume there is an implied summation over i,j and k with the body force dropped out. $\ddot{u}_i$ is the two order derivative of the ith displacement components with respect to time.

Here I discuss seismic velocity based on equation (2.11). Velocity is an important concept, especially in terms of seismic anisotropy. The usual way to solve equation (2.11) for a velocity is to substitute a general time-harmonic plane wave $u_k = U_k exp[i\omega(t - p_j x_j)]$ into equation (2.11) yielding the Kelvin-Christoffel equations (Tsvankin, 1997),

$$[G_{ik} - \rho V^2 \delta_{ik}]U_k = 0 \tag{2.12}$$

where δ_{ik} is Kroneker's symbol, V is the plane wave velocity or phase velocity, and G_{ik} is the symmetric Christoffel matrix,

$$G_{ik} = c_{ijkl}n_j n_l \tag{2.13}$$

in which, n is the unit vector in slowness (the reciprocal of phase velocity) direction; assuming there is an implied summation over repeated indices.

Setting the determinant of the coefficients of U_k in the Christoffel equation (2.12) to zero produces the characteristic equation which describes an eigenvalue problem. The eigenvalue problem has three real solutions for the root of phase velocity item ρV^2. In a more understandable way, the three real solutions reveal there are three body waves traveling at different velocities: one compressional wave (primary wave, or P-wave) and two shear waves (horizontally and vertically polarized shear waves, i.e., SH-wave and SV-wave). Substitute one of the three eigenvalues (three velocities) to equation (2.12) and the corresponding eigenvector is then solved, which is the corresponding wave polarization. Altogether three eigenvectors can be solved, which correspond to P-wave, SH-wave and SV-wave polarization. In general anisotropic media, the oscillations are not necessarily like that, particularly for two shear waves, because polarizations cannot be defined in the same way as in isotropic

media. Therefore S1-wave and S2-wave are considered in anisotropic media, which denote fast shear wave and slow shear wave respectively and are more useful than SH-wave and SV-wave. In anisotropic media, the three waves are normally quasi-compressional or quasi-shear, and therefore for this case the expressions qP-wave, qS1-wave or qS2-wave are used.

2.1.3 Anisotropic symmetry system in Earth's rocks

Anisotropic symmetry system is a geophysical term to describe the seismic elasticity of Earth's rocks, which intrinsically determines the rocks' seismic behaviors or attributes (velocity, amplitude, ray path, arriving time etc.). For example, when a P-wave propagates in a transversely isotropic medium, the velocity perpendicular to the symmetry axis is larger than the velocity in any other direction (Thomsen, 1986). Many alternative ways can be used to describe the symmetry system of an anisotropic medium, one of which is to introduce one or more sets of small homogeneous parallel planar cracks into isotropic background media (Winterstein, 1990). Each symmetry system is associated to a stiffness tensor with a unique form. Here I give a description of the most common symmetry systems in the following sections, each of which is illustrated by the form of its stiffness tensor, representation figures, and real case applications. Various anisotropic symmetry systems are greatly involved in 3D anisotropic seismic modelling in Chapter 3.

Isotropic medium

Many geophysical studies and applications on wave propagation are based on the assumption the geological models are isotropic, which significantly simplifies the derivation processes in mathematics and physics. For example, isotropic media, instead of anisotropic media, are considered in many circumstances in seismic data processing and interpretation (e.g. in velocity estimation and imaging techniques), specially for the case in more 20 years ago. An isotropic medium is the simplest medium type, or an extreme case of an anisotropic medium, and of the highest

symmetry system in Earth's rocks. In an isotropic medium there is no variation of its physical properties (P-wave velocity, S-wave velocity and density) in any measured direction. In terms of the description of an isotropic medium by introducing cracks, there are no cracks needed to be introduced (as shown in Figure 2.1). Isotropic media can be described in the following form of an elastic matrix:

$$C_{ISO} = \begin{Bmatrix} c_{11} & c_{12} & c_{12} & 0 & 0 & 0 \\ c_{12} & c_{11} & c_{12} & 0 & 0 & 0 \\ c_{12} & c_{12} & c_{11} & 0 & 0 & 0 \\ 0 & 0 & 0 & c_{44} & 0 & 0 \\ 0 & 0 & 0 & 0 & c_{44} & 0 \\ 0 & 0 & 0 & 0 & 0 & c_{44} \end{Bmatrix} \tag{2.14}$$

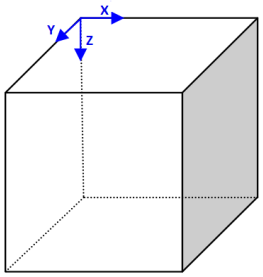

Figure 2.1: An isotropic medium. There are no aligned cracks or fractures in an isotropic medium.

It is more common to describe an isotropic medium by using Lame's parameters λ and μ, which have the relations with the element c in the matrix

$$c_{12} = \lambda, c_{11} = \lambda + 2\mu, c_{44} = \mu \tag{2.15}$$

The first Lame's parameter λ has no physical meaning and only serves for simplification. The second Lame's parameter, the shear modulus, is the ratio of the shear stress to the shear strain. In a more understandable way, the relation between P-wave velocity, S-wave velocity and density is expressed as

$$v_p = \sqrt{\frac{\lambda + 2\mu}{\rho}}, v_s = \sqrt{\frac{\mu}{\rho}} \tag{2.16}$$

Based on equation (2.15), it is clear that only two independent elastic parameters are required to describe the symmetry system of isotropic medium.

Transversely isotropic (TI) medium

Transverse isotropy is the simplest anisotropy in anisotropy categories except the isotropic case. It is the most common observed anisotropy in Earth's rocks, and the vast majority of existing studies on the mechanisms of seismic anisotropy are performed in TI media (Backus, 1962; Crampin, 1981; Hudson, 1980 and 1981; Thomson, 1986; Schoenberg and Douma, 1988). In a transversely isotropic medium, elastic properties are equivalent in all the directions that are perpendicular to the symmetry axis.

In practice, TI media can be classified into three categories according to the direction of the symmetry axis in the Cartesian coordinates: a TI medium with horizontal symmetry axis (HTI), with vertical symmetry axis (VTI), and with tilted symmetry axis (TTI). There are several causes for the formation of TI media in the subsurface. For example, many shale formations are horizontally layered, which may yield VTI media (Anderson, 1961); vertically aligned cracks/fractures may generate the seismic features of HTI anisotropy (Crampin, 1981, 1983 and 1985); a VTI formation may undergo dipping during sedimentation and tectonic processes, producing TTI features.

A VTI or HTI medium involves five independent elastic parameters (see equation (2.17) and (2.18)). A TTI medium has nine independent parameters, as stated in equation (2.19). Considering that TTI can be produced by rotating a VTI/HTI model around the Y-axis by a certain angle (except 0^o or 90^o), a TTI medium can be characterized by five independent elastic parameters (from VTI) plus one rotation angle, hence six independent parameters together. Furthermore, for practical applications in exploration geophysics, the five Thomsen parameters (Thomsen, 1986) are commonly used for the description of elastic wave propagation in TI media, which will be discussed later. Considering describing TI media by introducing one set of aligned cracks into an isotropic host medium, Figure 2.2a, b and c show the corresponding TI cases.

For the purpose of characterizing HTI media, azimuthal seismic attribute analysis is a common approach for estimating the intensity or preferential orientation of the

anisotropy. An Amplitude Versus Offset (AVO) survey on the interface of an isotropic-vertically fractured medium (HTI medium) normally shows an elliptical variation with azimuth, which can be used to determine fracture strike direction and relative fracture density (Ruger, 1997) or actual fracture density (Varela et al., 2007). The seismic P-wave velocity travels slower in the direction parallel to the symmetry axis of VTI or HTI medium than in the direction perpendicular to the axis, which can reveal, for example, the fracture properties in HTI media.

$$C_{VTI} = \begin{Bmatrix} c_{11} & c_{11}-2c_{66} & c_{13} & 0 & 0 & 0 \\ c_{11}-2c_{66} & c_{11} & c_{13} & 0 & 0 & 0 \\ c_{13} & c_{13} & c_{33} & 0 & 0 & 0 \\ 0 & 0 & 0 & c_{55} & 0 & 0 \\ 0 & 0 & 0 & 0 & c_{55} & 0 \\ 0 & 0 & 0 & 0 & 0 & c_{66} \end{Bmatrix} \tag{2.17}$$

$$C_{HTI} = \begin{Bmatrix} c_{11} & c_{13} & c_{13} & 0 & 0 & 0 \\ c_{13} & c_{33} & c_{33}-2c_{44} & 0 & 0 & 0 \\ c_{13} & c_{33}-2c_{44} & c_{33} & 0 & 0 & 0 \\ 0 & 0 & 0 & c_{44} & 0 & 0 \\ 0 & 0 & 0 & 0 & c_{55} & 0 \\ 0 & 0 & 0 & 0 & 0 & c_{55} \end{Bmatrix} \tag{2.18}$$

$$C_{TTI} = \begin{Bmatrix} c_{11} & c_{12} & c_{13} & 0 & c_{15} & 0 \\ c_{12} & c_{22} & c_{23} & 0 & c_{25} & 0 \\ c_{13} & c_{23} & c_{33} & 0 & c_{35} & 0 \\ 0 & 0 & 0 & c_{44} & 0 & c_{46} \\ c_{15} & c_{25} & c_{35} & 0 & c_{55} & 0 \\ 0 & 0 & 0 & c_{46} & 0 & c_{66} \end{Bmatrix} \tag{2.19}$$

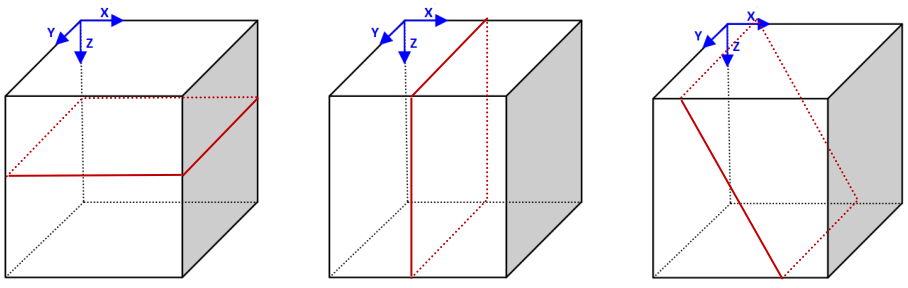

(a) (b) (c)

Figure 2.2: TI media. If aligned crack sets are introduced to describe TI media, the VTI medium (a) will contain one set of horizontal cracks, and HTI medium (b) will contain one set of vertical cracks, and TTI medium (c) will contain one set of dipping cracks. Red planes in the figure denote the plane directions of the aligned cracks.

Orthorhombic medium

If a medium has three mutually perpendicular symmetry axes in the coordinate system, each of which is parallel to one of the three system axes, it can be classified as an orthorhombic medium. There are nine independent elastic parameters in the stiffness matrix of an orthorhombic medium (equation (2.20), from Tsvankin, 1997). Comparing the form of equations (2.17), (2.18) and (2.20), it can be concluded that VTI and HTI media are two special cases of orthorhombic media. Therefore, similarly, an orthorhombic medium can be represented by introducing a set of vertical cracks and a set of horizontal cracks into an isotropic background medium, as demonstrated in Figure 2.3. In sedimentary geology one of the most common reasons for orthorhombic anisotropy is a combination of parallel vertical cracks and fine horizontally-layered formations in an isotropic background medium (e.g., Schoenberg and Helbig, 1997).

$$C_{ORI} = \begin{Bmatrix} c_{11} & c_{12} & c_{13} & 0 & 0 & 0 \\ c_{12} & c_{22} & c_{23} & 0 & 0 & 0 \\ c_{13} & c_{23} & c_{33} & 0 & 0 & 0 \\ 0 & 0 & 0 & c_{44} & 0 & 0 \\ 0 & 0 & 0 & 0 & c_{55} & 0 \\ 0 & 0 & 0 & 0 & 0 & c_{66} \end{Bmatrix} \tag{2.20}$$

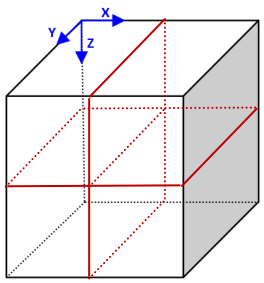

Figure 2.3: Orthorhombic medium. If aligned crack sets are introduced to describe an orthorhombic medium, it will contain one set of horizontal cracks, and one set of vertical cracks.

Monoclinic medium

Monoclinic medium has three symmetry axes, two of which are non-orthogonal to each other, but both of them are perpendicular to the third; the third axis is perpendicular to the X-Y plane. A monoclinic model involves 11 independent elastic parameters in the stiffness matrix (see equation (2.21), from Sayers and Simon, 2001). By demonstrating a monoclinic model with two crack sets, the crack sets are considered to be vertical but not orthogonal to each other, as seen in Figure 2.4. A simple rotation of a HTI model around the Z-axis by a certain angle (except 0^o or 90^o) will produce a monoclinic model.

$$C_{MONO} = \begin{Bmatrix} c_{11} & c_{12} & c_{13} & 0 & 0 & c_{16} \\ c_{12} & c_{22} & c_{23} & 0 & 0 & c_{26} \\ c_{13} & c_{23} & c_{33} & 0 & 0 & c_{36} \\ 0 & 0 & 0 & c_{44} & c_{45} & 0 \\ 0 & 0 & 0 & c_{45} & c_{55} & 0 \\ c_{16} & c_{26} & c_{36} & 0 & 0 & c_{66} \end{Bmatrix} \tag{2.21}$$

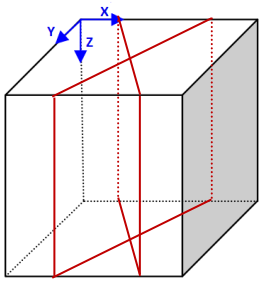

Figure 2.4: Monoclinic medium. If two aligned crack sets are introduced to describe a monoclinic medium, it will contain two vertical non-orthogonal crack sets, and thus the line of crack intersection is perpendicular to the X-Y plane.

In exploration geophysics, unlike the TI medium or orthorhombic medium, a monoclinic model is less often discussed due to its complicated symmetry system and uncommon cases. However, multiple vertical non-orthogonal fractures sets do exist in some fractured reservoirs, showing monoclinic features. To characterize this case with the two crack sets is a challenging task. Only in recent years, some relevant studies gradually appear (Sayers and Simon, 2001; Sayers, 2007). For example, Sayers and Simon (2001) give an approximate expression for P-wave reflection coefficients in monoclinic media using normal and tangential compliances to characterized non-orthogonal fracture sets.

Triclinic medium

Triclinic medium is the most general anisotropic medium, where the three symmetry axes are not orthogonal to each other. By describing a triclinic medium with one crack set in the Cartesian coordinate system, the symmetry axis of the crack set is not perpendicular to any of the three Cartesian coordinate planes (see Figure 2.5). In a triclinic medium all the elastic constants are independent, which leads to 21 independent parameters as expressed (Tsvankin, 2005),

$$C_{TRI} = \begin{Bmatrix} c_{11} & c_{12} & c_{13} & c_{14} & c_{15} & c_{16} \\ c_{12} & c_{22} & c_{23} & c_{24} & c_{25} & c_{26} \\ c_{13} & c_{23} & c_{33} & c_{34} & c_{35} & c_{36} \\ c_{14} & c_{24} & c_{34} & c_{44} & c_{45} & c_{46} \\ c_{15} & c_{25} & c_{35} & c_{45} & c_{55} & c_{56} \\ c_{16} & c_{26} & c_{36} & c_{46} & c_{56} & c_{66} \end{Bmatrix} \tag{2.22}$$

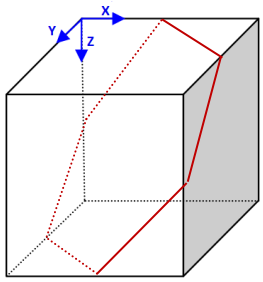

Figure 2.5: Triclinic medium. If aligned crack sets are introduced to describe triclinic medium, it will contain one set of cracks, whose symmetry axis is not perpendicular to any coordinate plane.

However, in practical geophysical applications, a triclinic medium is rarely discussed due to its complex symmetry system.

Medium invariance under the right-hand rectangular coordinate system

If one set of aligned cracks is considered in an isotropic host medium based on the wavelength limit, a rotation around its symmetry axis for any angle does not change the resulting stiffness matrix form and hence the medium property. For example, considering the case of VTI medium, if there is any rotation around z-axis under the right-hand rectangular coordinate system, the medium properties will not change.

This can be verified using the Bond transformation matrix for VTI medium as follows,

$$C_{VTI} = M_z \ * C_{VTI} * M_z^T \tag{2.23}$$

where M_z is the Bond transformation matrix considering a rotation around z-axis, and M_z^T is its transpose matrix.

For HTI medium, the axis for medium invariance is x-axis.

Weak elastic anisotropy and Thomsen's parameters

An early experimental report by McCollum and Snell (1932) reveals very strong velocity anisotropy measured with an outcrop of Lorraine Shale in which the velocity along the bedding direction is 40% larger than that perpendicular to the bedding direction. However, a well-known study (Thomsen, 1986) proves anisotropy is weak in most cases of Earth's rocks. In order to simplify the description of weak transverse isotropy with a vertical axis (VTI anisotropy), Thomsen (1986) introduced the following notations

$$\alpha = \sqrt{\frac{c_{33}}{\rho}}\ ; \quad \varepsilon = \frac{c_{11} - c_{33}}{2c_{33}}\ ;$$

$$\beta = \sqrt{\frac{c_{44}}{\rho}}\ ; \quad \gamma = \frac{c_{66} - c_{44}}{2c_{44}}\ ; \tag{2.24}$$

$$\delta = \frac{(c_{13} + c_{44})^2 - (c_{33} - c_{44})^2}{2c_{33}(c_{33} - c_{44})}$$

Here α and β refer respectively to P-wave and S-wave velocities of waves traveling perpendicular to the symmetry plane of a VTI medium, ε and γ are related to P-wave anisotropy and S-wave anisotropy respectively, δ represents wave front ellipticity, and ρ is the medium density. The table in Thomsen's paper (1986, pp. 1958) lists the anisotropy parameters measured from a variety of rock samples, in which the anisotropy parameters ε , γ and δ for most cases are less than 0.2. This demonstrates the fact of widely existing weak anisotropy.

The introduction of these five parameters for VTI media is considered as a milestone in seismic anisotropy applications. The five parameters have more physical meaning compared with stiffness vectors, which greatly facilitates to interpret seismic anisotropy in geophysical processes (seismic modelling, data processing and interpretation). What's more, HTI and TTI media can be regarded as two derivatives of a VTI medium, only with a rotation angle around the Y-axis and therefore the five parameters are also commonly used to describe HTI and TTI media.

One of the applications of weak elastic anisotropy is to express phase velocities with Thomsen's parameters. A detailed derivation for the three phase velocities in a VTI medium was given by Daley and Horn (1977). In any plane parallel to the VTI symmetry axis, the three velocities are angle-dependent and can be represented with five independent stiffness elements. Based on the assumption of weak elastic anisotropy, the three velocity expressions can be further simplified as (Thomsen, 1986)

$$\begin{aligned} v_{\mathrm{p}}^2 &= \alpha^2[1+\delta sin^2\theta cos^2\theta+\varepsilon sin^4\theta]; \\ v_{sv}^2 &= \beta^2\left[1+\frac{\alpha^2}{\beta^2}(\varepsilon-\delta)sin^2\theta cos^2\theta\right]; \\ v_{sh}^2 &= \beta^2[1+2\gamma sin^2\theta] \end{aligned} \tag{2.25}$$

where θ is the angle between the wavefront normal and the symmetry axis.

2.2 Equivalent medium theories in fractured media

Equivalent medium theories in fractured media are known as geophysical models that describe the overall anisotropic properties of a medium that contains cracks and fractures. If we wish to estimate the effective medium parameters of fractured media, some of the medium conditions have to be considered:

1) The sizes of the cracks or fractures;
2) The shape of the cracks or fractures;
3) The contained inclusions or phases;
4) The spatial relations between the cracks or fractures.

The sections below introduce the major equivalent medium theories in fractured media involved in my studies, including Backus's average (though it is not for cracks or fractures, it is an important base for other extended theories in fractured media), Hudson's model, Linear slip model, and Liu et al.'s model.

Backus' average

In Backus's model (Backus, 1962) a finely stratified inhomogeneous isotropic (or transverse isotropic) medium, with a certain thickness which is very small under the long wavelength assumption, is considered. His derivation result shows that the layered medium behaves as a single homogenous transversely isotropic medium with vertical symmetry axis (VTI): the overall effective density is obtained by averaging that of each of the components contained, and the elastic stiffness elements are obtained with the averaged combination of those of the components (Backus, 1962). Backus' model solves the effective properties by an algebraic average in a direct and understandable way, thus called 'Backus's average', which provides us with an approach to calculate the effective properties of finely stratified formations, for example, to calculate the effective properties of thinly layered sequences of shale. This average concept is very useful, and it is also applicable for some other equivalent medium theories. For example, Backus's model is extended to the case of arbitrary anisotropic components by Schoenberg and Muir (1989), in which each component layer is considered to be generally anisotropic.

Hudson's model

Hudson's model (Hudson, 1980 and 1981) is a most widely applied equivalent medium theory in fractured media, predicting the effective properties of the elastic background medium that is embedded with aligned, small, thin, penny-shaped ellipsoidal cracks or inclusions, based on the long wavelength assumption. He derives the effective stiffness by adding two-order crack-related stiffness corrections to the stiffness of the background medium, which can be expressed as (Mavko et al., 2009, pp. 194)

$$c_{ij}^{eff} = c_{ij}^{0} + c_{ij}^{1} + c_{ij}^{2} \tag{2.26}$$

where c_{ij}^{eff} is the effective stiffness tensor, c_{ij}^{0} is the stiffness tensor of the isotropic background medium, and c_{ij}^{1} and c_{ij}^{2} are the first- and second-order corrections, respectively, which are related with crack density. Note that in Hudson's model, it is assumed that cracks are isolated and therefore no interaction between cracks is considered.

Hudson's model is based on the ellipsoidal crack model first proposed by Eshelby (1957). Cheng (1993) points out that Hudson's model is consistent only for small-aspect-ratio cracks and small crack densities. In other words, the description of Hudson's model with c_{ij}^{1} and c_{ij}^{2} is only suitable for the case of weak infill material. For larger crack densities but small aspect ratios, the second correction is no longer applicable. Normally using the first-order correction is recommended rather than using both of them. To avoid the second-order correction problem, Cheng (1993) proposes a new expansion up to second order in crack density.

One of the advantages of Hudson's model is that different crack/inclusion types can be represented: (1) general 'weak infill' inclusion; (2) dry cavities by setting inclusion volume modulus to zero; (3) fluid-saturated cavities by setting the inclusion shear modulus to zero. This advantage allows us to easily simulate real Earth's rocks with different inclusions and to study the corresponding seismic response.

In Hudson's model, some points should be emphasized. Cracks are of small aspect ratio and lower crack density is assumed. Again, cracks are not interconnected and therefore no fluid flow occurs. Nevertheless, Hudson's model is a very convenient calculus for dispersed cracks with different inclusion types.

Linear Slip Model

In the Linear Slip model (Schoenberg, 1980) to be discussed, fractures normally are considered as long interfaces with negligible thickness, compared with the small dispersed cracks in Hudson's model. The Linear Slip Model, also called Discrete Fracture Model (DFM), simulates seismic wave behavior across an imperfectly

bonded interface (or slip interface, representing a fracture) between two elastic media. Across a slip interface the particle displacement is considered to be discontinuous, and the discontinuity is assumed to be linearly related with the stress traction. Here I give a detailed description of the Linear Slip model.

Use the effective elastic compliance tensor s_{ijkl} to relate the average strain ε_{ij} to the average stress σ_{ij} ,

$$\varepsilon_{ij} = s_{ijkl}\sigma_{ij} \tag{2.27}$$

This form is then expressed a two-term expression if a fracture is considered (Schoenberg and Sayers, 1995),

$$\varepsilon_{ij} = (s_{ijkl_b} + s_{ijkl_f})\sigma_{kl} \tag{2.28}$$

where s_{ijkl_b} is the compliance of the host medium, s_{ijkl_f} being the extra compliance caused by the presence of the fracture.

Based on the assumption of a linear relation between displacement discontinuity and stress the extra compliance in equation (2.28) is expanded by introducing a fracture system compliance tensor Z with components Z_{ij},

$$s_{ijkl_f} = (\, Z_{ik}n_l n_j + Z_{jk}n_l n_i + Z_{il}n_k n_j + Z_{jl}n_k n_i)/4 \tag{2.29}$$

where n_l are the components of the local unit normal to the fracture surface.

Here we discuss a simplest case. First define the normal compliance Z_N and the tangential compliance Z_T, which are related to the fracture based on the assumption that the fracture behavior is invariant with respect to rotation about an axis normal to the fracture. Hence Z_{ij} can be written as

$$Z_{ij} = Z_T\delta_{ij} + (\, Z_N - Z_T)\, n_i n_j \tag{2.30}$$

After the substitution of equation (2.30) into (2.29), the extra compliance is

$$\begin{aligned} s_{ijkl_f} = \frac{Z_T}{4}(\delta_{ik}n_l n_j + \delta_{jk}n_l n_j + \delta_{il}n_k n_j + \delta_{jl}n_k n_i) \\ + (\, Z_N - Z_T)\, n_i n_j n_k n_l \end{aligned} \tag{2.31}$$

If the fracture normal is along x-axis, which means $n_1 = (1,0,0)$, the final expression of the extra compliance in a 6 x 6 matrix form will be,

$$s_{ijkl_f} = \begin{Bmatrix} Z_N & 0 & 0 & 0 & 0 & 0 \\ 0 & 0 & 0 & 0 & 0 & 0 \\ 0 & 0 & 0 & 0 & 0 & 0 \\ 0 & 0 & 0 & 0 & 0 & 0 \\ 0 & 0 & 0 & 0 & Z_T & 0 \\ 0 & 0 & 0 & 0 & 0 & Z_T \end{Bmatrix} \tag{2.32}$$

If the host medium is isotropic, the fractured medium with the compliance $s_{ijkl} = s_{ijkl_b} + s_{ijkl_f}$ is a transverse isotropic medium (TI), which only depends on the two moduli of the host isotropic medium, μ_b and λ_b, and the two compliance components Z_N and Z_T . Therefore, it means that in the vicinity of a fracture in the host medium the seismic behavior is the similar as that in a homogenous TI medium. The relative magnitudes of the two compliances Z_N and Z_T control the medium anellipticity. Particularly, if $Z_N = Z_T$, the anellipticity vanishes and the medium is elliptical. An elliptical medium is a special case of a TI medium in which the qP wave surface is ellipsoidal and qS wave surface is a spherical. The modelling results in Chapter 4 confirm these features. Such a TI medium is also called TI (LSD) (Linear Slip Deformation). All the four parameters in a TI (LSD) medium are recoverable (Schoenberg and Sayers, 1995).

Compared with Hudson's model, which predicts the overall elastic parameters of an isotropic medium embedded with scattered isolated aligned cracks, DFM is able to calculate the elastic parameters in the neighboring region of the host medium (an isotropic medium or a general anisotropic medium) where individual fractures exist, and thus the seismic behavior of individual fractures can be examined.

Modelling of Linear Slip Model with finite difference

In order to model the seismic response of single or multiple fractures with the finite difference (FD) method, a calculus of fractures or faults through a FD grid is proposed by Coates and Schoenberg (1995). Here are the details.

Suppose there is a horizontal fracture with the length Δl enclosed in a 2D cell with the area ΔA. According to the group theory mentioned in Schoenberg and Muir (1989), the overall compliance for the fractured cell is,

$$\begin{aligned} s &= s_b + s_f \\ &= s_b + \frac{\Delta l}{\Delta A}\begin{Bmatrix} 0 & 0 & 0 \\ 0 & 0 & 0 \\ 1 & 0 & 0 \\ 0 & 1 & 0 \\ 0 & 0 & 1 \\ 0 & 0 & 0 \end{Bmatrix} \underline{Z} \begin{Bmatrix} 0 & 0 & 1 & 0 & 0 & 0 \\ 0 & 0 & 0 & 1 & 0 & 0 \\ 0 & 0 & 0 & 0 & 1 & 0 \end{Bmatrix} \end{aligned} \tag{2.33}$$

where s_b is the unfractured host medium compliance, s_f is the compliance as a result of fracturing, and $\frac{\Delta l}{\Delta A}$ is the coefficient used when 2D cells are considered while $\frac{\Delta a}{\Delta V}$ is used for 3D cells instead (Δa is the area of the 3D fracture in the cell and ΔV is the volume of the cell). $\underline{Z}$ is a fracture characteristic 3 x 3 compliance matrix when the fracture normal is along the x_3-axis , which is written as (Schoenberg and Muir, 1989)

$$\underline{Z} = \begin{Bmatrix} Z_N & 0 & 0 \\ 0 & Z_T & 0 \\ 0 & 0 & Z_T \end{Bmatrix} \tag{2.34}$$

Here Z_N and Z_T hold the same meaning as these in the previous section. Therefore, the fracture-related compliance is,

$$s_f = \frac{1}{L}\begin{Bmatrix} 0 & 0 & 0 & 0 & 0 & 0 \\ 0 & 0 & 0 & 0 & 0 & 0 \\ 0 & 0 & Z_N & 0 & 0 & 0 \\ 0 & 0 & 0 & Z_T & 0 & 0 \\ 0 & 0 & 0 & 0 & Z_T & 0 \\ 0 & 0 & 0 & 0 & 0 & 0 \end{Bmatrix} \tag{2.35}$$

$$\frac{1}{L} \equiv \frac{\Delta l}{\Delta A}, for\ 2D;\ \ \frac{1}{L} \equiv \frac{\Delta a}{\Delta V}, for\ 3D$$

For the case that the fracture is not in horizontal plane, the calculation can be performed in an internal fracture coordinate system and then a rotation is applied for the external coordinate system using Bond transformation. The inverse of the overall

effective compliance matrix is the effective stiffness matrix for the finite difference cell considered.

Here note that in literatures there is no explicit description about how much the cell size is suitable for the numerical modelling. Regarding this point further study is required. The implementation of the DFM in finite different grids gives a numerical solution of the effective elastic parameters when dealing with 2D/3D simulation of seismic wave in the DFMs, which enables us to observe and analyze various wave phenomena related to individual fractures, for example, scattering wave and scattering attenuation. Chapter 4 will discuss these wave phenomena based on 3D numerical modelling with the DFM.

Liu et al. (2000): the three models

Based on the same assumption that there is a linear relation between a displacement discontinuity and the stress traction stress in the DFM, Liu et al. (2000) conclude that a wide range of natural fractures can be classified into three categories, (a) a plane distribution of small cracks, (b) a plane distribution of isolated contacts and (c) thin layer of weak material infill, which he refers to as Model 1, Model 2 and Model 3 in their paper, respectively, as shown in below

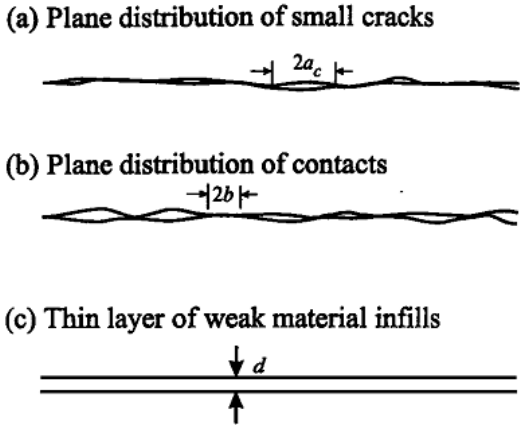

Figure 2.6: Schematic description of the three fracture models. (a) a plane distribution of small cracks, (a) a plane distribution of isolated contacts and (c) thin layer of weak material infill (from Liu et al., 2000)

The linear relationship is governed by the fracture compliance Z, which may be regarded as macroscopic parameters related to the microscopic structure of the fracture surface. Note that a natural fracture is simulated by a group of small cracks, which correspond to the case of Models 1 and 2. Model 3 represents the state of a fracture before the pressure drives its surface to contact. In the earlier stage of fracturing, with the pressure increasing, some parts of the fracture surface of fracture in Model 3 become close to form contacts, which is then represented by Model 2. In the later stage, further increased pressure makes the contact areas continue to grow and join up, leaving only few areas open, and this is represented by Model 1.

In Liu et al. (2000), the prediction of effective compliances for all of the three models is associated with the elastic constants of the isotropic host medium (the density and two Lamé constants), but in different ways. Also, the geometrical conditions and the inclusion in different models produce different additional variables, which affect the prediction. For Model 1, the variables mainly involve the crack density ϵ, and the two terms, U_{11} and U_{33}, which can be calculated based on the previous studies for different types of inclusions, for example, Hudson (1981). One important variable in Model 2 is the fracture density, which is different from the crack density (a fracture consists of a group of small cracks). Model 2 in Liu et al. (2000) does not take other infill materials into account, except dry fractures. As for Model 3, due to weak infill, the infill properties (two Lamé constants and viscosity), and probing wavelet frequency are considered. Model 3 is often used to represent hydraulic fractures. For the crack concentration in Liu et al. (2000), the crack density is considered to be smaller than 0.1, but the resultant prediction shows the theory may be applicable when the crack density is bigger than 0.1.

In addition, Liu et al. (2000) point out that, in all three models, the assumption of the compliance ratio $Z_N/Z_T \approx 1$ is valid for dry fractures when the Poisson's ratio ν is small (in the range $0.1 \leq \nu \leq 0.25$). For liquid infill, $Z_N/Z_T \approx 0$. From this point, the compliance ratio Z_N/Z_T can be used to infer the fluid content in fractures.

Assumptions and restrictions

All the equivalent medium theories discussed above are built on a series of assumptions. The assumptions help to simply the complexity of real fractured rocks, which leads to the relevant restrictions as well. The host medium for all models above (for Backus's average, each layered medium is taken into account) is assumed to be linearly elastic. The scale of either the cracks or fractures involved is much smaller than the seismic wavelength. In Backus's average, the thickness of each layer is small compared to the seismic wavelength, and conventionally the ratio of layer thickness to seismic wavelength is considered to be less than 1/10. For Hudson's model, cracks are isolated, aligned, penny-shaped with small aspect ratio, in which different types of inclusions can be assumed. In DFM and Liu et al. (2000), the fractures are assumed to be planar. Nevertheless these theories provide the theoretical fundamentals for the studies of seismic response in fractured media.

2.3 Fractured reservoir characterization with seismic anisotropy

Most carbonate reservoirs are naturally fractured with fractures ranging from micro-cracks to mile-length fracture clusters (fracture swath or fracture corridor). Figure 2.7 and 2.8 show some evidences of widely existing cracks/fractures at different scales. The fractures can create porous storage for fluid if they are capped by impermeable overlying strata, or they can form permeable pathways for fluid flow in connected pore space, which consequently has a great influence on reservoir production and recovery. Given the possible presence of geological structures and multiple-phase fluid flows contained in fractures, to characterize fractured reservoirs is considered to be extremely challenging. In a medium containing orientated inclusions, a S-wave tends to split into a fast S-wave (qS1) and a slow S-wave (qS2), which provides a useful means for geophysicists to diagnose anisotropic medium properties (Crampin, 1985). A converted PS-wave is regarded as another representation of S-waves, and thus the technique of S-wave splitting is still valid for medium analysis (Angerer et al., 2002). Moreover, a PS-wave, in media containing high-degree inclusions, may show azimuthal variation in its attributes (Qian and Chapman, 2007). However, S-

waves and PS-waves normally recorded in multi-component data have the shortcoming of high cost acquisition. On the other hand, the P-wave shows its advantages over the other two in terms of easier and cheaper acquisition and high quality data (Tsvankin and Lynn, 1999). Recent technology advances in 3D wide-azimuth P-wave acquisition allow geophysicists to characterize fractured reservoirs by means of P-wave azimuthal attribute analysis, analysis for example on amplitude, travel time, NMO velocity and attenuation (e.g. Ruger, 1997; Li, 1999; Grechka and Tsvankin, 1998; Qian, 2009; Dasgupta and Clarkz, 1998; Chichinina et al., 2006). Therefore, in the sections below, I review the relevant theories on fractured reservoir characterization based on three types of seismic data, P-wave, S-wave and PS-wave data.

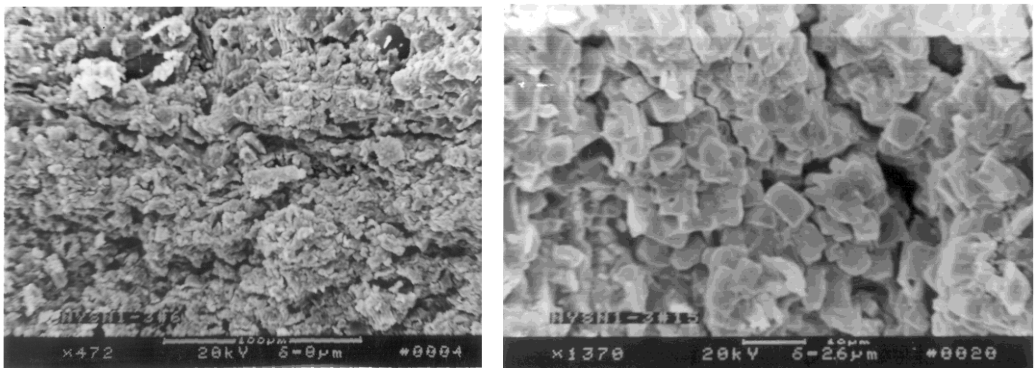

Figure 2.7: Cracks in micro slices of the cores from a well in the Nanyishan Oil Field, which is discussed in Chapter 6.

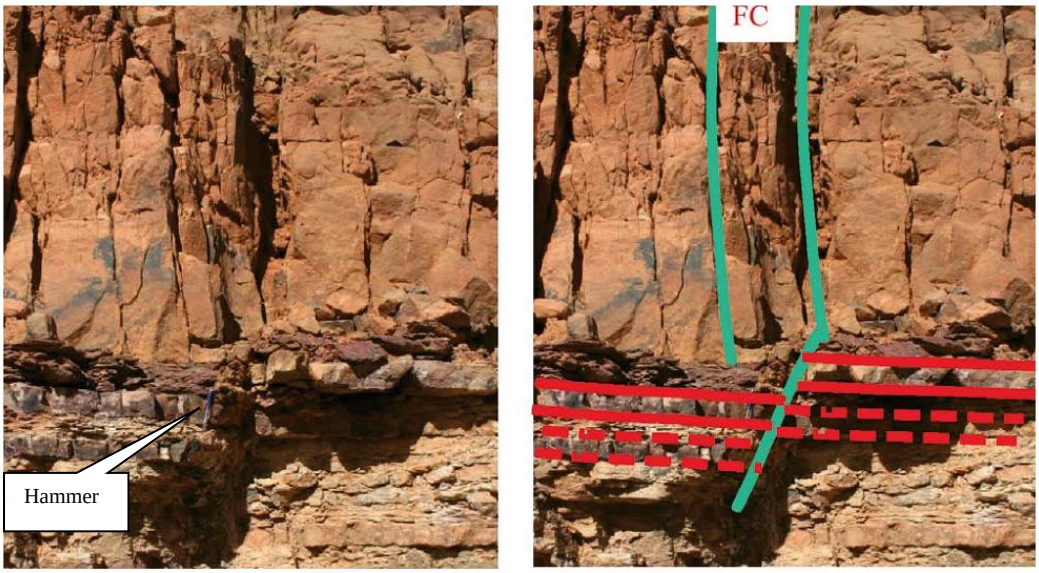

Figure 2.8: Fracture corridor in quartzite developed on the top of a small fault in shaly layers in the Paleozoic series of Algeria (Singh et al., 2008)

2.3.1 P-wave

A P-wave traveling in anisotropic media reveals preferential distortion in its various attributes. P-wave attributes, particularly in a TI medium, show azimuth- or incidence-dependent variation. In order to characterize fractured reservoirs, wide-azimuth P-wave acquisitions (either in land surveys or marine surveys) are routinely employed and then azimuthal attribute analysis is performed as an effective technique for providing fracture information.

Amplitude

Zoeppritz (1919) derived the classic analytical expression of reflection coefficients and transmission coefficients of a plane seismic wave at the interface of two isotropic media, which thereafter has become the theoretical base of AVO analysis in isotropic media. Due to the inconvenient parameterization in the analytical expression, a series of approximations covering a reasonable incidence range have been developed (e.g. Aki and Richards, 1980; Shuey, 1985; Smith and Gidlow, 1987). In practical

applications, signatures in the AVO response can help to determine rock properties. For example, AVO gradient and intercept can be used to interpret categories of gas reservoir (Castagna et al. 1998).

On the other hand, AVO analysis in fractured media normally takes azimuthal variation into account. Ruger (1997) derives approximate expressions for the P-wave reflection coefficient in VTI and HTI media. A further study (Ruger, 1998) extends the previous one into the more general case, P-wave reflection at a HTI/HTI interface, which explicitly shows the P-wave reflection coefficient vary with incident angles and azimuthal angles. Thomsen (2002) also gives a similar expression but at the isotropic/HTI interface. Nevertheless, the P-wave reflection coefficient versus incident angles and azimuthal angles at the isotropic/HTI interface can be unified as a two-term expression (modified from Thomsen, 2002, P3-20),

$$R_p(\theta,\varphi) \approx R_0 + R_2(\varphi)\sin^2(\theta) \tag{2.36}$$

$$R_2(\varphi) = R_{20} - R_{22}\sin^2(\varphi - \varphi_0) \tag{2.37}$$

where θ and φ are the incident angle and azimuth respectively, R_0 is the independent term only related to the reflection coefficient at the zero incident angle, and R_2 is the azimuth dependent term called the AVO gradient. In the gradient equation (2.37) R_{20} and R_{22} are constants, φ_0 is the dominant fracture direction.

Equation (2.36) and (2.37) reveal that the P-wave reflection coefficient (for a certain incident angle θ_0) and the AVO gradient both show elliptical variation versus azimuth φ. Moreover, the ellipticity of the variation represents the strength of seismic anisotropy. In other words, assuming this isotropic/HTI model is applied, reflection coefficients extracted from seismic data can be useful to invert for the dominant fracture direction and strength of seismic anisotropy (or relative fracture density). Note that not all incident angles are suitable for amplitude azimuthal analysis. As Qian (2009) points out, offset-to-depth ratios between 0.3 and 1.0 could help to obtain reliable results.

Based on the isotropic/HTI model (fractured model), the maximum AVO gradient could be either parallel or perpendicular to the symmetry plane, which generally leads to a 90^o uncertainty in the equivalent fracture strike direction, depending on

crack infill material, crack aspect ratio and other factors (Hall and Kendall, 2000; Tsvankin et al, 2010). Nevertheless, analysis of azimuthal variation in P-wave amplitude and AVO gradient is regarded as an effective technique for fracture property estimation or detection of fracture-contained inclusions.

NMO velocity and travel time

P-wave travel time and NMO velocity are other two important attributes, and they are normally related to each other. A well-known study on travel time and NMO velocity is Grechka and Tsvankin (1998), in which they derive the analytical expression for NMO velocity for both horizontal and dipping reflectors in arbitrary anisotropic media as follows (Thomsen, 2002, P2-38, modified from Grechka and Tsvankin, 1998)

$$\frac{1}{v_{nmo}^2(\varphi)} = \frac{\cos^2(\varphi+\varphi_0)}{v_{max}^2} + \frac{\sin^2(\varphi+\varphi_0)}{v_{min}^2} \tag{2.38}$$

where v_{nmo} is the NMO velocity, v_{max} and v_{min} being maximum and minimum NMO velocities when offset is fixed, φ being azimuthal angle and φ_0 being the dominant direction in the horizontal plane (in HTI media, the plane is parallel to the symmetry plane).

As Grechka and Tsvankin point out, the form of equation (2.38) indicates there is an elliptical relation between NMO velocity (or slowness) and azimuth. Applying this technique in HTI media (with vertical fractures) with P-wave seismic data, we can invert for the symmetry plane direction (fracture strike) and calculate the relative fracture density by fitting the elliptical variation.

Thomsen (2002) gives a similar elliptical expression for travel time in the general case (considering medium inhomogeneity, dipping reflectors and seismic anisotropy). Therefore in P-wave data applications, we can apply the same ellipse-fitting technique to travel times for fracture property inversion.

The discussion above is based on a 3D P-wave survey which allows fracture information to be mapped considering different azimuths. In certain circumstances, 2D P-wave data can also be useful for the purpose of fracture property inversion. For

example, Li (1999) develops a method to determine fracture orientation using two orthogonal intersecting 2D lines. In his study, for the horizontally layered models containing single HTI layer (the overburden is isotropic) or multiple HTI layers with single fracture orientation, the differential moveout can be written as

$$\Delta t(\phi, x) = (t_{\perp} - t_{\parallel})cos2\phi = B_0(x, \varepsilon, \delta)cos2\phi \tag{2.39}$$

where ϕ and x are the azimuthal angles to the fracture strike and offset, respectively, with $t_{\perp}$ being the travel time perpendicular to fracture strike, $t_{\parallel}$ being the travel time parallel to fracture strike, and B_0 being a function of x, ε, δ (ε, δ are Thomsen's parameters).

Equation (2.39) shows that the differential moveout has an elliptical relation with azimuthal angle by fixing the offset x. For the limitation of the technique, Li (1999) argues that the offset-depth ratio should be at least 1.0 for a reliable result.

Attenuation

Seismic attenuation is defined as a reduction in seismic wave amplitude or energy caused by the transmitting media or system (Sheriff, 2006). The physical mechanism of attenuation is associated with geometrical spreading, absorption (energy conversion into heat) and wave-mode conversion and so on (Sheriff, 2006). In geophysical exploration, seismic attenuation, normally qualified by seismic quality factor Q, is related to lithology and anelastic fluid flow, and thus it is usually used as an indicator of such rock properties (Parra and Hackert, 2002; Korneev et al., 2004). Aligned cracks or fractures in hydrocarbon reservoirs are considered as quality storage places or pathways for fluid, which leads to the preferential direction in contained fluid or fluid flow. This feature may further result in azimuth-dependent attenuation (Chichinina et al. 2006). Chichinina et al. (2006) derive an analytical relationship between attenuation and azimuthal angles based on the dispersive HTI model by proposed by Hudson et al. (1996). Their derivation shows the relationship is close to elliptical (strictly speaking, it is not elliptical), which thus can be used to direct our fracture property inversion with P-wave attenuation applied to seismic data.

On the other hand, in practice, quality factor Q is rarely well measured. The ideal measurement is from a zero-offset vertical seismic profile (VSP) (Tonn, 1991), which allows to directly measure the factor with geophones at the top and the bottom of the target layer in the borehole. Zero-offset means the source wave travels vertically from the source to the geophones in borehole. VSP Q measurement is taken only at a point location, without considering the lateral or spatial variation. To extend this into seismic reflection data, Dasgupta and Clark (1998) develop a classic Q measurement based on NMO-corrected CMP gathers, called the QVO method (Q versus offset). This method is based on the spectral ratio solution, giving a simple way to directly estimate Q from seismic data. They also point out the limitations, like assuming single-isolated-interface reflection and a NMO stretch effect.

Many approaches are available to measure the Q factor, and Tonn (1991) compares a variety of approaches based on VSP data, classified as time domain methods and frequency domain methods. Here I give a brief review of the spectral ratio method (one of the frequency domain methods) and the QVO method. Note that, the QVO method is a technique of applying the spectral ratio method in seismic reflection data.

In the spectral ratio method, the record signal $A(f)$ is related to the reference signal $A_0(f)$ (or source signal) using two absorbing terms, which is expressed in a logarithm relation

$$ln[\frac{A(f)}{A_0(f)}] = 2ln(RG) - \frac{2\pi(t-t_0)}{Q}f \tag{2.40}$$

where R is reflectivity, with G being the geometric spreading factor, f being frequency, and t and t_0 being the corresponding recording time for the two signals, respectively. From equation (2.40), after calculating the spectra ration $\frac{A(f)}{A_0(f)}$ from seismic data, a linear regression of the logarithm of the spectra ratio against the frequency f yields the intercept $2ln(RG)$ (containing reflectivity and geometric spreading) and the slope $-\frac{2\pi(t-t_0)}{Q}$ (containing Q).

Based on the spectral ratio method, the QVO method introduces an interval factor Q (Dasgupta and Clark, 1998) as follows:

$$Q_i = \frac{t_n - t_{n-1}}{\frac{t_n}{Q_n} - \frac{t_{n-1}}{Q_{n-1}}} \tag{2.41}$$

Here t_{n-1} and t_n are the recording time at the top and bottom of the target layer, respectively, and Q_{n-1} and Q_n are the quality factors of two corresponding two signals against the same reference signal.

As to azimuthal variation of P-wave attenuation in fractured media, the spectral ratio method is often used to calculate the Q factor at different azimuths for a certain offset. The ellipse fitting technique is then applied to the quality factors to obtain the dominant fracture strike (which corresponds to the major axis of the fitted ellipse) and the relative fracture density (which corresponds to the ellipticity).

2.3.2 Shear wave

Seismic wave propagation in anisotropic media is different from that in isotropic media in terms of different particle motion patterns (or polarization) of three body waves, which are normally referred to as a quasi P-wave (qP) and two quasi S-waves (qS1 and qS2). S-waves are very sensitive to seismic anisotropy of Earth's rocks, and anisotropy is normally associated with orientated inclusions, which are most likely aligned cracks or fractures in the Earth's rocks (Crampin, 1985). A special S-wave phenomenon in anisotropic media, particularly in aligned fracture media (or equivalent HTI media), is that two S-waves (qS1 and qS2) travel at different speeds in such media; this is called S-wave birefringence (Winterstein, 1990). As a result, the cumulative effect of S-wave birefringence is S-wave splitting. Figure 2.9 shows a S-wave splitting into two with a time-delay of δt after it passes a fractured medium, which has a symmetry plane (the bright blue plane in the figure) at an angle of $(90 - \phi)^{o}$ with the incident wave plane (the bright black plane in the figure). The splitting is a gradual process as the incident S-wave is going through the fractured medium. The fast S-wave (qS1) is polarized in the medium symmetry plane while the slow S-wave (qS2) is polarized perpendicular to the symmetry plane.

In practice, the idea above can be used to diagnose fracture properties. Assume that the medium discussed in Figure 2.9 is an aligned fracture medium. A two-component geophone is placed at the right side of the medium to record the arriving signals from the source on the left side. The two component seismic data are rotated mathematically around the ray path line by a certain angle until the two S-waves are completely separated. Consequently, the direction of fracture strike is related to the rotated angle and the time lag between the separated S-waves is representative of the relative fracture density.

Again, S-waves are highly sensitive to seismic anisotropy, and S-wave splitting is an important phenomenon of wave propagation in anisotropic media, particularly in media containing aligned fractures. More importantly, it can be applied as a useful technique to help to characterize fractured reservoirs by estimating fracture properties.

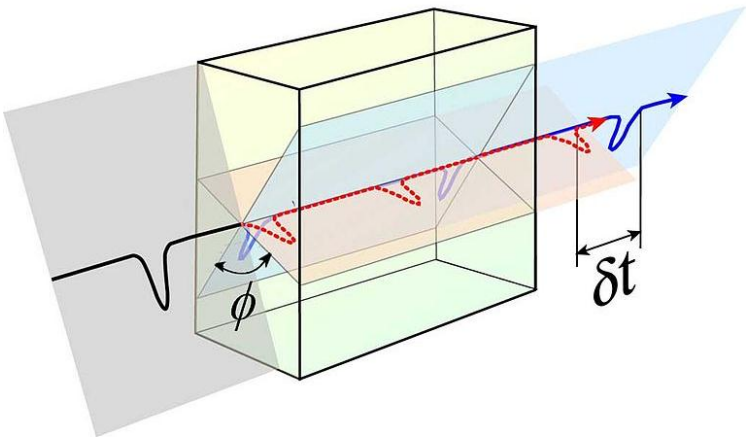

Figure 2.9: Schematic illustration of shear wave splitting in a fractured medium (this figure is from Wikipedia)

2.3.3 PS-wave

In recent years multi-component exploration have demonstrated the increased potential of mode-converted PS-waves in fractured reservoir characterization (Angerer et al., 2002; Vetri et al., 2003; Qian and Chapman, 2008; Dai and Li, 2010).

Using PS-waves to reveal fracture properties is a major aspect of these studies. PS-wave, also called converted wave, comprises a down-going P-wave to a reflector and an up-going converted S-wave from the reflector. Therefore, PS-wave trajectory is not symmetrical as P-wave or S-wave is due to velocity difference. Wave conversion is small for small incident angle, and PS-wave becomes more profound with increasing incident angle (Sheriff, 2006). Angerer et al. (2002) carry out a study of S-wave splitting in PS data, in which they argue that the asymmetry in the azimuthal variation of the time-delay of two split S-waves can be used to interpret dipping fracture sets. This idea is very useful to infer the dipping degree of fracture sets, and it can potentially influence the situation of fluid flow in fractures and thus directional drilling and wellbore stability (Angerer et al., 2002). Qian and Chapman (2008) perform a systematic multi-component study on azimuthal variation of PS-wave attributes (amplitude and travel time), in which they point out that by fitting the azimuthal variation of PS-wave attributes, fracture properties can be obtained, but only in a certain depth-offset ratio range. Their study shows that the azimuthal variation of PS-wave attributes in seismic data is analogous to that of PP-wave attributes. Dai and Li (2010) propose an approach to analyze anisotropic variation in the PS-wave velocity in a reservoir where vertical fracture sets develop. Their study shows the image improvement of the PS data sections after taking the azimuthal variation in PS stack velocity into account. From all the studies above we can see that azimuthal variation of PS wave attributes is a potential technique to characterize fracture properties in fractured reservoirs.

S-wave splitting in PS data is also a basic tool for revealing aligned fracture information. Here I review and explain how to determine fracture strike and time-delay in S-wave splitting in PS data. Figure 2.10 shows the X-Y plane view of a medium with dipping fractures, whose symmetry plane is perpendicular to the X-Y coordinate plane but at an angle of β with the source-receiver line (the source is denoted with the red solid circle; the receiver is denoted with the blue solid circle). A P-wave propagates from the source and is converted at an interface along the wavepath to an S-wave which arrives at the receiver. At the receiver location seismic signals are acquired as two component data (X-component and Y-component), which are then converted into the radial component (R-component) and the transverse

component (T-component). R-component is on the source-receiver extended line while T-component is perpendicular to the extended line. As discussed above, being an S-wave, the PS-wave will split, which can be diagnosed either in the R- or in the T-component. In order to completely separate the two S-waves in the R- and T-components, a local rectangular F-S coordinate system is introduced. Assuming there is a rotation angle of α between the F-S system and R-T system, we can calculate the new F-component and S-component as shown in equation (2.42)

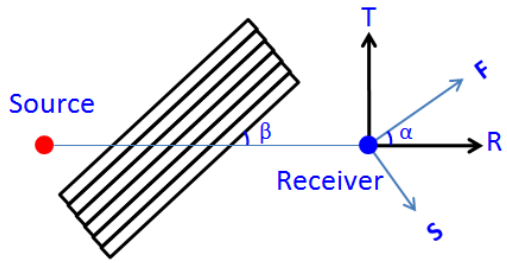

Figure 2.10: Schematic illustration of estimating fracture properties from PS wave data

$$F(t) = R(t)\cos(\alpha) + T(t)\sin(\alpha)$$
$$S(t) = R(t)\sin(\alpha) - T(t)\cos(\alpha) \tag{2.42}$$

where $R(t), T(t), F(t), S(t)$ represent R-component, T-component, F-component and S-component, respectively.

As we rotate the F-S system at different angles α, we find that the two S-waves in R- and T-component will completely separate when $\alpha = \beta$. Then the fast S-wave (qS1) will only appear in the F-component and the slow S-wave (qS2) will only appear in the S-component. The current scanning angle α $(= \beta)$ corresponds to the angle of fracture strike, and the time delay of the two S-waves can be clearly observed, which is associated with the strength of anisotropy in the medium , or the relative fracture density.

2.4 Summary

Due to tectonic processes and sedimentation processes in the subsurface, vertical fracturing and horizontal layering widely develop in natural Earth's rocks, which tend to cause various distinctive anisotropy phenomena. Apart from HTI and VTI media, other anisotropic media also can be represented in Earth's rocks. Therefore the study of anisotropic media is of great importance in understanding Earth's rocks and their seismic responses.

Equivalent medium theories in fractured media are the fundamental links between fractured media and the seismic responses, which make it possible to model seismic response in fractured media, and to invert fractured rock properties from seismic response. These theories are normally built on a series of assumptions, and different theories show different advantages and disadvantages over others in realistic applications.

In order to characterize fractured reservoirs, many inversion schemes are developed using seismic data, based on these equivalent medium theories. In 3D surveys, seismic attributes of P-wave or PS-wave, tend to show azimuthal variations or special seismic signatures. The azimuthal variation of attributes can be used to infer fracture properties. In addition, the feature in S-wave splitting can also be used to diagnose aligned fracture. To summarize, different seismic body waves show a great deal of potential to characterize fractured reservoirs. P-wave data, rather than the other two, are usually used for this purpose due to its cheaper acquisition, high resolution and data quality.

3 Chapter 3 Seismic modelling in 3D fractured media with Finite Difference

In this chapter, I describe and analyse several different methods for seismic modelling of 3D fractured media using the finite difference (FD) method, and introduce a specific method of my own which is used elsewhere in this thesis. First. I compare three finite difference schemes in seismic modelling, namely the standard staggered grid (SSG), the rotated staggered grid (RSG), and the diamond staggered grid (DSG) methods, in order to reveal their advantages and disadvantages for modelling applications. Based on an issue addressed in a comparison with the DSG, I propose a modified scheme, which can simplify the implementation of the finite difference method in general anisotropic media. For the purpose of modelling the generic seismic response of large-scale anisotropic media, I also introduce an optimized modelling workflow by separating model parameters into model medium parameters and model structure parameters; this is suitable for any of the three FD schemes. The final goal of this chapter is to implement 3D full wavefield modelling of the seismic response to elastic media with orthorhombic symmetry, which is

accomplished and validated by demonstrating a series of modelling examples with different FD modelling schemes. The completed FD modelling tool will be used to model the seismic response of different 3D Earth models containing aligned fracture sets in Chapter 4 and Chapter 5.

3.1 Introduction

Fractures in the subsurface have a great influence on fluid flow properties. They may also be induced by fluid flow involving changes in pore pressure. To understand in-situ signatures of fractures and fluid flow within them, we have to be able to understand the fracture system. An effective way in seismology is to study the seismic response of a fracture system based on seismic modelling, in comparison with data acquired in the field, for example to image 3D reservoirs of oil and gas. Seismic modelling in fractured media plays two important roles in fracture studies: revealing characteristics of the seismic response in various fractured media, and validating existing fracture inversion schemes. However, most inversion modelling studies on fractured models are restricted to the 2D situation (e.g., Nihei et al., 2002; Vlastos, 2005; Rao and Wang, 2009). 3D modelling studies are very limited due to the difficulties in implementation of 3D seismic modelling.

Here I first give details about the work of a previous PhD project, Vlastos (2005), from which some implications can be drawn for seismic FD modelling in 3D fractured media. Vlastos (2005) explored several topics of 2D modelling with the pseudo-spectral (PS) method based on discrete fracture models (DFM). His work gives us insights into using the PS method to simulate discrete fractures and how the individual fractures affect the mean wavefield. However, several issues remained unsolved due to limitations in the techniques he uses. First, the pseudo-spectral method is based on FFT/IFFT transformation, which involves much larger computation in 3D cases, compared with the finite difference method. More details on this will be given in the next section. Second, modelling in Vlastos (2005) was carried out in the 2D case, which does not consider the seismic response in the third

spatial dimension. However, the 3D seismic response of fractured media is of great importance because it makes possible to characterize fractures in their natural setting. One typical example is that full P-wave azimuth attribute analysis based on 3D data can help to invert fracture properties, which promotes our understanding of fracture systems. In this chapter, I intend to use the finite difference method to perform seismic modelling in 3D fractured media, extending the 2D fracture study by Vlastos (2005) to the 3D case.

Two important studies of 3D modelling in the DFMs were performed by Willis et al. (2006) and Grandi-Karam (2008). Both of them discuss a similar topic, which is how to use scattering waves to determine fracture orientation and fracture spacing based on 3D discrete fracture models. The synthetic data they use are generated with the finite difference method. However, they focus on the application of the existing finite difference tool to create the synthetic data, and don't cover the aspects related to finite difference modelling. I intend to discuss more details of FD modelling in fractured media, such as comparison of different FD schemes, and modelling optimization and implementation, which might provide more insights on the FD method itself and help to find a desirable and robust way of modelling in specific fractured models.

For general seismic modelling, many approaches are available, which are basically classified into three categories: direction methods, integration methods and ray-tracing methods (Carcione et al., 2002). Direct methods are the most commonly used methods in terms of full wave simulation, because there is no restriction on material variability and high accuracy can be achieved if sufficiently fine grids are used. In direct methods, geological models are discretized in fine grids for solving wave equations, and there are many implementation algorithms of direct methods, such as finite difference, pseudo-spectral and finite element (Carcione et al., 2002). Compared with other algorithms, finite difference is more easily implemented and normally costs less in computation time without compromising modelling accuracy. Therefore it is widely used in seismic modelling (e.g., Virieux, 1984 and 1986; Levander, 1988; Faria and Stoffa, 1994; Igel et al., 1995; Dong and McMechan,

1995; Graves, 1996; Saenger et al., 2000; Saenger and Bohlen, 2004; Lisitsa and Vishnevskiy, 2010).

Most seismic modelling studies with finite difference in anisotropic media (e.g., Levander, 1988; Igel et al., 1995; Dong and McMechan, 1995; Graves, 1996) are based on the standard staggered grid (SSG) method developed by Virieux (1984, 1986). In the standard staggered grid method, wavefield components are discretized in different numerical grids in order to solve the wavefield spatial derivatives at the required grid locations. This idea is very straightforward and easily implemented.

Some others (Lebedev, 1964; Saenger et al., 2000; Saenger and Bohlen, 2004; Lebedev, 1964; Lisitsa and Vishnevskiy, 2010) consider other staggered grid methods. Saenger et al. (2000) propose a rotated staggered grid (RSG) method, which solves the derivatives along grid diagonals. Lisitsa and Vishnevskiy (2010) introduce the Lebedev scheme (Lebedev, 1964) into seismic modelling, and the derivatives are solved along the coordinate axes. The Lebedev scheme (I call it DSG) is also a staggered grid method.

Lisitsa and Vishnevskiy (2010) quantitatively compare the RSG and DSG methods in general anisotropic media. However, more comparison of different FD schemes needs to be made to clarify their suitability in implementations and applications in specific anisotropic media (e.g., TTI and orthorhombic media), because such anisotropic media can simplify FD implementation and save computation due to the forms of their stiffness vectors. This is very important particularly in the 3D case, in that seismic modelling in large 3D anisotropic models normally takes days, weeks or even months. The comparison might also benefit other modelling-related applications in anisotropic media, such as reverse time migration and full waveform inversion.

In addition, 3D FD modelling should be able to model more complex or realistic models, for instance, 3D structural fractured models and orthogonal DFMs (I discuss these two applications in Chapter 4 and 5). As far as I know, 3D structural fractured models and orthogonal DFMs are rarely discussed in other's modelling work.

3.2 Theoretical background

3.2.1 Velocity-stress formulation of wave equation

There is a derivative form of the elastic wave equation based on equation (2.11) in Chapter 2, the first order velocity-stress formulations, which include the expression of Hooke's law (equation (3.1)) and the expression of Newton's second law (equation (3.2)).

$$\begin{Bmatrix} \dot{\sigma}_{xx} \\ \dot{\sigma}_{yy} \\ \dot{\sigma}_{zz} \\ \dot{\sigma}_{yz} \\ \dot{\sigma}_{xz} \\ \dot{\sigma}_{xy} \end{Bmatrix} = \begin{Bmatrix} c_{11} & c_{12} & c_{13} & c_{14} & c_{15} & c_{16} \\ c_{12} & c_{22} & c_{23} & c_{24} & c_{25} & c_{26} \\ c_{13} & c_{23} & c_{33} & c_{34} & c_{35} & c_{36} \\ c_{14} & c_{24} & c_{34} & c_{44} & c_{45} & c_{46} \\ c_{15} & c_{25} & c_{35} & c_{45} & c_{55} & c_{56} \\ c_{16} & c_{26} & c_{36} & c_{46} & c_{56} & c_{66} \end{Bmatrix} \begin{Bmatrix} v_{x,x} \\ v_{y,y} \\ v_{z,z} \\ v_{y,z} + v_{z,y} \\ v_{z,x} + v_{x,z} \\ v_{y,x} + v_{x,y} \end{Bmatrix} \tag{3.1}$$

$$\begin{cases} \rho \dot{v}_x = \sigma_{xx,x} + \sigma_{xy,y} + \sigma_{xz,z} \\ \rho \dot{v}_y = \sigma_{xy,x} + \sigma_{yy,y} + \sigma_{yz,z} \\ \rho \dot{v}_z = \sigma_{xz,x} + \sigma_{zy,y} + \sigma_{zz,z} \end{cases} \tag{3.2}$$

where σ with two indices represents different stress components, with one dot above denoting the first order time derivatives, and the third index denotes the corresponding first order spatial derivatives; v_x , v_z and v_z are wavefield particle velocities along the x-, y- and z-axis, respectively. v_x , v_z and v_z with a second index refer to the corresponding first order spatial derivatives, with a dot above denoting the corresponding first order time derivatives. See Chapter 2 for other notations used in the thesis. Many numerical modelling algorithms are built on the first order velocity-stress formulations, two typical of which are the pseudo-spectral method and the FD staggered grid method. To solve the equations (3.1) and (3.2) numerically, the major point is to calculate the spatial derivatives of the particle velocity components and the stress components. Normally different numerical modelling algorithms employ different ways to solve the spatial derivatives in equations (3.1) and (3.2).

3.2.2 The pseudo-spectral method and the staggered grid method

The pseudo-spectral method

The pseudo-spectral method intends to solve the derivatives with the FFT/IFFT transformation. Here are the equations of the discrete FFT/IFFT in 2D case,

$$F(u,v) = \frac{1}{N}\frac{1}{M}\sum_{x=0}^{N-1}\sum_{y=0}^{M-1} f(x,y)e^{-j2\pi(\frac{ux}{N}+\frac{vy}{M})} \tag{3.3}$$

$$f(x,y) = \sum_{u=0}^{N-1}\sum_{v=0}^{M-1} F(u,v)e^{j2\pi(\frac{ux}{N}+\frac{vy}{M})} \tag{3.4}$$

where $f(x,y)$ is a 2D wavefield component (which can denote any wavefield component) in 2D space domain and $F(u,v)$ is its discrete FFT transformation in 2D frequency domain. For simplicity, we can use the following expression for FFT/IFFT

$$f(x,y) \leftrightarrow F(u,v) \tag{3.5}$$

Similarly, we can use the feature of FFT to express the derivatives of $f(x,y)$ with respect to x and y,

$$\frac{\partial f(x,y)}{\partial x} \leftrightarrow F(u,v)\, j2\pi\frac{ux}{N} \tag{3.6}$$

$$\frac{\partial f(x,y)}{\partial y} \leftrightarrow F(u,v)\, j2\pi\frac{vy}{M} \tag{3.7}$$

According to the relations above, the workflow of solving the spatial derivative in equations (3.1) and (3.2) is: (1) taking a 2D wavefield component and perform FFT transformation based on equation (3.3); (2) $F(u,v)$ is then multiplied by the extra term $j2\pi\frac{ux}{N}$ and apply the IFFT based on (3.6); (3) we get the spatial

derivative $\frac{\partial f(x,y)}{\partial x}$. This process can applied to any of the spatial derivatives in equations (3.1) and (3.2) using similar extra term in 3D case.

From equation (3.3), we note there is an important feature related to FFT: to solve any FFT at specific point, for example, $F(u_1, v_1)$, the summation computation is over all points (from 1 to $N-1$, from 1 to $M-1$) in $f(x,y)$ domain with $u = u_1, v = v_1$. IFFT has the same summation feature. We can see, the derivative solution based the FFT and IFFT transformation involves much large computation since all points in 2D/3D case in one domain are considered to calculate one point in the other domain. The current computer power is powerful enough to handle this feature in 2D case. However, in 3D case, the overall computation increases dramatically, which makes large scale seismic modelling very difficult, especially in anisotropic media where many more elastic parameters are involved . This is the weakness of the pseudo spectral method.

The finite difference staggered grid method

The staggered grid method has many different implementation forms, or different schemes, but the common feature is: (1) at least two FD grid in modelling; (2) one grid is at the middle point of the other, ensuring to solve the spatial derivatives with central difference; (3) only adjacent few points at the derivative location are involved in computation rather than all points in the wave field involved in the pseudo-spectral method.

Here take the example of figure 3.1a, which is a 2D FD standard staggered grid (more details are discussed later). From the figure, if the spatial derivative of the stress component σ_{xx} with respect to x-axis at the upper red circle location (where v_x is) is to be solved, we just use the two values of σ_{xx} which are at the two sides of the location v_x to calculate it based on central difference. At this point, the computation in the FD staggered grid is much less than that in the pseudo-spectral method, particularly in 3D case.

There are three different staggered grid schemes in terms of different spatial discretization of the wavefield components and medium parameters:

(1) Standard Staggered Grid (SSG - Virieux, 1984 and 1986)
(2) Rotated Staggered Grid (RSG - Saenger et al., 2000),
(3) Lebedev scheme (LS - Lebedev, 1964; Lisitsa and Vishnevskiy, 2010), or the alternative term, Diamond Staggered Grid (DSG). The term 'diamond staggered grid' is my suggestion, as the grids are of diamond shape in both the 2D and 3D case, analogous to the first two schemes. Note there is no difference between the LS and the DSG, only difference terms.

Each of these schemes has its own advantages and weakness compared with the others.

3.2.3 Fractured media in seismic modelling

Before I go into the details of different finite difference schemes, it is necessary to know exactly what is meant by the 'fractured media' involved in seismic modelling. There are two major types of fractured media in terms of the different anisotropic equivalent medium theories applied, namely, a homogenous fractured medium and a discrete fracture medium.

In a homogenous fractured medium, cracks or factures are randomly distributed in the background medium though they may show preferential alignments; these cracks or fractures cannot be 'seen' individually by the seismic wave, though the properties of the total crack population (density and percentage anisotropy of alignment) affects the bulk seismic properties. In this case the fractured medium is equivalent to a homogenous anisotropic medium, which means that the elastic parameters can be calculated with fully analytical equivalent medium theories (e.g., Hudson, 1980) as a block of homogeneous medium.

In a discrete fracture medium, when numerical modelling is considered, the Coates-Schoenberg method (Coates and Schoenberg, 1995) is normally used to calculate the equivalent medium parameters at the elementary scale of the fractured

grids, and the bulk properties are an emergent property of the discrete (inhomogeneous) crack population on larger scales. Other unfractured grids have the same parameters as the host medium. In discrete fracture media, the wavefield is normally complex because each fracture causes wave reflection and transmission, which resulting in multiple seismic scattering that can degrade the quality of seismic sections or wavefield snapshots. As a consequence, there has been increased interest in the area of seismic scattering (Vlastos 2005; Willis et al., 2006; Grandi-Karam, 2008).

3.3 Comparison of the three finite difference schemes

3.3.1 Qualitative comparison

In seismic modelling three FD schemes are available as stated, and therefore the choice has to be made regarding which one is more suitable for specific forms of stiffness vectors in fractured media. In this section, I discuss both their advantages and disadvantages for modelling various anisotropic media or fractured media.

The SSG scheme

The first scheme, the standard staggered grid (SSG), is introduced by Virieux (1984, 1986) to solve wave propagation in 2D isotropic medium, where there are four different staggered grids (Figure 3.1a). This is the first time the idea of staggered grids comes to seismic modelling. The 2D SSG scheme is fully extended into the case of 3D viscoelastic anisotropic modelling by Dong and McMechan (1995), which involves seven different grids (Figure 3.1b). In the SSG (Figure 3.1a and b), some grids are at the midpoints of others. Different wavefield components, either stress components or velocity components, are distributed on different grids. Some coincide on the same grid. This wise idea allows solving each derivative with central differences. The SSG scheme is easily implemented, computationally fast and of low cost, and therefore most modelling applications are based on the FD SSG scheme.

However in the SSG, interpolation of velocity components is required if it is employed in an anisotropic medium whose symmetry system is lower than that of orthorhombic media. Let me take the first expression in equation (3.1) for example, $\dot{\sigma}_{xx} = c_{11}v_{x,x} + c_{12}v_{y,y} + c_{13}v_{z,z} + c_{14}(v_{y,z} + v_{z,y}) + c_{15}(v_{x,z} + v_{z,x}) + c_{16}(v_{x,y} + v_{y,x})$. In an triclinic medium (or general anisotropic media) where c_{14} c_{14} is not zero, the derivatives of v_y with respect to z, i.e., $v_{y,z}$, cannot be solved at the location of σ_{xx} σ_{xx} with central differences, and therefore interpolation of the adjacent v_y v_y is required in order to approximate $v_{y,z}$. Also the same problem exists for $v_{z,y}$. Other elastic constants$c_{15}, c_{16}, c_{24}, c_{25}$, c_{36}, c_{45}, c_{46} and c_{56} have the same problem as c_{14} if they are not zero. From this point, extra numerical errors will occur if the SSG scheme is applied to those anisotropic media (e.g., TTI, monoclinic and triclinic) where such elastic constants are not zero. Nevertheless, the SSG scheme works very well at handling VTI, HTI, and orthorhombic media. Here are four points concluded for the SSG:

1) Seven grids involved;
2) Fast computation and small memory cost;
3) Handle orthorhombic media very well;
4) Any symmetry system lower than orthorhombic media results in wave field interpolation.

The discrete SSG forms of the first expressions from both equations (3.1) and (3.2) are written as (in orthorhombic medium),

$$TXX_{i,j,k}^{t} = TXX_{i,j,k}^{t-1} + \mathrm{C11}_{i,j,k}\frac{VX_{i,j,k}^{t-1} - VX_{i,j,k-1}^{t-1}}{\Delta x} + \mathrm{C12}_{i,j,k}\frac{VY_{i,j,k}^{t-1} - VY_{i,j-1,k}^{t-1}}{\Delta y} + \mathrm{C13}_{i,j,k}\frac{VZ_{i,j,k}^{t-1} - VZ_{i-1,j,k}^{t-1}}{\Delta z})\Delta t \tag{3.8}$$

$$VX_{i,j,k}^{t} = VX_{i,j,k}^{t-1} + \left(\frac{TXX_{i,j,k+1}^{t-1} - TXX_{i,j,k}^{t-1}}{\Delta x} + \frac{TXY_{i,j,k}^{t-1} - TXY_{i,j-1,k}^{t-1}}{\Delta y} + \frac{TXZ_{i,j,k}^{t-1} - TXZ_{i-1,j,k}^{t-1}}{\Delta z}\right)\Delta t / RHO_{i,j,k} \tag{3.9}$$

where $TXX_{i,j,k}^{t}$ is σ_{xx} at the point i,j,k at the time t, similar meaning with the three velocity components $VX_{i,j,k}^{t}$, $VY_{i,j,k}^{t}$ and $VZ_{i,j,k}^{t}$ (which denote v_x, v_y, v_z respectively), Δx and Δy and Δz are the grid size along three coordinate axis, Δt is the time interval. C and RHO are stiffness elements and medium density respectively.

The RSG scheme

On the other hand, the interpolation problems above can be tackled by introducing a new staggered grid, the rotated staggered grid (RSG, Saenger et al., 2000), where there are only two staggered grids in either the 2D or 3D case (Figure 3.1c and d). Fewer grids means a simpler implementation. All velocity components are on one grid and all stress components are on the other. But the difference is, for solving each derivative (for example one stress derivative at the central red location in Figure 3.1d), other 4 derivatives are first calculated along the 4 grid diagonals (4 yellow dashed lines) and then they are linearly combined to calculate the expected derivative at the centre of the FD grids. The process works for both stress and velocity derivatives. This feature allows seismic modelling in general anisotropic media (up to triclinic symmetry) without any interpolation of wavefield components as in the SSG. The shortcoming is that solving an extra 4 diagonal derivatives leads to much more computation than that in the SSG. Additionally, derivative calculation along diagonals requires more computation memory for the same accuracy to be maintained as in the SSG schemes, where derivative calculation is computed along the sides of FD grids, namely, along the coordinate axes. Here are four points concluded for the RSG:

1) Two grids involved;
2) More computation and more memory cost compared with the SSG;
3) Handle arbitrary anisotropic media very well;
4) A linear combination of the diagonal wavefield components is required to solve spatial derivatives.

The discrete RSG forms of the first expressions from both equations (3.1) and (3.2) are written as (in arbitrary anisotropic media),

First four diagonal elements：

$D1=VX_{i+1,j+1,k+1}^{t-1}-VX_{i,j,k}^{t-1}$

$D2=VX_{i,j+1,k+1}^{t-1}-VX_{i+1,j,k}^{t-1}$

$D3=VX_{i+1,j,k+1}^{t-1}-VX_{i,j+1,k}^{t-1}$

$D4=VX_{i,j,k+1}^{t-1}-VX_{i+1,j+1,k}^{t-1}$

Linear combination of the elements to solve the three derivatives of v_x:

$$\frac{VX}{\Delta x}=(D1+D2+D3+D4)/(4\Delta x)$$

$$\frac{VX}{\Delta y}=(D1+D2-D3-D4)/(4\Delta y)$$

$$\frac{VX}{\Delta z}=(D1-D2+D3-D4)/(4\Delta z)$$

Similar to solve the other six derivatives of $v_y,\ v_z$:

$$\frac{VY}{\Delta x},\frac{VY}{\Delta y},\frac{VY}{\Delta z},\frac{VZ}{\Delta x},\frac{VZ}{\Delta y},\frac{VZ}{\Delta z}$$

Therefore,

$$TXX_{i,j,k}^{t}=TXX_{i,j,k}^{t-1}+\mathrm{C11}_{i,j,k}\frac{VX}{\Delta x}+\mathrm{C12}_{i,j,k}\frac{VY}{\Delta y}+\mathrm{C13}_{i,j,k}\frac{VZ}{\Delta z}+ \tag{3.10}$$

$$\mathrm{C14}_{i,j,k}\left(\frac{VY}{\Delta z}+\frac{VZ}{\Delta y}\right)+\mathrm{C15}_{i,j,k}\left(\frac{VX}{\Delta z}+\frac{VZ}{\Delta x}\right)+\mathrm{C16}_{i,j,k}\left(\frac{VY}{\Delta x}+\frac{VX}{\Delta y}\right))\Delta t$$

Similar to the process above, the derivatives $\sigma_{xx,x},\sigma_{xy,y},\sigma_{xz,z}$ can be solved with the linear combination: $\frac{TXX}{\Delta x},\frac{TXY}{\Delta y},\frac{TXZ}{\Delta z}$

$$VX_{i,j,k}^{t}=VX_{i,j,k}^{t-1}+\left(\frac{TXX}{\Delta x}+\frac{TXY}{\Delta y}+\frac{TXZ}{\Delta z}\right)\Delta t/\ RHO_{i,j,k} \tag{3.11}$$

where the notation starting with *D* means the combination along the four diagonals in 3D case, and other notation is of the same representation in the SSG scheme.

The DSG scheme

In contrast to the two schemes discussed above, the third one, the Lebedev scheme (LS), or the diamond staggered grid (DSG), was originally studied by Lebedev (Lebedev, 1964) in mathematical physics, and it has only recently attracted geophysicists' attention in seismic modelling (Lisitsa, 2007; Lisitsa et al., 2009; Lisitsa and Vishnevskiy, 2010). We (Xu and Li, 2009) explored the same idea after we studied the SSG and RSG schemes, and have discussed the feasibility of 2D/3D DSG (without referring to Lebedev, 1964, and Lisitsa et al., 2007) in the report of the 2009 Edinburgh Anisotropy Project (EAP) meeting. In the DSG scheme (Figure 3.1e and f), the grids that contain the same wavefield components are like diamonds (the red and yellow dashed line object in Figure 3.1e and f), and these grids ensure all derivatives can be easily solved with central differences along three coordinate axes at the expected grid locations in general anisotropic media, without the derivative combination in the RSG or any component interpolation in the SSG. For example, taking the red dash diamond grid in Figure 3.1f, three velocity derivatives along three axes could be solved at the centre of the diamond with the 6 velocity components at the 6 vertexes of the diamond. It is the same with the stress derivatives. The DSG is easier to understand in term of the complexity existing in the SSG and RSG. However, regarding the details of the diamond grids, I find each unit cell (Figure 3.2c) has more component nodes, and hence costs more in computational memory. Also more component grids cause more computation time. Therefore the natural question here is how the computation compares between the RSG and DSG. The next section will discuss this in more details. Moreover, this unusual diamond feature causes difficulties in the implementation since computers are favour of 2D/3D regular rectangular grids. Regarding this usual feature, I will propose a modified method to adapt it to FD modelling. Nevertheless the advantage of the DSG scheme is that there are only two grids involved, and no interpolation and no combination of wavefield components are needed for modelling in general anisotropic media. Here are four points concluded for the DSG:

1) Two grids involved;
2) More computation and more memory cost compared with the SSG, but both are less than those in the RSG;
3) Handle arbitrary anisotropic media very well;

4) Grids are of diamond shape.

The discrete DSG forms of the first expressions from both equations (3.1) and (3.2) are written as (in arbitrary anisotropic media),

$$\frac{VX}{\Delta x} = (VX_{i,j,k+1}^{t-1} - VX_{i,j,k-1}^{t-1})/\Delta x$$

$$\frac{VY}{\Delta x} = (VY_{i,j,k+1}^{t-1} - VY_{i,j,k-1}^{t-1})/\Delta x$$

$$\frac{VZ}{\Delta x} = (VZ_{i,j,k+1}^{t-1} - VZ_{i,j,k-1}^{t-1})/\Delta x$$

$$\frac{VX}{\Delta y} = (VX_{i,j+1,k}^{t-1} - VX_{i,j-1,k}^{t-1})/\Delta y$$

$$\frac{VY}{\Delta y} = (VY_{i,j+1,k}^{t-1} - VY_{i,j-1,k}^{t-1})/\Delta y$$

$$\frac{VZ}{\Delta y} = (VZ_{i,j+1,k}^{t-1} - VZ_{i,j-1,k}^{t-1})/\Delta y$$

$$\frac{VX}{\Delta z} = (VX_{i+1,j,k}^{t-1} - VX_{i-1,j,k}^{t-1})/\Delta z$$

$$\frac{VY}{\Delta z} = (VY_{i+1,j,k}^{t-1} - VY_{i-1,j,k}^{t-1})/\Delta z$$

$$\frac{VZ}{\Delta z} = (VZ_{i+1,j,k}^{t-1} - VZ_{i-1,j,k}^{t-1})/\Delta z$$

$$TXX_{i,j,k}^{t} = TXX_{i,j,k}^{t-1} + \mathrm{C11}_{i,j,k}\frac{VX}{\Delta x} + \mathrm{C12}_{i,j,k}\frac{VY}{\Delta y} + \mathrm{C13}_{i,j,k}\frac{VY}{\Delta y} + \mathrm{C14}_{i,j,k}\left(\frac{VY}{\Delta z} + \frac{VZ}{\Delta y}\right) + \mathrm{C15}_{i,j,k}\left(\frac{VX}{\Delta z} + \frac{VZ}{\Delta x}\right) + \mathrm{C16}_{i,j,k}\left(\frac{VY}{\Delta x} + \frac{VX}{\Delta y}\right))\Delta t \quad (3.12)$$

when $i + j + k = odd\ number$ (see section 3.4)

$$VX_{i,j,k}^{t} = VX_{i,j,k}^{t-1} + \left(\frac{TXX_{i,j,k+1}^{t-1} - TXX_{i,j,k-1}^{t-1}}{\Delta x} + \frac{TXY_{i,j+1,k}^{t-1} - TXY_{i,j-1,k}^{t-1}}{\Delta y} + \frac{TXZ_{i+1,j,k}^{t-1} - TXZ_{i-1,j,k}^{t-1}}{\Delta z}\right)\Delta t / RHO_{i,j,k} \quad (3.13)$$

when $i + j + k = even\ number$ (see section 3.4)

Note the assumption for equations (3.12) and (3.13) is the odd/even condition in section 3.4.

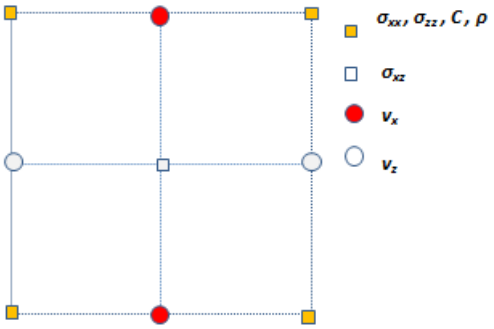
σxx, σzz, C, ρ
σxz
vx
vz

(a)

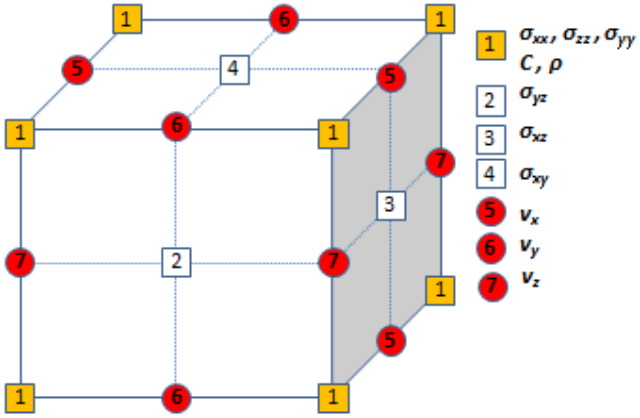
1
σxx, σzz, σyy
C, ρ
2
σyz
3
σxz
4
σxy
5
vx
6
vy
7
vz

(b)

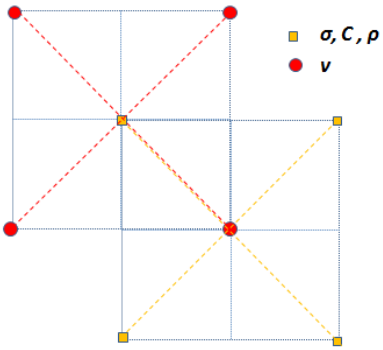
σ, C, ρ
v

(c)

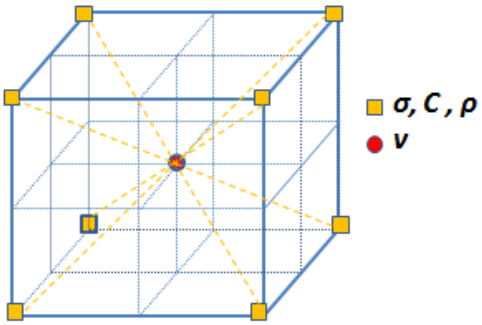
σ, C, ρ
v

(d)

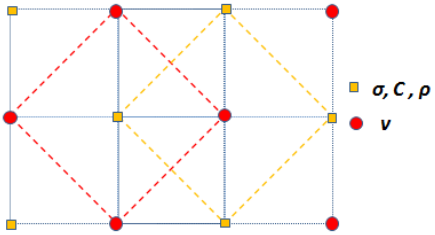
σ, C, ρ
v

(e)

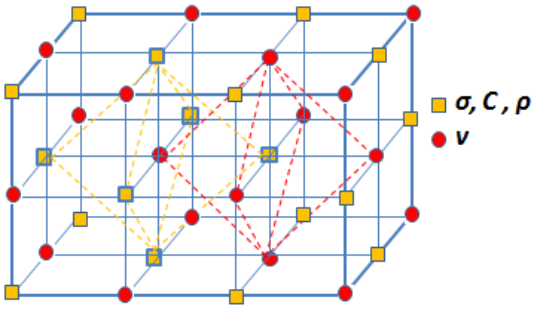
σ, C, ρ
v

(f)

Figure 3.1: Three different staggered grids: standard staggered grid in 2D case (a) and 3D case (b), rotated staggered grid in 2D case (c) and 3D case (d), and diamond staggered grid in 2D case (e) and 3D case (f). For all staggered grids, the derivatives of velocity components are solved with central differences at the location where the stress components are defined, and vice versa. The number of grids in the SSG is more than that in the RSG or DSG. The RSG solves the wavefield derivatives along the diagonals in the grids. The DSG solves the wave field derivatives along the coordinate axes, but leading to non-rectangular grids.

3.3.2 Quantitative comparison

Seismic modelling is a precise process when it comes to the computation time, memory cost and other computational aspects. Current computer power never satisfies geophysicists' modelling demand, particularly in 3D cases, so compromises and special treatments have to be considered. Here I try to quantitatively compare the three FD schemes in 3D orthorhombic media based on Figure 3.2. According to Lisitsa and Vishnevskiy (2010), the dispersion relations are the same for the SSG and DSG schemes (assuming the 2nd order in space),

$$\frac{\sqrt{3}\tau \, max\,|V_{qP}|}{h^L} \leq 1 \tag{3.14}$$

where τ is the sample rate in modelling, V_{qP} is the qP velocity, and h^L is the cell spacing in the DSG and SSG scheme. As for the RSG schemes, the dispersion relation is

$$\frac{\tau \, max\,|V_{qP}|}{h^R} \leq 1 \tag{3.15}$$

where h^R is the grid spacing in the RSG scheme and others are the same as in equation (3.14). Note that there is a $\sqrt{3}$ difference between equation (3.14) and (3.15).

Here I make assumptions for the comparison: seismic FD modelling is performed in 3D orthorhombic media (avoiding the interpolation problem), to the 2nd order in space and the 2nd order in time; and the models for the three schemes are of the same size in space; the same numerical accuracy has to be maintained for the three

schemes. Based on these assumptions, I have derived the related parameter comparison of seismic modelling as shown in Table 3.1. The details in the table are

- Sample rate: assuming the same value τ;
- Cell spacing: the spacing is h^L, $h^L/\sqrt{3}$ *and* h^L respectively for the three schemes based on equations (3.14) and (3.15). The spacing in the RSG is smaller than those in the other two, so more cells are required in the RSG if the models in the three schemes are of the same size.
- Number of cells along one axis: to keep the same model size for each scheme, more cells ($\sqrt{3}n$) are required along one coordinate axis for the RSG;
- Number of cells in the 3D model: multiplication of the numbers of cells in the three axis directions generates the total number of cells in the 3D model;
- Variables in each cell:
    - SSG: I combine the medium parameters, 9 elastic constants in orthorhombic media and 1 density, into 1 medium parameter, which will be discussed later in the section 3.5. There are 10 variables, including 9 wavefield components and 1 medium parameter as shown in Figure 3.2a;
    - RSG: 10 variables, same as SSG, as shown in Figure 3.2b;
    - DSG: 40 variables, which are 4 times of that in RSG, due to 4-times the number of nodes as in RSG as shown in Figure 3.2c.
- Memory cost for all variables in the 3D model: (Variables in each cell) * (Number of cells in the 3D model)
- Derivative operation in each cell: calculation of each derivative, like $\frac{v_x^i - v_x^{i-1}}{dx}$, is regarded as one operation. Based on equation (3.1) and (3.2), 18 derivatives have to be solved.
    - Therefore in SSG, it is 18;
    - In RSG, the derivative combination is made along the 4 diagonals leading to 4 times the operations in SSG; however, half of the derivative operation can be re-used for the 4 diagonal combinations. Finally, there is only 2 times the operation in SSG.

- In DSG, 4 times the nodes used in SSG leads to 4 times the operations in SSG;

- Total derivative operation: (Derivative operation in each cell) * (Number of cells in the 3D model).

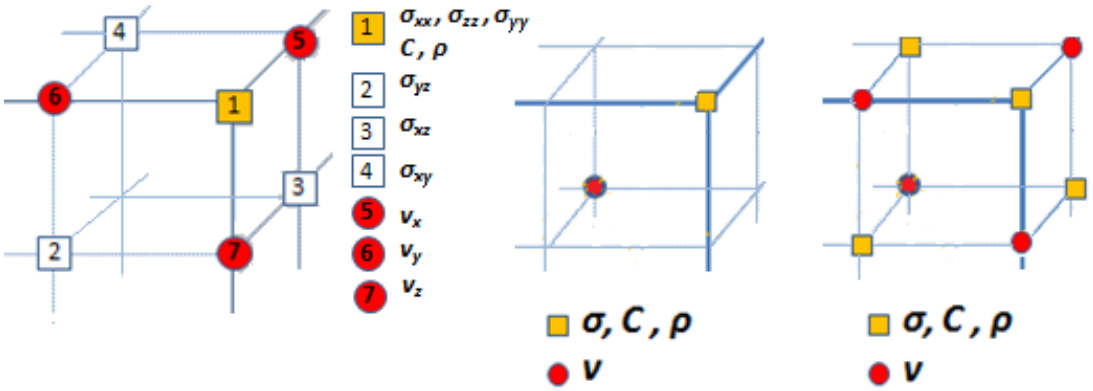

(a) (b) (c)

Figure 3.2: Unit cells in the three schemes: SSG(a), RSG(b) and DSG(c). Note the length of the unit cells here are half the cell spacing due to the staggered grid.

	SSG	**RSG**	**DSG**
Anisotropic medium can be handled	*Orthorhombic medium*	*Arbitrary anisotropic media*	*Arbitrary anisotropic media*
Sample rate	τ	τ	τ
Cell spacing	h^L	$h^L/\sqrt{3}$	h^L
Number of cells along one axis	n	$\sqrt{3}n$	n
Number of cells in 3D model	$n*n*n$	$3\sqrt{3}*n*n*n$	$n*n*n$
Variables in each cell	10	10	40
Memory cost for all variables in the 3D model	$n*n*n*10 = M$	$3\sqrt{3}*n*n*n*10 \approx 5.2M$	$n*n*n*40 = 4M$
Derivative operations for each cell	*18*	*18*2*	*18*4*
Total derivative operations	$n*n*n*18 = T$	$3\sqrt{3}*n*n*n*18 * 2 \approx 10.4\,T$	$n*n*n*18*4 = 4T$

Table 3.1: The detailed quantitative comparison

3.3.3 Discussion on comparison

From the comparison results in Table 3.1, I find the SSG has the best performance both in memory cost and the total derivative operation, based on the assumptions I made. The DSG requires 4 times the memory cost and total derivative operation in the SSG. The RSG needs more memory and particularly more derivative operations compared with the other two. The total derivative operations, to some extent, represent the total computation time required.

Studies in seismic modelling with the DSG have been active since 2007. Even as I am completing my thesis, Bernth and Chapman (2011) give a full comparison of dispersion relations between the RSG and DSG scheme. They make the following conclusions:

- The field variables per volume of DSG ≈ 0.77 times of that in RSG
- The CPU cycle per volume of DSG ≈0.38 times of that in RSG

Similarly, I compute the two ratios in my comparison, which are 0.77 (4/5.2) and 0.38 (4/10.4), respectively. These two ratios are exactly consistent with the two ratios given by Bernth and Chapman (2011). Note that, in the RSG, the combination calculation will cost extra computation, and the final computation ratio will be even smaller than 0.38. Based on the comparison above, the DSG has better performance than the RSG in seismic modelling. I note that all current seismic modelling in TTI media (e.g. Hokstad et al., 2002; Bansal and Sen, 2008) are based on the SSG or the RSG. Since we see the advantages of the DSG, it probably will change this situation.

Seismic modelling in media with anisotropic symmetry lower than orthorhombic symmetry is very important in terms of solving anisotropic wave propagation in such media. The DSG method can enhance our capability to develop efficient tools for modelling-based process in more complex and realistic Earth models. For example, reverse time migration (RTM) and full wave form inversion in TTI media, bother of which are based on anisotropic wave propagation, can help to image the spatial distribution of dipping fracture sets in the subsurface.

On the other hand, if we do hope to include SSG modelling in such complex media (Hokstad et al., 2002), the suggested way is to reduce the SSG cell spacing, which to some extent, cancels out some of the extra error caused by interpolation in the SSG. But how much we need to reduce the cell spacing, in order to have the comparable model size and similar accuracy to those in the RSG and DSG, is still unknown, and therefore more academic effort is needed.

3.4 A modified implementation with the DSG scheme

Lisitsa and Vishnevskiy (2010) give a detailed description of the Lebedev scheme in seismic modelling in general anisotropic media. However, there is no direct description of how they deal with the diamond grids and apply it in their practical modelling. Normally，difference components or parameters are saved separately in rectangular or cubic arrays during implementation, but in this scheme, it is inconvenient to save the components or parameters in such arrays because the grids are like diamonds. Based on my study, the diamond grids can be specially treated during implementation or more specifically, the two different diamond grids can be merged to form a regular rectangular one in order to handle all wavefield components and easily calculate the derivatives in the DSG scheme.

Based on the DSG in 3D case (Figure 3.1f), I combine all of the grid σ and the grid v to form a new grid T, and therefore there is a T at every grid location in the 3D model, which is then of rectangular shape (see Figure 3.3), and there is only one grid in the whole model. The condition for such a combination is, if the sum $i+j+k$ of the $T(i,j,k)$ subscripts is odd, $T(i,j,k)$ represents stress components; if $i+j+k$ of the $T(i,j,k)$ subscripts is even, $T(i,j,k)$ represent velocity components; it is the same if the sum is even for stress components, odd for velocity components symmetry in the velocity/stress component distribution. The advantage is, equations (3.16) can be used to approximate the three spatial derivatives of either stress components or velocity components along three axes under the condition.

$$\frac{T^{i+1,j,k}-T^{i-1,j,k}}{\Delta x},\frac{T^{i,j+1,k}-T_v^{i,j-1,k}}{\Delta y},\frac{T^{i,j,k+1}-T^{i,j,k-1}}{\Delta z} \tag{3.16}$$

where $T^{i+1,j,k}$ gives the component at the location $(i+1,j,k)$, and similarly with the others; Δx, Δy and Δz are the discretized spacing along the x-, y- and z- axes, respectively. The three equations above represent the derivatives of T at the location (i,j,k) with respect to x, y and z, respectively. This greatly simplifies the calculation of the derivatives with the subscripts of the new grid T.

To implement the SSG or RSG, we need to carefully examine grid locations in Figures 3.1a and b, or Figures 3.1c and d in order to solve the derivatives correctly with the proper subscripts. For the DSG, with equations (3.16) and the odd/even condition, the derivatives can be solved without referring to Figures 3.1e and f, because the three to-be-solved derivatives at (i, j, k) can always be solved with the adjacent 6 components at the 6 vertexes of the diamond as shown in equations 3.16. With this way to process the grids, the DSG scheme is the simplest scheme to implement among the three schemes, and in particular, it works in general anisotropic media.

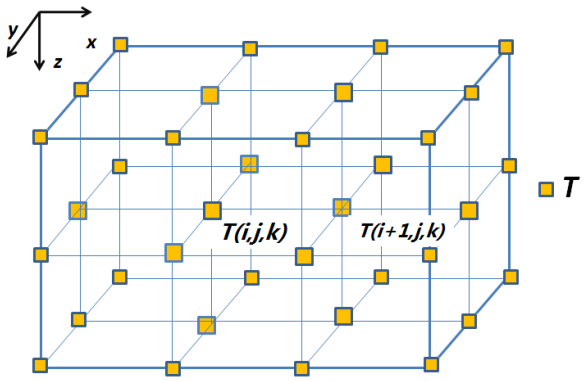

Figure 3.3: The modified implementation of the DSG scheme, where two grids are merged into one. This greatly simplifies the calculation of the derivatives with the subscripts of the new grids. Note that when $i+j+k$ *is* even , $T(i,j,k)$ represents velocity components; when $i+j+k$ is odd , $T(i,j,k)$ represents stress components

3.5 An optimized modelling workflow, source setting and absorbing boundary condition

3.5.1 Modelling scheme choice and an optimized modelling workflow

My modelling applications in Chapters 4 and 5 deal with discrete fracture models and 3D HTI models, which involve anisotropic media with lower order symmetry, as far as orthorhombic. Based on the comparison in section 3.3, the SSG scheme is sufficient to handle such fractured models in my application, and hence it is chosen as the FD scheme for my 3D implementation.

In terms of 3D modelling, two aspects cannot be neglected: computation time and memory cost, as I discussed in section 3.3. Once the scheme is determined the computation time is normally fixed. However, special treatment of modelling parameters can save memory and therefore enable building larger realistic 3D fractured models. For example in Chapter 5, larger 3D fractured models are required for P-wave azimuthal analysis. Seismic modelling in a 3D orthorhombic medium involves 6 stress components, 3 velocity components, 9 elastic constants, and 1 medium density. Altogether at least 19 3D cubic variables are needed.

Usually a model is composed of several layers or blocks in a 3D situation. Based on this assumption, I use different indices to distinguish different layers or blocks in 3D models (the index is the medium structure parameter here). Then I link each index to medium elastic parameters. Therefore 9 elastic constants and 1 medium density are merged into 1 medium structure parameter, which means only 10 3D variables are needed, around half of the original 19, and a significant reduction in complexity. During modelling, the medium elastic parameters can be obtained by examining the indices.

Figure 5.3 describes the general optimized modelling steps which are suitable for any of the three staggered grid finite difference schemes. First, three types of parameters are defined: medium structure parameters, medium elastic parameters, and modelling parameters. These parameters are input to the right hand of equation

(3.1) to solve the velocity derivatives. Then the stress components on the left hand of equation (3.1) are solved with these velocity derivatives and the stress components at the previous time step (FD in time). The solved stress components are used to solve their derivatives on the right hand of equation (3.2) which then are substituted to calculate the velocity components on the left hand of equation (3.2). The final step in Figure 5.3 is to output the velocity components at the geophone location as the seismic records. After all of this, a new loop repeats as above. Note that during the loops, the boundary condition and the source setting are considered.

3.5.2 Source setting and absorbing boundary condition

Due to the difference existing in the three staggered grids, source setting is different, but the common way is to add an explosive source with a series of magnitudes of discrete Ricker wavelet (equation (3.17), Sheriff, 2002) to the two (σ_{xx} and σ_{zz} in 2D) or three (σ_{xx} , σ_{yy} and σ_{zz} in 3D) normal stresses near the source coordinate. In our implementation, we apply the Ricker wavelet series on the points listed in Table 3.2 when different schemes are considered.

$$f(t) = (1 - 2(\pi f_M t)^2)e^{-(\pi f_M t)^2} \tag{3.17}$$

Different FD schemes	Grid locations to be applied the source wavelet on the normal stresses
2D SSG	The 4 yellow points in Figure 3.1a
3D SSG	The 8 yellow points in Figure 3.1b marked with number 1
2D RSG	The 4 yellow points in Figure 3.1c
3D RSG	The 8 yellow points in Figure 3.1d
2D DSG	The 4 yellow vertexes of the yellow diamond in Figure 3.1e
3D DSG	The 6 yellow vertexes of the yellow diamond in Figure 3.1f

Table 3.2: Grid locations to be applied the source wavelet on the normal stresses in different FD schemes.

Once the source is triggered, the wave will propagate away from the source location. If the propagation time is long enough, the wave will hit the model boundaries and

reflect backwards. Normally the reflection from the model boundaries is not useful and an absorbing boundary with a certain thickness from the model sides is applied. In our implementation, the absorbing function ($G = \exp\{-[0.015(20-i)]^2\}$, Cerjan et al., 1985) is employed to attenuate the energy at the boundary of the 2D/3D models. The number 20 means the boundary thickness with 20 grids. For the FD operator, the 8^{th} order in space and 2^{nd} order in time are considered.

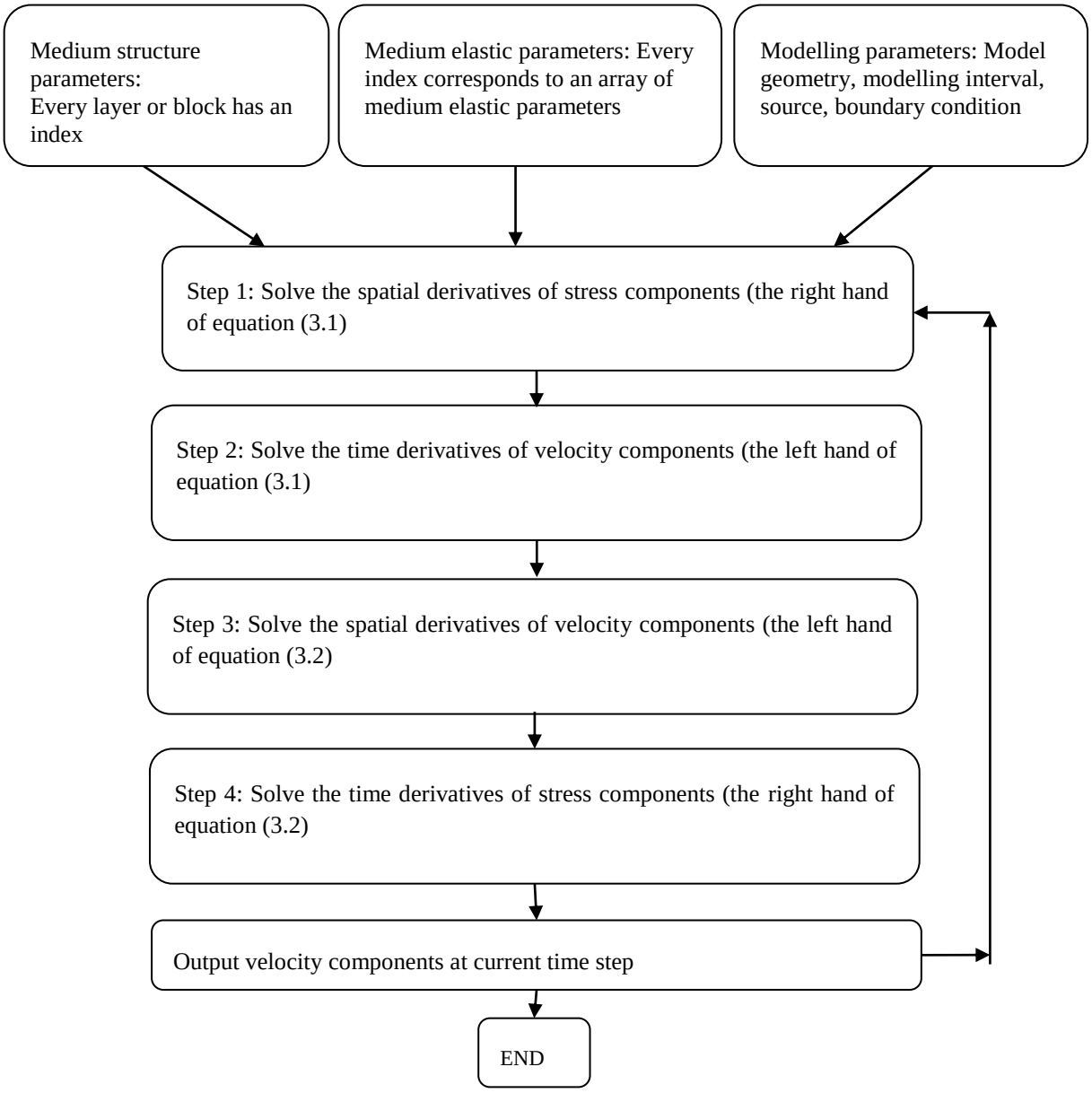

Figure 3.4: The optimized 3D modelling workflow. In this workflow, medium parameters are separated into medium structure parameters and medium elastic parameters, which enables us to save computation memory and build larger fractured models.

3.6 Example comparison and 3D algorithm validation

Though I chose the SSG scheme to implement my 3D modelling, I first implement all three schemes in the 2D case in order to understand their advantages and disadvantages in seismic modelling. Here I carry out a series of 2D examples in various anisotropic media with different FD schemes. A 3D three-layer example with the SSG scheme is also given to demonstrate the 3D implementation. Most importantly, the 3D results are validated with results from the reflectivity method implemented in ANISEIS.

3.6.1 Examples: 2D Seismic modelling with the SSG, RSG and DSG

Figure 3.5 demonstrates two isotropic modelling examples with the SSG (Figure 3.5a) and the RSG (Figure 3.5b). All the model parameters are the same and only the schemes (SSG or RSG) are different. The details of the modelling parameters are given in the caption of Figure 3.5. As expected, the wavefront of the P-wave in the snapshots for this 2D Isotropic medium are circles. More numerical dispersion is observed inside the wavefront in Figure 3.5b; the reason is that in the RSG the dispersion relation requires smaller grid size to maintain the same accuracy as in the SSG or DSG. Figure 3.5c shows two overlaid traces extracted from the two red line locations in Figure 3.5a and b, where the fluctuations further confirm the numerical dispersion in the RSG scheme.

This is important because the numerical dispersion results in waveform properties similar to those of seismic scattering but not present in the model, leading to possible ambiguity in interpreting real data.

Two anisotropic examples with the SSG and RSG schemes are shown in Figure 3.6. Figures 3.6a and b are the x-component and the z-component snapshots respectively in a VTI medium, which are calculated with the SSG. Figures 3.6c and d are the x-

component and the z-component snapshots respectively in a TTI medium, which are calculated with the RSG. The TTI medium is generated by rotating the VTI medium 30 degrees anticlockwise around the y-axis. All other parameters are the same. Anisotropic parameters are given as Thomsen's parameters. From the plots in Figures 3.6c and d, we can clearly see the rotation angle in the snapshots. In the two examples, both the P-wave and S-wave are observed, and the long axes of the P-wave wavefront point to the system plane direction in both the VTI and TTI media. Because the geometry parameters are the same for the SSG and DSG, numerical dispersion is observed as well in Figures 3.6c and d. The two examples demonstrate that the SSG is able to handle up-to-orthorhombic media, whilst the RSG is capable of general anisotropic media.

Figure 3.7 shows two similar examples to Figure 3.5, but with the DSG scheme. Figures 3.7a and b show the x-component and z-component snapshot respectively in a VTI medium. Figures 3.7c and d shows the corresponding snapshots in the TTI medium generated by clockwisely rotating the VTI medium in Figure 3.7a and b 45^{o}. The red dashed lines in the plots are the contours of the corresponding group velocities, which show a good consistency with the P-wave fronts. To some extent, this validates the implemented 2D DSG scheme. The dispersion relations (from equation (3.14)) in the two examples are the same, so they are of the same accuracy. No numerical dispersion is observed in any of them. The two examples indicate the capability of the DSG in a general anisotropic medium.

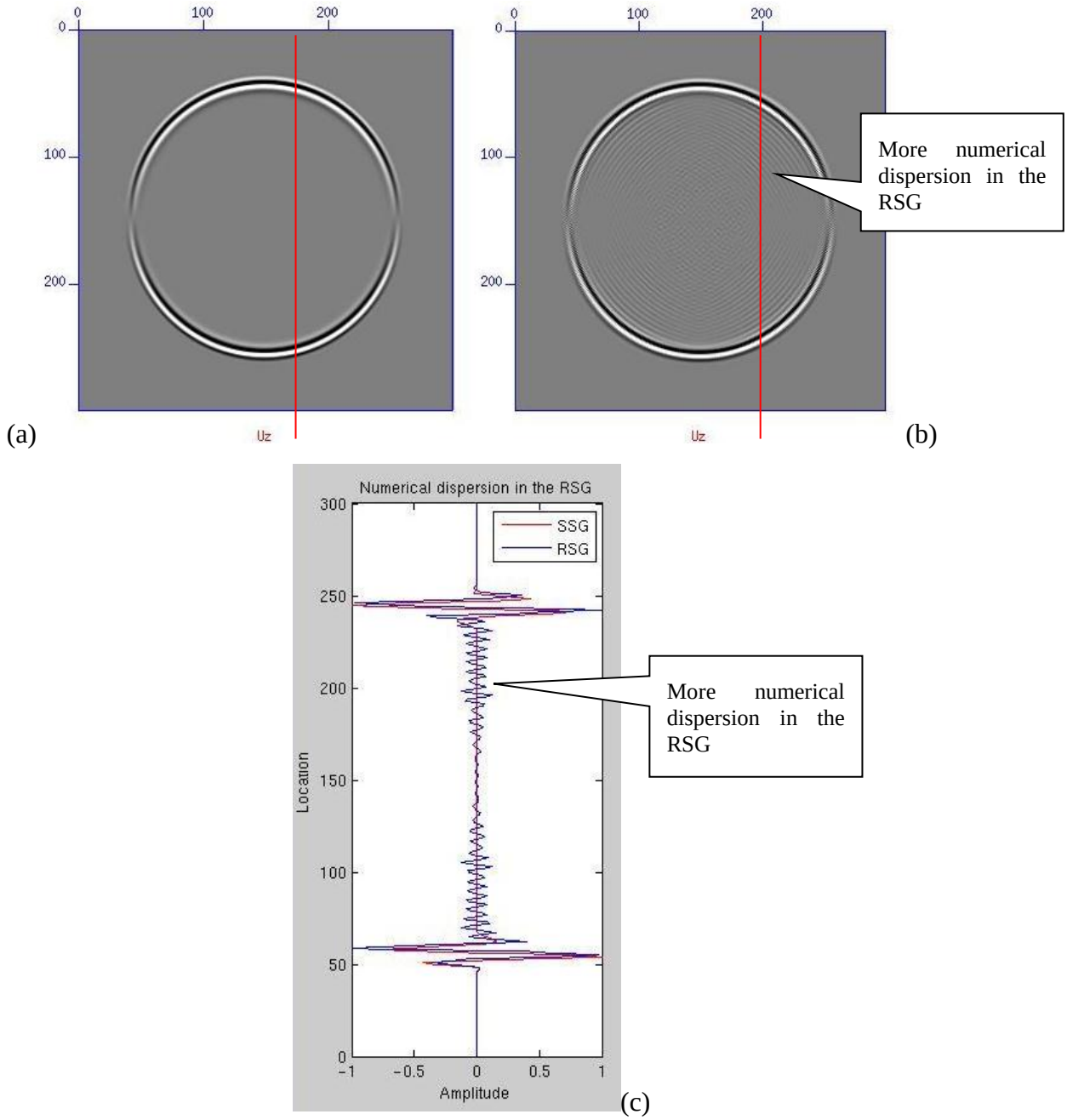

Figure 3.5: Velocity Z-component snapshots taken with the SSG (a) and RSG (b) in an isotropic medium, and two overlaid traces (c) extracted from the two red line locations in (b) and (c). The medium parameters are, P-wave velocity 3.5 km/s, S-wave velocity 2 km/s and density 2.2 g/cm^3. An explosive source is set in the middle of the model; the time interval is 1 ms; A Ricker wavelet is applied with the dominant frequency 40 Hz; the record time is 0.5s; the model size is 300x300, and the grid size is 10m x 10m. All the modelling parameters are the same except with different schemes. Inside the wavefront in (b) a lot of scattering-like wave occurs, which is from numerical dispersion. Compare the traces from SSG and RSG, the fluctuations are very obvious, but the SSG shows good accuracy. Unit for the axes is grid number in (a) and (b).

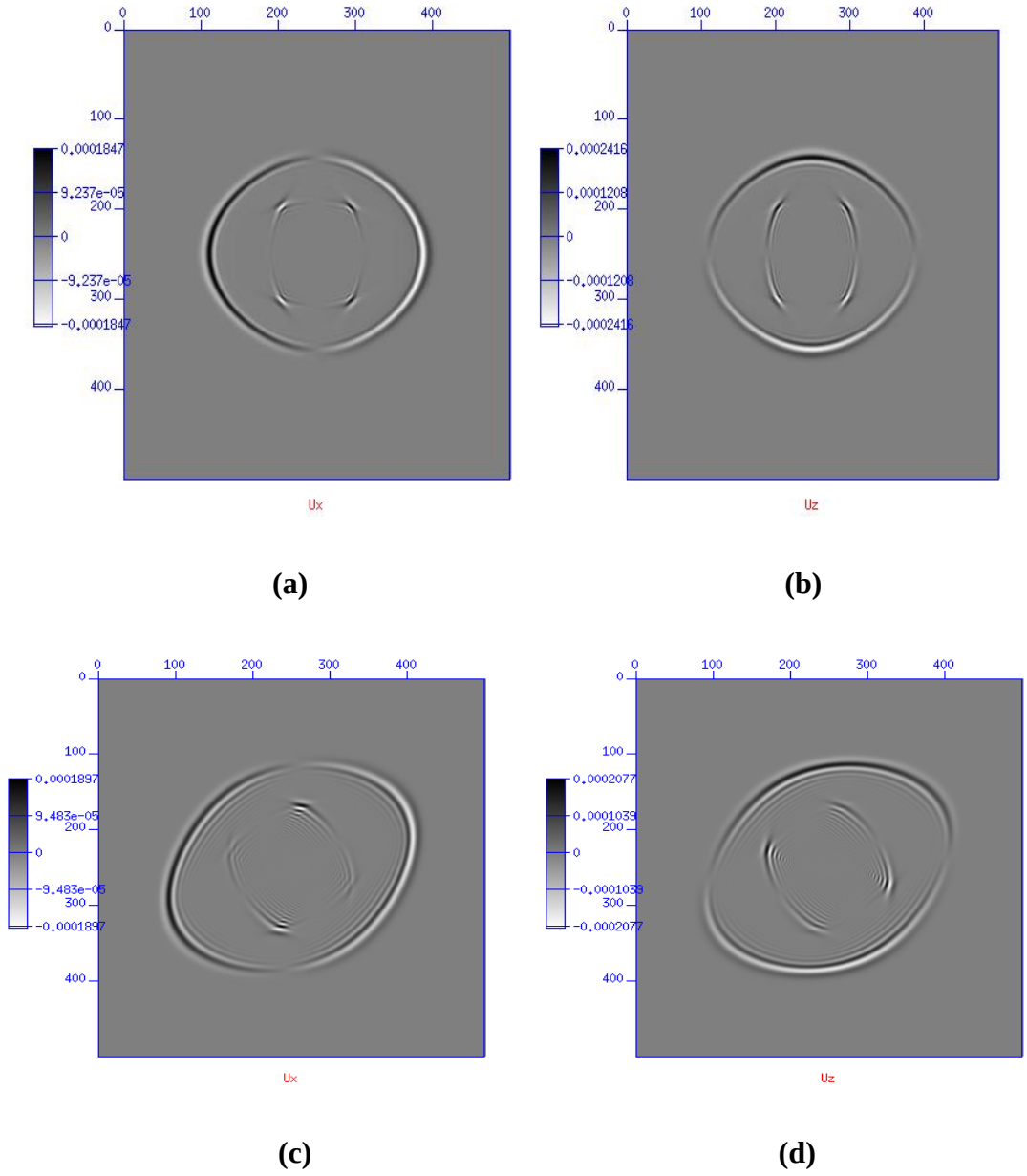

Figure 3.6: Snapshots of velocity components with the RSG scheme. (a) and (b) are the snapshots of velocity x-component and z-component respectively in a VTI medium with Thomsen's parameters, α_0 =2.4495 km/s, β_0 =1.4142 km/s, ε =0.3333, δ = 0.0885, γ =0.2500 and ρ =1 g/cm^3. (c) and (d) correspond to (a) and (b) respectively with application of a 30 degree anticlockwise rotation of the VTI medium around the y-axis, namely, a TTI medium. The grid size is 500x500; a explosive source is set in the middle of each model; the time interval is 0.5 ms; a Ricker-wavelet is applied with the dominant frequency 40 Hz; the grid size is 5m x 5m; the record time is 0.3s. Unit for the axes is grid number.

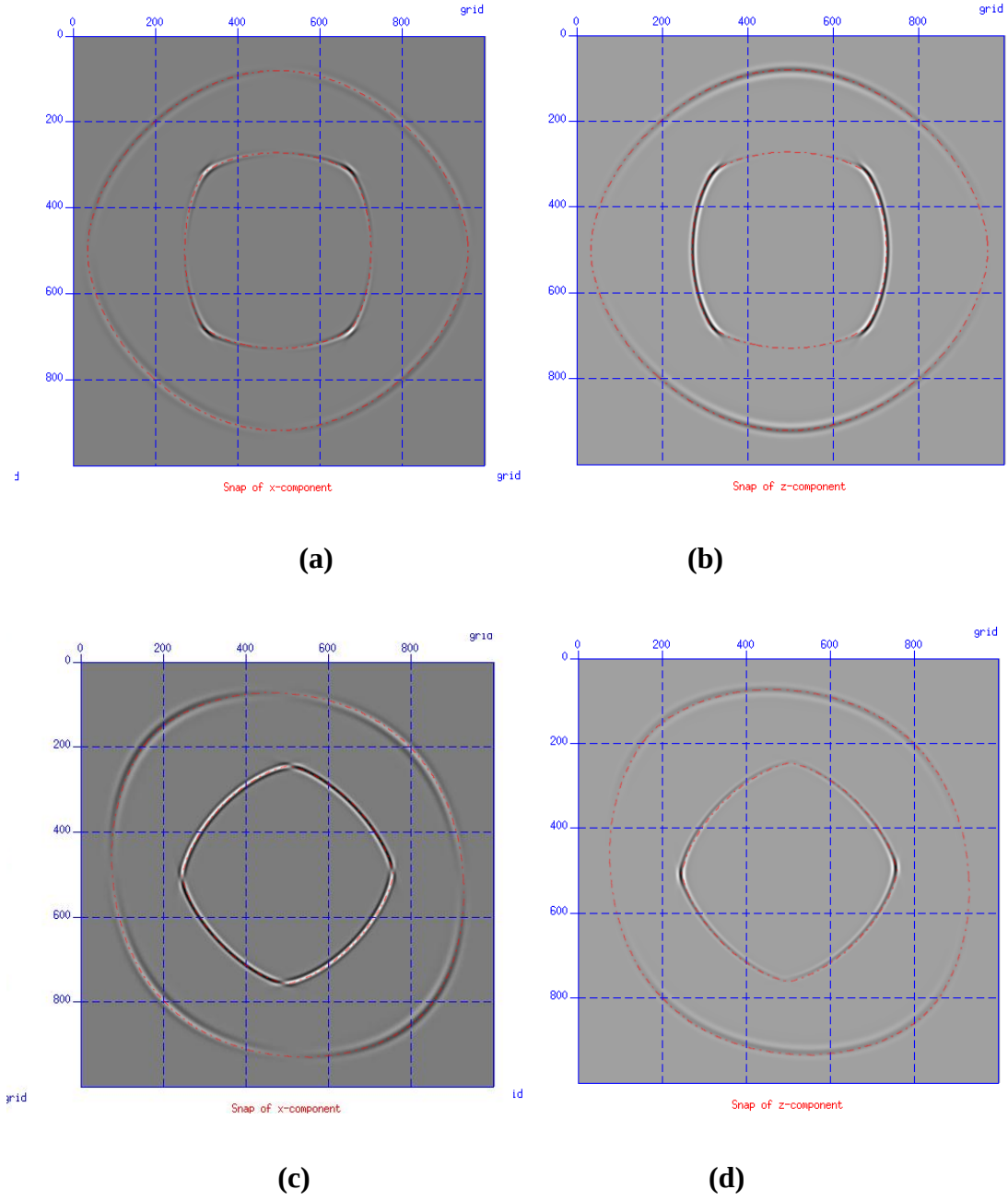

Figure 3.7: Snapshots of velocity components with the DSG scheme. (a) and (b) are the snapshots of velocity x-component and z-component respectively in a VTI medium with Thomsen's parameters, α_0=3.368 km/s, β_0=1.829 km/s, ε=0.11, δ=-0.035, γ=0.255 and ρ=2.5 g/cm^3(from Thomsen, 1986). (c) and (d) correspond to (a) and (b) respectively after application of a 45 degree clockwise rotation of the VTI medium around the y-axis, i.e., a TTI medium. The model size is 1000 *1000; an explosive source is set in the middle of each model; the time interval is 1 ms; the grid size is 5m *5m; a Ricker-wavelet is applied with the dominant frequency 20 Hz; the record time is 0.72s. Unit for the axes is grid number.

3.6.2 An example: 3D seismic modelling with SSG and algorithm validation

In this chapter, the implementation of seismic modelling in 3D fractured media is my major objective, which is an important extension from the 2D case. Chapters 4 and 5 will employ this technique to reveal more insights into azimuthal characteristics of seismic response in 3D fractured media. A 3-layer model is given here to demonstrate my 3D implementation, which is then validated by comparing the example synthetic sections with the corresponding sections obtained using the reflectivity method.

Model

Figure 3.8 shows the 3-horizontal-layer model, with the middle layer being a HTI (or fractured) layer and the other two being isotropic layers. Table 3.2 lists the parameter details for the three layers. The size of the model is 1000m * 1000m *2000m, corresponding to the grid size 100 *100 *200. The source (the red dot in Figure 3.8(a)) is located at the grid location (0m, 0m, 0m), which is at the corner of the model at the surface. The geophones (the blue dots in Figure 3.8a) are distributed at each grid location at the surface. Note the values in the color bar of Figure 3.8b are the medium structure parameters, which are linked to the medium elastic parameters in Table 3.2 during modelling. As I discussed in section 3.5, this arrangement can help to save memory in building large 3D models. In practice, there is a layer that surrounds the whole 3D model, which is used to attenuate the energy to the boundary to avoid further reflection from the boundary. The attenuation layer is not taken into account in the parameters. A 15Hz Ricker wavelet is used as the source. Once all parameters are set, a 3D shotgather is recorded within 2 seconds in time.

	Layer 1	Layer 2	Layer 3
Medium	Isotropic	HTI	Isotropic
Thickness	700m	800m	500m
Grid number	70	80	50
Elastic parameters	v_p = 2.0 km/s, v_s = 1.2 km/s ρ = 1.8 g/cm^3	HTI: a rotation of the VTI below 90^o around the Y-axis; VTI: α_0 =3.292m/s, β_0 = 1.768m/s, ε = 0.195, δ =−0.220, γ= 0.180 ρ = 2.075 g/cm (shale, from Thomsen, 1986)	v_p = 2.5 km/s, v_s = 1.5 km/s ρ = 2.0 g/cm^3

Table 3.3: The parameters of the 3D 3-layer model

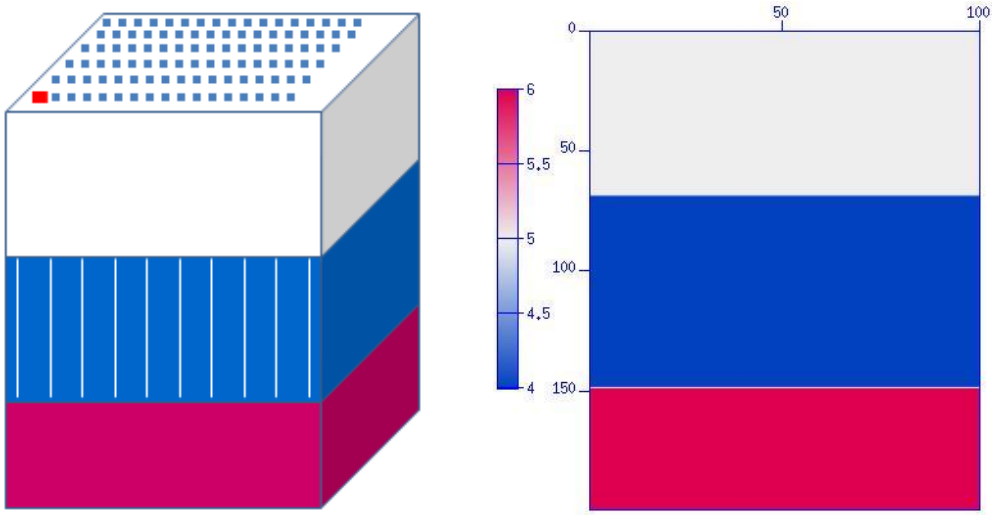

(a) **(b)**

Figure 3.8: The 3D three-layer model (a) with the model size 100 *100 *200 and the grid size 10m *10m *10m. The 2D section (b) in the X-Z plane shows the thickness of the layers. The values in the colour bar in (b) represent the medium structure parameters, three layers corresponding to 5, 4 and 6, respectively. During modelling, these values are linked to the medium elastic parameters in Table 3.2. An explosive source is set at the grid point (0, 0, 0); a Ricker-wavelet is applied with the dominant frequency 15 Hz; all the geophones (blue dots) are at the same depth as the source (red dot); the time interval is 1 ms; the record time is 2s. Unit for the axes is grid number.

Results and analysis

Two z-component sections are extracted from the 3D shotgather for analysis, i.e., a X-Z section (Figure 3.9) and a Y-Z section (Figure 3.10), both passing the source location. According to the geometry, the X-Z section is parallel to the fracture normal, the Y-Z plane is parallel to the fracture strike. I use the software ANISEIS (based on the reflectivity method, Taylor, 2005) to generate two new sections using the same modelling parameters, corresponding to the two extracted sections. Note the black wiggles in the plots (Figure 3.9 and 3.10) are the sections I generate with the SSD, and the red are the sections from ANISEIS. From the overlying wiggles in Figures 3.9 and 3.10, we can see a very good match, both in the amplitudes and in the phases, which validates my 3D implementation.

The black, blue and red arrows in Figures 3.9 and 3.10 point to the reflected P-wave from the first interface, PS-wave from the first interface, and P-wave from the second interface, respectively. Comparing the X-Z section and the Y-Z section, I find there is a noticeable difference in amplitude in the P-wave reflection from the top of the HTI layer, particularly in far offset (in the big ellipses), which reveals the difference in P-wave AVO response at the two different azimuths. In order to see the full azimuthal AVO (AVOA) response at the top of the HTI layer, I extract the maximum amplitudes of the first P-wave at all the geophone locations, which is then plotted in Figure 3.11. The AVOA in Figure 3.11 shows an elliptical variation within the offset range 400m-600m (the incident angles range approximately from 25°-30°), which reveal that the major axis of the elliptical variation coincides with the fracture strike direction. In Figures 3.9 and 3.10, the first P-wave has the same travel time, whilst for the second reflected P-wave, the travel time is a little larger at far offset (in the smaller blue ellipse zone) of the X-Z section (corresponding to the fracture normal direction), which agrees with the fact that P-wave velocity is smaller along the fracture normal direction.

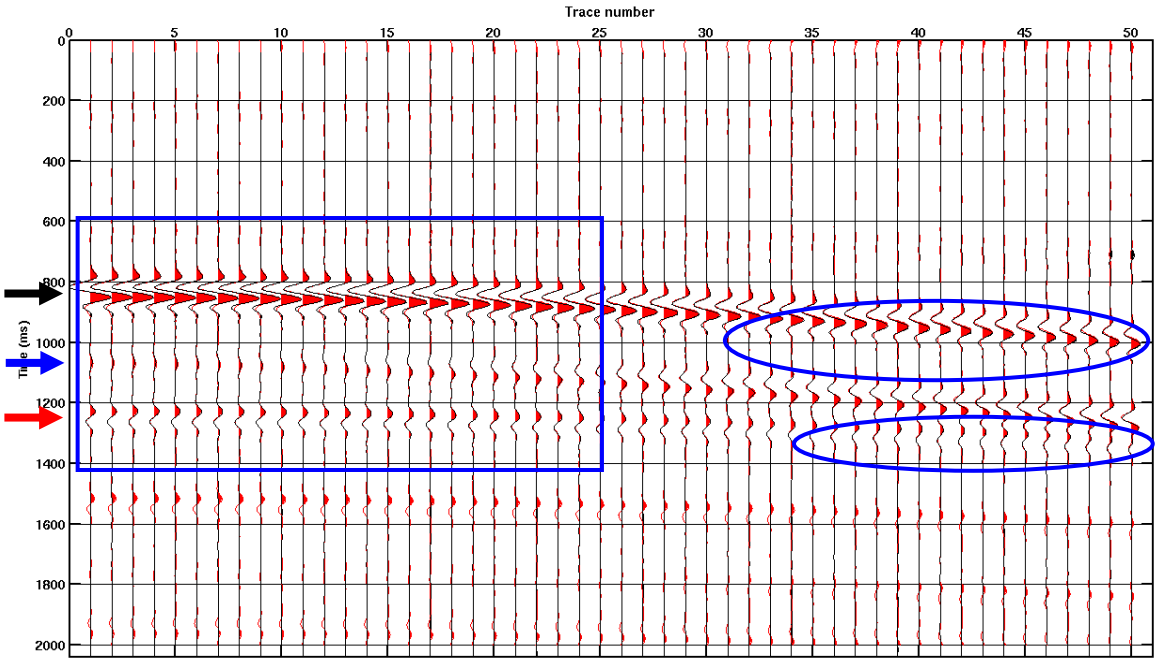

(a)

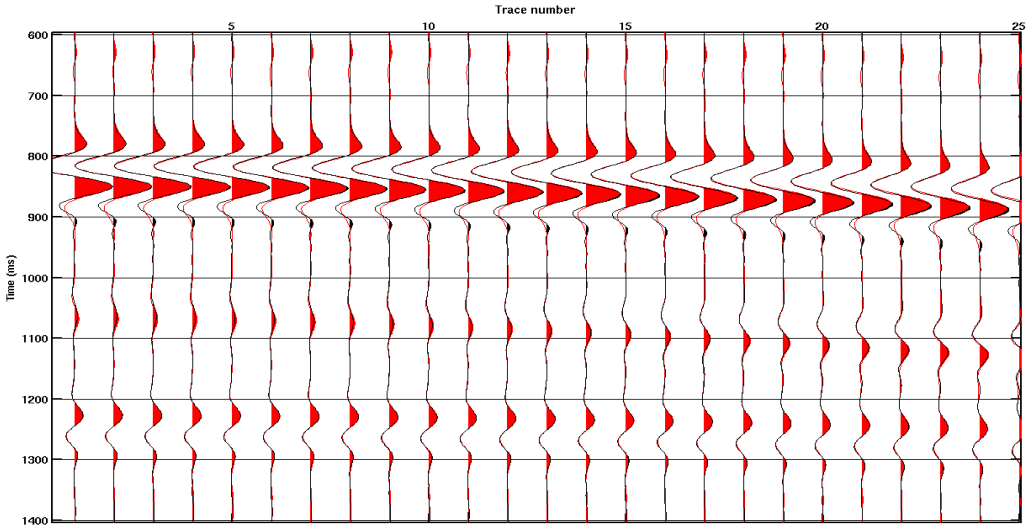

(b)

Figure 3.9: The synthetic section (a) of z-component in the X-Z plane, which passes the source and is perpendicular to the fracture strike. (b) is an expanded view of the blue rectangular zone in (a). The trace spacing is 20meters. The black traces are generated with the 3D SSG scheme; the red ones are generated with the reflectivity method (from the commercial software, Aniseis), with the same model as in Figure 3.8. We can see there is a clear match in the amplitudes between the sections. Two blue ellipses are marked for comparison with the Figure 3.10.

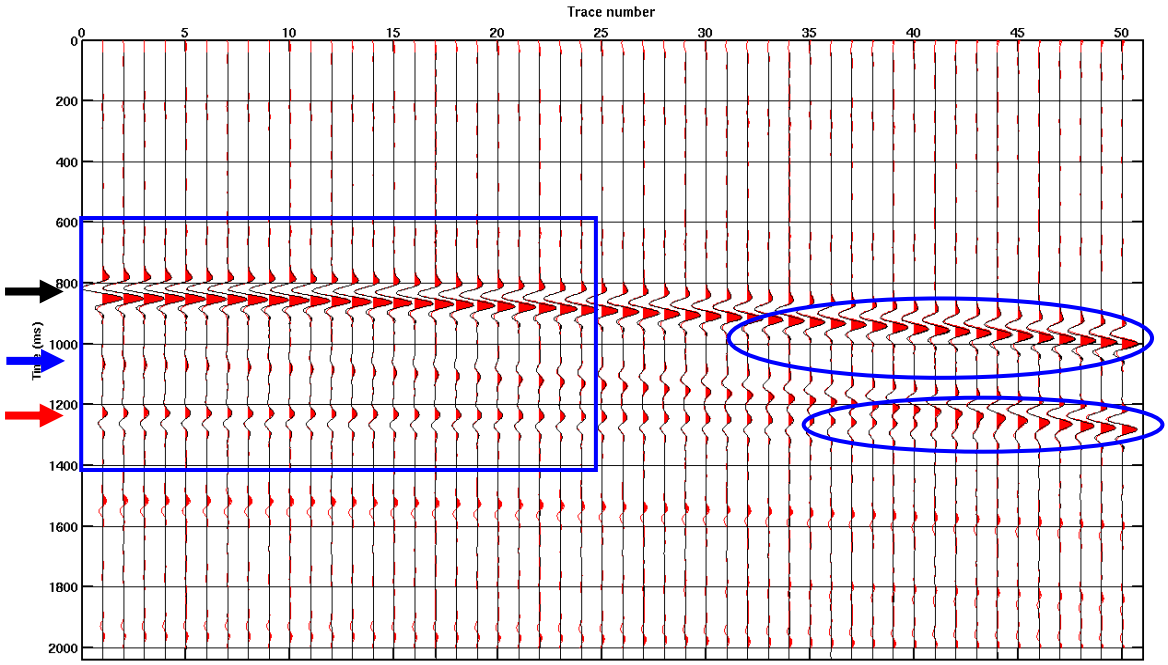

(a)

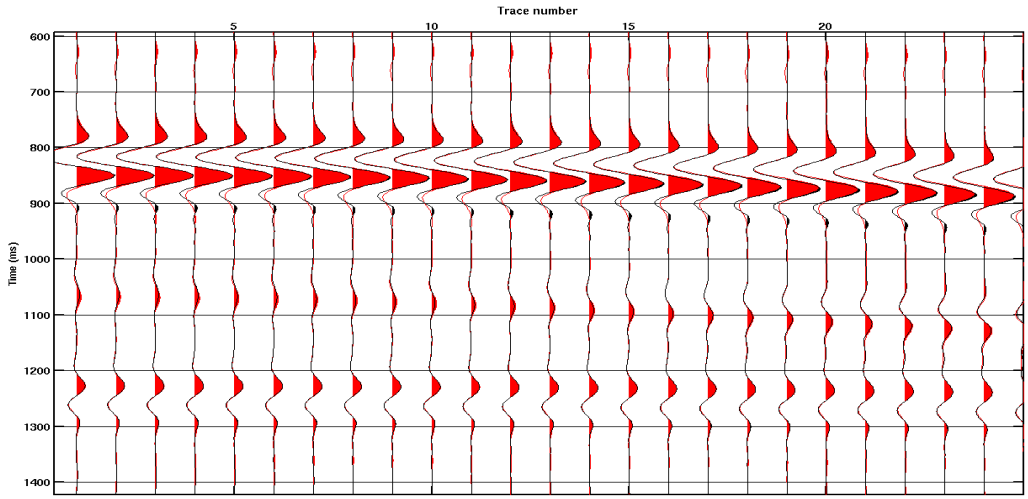

(b)

Figure 3.10: The synthetic section (a) of the z-component in the Y-Z plane, which passes the source and is parallel to the fracture strike. (b) is expanded view of the blue rectangular zone in (a). The trace spacing is 20meters. The black traces are generated with the 3D SSG scheme, the red ones are generated with the reflectivity method (from the commercial software, Aniseis), using the same model as in Figure 3.8. We can see there is a clear match in the amplitudes between the sections. Two blue ellipses are marked for comparison with the Figure 3.9.

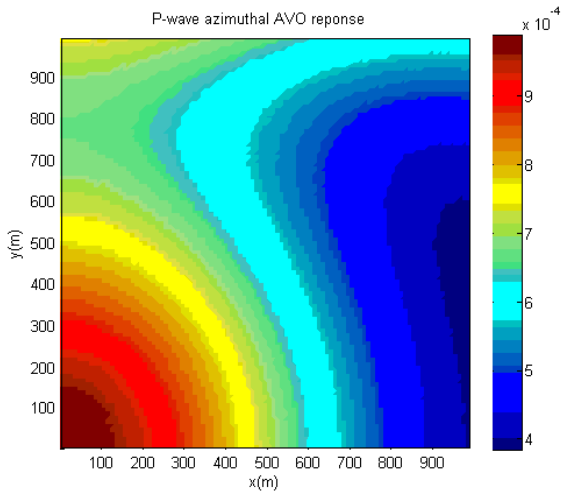

Figure 3.11: P-wave azimuthal AVO response at the top of the HTI layer. The response is at the horizontal plane and the colour denotes the amplitude magnitude from 0 to 90 degrees. The color reveals an elliptical variation. The Y axis denotes the fracture strike.

3.7 Computation issues

3D modelling is desirable in modelling realistic geological structures. Moreover, modelling in 3D fractured media is able to generate full-azimuth synthetic dataset for analyzing azimuthal variation in seismic attributes, while modelling in 2D case isn't. In Chapter 4 and 5, I will demonstrate these two points for realistic modelling in 3D fractured models. However, 3D modelling comes with a large computational cost with code development and CPU time. I have overcome this by extending the previous PhD work by Vlastos (2005), 2D modelling in fractured media, and by using a parallel computational library. The work in this chapter has taken 12 months.

Seismic modelling in 3D fractured media involved in this thesis has been implemented by myself as a independent fully-functioning software package. Use of this package is free for Edinburgh Anisotropy Project (EAP) staff, students and sponsors. The package uses a command line interface that is similar to the widely-used free seismic processing package, Seismic Unix (Stockwell, 1999). The modules below are included in the package:

1) Seismic data inputting, outputting, and sorting
2) Trace header setting
3) CDP binning
4) Numerical modelling: 2D SSG/RSG/DSG
5) Numerical modelling: 3D SSG (the major 3D modelling module)
6) Horizontally-layered-model building
7) Discrete-fracture-model building

For more practical modelling applications, parallel computation and environments are considered. The code is parallel-programmed with the library OpenMP, which allows using multiple CPU cores in a single PC to compute one or more shot gathers. Meanwhile, a series of shot gathers in 3D modelling surveys can be computed simultaneously on a PC Linux cluster by using Sun Grid Engine (SGE) job dispatch system.

3.8 Summary

Seismic modelling provides an important way to study the seismic response of a fractured medium. Regarding different modelling approaches, FD modelling shows its superiority over the PS methods, particularly in 3D fractured media. The comparison among the three different FD schemes, the SSG, the RSG and the DSG, demonstrates their advantages and issues when they are used in modelling applications.

Of the three schemes, the SSG scheme has the best performance when the media with up-to-orthorhombic symmetry system are considered. For more complex anisotropic media (monoclinic, TTI and triclinic), the DSG scheme is the preferred choice over the RSG, though its diamond grid feature poses an inconvenience in implementation, which however can be overcome by the modified method I have introduced. The modified method greatly simplifies the implementation of the DSG, which provides the theoretical base for developing new modelling-based anisotropic algorithms, such as reverse time migration and full wave inversion in TTI media.

Also, the quantitative comparison result of the RSG and the DSG has been confirmed by the recently released work (Bernth and Chapman, 2011). Based the comparison and the requirement in the later chapters, I chose the SSG scheme for 3D modelling implementation in the media with up to orthorhombic symmetry, and meanwhile, I introduce an optimized workflow for large 3D modelling, which is applied by separating medium parameters into medium structure parameters and elastic parameters. The 3D SSG modelling tool, which is considered as one major outcome in this thesis, provides a practical means to study various seismic phenomena of wave propagation in 3D fractured media.

To enhance my understanding of the three FD modelling schemes, I have demonstrated a series of 2D/3D anisotropic modelling examples. Most importantly, the 3D SSG example shows very good consistency with the results of the reflectivity method, which therefore validates my 3D SSG implementation.

4 Chapter 4 Seismic response of discrete fracture models: 3D numerical studies

In this chapter, I explore a variety of seismic characteristics in 3D discrete fracture models (DFM) using the FD modelling technique that I implemented in Chapter 3. I focus on two aspects of DFMs: (1) the effect of fracture spacing on seismic anisotropy and scattering, and (2) azimuthal AVO response and scattering attenuation. For the first aspect, a series of DFMs with different fracture spacing are designed to examine the effect of fracture spacing on seismic response. From the wavefield snapshots, I find the P-wave seismic anisotropy increases with decreasing fracture spacing, and also the scattered energy shows different patterns associated with the ratio of the spacing to the wavelength. For the second aspect, two DFMs (a vertical DFM and an orthogonal DFM) and an isotropic model are designed. I compare the difference in the snapshots, the shotgathers, the AVO response and the spectra content to reveal the effect of different discrete fracture sets on the seismic

response. The results show many unique phenomena in such DFMs. The two studies in this chapter aim to provide more insights of seismic response in the DFMs using seismic modelling, and therefore give some implications to invert the spatial distribution of discrete fractures in the subsurface.

4.1 Introduction

Fractured reservoir characterization and fracture property inversion are normally based on equivalent medium theories (e.g., Hudson, 1980; Schoenberg, 1980; Cheng, 1993; Schoenberg and Sayers, 1995). These effective medium theories mainly deal with two types of fractured media, i.e., homogenous fractured media and discrete fracture media, as discussed in Chapter 3. To date most fracture studies are based on the assumption of homogenous fractured media, because most individual cracks or fractures in the subsurface are too small be 'seen' by seismic waves. Instead the overall population of small cracks results in average or bulk effective medium properties that can be inferred from the wavefield. However, individual fractures cannot be neglected when they are comparable to or larger than the wave length of seismic waves. Similarly clustering of fractures is quite common in the geological record, and can lead to inhomogeneous (spatially variable) effective medium properties. For example in some fractured reservoirs, fractures tend to cluster to form fracture swaths or fracture corridors (see Figure 2.8) which may form porous storage or a highly permeable pathway for fluid flow in reservoirs. Singh et al. (2008) define such features as follows:

> "Fracture corridors (FCs) are an extraordinary cluster of a huge number of quasi-parallel fractures. FCs vary in size and extension (vertical and lateral). Their dimensions can vary over a wide range. For instance, some of them have been found to be 10 m wide, 100 m high and 1000 m long. Such FCs can contain more than hundreds to ten thousand fractures and have a permeability well above 10 Darcy."

From the viewpoint of seismic modelling, FCs can be simplified into tens or hundreds of vertical or horizontal discrete fractures (Grandi-Karam, 2008). This

heterogeneity at different scales relative to the seismic wavelength can be examined in a straightforward way using the DFM technique, especially when calibrated by real case studies, and is a prime motivation for the work described in this chapter.

There are a few previous studies on seismic response in DFMs. Daley et al. (2002) investigate the effect of different fracture stiffness on the P-wave and PS-wave scattering, which implies that it is possible to image gas-filled spaces by observing the scattered energy. Vlastos et al. (2003) study the effect of discrete fracture sizes and distributions on seismic responses with seismic modelling. Vlastos et al. (2007) further investigate seismic attenuation for different stages of fracture evolution, using numerical models for the growth of a fracture population with realistic length distributions and clustering properties as a starting point. Rao and Wang (2009) use seismic waveform tomography to characterize fractures with a group of models with different dipping fractures. These papers study the seismic response of discrete fractures based on synthetic data, aiming to reveal unique signatures of seismic response in DFMs. However, they are restricted to 2D cases, largely due to the computational challenges. As a result work in 3D cases is very limited. As mentioned in Chapter 3, Willis et al. (2006) and Grandi-Karam (2008) are the two major attempts to study DFMs based on 3D seismic modelling. Both studies use the scattering indexing (SI) method to invert for fracture spacing and orientation.

In 2D seismic modelling, normally the X-Z plane is considered, where discrete fractures are simulated as finite segments (horizontal, vertical or dipping) with vanishing thickness, whilst in 3D cases, fractures behave as 3D planes, which makes it possible to characterize individual fractures or fractured media at different azimuths. I conclude there are three advantages for 3D seismic modelling in DFMs,

(1) Amplitudes of synthetic data are close to the real field data in terms of 3D geometrical spreading and possible 3D curved raypaths in fractured media ;
(2) In 3D cases the seismic response can be characterized in the Y-Z plane. For example, the first numerical example in this chapter shows how reflection waves and transmission waves interfere with each other, which results in unique wave circles in the wave field snapshots.

(3) In 3D cases the seismic response can be characterized in the X-Y plane. This makes it possible to record seismic reflections from the top or the bottom of anisotropic target layers over the full azimuth range. More specifically, anisotropy (or fracture properties) can be studied by means of analysis of azimuthal AVO or velocity variation at different azimuths.

3D studies in Willis et al. (2006) and Grandi-Karam (2008) didn't cover some important aspects, such as seismic anisotropy, azimuthal AVO response, and multiple discrete fracture sets. In this chapter, I intend to cover such aspects to get more understanding of various seismic characteristics in DFMs, using seismic modelling in 3D fracture media. The only disadvantage in 3D modelling is the large computation time, which however is overcome by using a parallel code library to accelerate the computation process.

4.2 Fracture compliance in discrete fracture models

The basic building block for the discrete fracture model is the fracture compliance, normally expressed in terms of orthogonal normal tangential components. All examples of DFMs mentioned in the previous section require the knowledge of these two compliances. Based on mathematically analysis, Liu et al. (2000) argue that the compliance ratio Z_N/Z_T can be used to infer the fluid contents in fractures. They point out, for a dry (gas-filled) fracture, if there is a planar distribution of imperfect contacts, the ratio of the normal compliance to the shear compliance is approximately 1. For liquid inclusions, the ratio can be very small, approximately zero. On the other hand, the ratio of the magnitudes of two compliances is normally estimated from laboratory samples or field rocks. Lubbe et al. (2007) have carried out laboratory measurements to estimate the compliance ratio, which confirms the fact the ratio is dependent on the fluid content. A ratio of 0.05 has been obtained when the fracture was honey-saturated. In addition, based on their estimated ratios (0.2-0.5) under higher confining pressure, they point out that the high ratios (≈ 1.0) are more nearly met at high confining pressure. Lubbe and Worthington (2006) have done a field

investigation of fracture compliance, in which they try to determine how compliance scales with fracture size. Their estimates of normal fracture compliance within a range from 2.5×10^{-13} m/Pa to 3.5×10^{-13} m/Pa are obtained from both cross-hole data and sonic-log data.

From the viewpoint of seismic modelling, Worthington (2007b) demonstrates a series of 2D fracture modelling examples considering the magnitude range of the two compliances, in which he indicates that compliances of the order of 10^{-10}-10^{-11}m/Pa are required for measurable P-wave anisotropy.

In practice, it is hard to estimate the two compliances properly due to many unknown factors and difficulties in laboratory tests and field investigations. DFMs can help by providing an alternative method of constraining the unknown compliances as model parameters, and hence improving the accuracy of their estimation and their effect on seismic modelling (Lubbe et al., 2007).

4.3 The effects of discrete fracture spacing on seismic anisotropy and scattering

Based on DFM and some existing studies (e.g., Vlastos et al., 2003; Grandi-Karam, 2008), we know that fracture spacing plays a certain part in wave propagation, or more specifically, they affect the seismic wavefields and the final time sections recorded. Vlastos et al. (2003) have investigated the effects of different statistical distributions of discrete fractures (different locations or scales of discrete fractures) on seismic response based on 2D DFMs, which involve different fracture spacing inside the models, but this study does not explicitly address this point. Grandi-Karam (2008) discuss the use of the scattering indexing (SI) method developed by Willis et al. (2006) to invert fracture spacing and fracture orientation, which involves different fracture spacing, but they focus on the scattered waves and the inversion with the SI method. They did not include the possible variation in seismic anisotropy. Here I investigate the effect of different fracture spacing on the seismic response in then presence of seismic anisotropy. First I design a group of fractured models which

have gradually increasing fracture spacing from model to model. Each model consists of an isotropic host medium and an array of vertical fractures embedded into the host medium. In 3D models, a vertical fracture is a vertical line in the X-Z plane, but it is a plane in the Y-Z coordinate plane. All parameters of the models are the same except the fracture spacing. The Coates-Schoenberg method is used to calculate the elastic parameters for the grids where vertical fractures pass through. The calculation involves the elastic parameters of the isotropic host medium, the normal compliance Z_N and the tangential compliance Z_T of the fractures, which are discussed in the previous section, and the grid size. The actual calculation is based on equations 2.33. Vlastos et al. (2003) study the effect of different fracture distribution and size by analyzing the wavefield snapshots in the 2D planes analysed. Here similar wavefield snapshots are taken for 2D sections of the 3D model in different coordinate planes to illustrate the properties of the wavefield produced by the DFM in relation to the model fractures.

4.3.1 Models and data

The size of each model is 4500m *4500m *4500m with a grid size of 10m *10m *10m. The thickness of the model fractures is also 1 grid unit, i.e., 10 meters, and thus represents not only the fracture, but also the effect of its immediate damage zone. The host medium parameters are the P-wave v_P =3300m/s, the S-wave velocity v_s=2000m/s and the density ρ=2200kg/m^3,, and I assume discrete fractures are gas-saturated and their compliances are $Z_N = Z_T$=5.6x10-10 m/Pa (all of the medium parameters are set the same as those in Vlastos et al., 2003, compatible with the compliance range given by Worthington, 2007b). Note that the fracture compliances in the models of Vlastos et al. (2003) are tapered to zero at either end of the fractures when they are applied in modelling, which avoids a big contrast of elastic parameters between the host medium and fracture ends. However, in my models, there is no need for that because the fractures run from the top to the bottom of the models. The density of the fracture region remains the same as the host medium. I use a 20Hz Ricker wavelet (the P-wave wavelength in the host medium is 165 meters, and the S-

wave wavelength is 100 meters) as the modelling source, which is placed at the centre of each model. The fracture spacing changes from 160m, 120m, 80m, 40m, 20m to 10m (the last three cases are shown in Figure 4.1 b, c and d). For comparison, two end-member models are constructed, a model only containing the host isotropic medium without fractures (Figure 4.1a, infinite distance between fractures), and a model with vertical fractures in all grids (which is equivalent to a HTI model, Figure 4.1e, with zero distance between fractures). Therefore, the ratios of fracture spacing to wavelength for P-wave propagation in the models shown in Fig 4.1 (a-e) are (∞, 4/16, 2/16, 1/16 and 0) respectively. I also analysed ratios of 12/16 and 8/16 not shown.

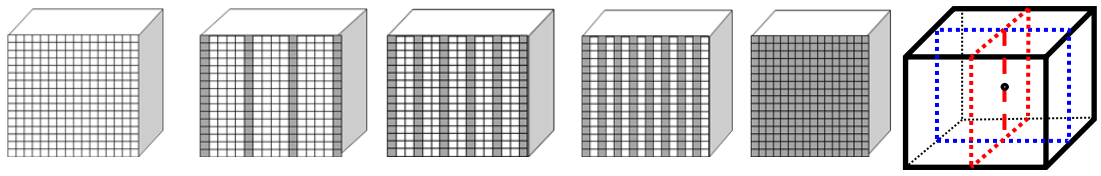

(a) (b) (c) (d) (e) (f)

Figure 4.1: The models above shows an isotropic host medium interleaved with parallel vertical fractures aligned in the Y-Z plane. White grid elements on the X-Z plane on the face of the blocks represent the host medium and dark ones represent those containing the vertical fractures. The grid spacing is uniform, representing 10 meters for each cell. The fracture spacing remains constant in each model but different among the models: (a) Isotropic model; Model with fracture spacing (b) 40m, (c) 20m, (d) 10m, (e) 0m (HTI). The seismic sources are set at the centre of the models. (f) represents the geometry of the extracted seismic sections in Figure 4.2: 'o' is the source location which is at the centre of the models; the X-Z sections listed in Figure 4.2 correspond to the location of the blue dot rectangle; the Y-Z sections listed in Figure 4.2 correspond to the location of the red dot rectangle.

4.3.2 Analysis of results

P-wave anisotropy

Snapshots of the resulting wave field calculated by the DFM are taken at a time of 600 ms following the source pulse applied at the centre (Figure 4.1f) of the model cube are shown in Figure 4.2. This time is chosen to be large enough to see the main effects of the direct wave propagation, without interference from reflections off the sides of the 3D cube. First, I examine the subplots in the central X-Z plane

containing the source pulse (Figures 4.2a1-h1). The P-wave wavefronts look like a series of unique 'ellipses' (the single quotes means they may not be exact ellipses). As shown in the figures, the 'ellipticity' of the P-wave wavefront increases gradually with decreasing fracture spacing, and reaches the maximum case when the spacing is 0m. The major axis length remains constant, but the minor axis length decreases with decreasing fracture spacing. This is because the vertical fractures do not affect the P-wave velocity along the fracture strike, but do reduce the velocity perpendicular to the fracture strike, and the reduction becomes stronger (the velocity becomes slower) with decreasing fracture spacing.. In the extreme case, when the fracture spacing is infinite, which corresponds to the isotropic model for the host medium, the P-wave wavefront is a circle as shown in Figure 4.2a1 and no seismic anisotropy is shown, as expected. In the other extreme case, when the spacing is 0m, the model is a homogeneous HTI model and seismic anisotropy reaches its strongest value, as shown in Figure 4.2h1. Because the fractures do not affect the velocity along the fracture plane or in the Y-Z plane, the P-wave wavefronts are circles as shown in Figure 4.2a2-h2. Note the suffix 1 on the figure labels implies a cross section in the X-Z plane, and a suffix 2 a cross section in the Y-Z plane.

The P-wave anisotropy is quantified by the ratio r of the minor and major axes of the 'ellipses'. From Figure 4.3, this metric varies non-linearly with the P-wave fracture spacing s. Instead it takes the form of an exponential transient of the form

$$r = r_0 + (1 - r_0) * (1 - e^{-\frac{s}{s_0}}) \tag{4.1}$$

where r_0 (≈ 0.56) is the ratio at zero spacing, $s_0(\approx 54.32m)$ is a characteristic distance, and the horizontal asymptote at the ratio 1.0 corresponds to an infinite spacing, i.e. the isotropic host medium case. This form means the sensitivity of the ellipticity ratio to fracture spacing (the slope dr/ds) decreases with increasing fracture spacing.

Scattering pattern

As shown in Figures 4.2b1 to g1 and b2 to g2, the vertical fracture planes trap a lot of scattered energy among them. The energy content contains P-waves and S-waves

reflected and transmitted off the fractures. These interfere with each other, resulting in a complex scattered wavefield in both planes, reflecting systematic trends with respect to the fracture spacing.

In the X-Z plane, from Figures 4.2b1 to d1, P-waves reflected and transmitted from the fracture planes form a series of clear curves along the vertical direction. The curve spacing is associated with the fracture spacing, and the curves become closer with decreasing fracture spacing. From the curves in the snapshots, the P-wave seismic response can distinguish different fracture spacing within the range (160m, 120m, and 80m, and the ratios are 1, 3/4, and 1/2), but it cannot distinguish for the cases of fracture spacing 40m, 20m and 10m (the ratios are 1/4, 1/8, and 1/16). This basically agrees with the geophysical understanding that a seismic wave can distinguish an object with a scale of more than 1/4 wavelength. In these cases scattered energy is clearly observable in the middle zone of the models. However, Figures 4.2e1 and f1 show that the scattered energy becomes fainter as the corresponding models become closer to homogenous HTI models.

In the Y-Z plane, from Figure 4.2a2-h2, the scattering waves form a series of complex concentric circles. This orthogonal scattering by definition cannot be observed in 2D modelling. It also represents an energy loss in the X-Z plane that will affect the propagation in the X-Z plane compared to a simple 2D model. This highlights the necessity to consider the third dimension in wave scattering problems, even in the case of parallel fractures. The circle energy is stronger at larger fracture spacing, but becomes fainter at smaller spacing.

In addition, from all the subplots, the discrete fractures show no effect on the S-wave velocity since the S-wave wavefronts are circles.

From the observations above, I conclude that energy scattering is linked to the fracture spacing. In particular systematic trends in the ellipticity of the anisotropy emerge in the scattered wavefield. These could be used in principle to infer fracture spacing in natural data.

4.3.3 Interpretation of results

The major conclusion drawn from the previous section is the observation of systematic trends in P-wave seismic anisotropy with respect to changes in fracture spacing. The result can be interpreted in this way: the values of the micro crack statistics inferred from data using an idealized theory based on circular cracks (such as Hudson's model) will be a quantitative measure of the statistics of an actual discrete fracture (Liu et al. 2000, reviewed in Chapter 2). In other word, each of these DFMs, to some extent, corresponds to an anisotropic model that contains vertical aligned micro cracks which is based on, for example, Hudson's model (Hudson, 1980 and 1981). A bigger discrete fracture spacing corresponds to a sparser micro crack distribution (or smaller crack density), which leads to weaker P-wave anisotropy in the DFMs.

4.3.4 Summary and interim conclusions

In this section I have conducted a 3D numerical study of the effect of fracture spacing on P- and S-wave wavefields for macroscopic parallel fractures. A group of DFMs were designed with different fracture spacing, which in turn are comparable to the probing wavelet. The discrete fractures are considered to be gas-saturated. The Coates-Schoenberg method is then applied to calculate the equivalent anisotropic medium parameters for 3D fractured grids. The 3D SSD FD modelling technique developed in Chapter 3 is used to generate the synthetic data, which enables us to simulate the seismic response in full 3D space. A series of X-Z and Y-Z wavefield snapshots are taken from the DFMs.

The major conclusion is that P-wave seismic anisotropy increases systematically with decreasing vertical fracture spacing, and P-wave wave fronts show characteristic elliptical variations in the X-Z plane (Variation in the X-Y plane is the same due to aligned discrete fractures). The P-wave ellipticity ratio in the X-Z plane varies as an exponential transient with respect to the fracture spacing, holding out the possibility of mapping fracture spacing in natural examples from anisotropy of the

wavefield if the ratio of the spacing to the wavelength is more than 1/4. Moreover, scattered energy becomes weaker with the decrease of the fracture spacing in both the X-Z and Y-Z planes. In particular, the scattered energy forms different patterns of complex concentric circles in the Y-Z planes - a unique phenomenon that cannot be simulated with 2D modelling. This example justifies the additional effort of constructing a 3D model, even for a medium with strong fracture alignment. The scattering pattern also depends systematically on the fracture spacing. In the models with bigger fracture spacing, the scattering is more profound.

From all of these observations above, I find that the patterns of P-wave seismic anisotropy and scattered energy are associated with fracture spacing in this study. This provides method of characterizing large discrete fractures in relevant real field cases, an important aspect of this work is that it enriches our understanding of the seismic response of truly 3D DFMs, even for a model with a strong 2D 'grain'.

X-Z plane **Y-Z plane**

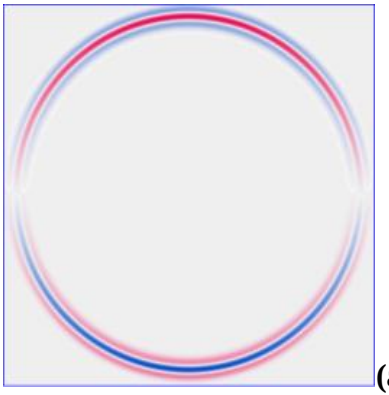

(a1)

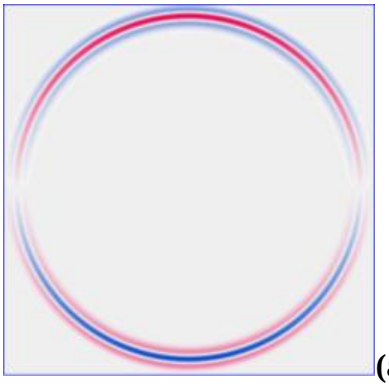

(a2)

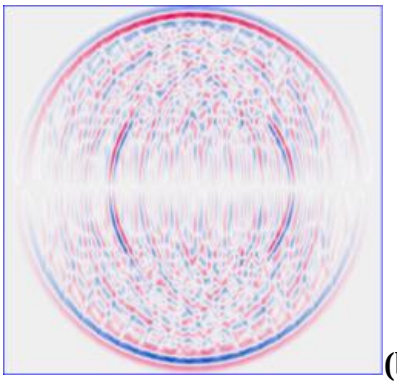

(b1)

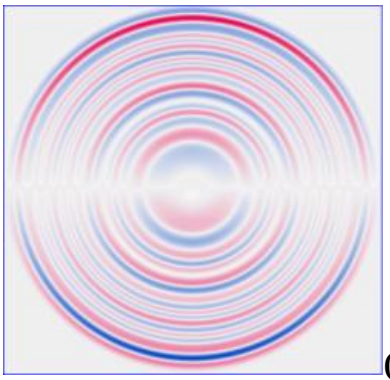

(b2)

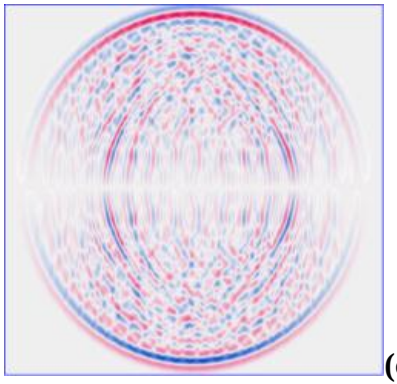

(c1)

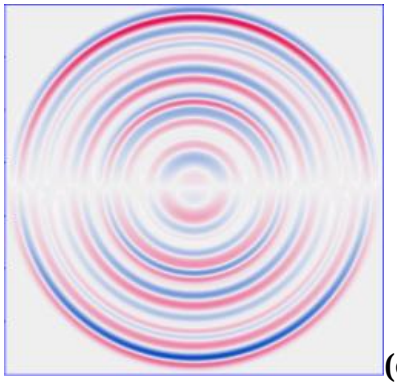

(c2)

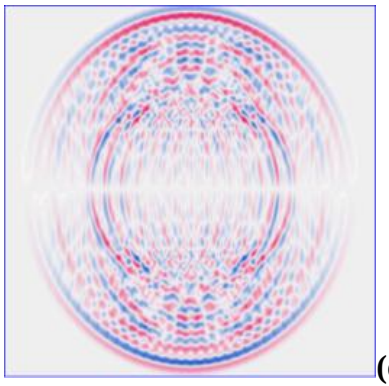

(d1)

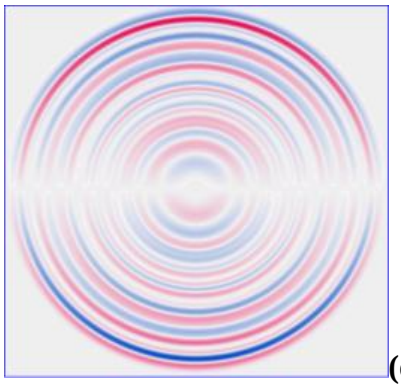

(d2)

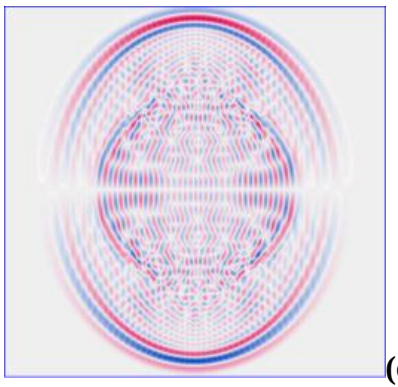

(e1)

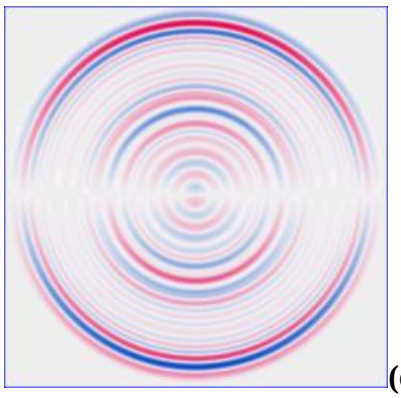

(e2)

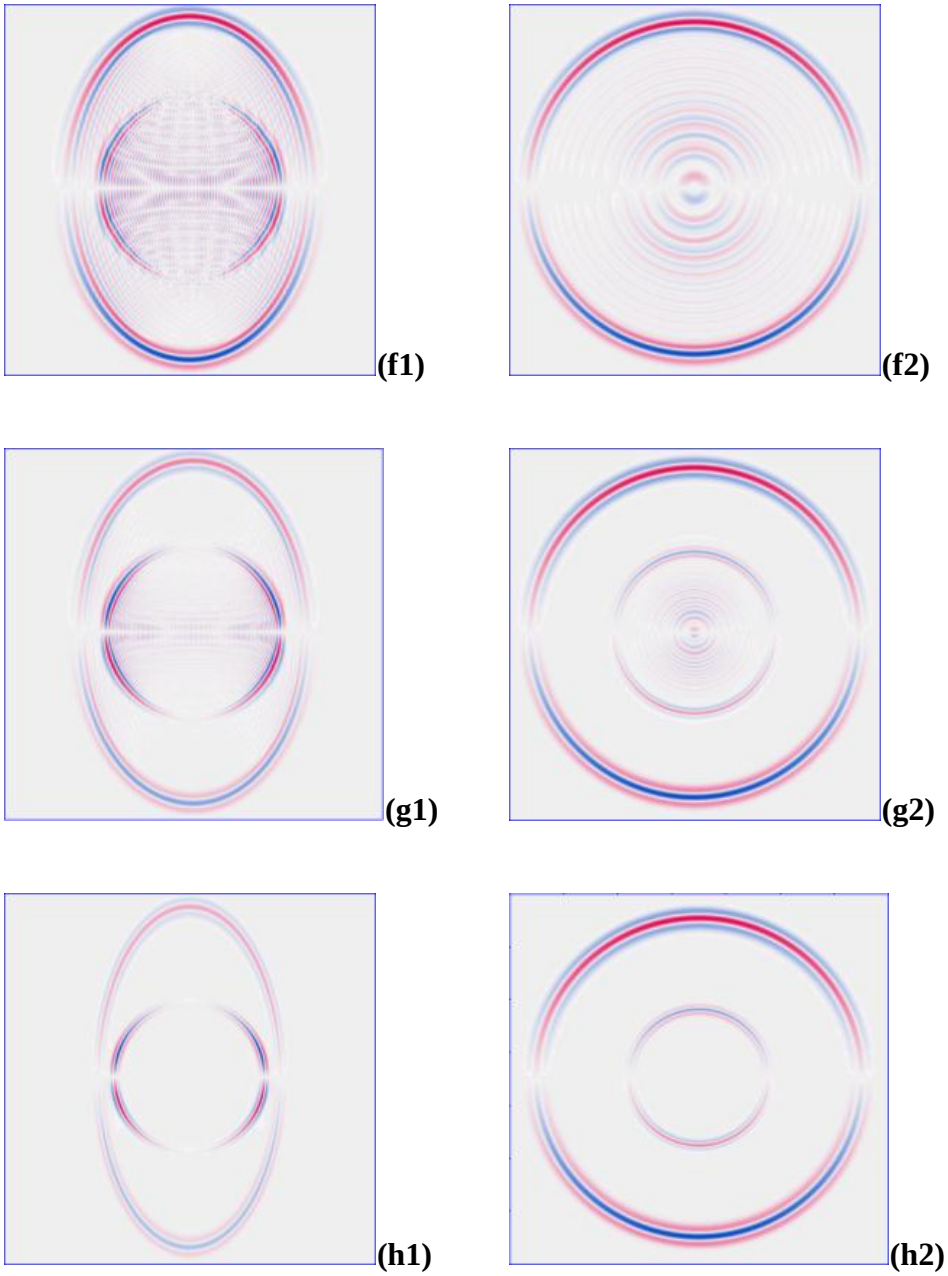

Figure 4.2: Snapshots of the Z-component wavefront are taken cross the centre of the models after 600ms in X-Z (columns 1 and 3) and Y-Z planes (columns 2 and 4). Wavefront snapshots for (a) the isotropic model; models with fracture spacing (b) 160m, (c) 120m, (d) 80m, (e) 40m, (f) 20m, (g) 10m, and (h) 0m (an equivalent HTI model).

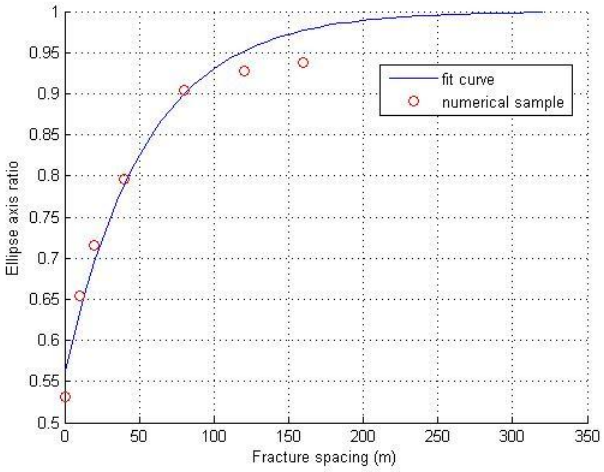

Figure 4.3: The variation of the ratio of short to long axis of the P-wave wavefront ellipse in Figure 4.2 with fracture spacing. The lower the ratio, the stronger the P-wave anisotropy. The ratio zero means the strongest anisotropy (HTI medium), and when the spacing goes to infinity, the ratio approaches 1.0 (isotropic medium).

4.4 Azimuthal AVO and seismic scattering attenuation

In seismic modelling, the common way to study DFMs is to examine wavefield snapshots and scattered energy (e.g., Vlastos et al., 2003, Vlastos et al. 2007, Rao and Wang, 2009). More practical studies of DFMs should be able to consider the seismic signatures in time sections, seismic amplitudes, and frequency content. Seismic amplitude analysis in homogeneous fractured media normally involves AVO or AVOA analysis (e.g., Ruger, 1997; Varela et al., 2007) based on various equivalent medium theories (Hudson, 1980 and 1981; Cheng, 1993; Chapman, 2003). However, AVO or AVOA analysis is rarely performed with DFMs. None of the papers above discuss this point or related areas. I conclude that there are some difficulties for such analysis, notably:

1. Many factors affect the estimation of fracture compliances in the laboratory or in the field;
2. Realistic discrete fracture models are difficult to build;

3. There are difficulties in seismic modelling, particular in 3D DFMs (sometimes it is easy to generate 3D snapshots, but not easy to generate 3D shot gathers with proper geometry information).

For the first point, as Worthington (2007b) states, knowledge of the two fracture compliances is still limited. Grandi-Karam (2008) and Willis et al. (2006) have overcome the last two points in DFMs with seismic modelling. However, they focus on the scattered waves, not the reflected amplitudes from the top/bottom of the target fractured layer.

In this section I attempt to overcome the last two points by using the FD scheme developed in Chapter 3, and reveal amplitude and spectral features in the target reflection. Based on this realisation, three discrete fracture models are designed in this study: a vertical fracture model (VFM, containing one vertical fracture set), an orthogonal fracture model (OFM, containing two vertical fracture sets which are orthogonal to each other), and a reference isotropic model (IM, containing no fractures) for comparison. In addition, more scattering issues will be discussed in this study.

4.4.1 Models and data

Based on the fracture modelling tool developed in Chapter 3, I build three 3-layer models considering different discrete fracture sets. The first one is an isotropic model (IM, Figure 4.4 left). The parameters for the first layer and third layer are the same, which are, P-wave velocity v_P=2900m/s, S-wave velocity v_s=1900m/s and density ρ=2000kg/m^3. The parameters for the second layer are P-wave velocity v_P=3500m/s, S-wave velocity v_s=2000m/s and density ρ=2200kg/m^3. The other two discrete fracture models are built by inserting one vertical fracture set or two orthogonal fracture sets (Figure 4.4 right) into the second layer of the isotropic model. Thus a vertical fracture model (VFM) and an orthogonal fracture model (OFM) (see Figure 4.4 right) are obtained. The fracture spacing is 60m in the latter two discrete fracture models. I assume the fractures are open and gas-saturated, and the normal and tangential fracture compliances are $Z_N = Z_T$ =5.6x10-10 m/Pa (the same as the

previous compliance). The wavelet used in the modelling is a 23Hz Ricker wavelet, which has a P-wave wavelength of 142m and S-wave wavelength of 100m in the fracture host layer. The size of the models is 2000m *2000m *2000m with the cell size 10m *10m *10m. The thicknesses of the three layers are 500m, 1000m and 500m respectively. The source is set at the corner of the models (0m, 0m, 0m) and the geophones are located at the model surface. In order to find out how seismic waves propagate in the discrete fracture layers in VFM and OFM, I take wavefield snapshots at different coordinate planes in the second layer medium as shown in Figure 4.5. Following the setting of coordinate axes at the surface of the models, shotgathers at different azimuths are recorded for analysis (Figure 4.6).

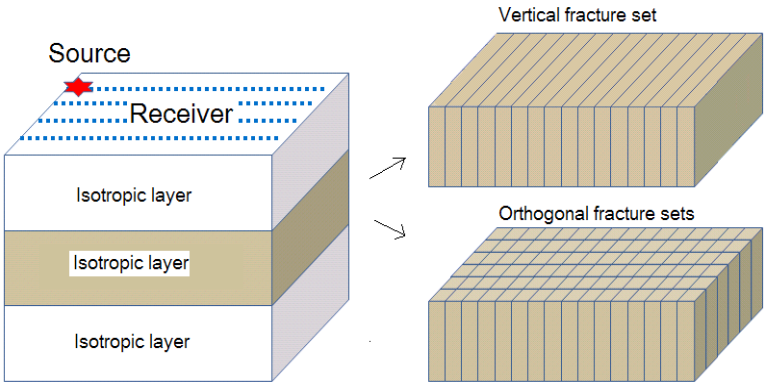

Figure 4.4: The three constructed models in the study: on the left is the three-layer isotropic model (IM) for comparison. The vertical fracture model (VFM) and the orthogonal fracture model (OFM) are obtained by inserting the vertical (top right) and the orthogonal (bottom right) fracture sets, respectively, into the second layer of the IM.

4.4.2 Analysis of results

Wavefield signatures in snapshots and shot gathers

Before I do the actual shotgather modelling with the acquisition geometry in Figure 4.4, I build other three cubic models which only contain the isotropic host medium, the vertical fractured layer, and the orthogonal fracture layer, respectively, similar to the models in the previous study as shown in Figure 4.1, in order to compare the difference in the resulting wave fields (The snapshots are shown in Figure 4.5). The wave field snapshots in Figure 4.5 represent the z-component of particle velocity on

different coordinate planes, and the snapshots are taken at a time lag of 0.5s after the source time. From Figures 4.5a, b, d and e, it is clear that the P wave travels more slowly in the direction perpendicular to the fracture strike than it does in the direction parallel to the fracture strike. Compared with the IM case (Figure 4.5f), the presence of discrete fractures does not affect the velocity along the direction parallel to the fracture strike (Figures 4.5a, b, d and e). The snapshots from the VFM (Figures 4.5a, b and c) demonstrate a similar seismic response to that I discussed in the previous study of this chapter, showing the same curves along the fracture planes and the concentric circles in the Y-Z planes. The seismic response of the OFM (Figures 4.5d and e) shows quite different signatures (more complex) from those of the VFM (Figures 4.5a and b). In the OFM model scattered waves interfere with each other, resulting in energy cancellation in the central area of the wavefield (Figures 4.5d and e), compared with the VFM. The reason for this is there are two orthogonal fracture sets, which interact with the waves in two orthogonal directions. The snapshot observations indicate that different fracture sets affect the final seismic response differently, and scattered waves from two orthogonal fracture sets are weaker than those from one fracture set.

Figure 4.6 shows the shotgathers from the three models at different azimuths based on the acquisition geometry in Figure 4.4, from which we can clearly observe the two P-wave reflections from the top and the bottom of the second layers of the models, with scattered waves lagging behind. Scattered waves in the shotgathers show different features in the VFM and OFM, and the azimuthal variation of the scattered waves is more profound in the VFM than that in the OFM. In the VFM, from the azimuth 0^o, 45^o to 90^o (from Figure 4.6a, 4.6b to 4.6c) the dip angles of scattered waves become gentler and gentler, whilst in the OFM the scattered waves are extremely weak except at far offset (corresponding to the maximum incident angle of around 45^o), most likely due to the cancellation effect of the two orthogonal fracture sets. Note that azimuth 0^o is along the X-axis and azimuth 90^o is along the Y-axis. In the OFM the scattered waves in the shotgathers are not as strong as expected from the corresponding snapshots. The scattered waves at the far offset in Figure 4.6g are more complex than those at the far offset in Figure 4.6f (they correspond to the azimuths 0^o and 45^o, respectively). The reason for this is that a

special spatial relation exists between the two orthogonal fracture sets and the azimuths. I do not show the shotgather figure at the azimuth 90^o for the OFM because it is the same as that at the azimuth 0^o for two orthogonal fracture sets. These observable features in this study may help to distinguish two different types of fracture set in fractured reservoirs.

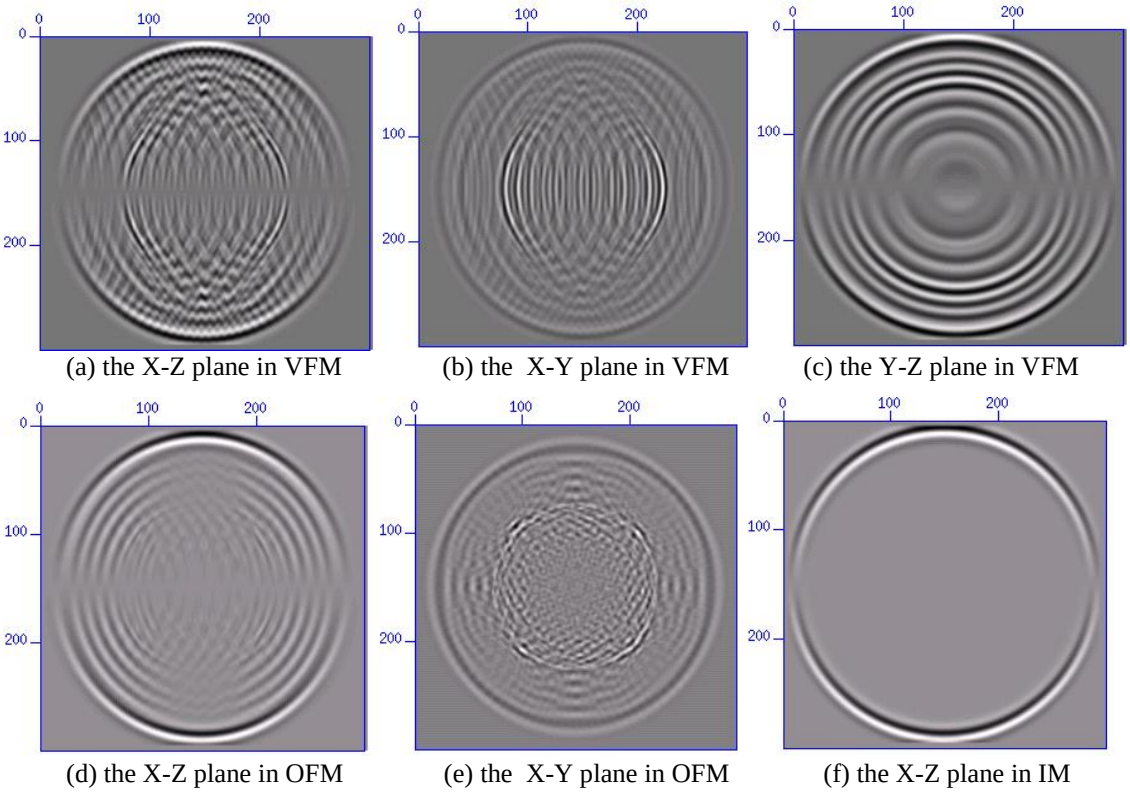

Figure 4.5: Snapshots of z-component of particle velocity at 0.5s for different axis planes in the middle layers of VFM, OFM and IM as shown in Figure 4.2.

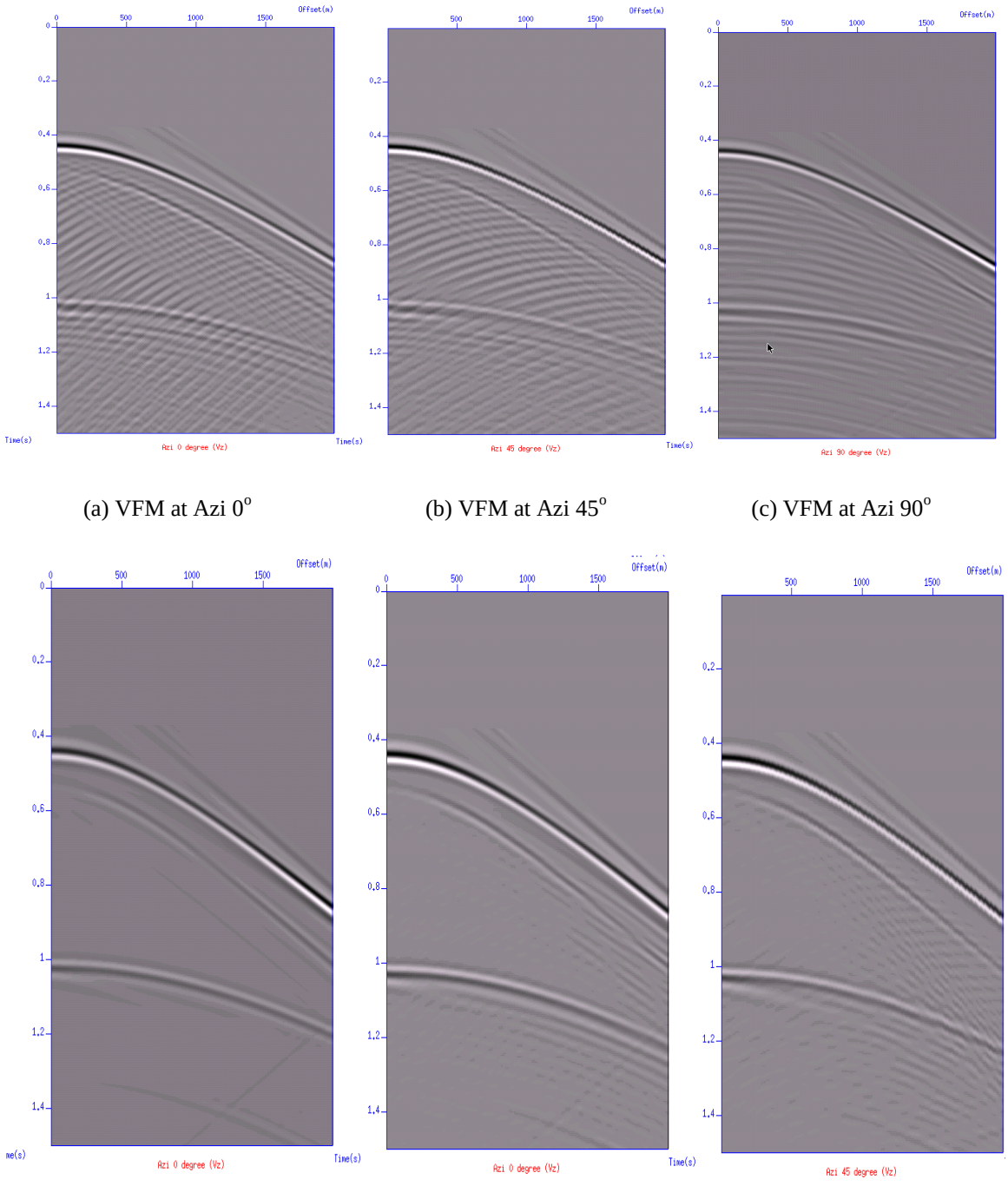

(a) VFM at Azi 0^o (b) VFM at Azi 45^o (c) VFM at Azi 90^o

(e) IM at Azi 0^o (f) OFM at Azi 0^o (g) OFM at Azi 45^o

Figure 4.6: Shot gathers of velocity z-component for the corresponding models at different azimuths: 0 °is along x-axis (fracture normal) and 90 °is along y-axis (fracture strike).

Analysis of azimuthal AVO

In this section I analyze the P-wave azimuthal AVO response from the top of the fractured layers of the three models (Figure 4.7). Maximum amplitudes of the P-wave reflection are picked from azimuths 0^o to 90^o. As we can see from Figure 4.7d, the reflected amplitudes of the two fractured models are smaller than those at the corresponding location (the same azimuth and the same offset) in the isotropic model, and the amplitudes of the OFM are even smaller than those of the VFM. The reason is the presence of fractures, more fractures resulting in smaller reflected amplitudes in the case of this study. Obvious azimuthal AVO variation is observed in the VFM (Figure 4.7b), and the variation indicates the fracture strike direction as expected. This AVO variation is similar to that at the interface between an isotropic medium and a homogenous HTI medium. Therefore this variation can be used to indicate facture strike when only one discrete fracture set exits. However, there is hardly any observable azimuthal AVO variation in the OFM, which does not show any indication of the two fracture strike directions. This confirms that orthogonal fracture sets may cancel out the azimuthal response, and care should be taken in such cases in the application of azimuthal AVO for fracture detection, especially when multiple fracture sets exist.

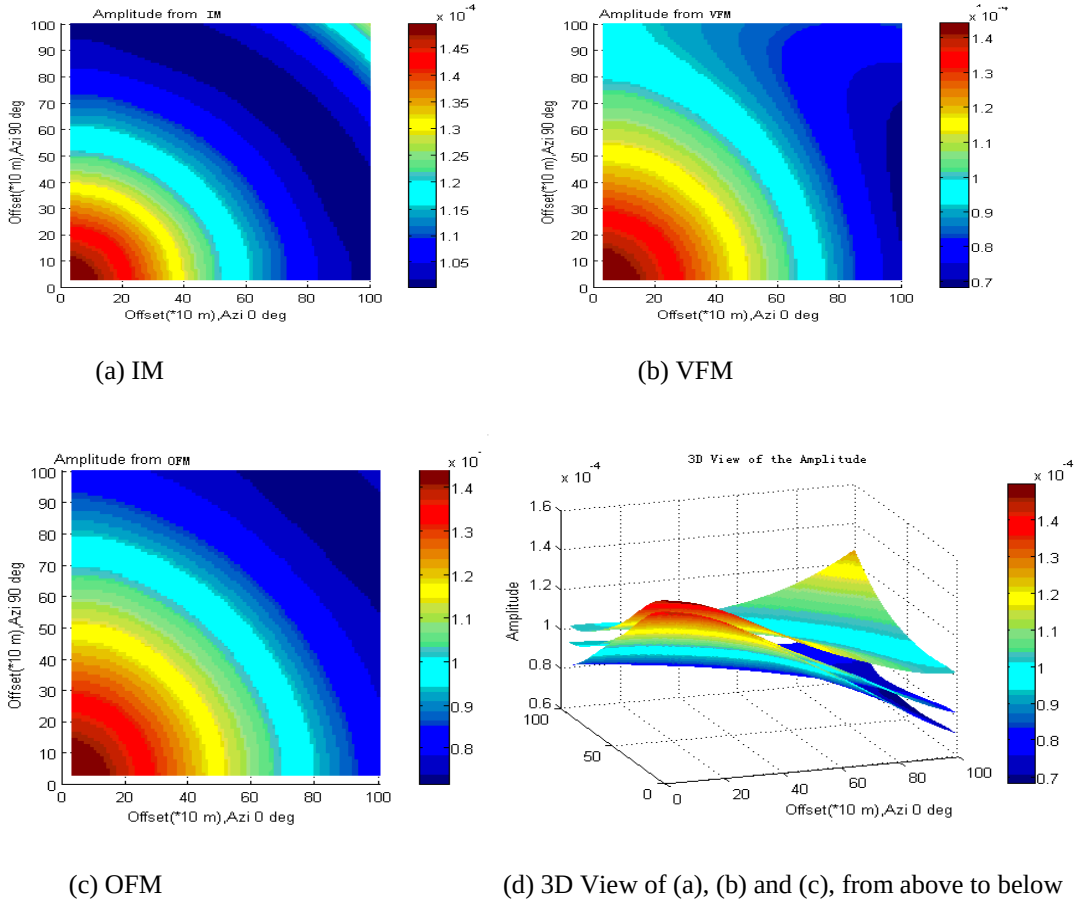

(a) IM (b) VFM

(c) OFM (d) 3D View of (a), (b) and (c), from above to below

Figure 4.7: Variations of the reflected amplitude with offset and azimuth from the top of the second layers of the three models: (a) IM, (b) VFM, and (c) OFM; (d) is the 3D view of (a), (b) and (c), from top to bottom, respectively

Amplitude spectra and scattering attenuation

The analysis in the sections above is based on variation in amplitudes in space or time. In this section, I perform the analysis in the frequency domain with a FFT. I calculate the amplitude spectra of the windowed reflected waves from the bottom of the second layers in the models at different azimuths (Figure 4.8), and the scattering attenuation related to the waves is calculated using the spectral ratio method (Rahul and Roger, 1998) (Figure 4.9).

Figure 4.8 shows the amplitude spectra at different azimuths in the three models, and the amplitude spectra from different models demonstrate different features. There are obvious discontinuities in Figures 4.8b and 4.8c, corresponding to the

spectra at the azimuth 0^o and 45^o (Figures 4.8b and 4.8c), which are associated with the corresponding locations of the vertical fractures. A greater number of discontinuities exist at azimuth 0^o, which means the waves pass through more fractures in the direction perpendicular to the fracture strike. At azimuth 90^o in the VFM, no discontinuity is observed because the section is acquired along the fracture strike. Similar discontinuities exist in the OFM (Figures 4.8e and 4.8f), but they are more faint, again possibly due to the cancellation effect of the two orthogonal fracture sets. Another feature in the spectra of the two fracture models is that the spectra in the VFM and OFM (Figures 4.8b, 4.8c, 4.8d, 4.8e and 4.8f) are narrower than that in the IM (Figure 4.8a), which means there is energy loss in the two DFM models, particularly at high frequency. In addition, energy gradually decreases from near offsets to far offsets in Figure 4.8, the reason for which is geometrical spreading in 3D space. All these features in the amplitude spectra, especially the discontinuities, can help to diagnose discrete fractures, and the presence of different fracture sets in the characterization of fracture properties.

I use the relatively broadband source wavelet as the reference trace for the estimation of scattering attenuation. The estimation is applied to the same windowed bottom reflections of the second layers in the two fracture models. Figure 4.9 shows the estimated scattering attenuation (*1/Qs, Qs* denotes the scattering quality factor), which is calculated based on the traditional *Q* equation (equation (2.40)). The model is purely elastic, so there is no intrinsic attenuation, and hence all attenuation revealed by the spectral ratio is due to scattering, and there is no net energy loss. Instead, energy is transferred preferentially from low to high frequencies, resulting negative scattering attenuation. The scattering attenuation is overall small, but shows characteristic fluctuation as the wave travels across the fractures. Again, these fluctuations are stronger in the VFM than those in the OFM due to the interference from the two orthogonal sets. Also, the fluctuation are stronger when perpendicular to the fracture strike (azimuth 0^o), and they gradually decrease with azimuth. This is a good indicator of the presence of discrete fractures.

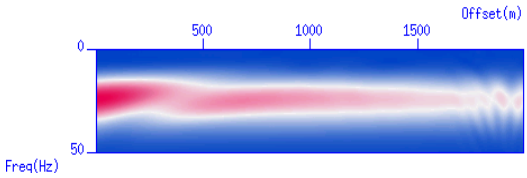

(a) IM at Azi 0^o

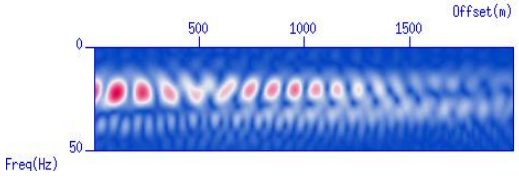

(b) VFM at Azi 0^o

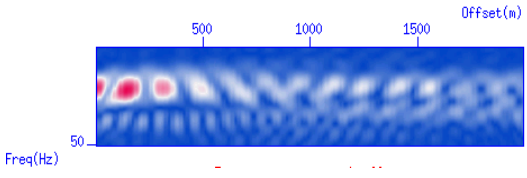

(c) VFM at Azi 45^o

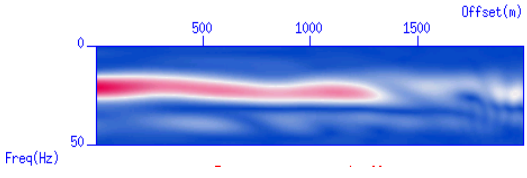

(d) VFM at Azi 90^o

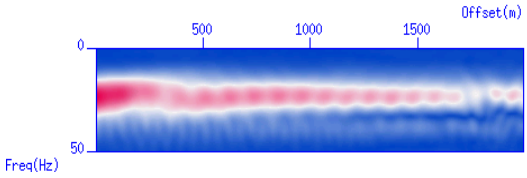

(e) OFM at Azi 0^o

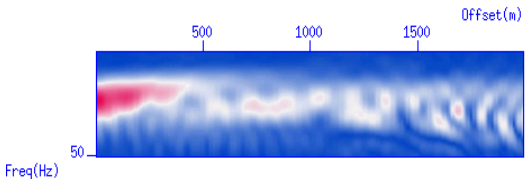

(f) OFM at Azi 45^o

Figure 4.8: Amplitude spectra versus offset for the reflection from the bottom of the second layer for different models and azimuths: (a) is IM at azimuth 0^o; (b), (c) and (d) are VFM at azimuths 0^o, 45^o and 90^o respectively; (e) and (f) are OFM at azimuths 0^o and 45^o, respectively.

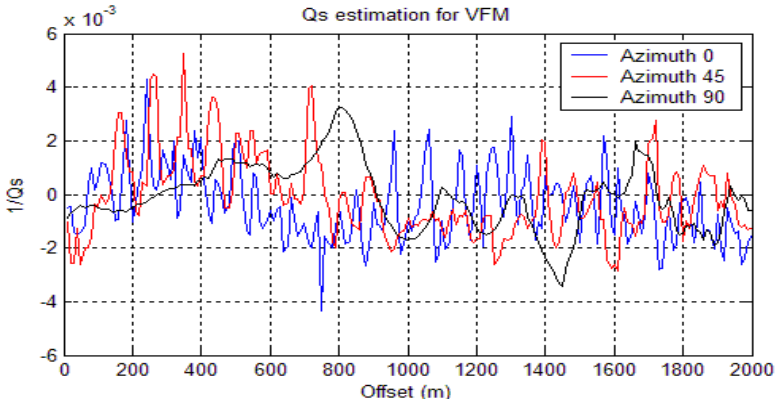

(a)

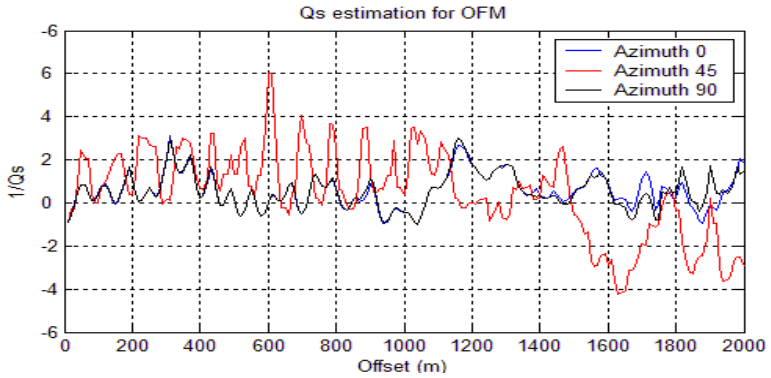

(b)

Figure 4.9: The estimated scattering attenuation (1/*Qs*) (a) VFM and (b) OFM at different azimuths: blue-azimuth 0°; red-azimuth 45°; black – azimuth 90°.

4.4.3 Summary and interim conclusions

In the study described in this section I have constructed two discrete fracture models and one isotropic model, and have studied their snapshots, shotgathers, azimuthal AVO responses and scattering attenuation using 3D FD modelling. There are significant differences both in wavefields or shotgathers between the VFM and the OFM. Reflections and scattering in the wavefield snapshots and shotgathers in the VFM are more profound than these in the OFM. Two orthogonal fracture sets tend to cancel out part of the energy of the reflection and scattering. The scattering in the wavefield snapshots in the OFM is clear compared with that in the IM, whilst there are merely small differences in their shotgathers, which confirms the difficulties in prediction of multiple fracture sets, particularly when they intersect at high angles. From the publications, both theoretical and application work on prediction of

multiple fracture sets (e.g., Sayers, 2007) is much less than that for single fracture sets.

Also, scattered energy shows different patterns in the wavefield snapshots and shotgathers both in the VFM and the OFM. Even for the first time, we could observe the AVO response of the DFMs from this study, which has rarely been discussed before by others. Based on the AVO response in the VFM result (Figure 4.7b), it reveals similar features to equivalent homogenous HTI models, with similar elliptical variation, which to some extent, implies the link between macro fractures and aligned micro cracks like I discussed in the section 4.3.. However, there is no obvious azimuthal variation in the amplitudes from the OFM. From the discussion in the Section 4.3.3, the VFM, to some extent, is equivalent to a homogeneous HTI model, and the OFM is equivalent to a homogeneous orthorhombic model. Therefore, the corresponding overall seismic responses show similarity.

The different patterns of the discontinuities in the VFM spectra at different angles indicate different fracture spacing along the ray path. A cancellation effect also exists in the OFM spectra. There is another way to analyse the scattered wave, which is using F-K transform on time sections (Grandi-Karam, 2008), because the dipping horizons of time sections at different DFMs or at different azimuths show more obvious features in the F-K domain. This should be included in future studies.

As to the measured scattering attenuation, based on the two DFMs in this study, the scattering attenuation is very small, and wavefield cancellation in the OFM results in less fluctuation in the attenuation than that in the VFM. Also, different patterns in the scattering attenuation are exhibited at different azimuths, particularly for the VFM.

Generally speaking, based on the results in this study, the discrete fracture models possess a strong contrast in the compliances between the fracture and the host medium. This generates more scattering and interference in the synthetics, resulting in various scattered waves as shown in Figures 4.5 and 4.6, azimuthal AVO variation in Figure 4.7, discontinuities in the amplitude spectra in Figure 4.8, and fluctuation in the scattering attenuation in Figure 4.9. The differences in features either between the VFM and OFM, or at the different azimuths in the two DFMs, could help to diagnose

discrete fractures and the presence of multiple discrete fracture sets from seismic data in real applications.

4.5 General conclusions

In addition to the conclusions presented separately for the two studies described in sections 4.3. and 4.4, it is possible also to make some general points that refer to the chapter as a whole. First, the seismic response both in P-wave velocity and AVO features confirms the link between DFMs and homogenous anisotropic media (Liu et al, 2000). Second, scattered waves in the 3D cases show some unique wave phenomena (e.g., scatter patterns and circles) either in the wavefield or shotgathers, many of which cannot be observed in 2D modelling. Third, the ratio of fracture spacing to wavelength matters for the final seismic response. Fourth, scattered wave features need more quantitative confirmation, and it is possible to get some implications from Willis et al. (2006) and Grandi-Karam (2008). Nevertheless, the results from the two studies described here show different and unique features in the time and frequency domains, and in different seismic attributes, which provides useful information to diagnose discrete fractures in the subsurface and to help to characterize discrete fractures in reservoirs.

5 Chapter 5 The effect of anticlines on fracture property inversion

In this chapter, I present a 3D numerical study of the effect of an anticline on seismic fracture density inversion by using the singular value decomposition (SVD) technique in a field area where a pilot application study with the same technique has previously been carried out. The effect of the anticline structure is studied by inverting synthetic datasets which are generated using 3D finite difference (FD) modelling in fractured media. I design two 3D anisotropic models with different thicknesses for the fractured reservoir as well as one 3D isotropic model, and use the modelling tool developed in Chapter 3 to generate 3D full wave synthetic datasets. The SVD inversion technique is then applied to the three datasets in order to assess the influence of the anticline on the fracture density inversion. From the outcome of this study, I find that fracture density is well resolved at the top of the anticline whilst it is over-estimated at the two flanks of the anticline. Moreover, the results indicate the leading term in the SVD decomposition is the most robust and reliable attribute for fracture density inversion.

5.1 Introduction

Considerable efforts have been made to reveal the characteristics of natural fracture networks in fractured reservoirs. Many such efforts involve the analysis of Amplitude variation with Offset and Azimuth (AVOA) in P-wave seismic data in order to estimate fracture orientation and fracture density distribution (e.g., Ruger, 1997; Sayers and Rickett, 1997; Li, 1999). Accurate estimation of these fracture properties can help to reduce uncertainties and to optimize production of fractured hydrocarbon reservoirs. However, the estimation process poses a big challenge in terms of inversion schemes to be applied, integration of different types of data and possible geological complexity in the subsurface.

In this work, I examine the effect of an anticline on fracture density inversion by means of FD modelling in 3D fractured media and an inversion technique based on the Singular Value Decomposition (SVD) of the AVOA response (Varela et al., 2007). General AVOA analysis assumes that the earth models are horizontally layered; however, in this study an anticline dominates the target fractured reservoir, and the presence of the anticline structure obviously violates that assumption. From this point, the motivation of this study is to explore the effect of the presence of the anticline on the fracture estimates, through SVD inversion analysis on 3D synthetic datasets.

5.2 The study area

The numerical models in this study are based on a geological structure which contains a relatively thin tight gas fractured reservoir within an anticline. I focus my analysis on the variation of the P-wave AVOA response from the top of the fractured reservoir. In previous work by Chao and Maultzsch (2010), an pilot inversion study for fracture density and fracture orientation using a combined Ruger-SVD method

(Ruger, 1997; Varela et al., 2007) revealed an area of high fracture density in the fractured reservoir around an existing well. Figure 5.1a shows the previous result of the fracture density inversion and the existing well (marked with the small yellow circle in Figure 5.1a). The inversion results were consistent with the FMI (Formation Micro Imager) logs at the well location, both in fracture density (the fracture density inverted at this location is up to 0.26) and in the fracture orientation (Figure 5.1b). The dark arrow in Figure 5.1a represents the anticline orientation and the red line in Figure 5.1a represents a 2D simplified velocity section running across the anticline as shown in Figure 5.1c. In the 2D velocity section, we can see the existing well (the vertical black line in Figure 5.1c) at the middle of the structure just reach the thin tight gas fracture reservoir (the red layer in the section). The 2D model is simplified for the purpose of numerical modelling, based on the previous interpretation of the well logs and the 3D velocity model from data processing. As shown in Figure 5.1c, four layers are contained in the 2D model and all the related modelling parameters are selected from the interpretation, and are shown in Tables 5.1 and 5.2.

In order to investigate the influence of the anticline, 3D synthetic fractured models are constructed, based on the 2D velocity section in Figure 5.1c with the parameters in Tables 5.1 and 5.3. Note that the stiffness vectors of the fractured layer are calculated with the parameters in Table 5.3 based on Chapman's model (2003). Note that, for computational convenience, only the real part of the computed complex stiffness vector based on Chapman's model is considered for the elastic seismic FD modelling and the reflectivity computation in the SVD method. Subsequently, synthetic datasets are generated with the FD modelling technique, and the SVD inversion method is applied to obtain fracture density from the synthetic data. In this way, inverted fracture density as a function of position above the anticline can be compared with the true fracture density pre-set in the model parameters to assess the anticline effect.

The fractured layer, as shown in Figure 5.1c, is relatively gentle with a dipping angle range of 7-12 degrees, and the fractures in the layer are still considered to be vertical (Figure 5.1d) rather than the distorted dipping case as shown in Figure 5.1e.

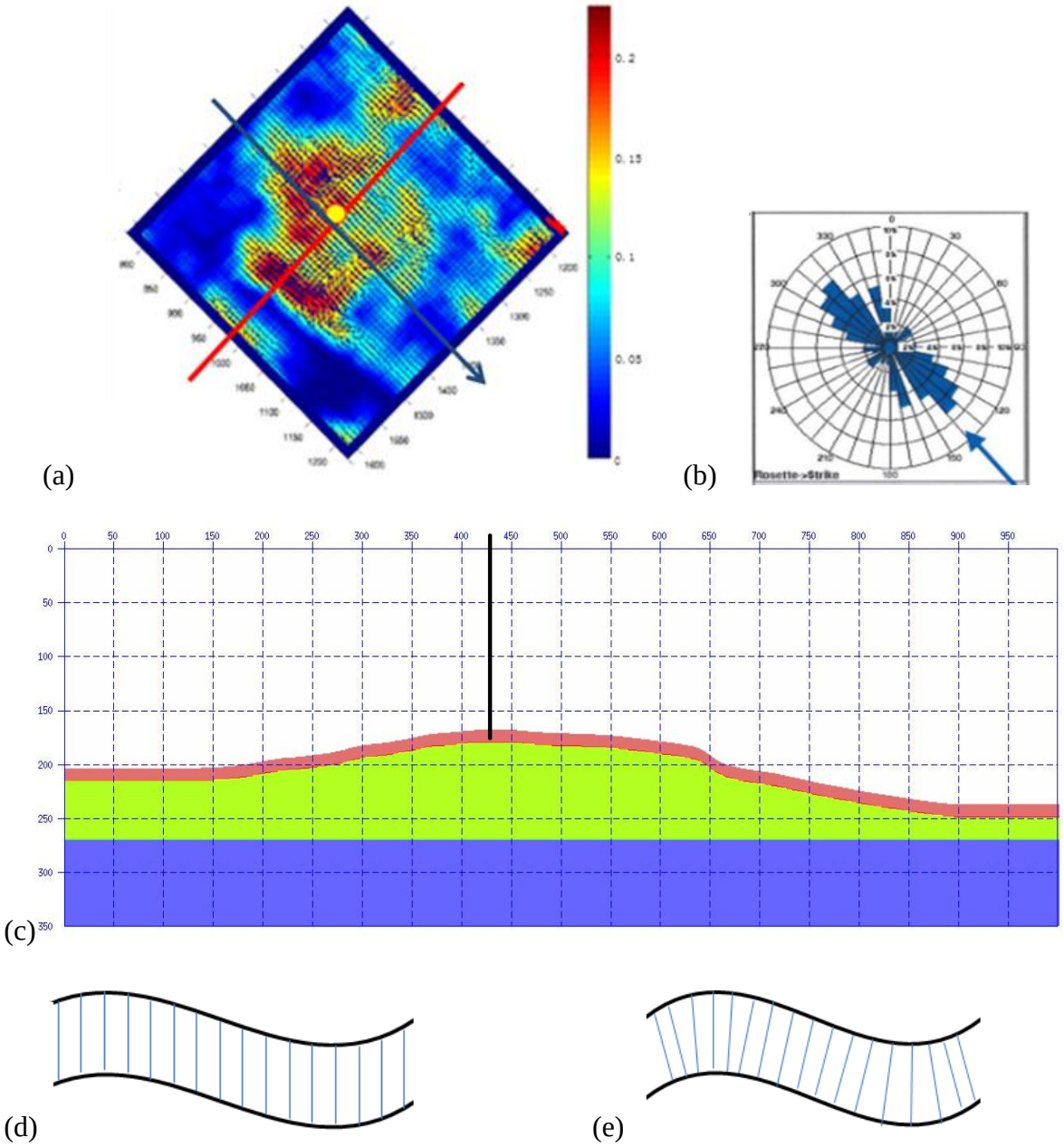

Figure 5.1: The numerical models are based on the velocity section (c) which is extracted from the red line location in the study area (a), which runs cross the anticline. The dark arrow in (a) represents the anticline orientation. The colours in (a) represents the inverted fracture density plot with fracture density up to 0.26. The yellow dot in (a) shows the location of the drilled well, where the results of the FMI logs are shown in (b). The fractures in the layer are still considered to be vertical (d) rather than the distorted fracture case (e).

Layer	Medium	Thickness(m)	v_p(km/s)	v_s (km/s)	ρ (g/cm3)
1 (white)	Isotropic	1680	3.4567	1.7133	2.667
2 (red)	Fractured layer	110	4.60	2.72	2.607
3 (green)	Isotropic	910	4.60	2.72	2.607
4 (blue)	Isotropic	800	4.21	2.30	2.651

Table 5.1: The medium parameters in the fractured models

5.3 Theoretical background and the inversion workflow

Next, I will discuss some related theoretical aspects of the theoretical background and the workflow for the inversion.

5.3.1 Poroelastic models

In this chapter, the poroelastic model, Chapman's model (2003), is used to calculate the effective elastic constants of the rock physics models in the SVD method for fracture density inversion. Here I give a brief review of some related poroelastic models.

Wave-induced fluid motion and exchange in porous rock have been studied for many years. In the context of fluid motion, pores, micro-cracks or meso-scale fractures are interconnected in some ways (rather than isolated cracks in Hudson's model discussed in section 2.2), which allows fluid to move between them. Fluid in porous rocks under such pressure tends to achieve a new equilibrium between voids within a period of time (called relaxation time). Three states of fluid exchange are often discussed: (1) fluid pressure takes longer time than wave period to relax (representing the high frequency limit); (2) the pressure can reach the new equilibrium within wave period time (representing the low frequency limit); (3) any

state between (1) and (2) (representing the transition frequency state, or the squirt flow).

A well-known early effort made by Gassmann (1951) gives the prediction of effective medium bulk modulus of Earth's rocks with fluid-saturated grain-size pores. The bulk modulus equation (Wang, 2001) is,

$$K^* = K_d + \frac{(1 - \frac{K_d}{K_m})^2}{\frac{\phi}{K_f} + \frac{1-\phi}{K_m} - \frac{K_d}{K_m^2}} \tag{5.1}$$

where K^* is the predicted effective bulk modulus of a porous rock saturated with a fluid of bulk modulus K_f, K_d is the frame bulk modulus, K_m is the matrix bulk modulus, and ϕ is the porosity. It must be noted that frame modulus is not dry modulus of the porous rock, and it should be measured at irreducible saturation conditions of wetting fluid (normally water). The effective shear modulus is equal to frame modulus. In Gassmann's theory, the wavelength is long compared to the grain and pore size in rocks, and the pores are well interconnected or communicating, which ensures full equilibrium of the pore fluid flow within half of a wave period time (corresponding to the low frequency limit). The low frequency limit makes it hard to verify in the laboratory due to the fact that it is difficult to create a core with a length of at least half the wavelength. Nevertheless, the Gassmann's equation provides an important tool for calculating the effect of fluid substitution on seismic properties and has a wide application in energy industry.

Biot (1956) develops a rock physics model by introducing a compressible viscous fluid into a porous elastic rock, in which viscosity and frame permeability are taken into account compared to the Gassmann's theory. Fluid motion between interconnected pores is assumed, which results in energy loss when wave propagates in such porous rocks. Biot's model is compatible with the Gassmann's theory at the lower frequency limit, and extends the theory to the full frequency range. Based on his derivation, P-wave and S-wave velocities are shown frequency-dependent, but the dependency is small over the full frequency range for most reservoir rocks (Wang, 2001). Therefore, the Gassmann's theory is often applied for fluid substitution analysis. Biot (1956) also reveals that there are two compressional waves

propagating in the model: one is the normally observed P-wave, and the second is a rapidly attenuated slow P-wave which generally cannot be obviously acquired in the real survey record.

One typical model developed by Chapman et al. (2002) considers a poroelastic rock consisting of two kinds of voids, a randomly orientated collection of small aspect ratio (or elliptical) cracks and spherical pores. This model is a squirt flow model, and it is consistent with the Gassmann theory at the lower frequency limit and predicts the existence of the slow P-wave revealed in Biot's theory as well. In Chapman et al. (2002), it is found that the predicted seismic properties are strongly dependent on probing wave frequency, field pressure, fluid viscosity and permeability.

As to the effect of fluid on elastic anisotropy, an early attempt made by Thomsen (1995) reveals that the fluid exchange between aligned penny-shaped cracks and pores in some Earth's rocks has a very strong influence on the prediction of elastic anisotropy. He argues that qP-wave velocity follows a $cos2\theta$ angle dependence at low frequency and a $cos4\theta$ angle dependence at high frequency. Thomsen's theory has a good consistency with the empirical result done by Rathore et al. (1995).

Chapman (2003) extends the poroelastic model of Chapman et al. (2002) by introducing a third void, aligned meso-scale fractures. In Chapman (2003), the three kinds of voids are small compared to wavelength, but elliptical cracks and spherical pores are at the same grain scale, whilst the fractures are at a larger scale. This model has shown frequency-dependent anisotropy in P-wave velocity, S-wave velocity and attenuation in the seismic band due to the presence of aligned meso-scale fractures. In addition, Chapman's model confirms the argument of angle dependence in Thomsen (1995). The predicted effective elastic stiffness in Chapman's model follows (modified from Chapman et al. 2003, pp 201)

$$C = C_0 - \phi_p C_1 - \varepsilon_c C_2 - \varepsilon_f C_3 \tag{5.2}$$

where C_0 is the stiffness tensor of the isotropic rock matrix, C_1, C_2 and C_3 are the stiffness tensor contribution from pores, micro-cracks and meso-scale fractures, respectively. ϕ_p , ε_c and ε_f are porosity, crack density and fracture density

respectively. Based on the derivation in Chapman (2003), C_1, C_2 and C_3 are related to isotropic rock matrix properties, crack, fracture and fluid properties, frequency and relaxation time. Two kinds of void scales correspond to two time-scale constants emerging from the derivation, the constant related to the standard micro structural squirt flow frequency (denoted with τ_m) and the other related to the fracture-related lower frequency (denoted with τ_f), the relation of which is written as

$$\tau_f = (\frac{a_f}{\varsigma})\tau_m \tag{5.3}$$

where a_f is the fracture radius, and ς is the crack/pore radius. equation (5.3) implies that the time scale for pressure equalization depends on the fracture radius and larger fracture leads to lower squirt-flow characteristic frequencies.

5.3.2 The SVD method

A common approximation expression of the Zeoppritz equation in isotropic media is (Causse et al., 2007),

$$R(\theta) \approx R_0 + G\sin^2(\theta) + A_3\sin^2(\theta)\tan^2(\theta) \tag{5.4}$$

where R_0 and G are referred to as AVO intercept and AVO gradient, respectively. The third term is often omitted. The resulting two-term form from on equation (5.4) is inaccurate when the incident angle approaches the critical angle or the seismic parameter contrasts are large. Causse et al. (2007) develop an optimal AVO approximation by constructing a group of basis functions through the singular value decomposition method (SVD) to improve the accuracy, which can be written as

$$R(\theta) \approx C_1 f_1(\theta) + C_2 f_2(\theta) + C_3 f_3(\theta) + \cdots \tag{5.5}$$

where the reflection coefficient R is written as a linear combination of coefficient C_i and basis function $f_i(\theta)$. The task here is to find the basis functions $f_i(\theta)$ for any given AVO case. In the process of AVO analysis, rock-physics models or log information are used as prior information to build N reflector models or expected AVO response modelled with the Zeoprittz equation or other AVO modelling. These reflector models are arranged into a reflection coefficient matrix R according to M

different incident angles. Every row in the matrix R corresponds to a different incident angle, and every column corresponds to a different realization of the distribution of rock properties (e.g. P-wave velocity, S-wave velocity and medium density). To find the basis function, the singular value decomposition is applied on the matrix, which gives,

$$\boldsymbol{R = FDV = FW} \tag{5.6}$$

Constructing the SVD decomposition, $\boldsymbol{V}$ is orthogonal, $\boldsymbol{D}$ is diagonal and the columns of $\boldsymbol{F}$ are orthonormal. The ith column of $\boldsymbol{F}$ can be used as the ith basis function f_i while the ith row of $\boldsymbol{W}$ can be used as the ith coefficient (or called attritube) C_i. The basis function can be used to fit any real case AVO response with the least square fitting technique for solving the new attributes C_i'. Causse et al. (2007) have demonstrated two-term and three-term approximation based on equation (5.5) and the approximated coefficient show a very good consistency with the exact AVO response at different incident angles.

Based on the similar process, the inversion scheme used in this study is the SVD method developed by Varela et al. (2007), which recast the incidence dependent basis function in isotropic media (Causse et al., 2007) to the azimuthal dependent basis function in fractured media. In the new SVD method, the first step is to construct a reflection coefficient (or reflectivity) matrix based on the anisotropic Zoeppritz equations (Schoenberg and Protazio, 1992) at the interface between the upper isotropic medium and the lower fractured/HTI medium. The rock properties of the two media are normally obtained from well logs. Realizations of the elastic values are taken to account for lateral variations away from the well. In this study, Chapman's anisotropic rock physics model (Chapman, 2003) is used to calculate the equivalent elastic constants of the lower medium based on the rock properties from the well logs. In order to calculate the reflectivity matrix ($\boldsymbol{R}$), a full range of fracture densities, incident angles and azimuthal angles, is considered. Therefore, the calculated matrix contains the full AVOA response of the reservoir. This process is shown in Figure 5.2. Tables 5.3, 5.4, and 5.5 list all the parameters for calculating the reflectivity matrix in this study. A singular value decomposition of the matrix ($\boldsymbol{R}$) yields basis functions ($\boldsymbol{F}$) and seismic attributes ($\boldsymbol{C}$) as follows,

$$R(fd,\theta,\phi) = C_1(fd,\theta)f_1(\phi) + C_2(fd,\theta)f_2(\phi) + C_3(fd,\theta)f_3(\phi) + \cdots \tag{5.7}$$

In equation (5.7) the basis functions (f_1 , f_2 and f_3) change with azimuth (ϕ), and the seismic attributes (C_1 , C_2 and C_3) are associated with fracture density (fd) and incident angle (θ).

Figure 5.3 shows the decomposed basis functions and seismic attributes for this study based on the parameters in Tables 5.1, 5.2 and 5.3. From Figure 5.3, it is clear that the basis function is a periodical function with respect to azimuth and it is independent of incident angles or fracture density. All the parameters in the three tables are from the well logs or empirical values. Seismic attributes show the variation with incident angle and fracture density, but different attributes have different variation patterns, and there is no rule for these patterns, which are considered only to be related to the case study.

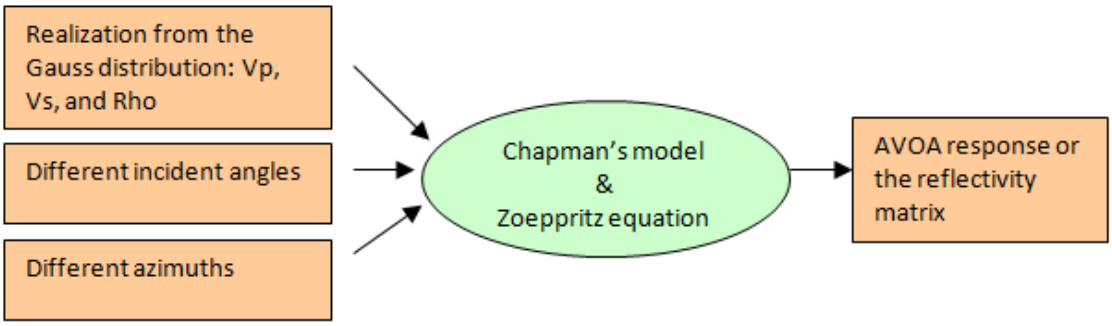

Figure 5.2: Schematic for the calculation of the reflectivity matrix based on rock physical modelling.

For the actual rock physics model in this study, I don't consider the realization of the distribution of the input rock properties, and only different incident angles and different azimuthal angles are considered for the SVD method. The reason for this is, our study approach is based numerical modelling and the aim mainly focuses on the anticline effect.

Parameters in the upper isotropic layer	**Values**
v_p	3.4567 km/s
v_s	1.7133 km/s
ρ	2.667 km/s

Table 5.2: The rock properties in the upper isotropic media

Parameters in the lower isotropic layer	**Values**
v_p	4.6 km/s
v_s	2.72 km/s
ρ	2.607 km/s
Mean frequency(f)	20 HZ
Micro-crack density(cd)	0.0
Initial fracture density(fd)	0.01
Fracture radius (fr)	0.01 m
Crack / fracture aspect ratio (ar)	0.001
Matrix porosity(por)	0.12
Relaxation time (tau)	2E-7 s
Fluid bulk modulus (kf)	3.3E8 Pa

Table 5.3: The rock properties in the lower fractured medium

Parameters	**Values**
Incident angle range	0^o-45^o
Azimuthal angle range	0^o-360^o
Fracture density range	0.01-0.40

Table 5.4: The scanning parameters for calculating the reflection matrix.

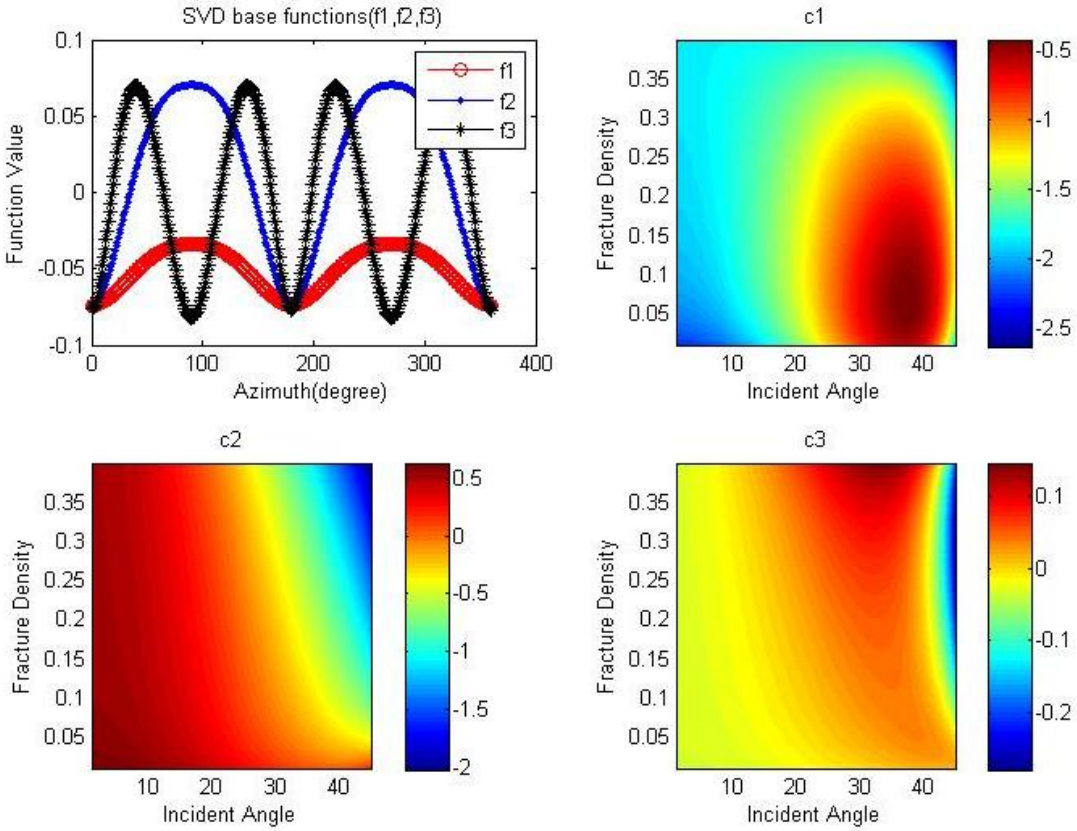

Figure 5.3: SVD decomposition of the reflectivity matrix yields the base functions f_1 , f_2 and $f_3$which show azimuth dependence and seismic attributes C_1 , C_2 and C_3, which present a direct mapping with fracture density over the complete range of incident angles considered in this study. Three attributes show different sensitivity to fracture density at different offsets/incident angles.

5.3.3 The inversion workflow

From equation (5.7), the basis functions (***F***) are only dependent on azimuthal angles, and the attributes (***C***) are dependent on incident angles and fracture density. During the inversion, a new reflection matrix $\boldsymbol{R}'$that is extracted from synthetic dataset or field dataset is expected to share the same basis functions with the matrix $\boldsymbol{R}$. Therefore, a group of new seismic attributes ($\boldsymbol{C}', or\ C_1'$, C_2' ,C_3' …) from the new reflection matrix can be inverted, which then are correlated with the old seismic attributes ($\boldsymbol{C}, or\ C_1$, C_2 ,C_3 …) to invert for fracture density at different incident angles in the synthetic dataset or field dataset. Figure 5.4 shows the whole workflow for the fracture density inversion. Note that normally the Ruger method (Ruger, 1997)

is used to invert for fracture orientation with the ellipse fitting technique discussed in Chapter 2.

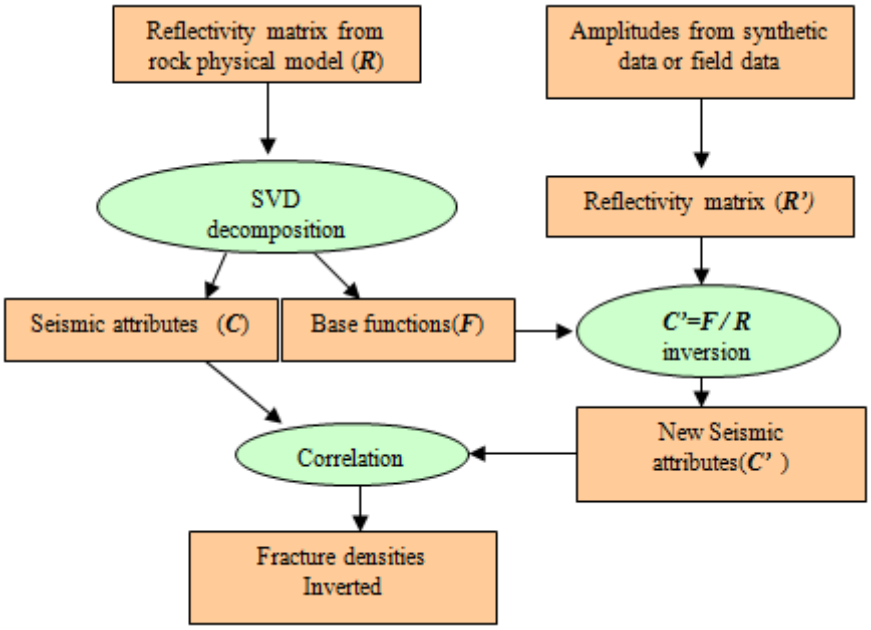

Figure 5.4: Schematic for fracture density inversion using SVD scheme

5.4 Preliminary test

Seismic anisotropy in the fractured reservoir models

In order to examine the strength of the seismic anisotropy based on the parameters in Tables 5.1 and 5.2, I calculate the phase velocities for the P-wave and S-wave in the fractured layer that is shown in Figure 5.5. From Figure 5.5, it is found that the phase velocities change significantly with azimuth, and there is a velocity variation of 20% for P-wave velocity and 33% for S-wave velocity when the azimuth angle changes from the plane normal to the fracture plane. The P-wave and fast S-wave travel at their maximum velocities in the direction parallel to the fracture plane while they travel at their minimum velocities in the direction perpendicular to the fracture plane.

I calculate reflection coefficients for the full range of azimuthal angles and incident angles at the interface between the upper isotropic layer and the lower fractured layer, which is shown in Figure 5.6. Note that larger reflection coefficients are obtained along the fracture normal direction. From the figure we can clearly observe the variation of the reflection coefficients with azimuthal angles and incident angles. If the incident angle is fixed, the fitted variation in the reflection coefficients can allow the fracture properties to be inferred.

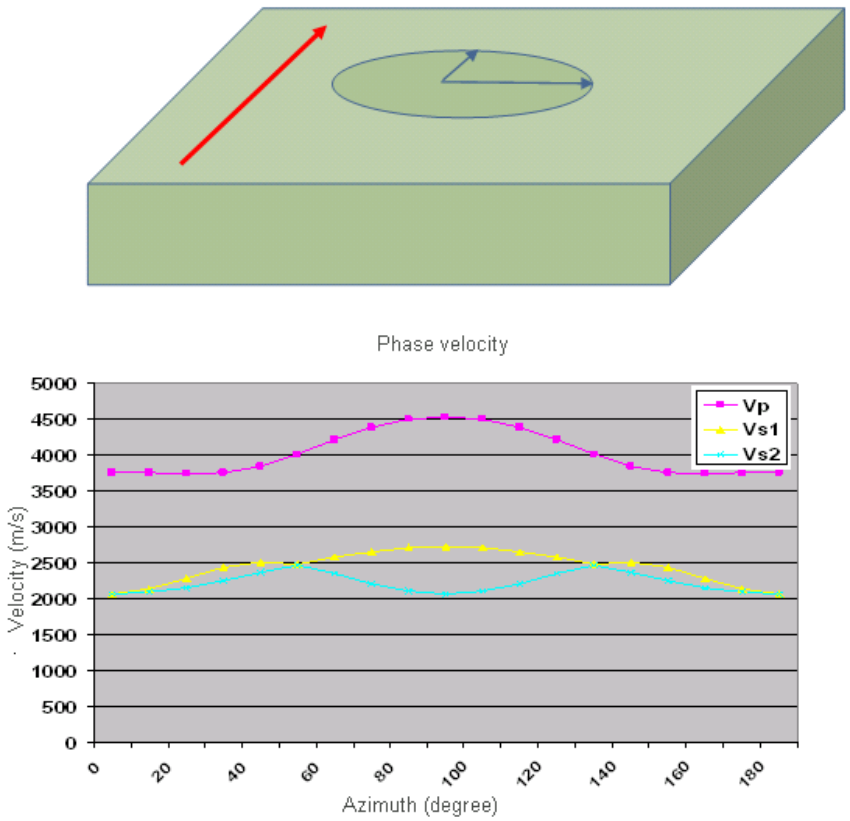

Figure 5.5: Phase velocities as a function of azimuth. In the upper subplot, I assume azimuth 0 ° is in the X-axis direction, and the red arrow is the Y-axis direction as well as the fracture strike).

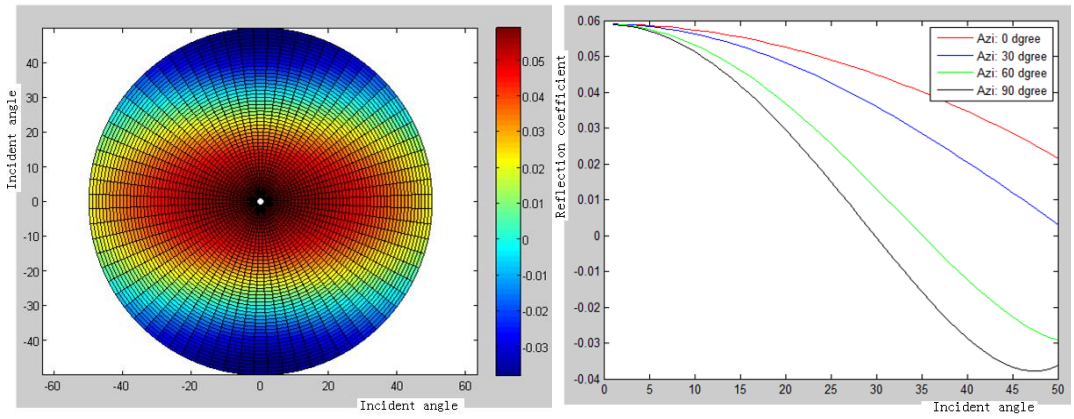

(a) (b)

Figure 5.6: Reflection coefficients as a function of azimuth and incident angle in the polar system. The angle in the polar system is the azimuth, with azimuth 0 ° perpendicular to the fracture strike; the radius refers to the incident angle increasing from 0 ° to 50 °. Four curves extracted from (b) are plotted in (a), from which we see the values increasing with decreasing azimuth. (a) is shown in the polar system: radius is incident angle and polar angle is azimuth. The colour in (a) denotes the magnitude of the reflection coefficient.

Effects of the anticline in simplified fractured models

To get a basic understanding of the influence of the anticline in the synthetic data, I perform a series of simple 3D modelling tests with different anticlines (Figure 5.7) using three isotropic models and three fractured models. Figure 5.7(1) corresponds to the X-Z section of the horizontally layered 3D models, and Figure 5.7(3) corresponds to the X-Z section of the steepest anticline. There is no variation of medium properties along the Y-axis. The elastic parameters of the two layers in the isotropic models are from Table 5.1 without considering fractures. For the fractured models, fractures (Table 5.2) are considered. Note that in these models, the stiffness vectors for the fractured layer used in numerical modelling are calculated with the parameters in Tables 5.1 and 5.2. Seismic sources are placed at the centre of the surface. Six shotgathers are recorded. The reflected amplitudes from the interfaces are extracted for the full range of azimuth angles and different offsets (corresponding incident angles from 0^o to 45^o). Therefore, six shotgathers are recorded as shown in Figure 5.7.

In Figures 5.7b, c, f and g, I observe the azimuthal AVO response at the near offsets (the black areas) which is apparently caused by the presence of the anticline. The

long axes of the black areas represent the fracture strike direction. In the different dipping cases (Figure 5.7b vs. c, or Figure 5.7f vs. g), the back areas in the centre are the narrowest when model (3) is considered. The AVOA response in Figure 5.7e is purely caused by the aligned fractures since there is no anticline. From this observation, I conclude that the presence of the anticlines does affect the azimuthal AVO response, especially at near offsets. In practical modelling cases, we normally perform AVOA in CMP gathers, which are sorted from shotgathers. Therefore these results indicate that it is certain that the effects of anticlines will be brought into CMP gathers.

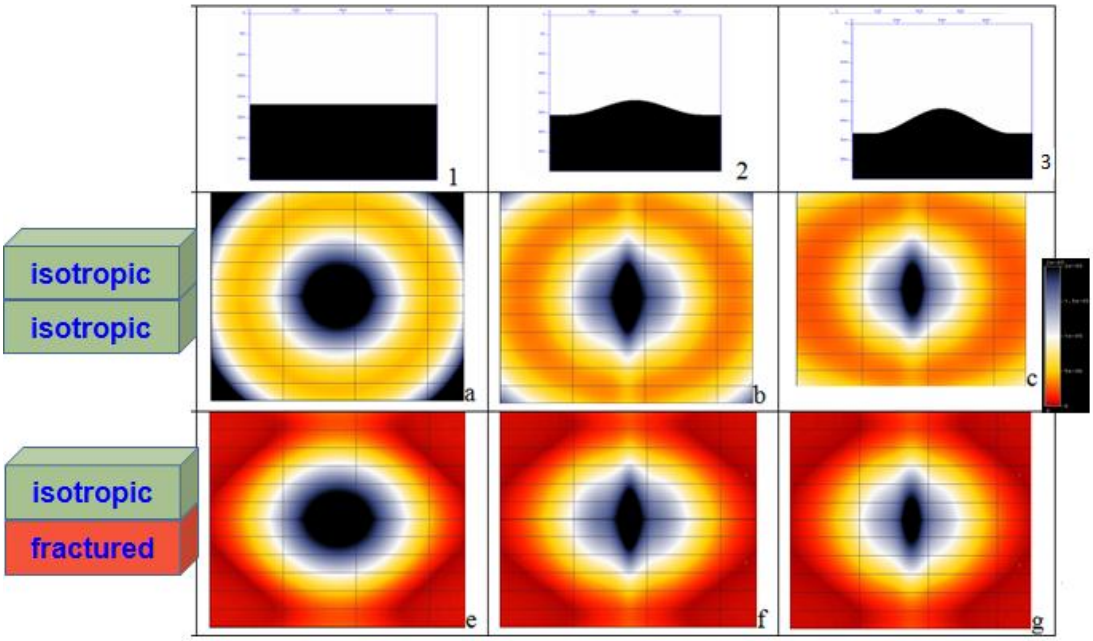

Figure 5.7: The amplitudes from the interface (horizontal or with anticlines) in shot gathers; (1), (2) and (3) show the 3D different models in the X-Z plane, and in the Y-direction model parameters do not vary. The corresponding AVOA responses in shotgathers are plotted in (a) to (g) for the isotropic and fractured models. Fracture strike is along the Y-axis.

5.5 3D modelling and synthetic data processing

5.5.1 Models

In Table 5.1, we find the fractured layer is very thin, only 110 meters, which possibly affects the inversion results based on the SVD method. In order to quantitatively assess the effect of the anticline as well as the possible thin layer effect (or tuning effect) on the fracture density inversion, I design 3 models: Model 1 (Figure 5.9a) which is directly taken from the velocity section (Figure 5.1c) and contains an anticline and a thin fractured layer; Model 2 (Figure 5.9b), obtained by merging the second and the third layer in Model 1, with the parameters from the fractured layer of Model 1; Model 3 (Figure 5.9c) obtained by merging the second and the third layer in Model 1, but with the parameters from the third layer of Model 1. The colours in Figure 5.9 represent the different layers in Table 5.1. These three models are actually 3D as shown in Figure 5.8 and only the three X-Z sections are shown in Figure 5.9. The medium properties of the three models do not vary along the Y-axis.

Variation of the inverted fracture density in Model 1 at different positions across the anticline, if it exists, can indicate the effect of the anticline. By comparing the inverted fracture densities from Model 1 and Model 2, I can reveal possible thin layer effects. For Model 3, the inverted fracture density, or the fake fracture density (because there is no fracture), if it exists, also shows the effect of an anticline.

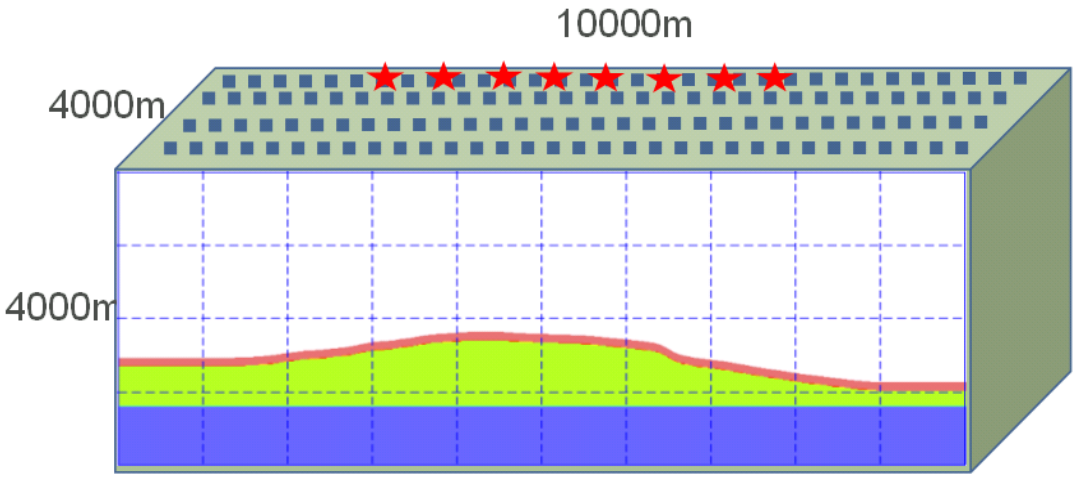

Figure 5.8: The 3D model with its specific geometry configuration; the model size is 10000m*4000m*4000m (x*y*z)

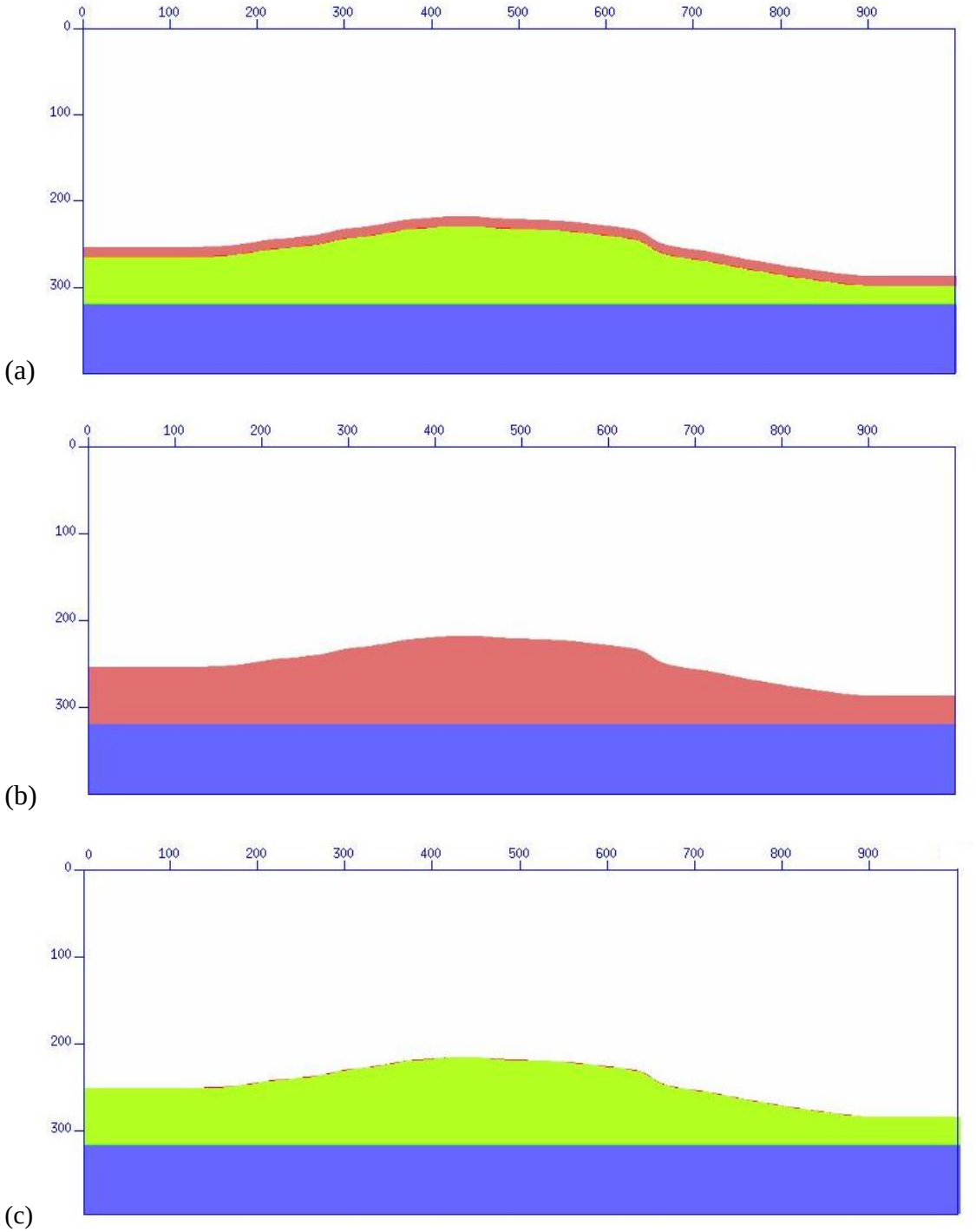

Figure 5.9: Sections view of the 3D models: (a) the model extracted from the field velocity data, which has the thin fractured layer(referred to as Model 1); (b) the model which has a thick fractured layer (Model 2); (c) the isotropic model. Refer to the Table 5.1 for the medium type and parameters.

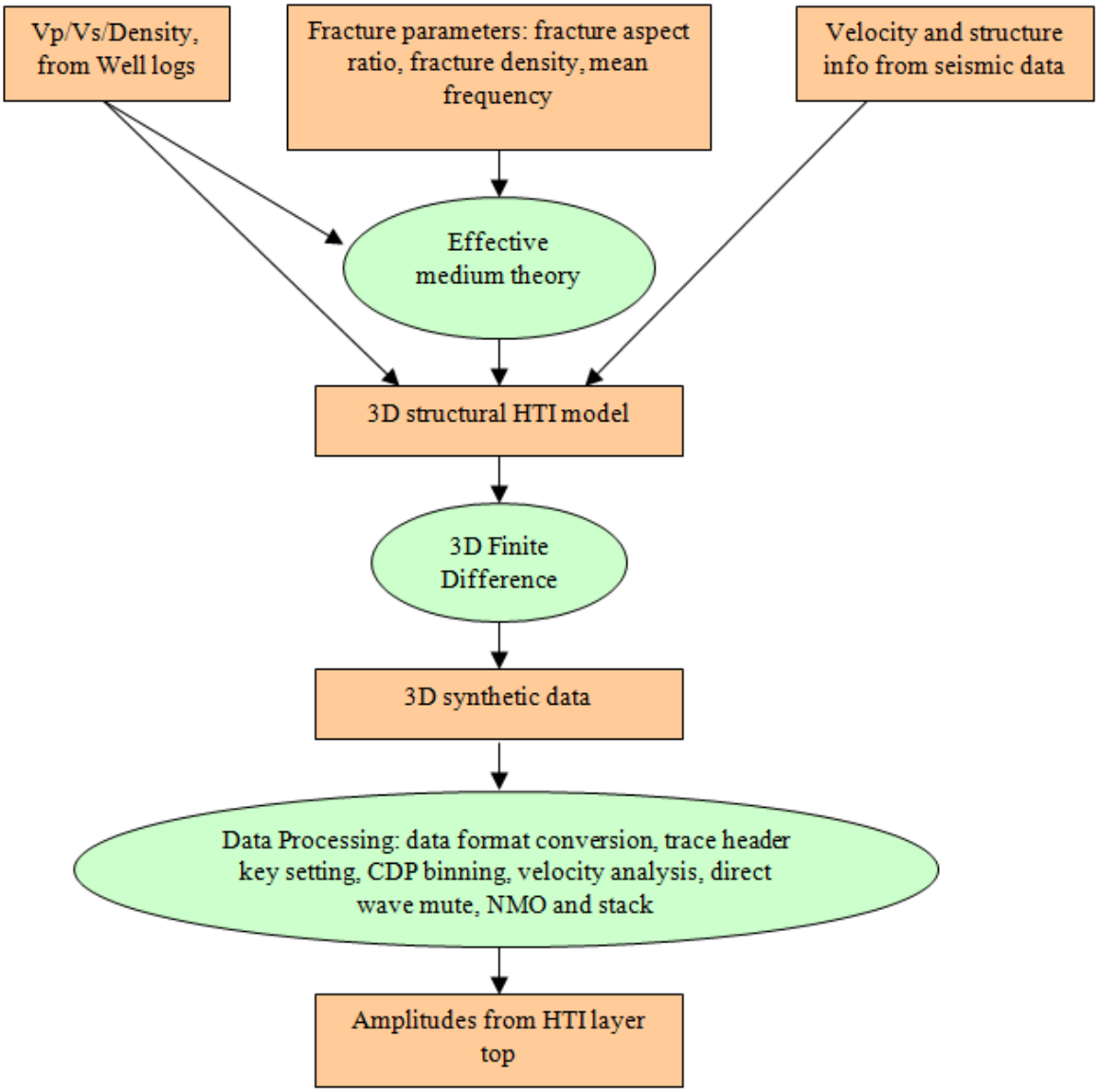

Figure 5.10: Schematic workflow used for model building and synthetic data generation in the 3D fracture reservoir models.

5.5.2 Modelling

Here let me discuss the modelling steps based on the workflow in Figure 5.10. Firstly, medium property parameters are selected for each layer from well logs, laboratory measurement or interpretation results. Based on Chapman's model, I calculate the stiffness vectors for the fractured layer. The FD modelling technique developed in Chapter 3 is used to generate the synthetic data for the three 3D models. Figure 5.8

shows the geometry, with more details listed in Table 5.5. I acquire 117 shotgathers for each model. Each shotgather takes 48 hours on a 2.2G-CPU 8G-MEM 2-core PC. All the calculation is performed in a Linux PC-Cluster environment.

Parameters	**Values**
Model size	10000m*4000m*4000m (x*y*z)
Grid size	10m*10m*10m (dx*dy*dz)
Geophone depth	500m
Absorbing boundary thickness	400m
Source line coordinates	(3360m, 700m, 500m) --- (8500m, 700m, 500m).
Sample rate	0.75ms
Record time	2.4 seconds
Wavelet frequency	20 Hz

Table 5.5: The modelling geometry parameter

5.5.3 Synthetic data processing

After the acquisition of the shotgathers for the three models, a conventional seismic data processing flow of P-wave data follows: trace header setting, CMP binning, velocity analysis, NMO, stack and horizon picking (Figure 5.10).

In real field 3D survey, thousands of shots are normally fired for wide offset and full azimuth acquisition geometry. However, for 3D numerical seismic modelling, the limit computation power restricts such practical acquisition geometry. In this study, only 117 shots are fired, which firms one source line. In order to obtain full azimuth CMP gathers, a technique is developed to generate full azimuthal CMP gathers from the synthetic data. During synthetic data processing, the CMPs along the Y direction are merged to form a single CMP which hence is able to contain full azimuthal (from 0° to 180°) amplitudes for the later AVOA analysis, as shown in

Figure 5.11. The merging process works because there is no medium property variation along the Y-direction. Therefore, I have one 3D CMP line for each model.

I pick the P-wave horizon as the reflection from the first interface of the models. The picked time in the stack section is then projected back to the NMO-corrected CMP gathers to extract the full azimuth amplitudes for each CMP gather. The amplitudes of each CMP gather are then converted to reflection coefficients using the original velocity model for the final objective, the SVD inversion.

Here I discuss some details in data processing. After CMP binning, I perform velocity analysis for a selection of CMP gathers. Figures 5.12, 5.13 and 5.14 demonstrate the velocity analysis for Model 1 at three CMP locations, which are away from the anticline, at the flank of the anticline and at the top of the anticline, respectively. I intend to look for the difference in velocity analysis that is caused by the anticline, but it is hard to find any except the difference in the velocity due to the difference in the first interface depth. After the velocity analysis, the obtained velocity is applied to the pre-stack CMP for NMO-correction and stack. Figures 5.15a, b and c represent the three stack section for Model 1, Model 2 and Model 3, respectively. There are two reflections in Figure 5.15a which are reflected from both the top and the bottom of the thin fractured layer. Compared with Figures 5.15a and b, it is hard to say if the thin layer affects the amplitudes. This effect can only be examined in the inversion results. Also, merely from three sections, it is impossible to conclude that there is any effect of the anticline. It seems there is no difference between the stack sections (Figures 5.15b and c) of Model 2 and Model 3.

After stacking, I pick the travel time from the top of the fractured layer in Model 1 (the travel time for other two models should be the same due to the same thickness and velocity in the first layer for the three models). The picked time is projected to the NMO-corrected CMP gather to pick the amplitudes from the bottom of the first layer in the three models, which are then converted into the reflection coefficients using the velocity models. Therefore for each CMP, I have a group of reflection coefficients (RCs) at different offsets (or incident angles) and at different azimuthal angles. The next is to average the RCs in each group at an incident angle interval of 1^o and an azimuthal interval of 20^o. Figure 5.16 shows three average RC example

groups at location CMP 449 for the three models, where the X-axis represents the azimuthal angle and the Y-axis represents the incident angle. From Figures 5.16a and b, the elliptical variation in RCs is clearly observed at the near and middle incident angles (5^o-30^o) due to the presence of the aligned fractures. From Figure 5.16c, which corresponds to the isotropic model, it seems there is no similar variation.

5.5.4 Fracture density inversion

Once each average RCs group of RCs at each CMP locations is ready, these RCs are then used as the reflectivity matrix ***R'*** (in Figure 5.4) along with the basis functions (***F***) from the SVD decomposition to invert an array of new seismic attributes (***C'***) based on the workflow in Figure 5.4. Then the correlation between the ***C'*** values and the old ***C*** values at the specific incident angle will generate the absolute fracture density from the colour map in Figure 5.3.

Here are the details for the inversion process. I take the reflectivity matrix in Figure 5.16a as an example. If we fix the incident angle in Figure 5.16a at, for example, 20^o, we can get an array of RCs which only vary with azimuthal angle. For the incident angle 20^o, an array of seismic attributes ($\boldsymbol{C'}$) can be inverted using the array of RCs (***R'***) and the basis functions (**F**) in Figure 5.3. After seismic attributes ($\boldsymbol{C'}, or\ C_1'$, C_2' ,C_3' …) are obtained, we fix the incident angle 20^o in the colour maps of Figure 5.3, and compare the value of $\boldsymbol{C'}$(C_1', C_2' ,C_3') and the value of $\boldsymbol{C}$ (C_1 , C_2 ,C_3); we can find a corresponding value on the Y-axis of the colour maps in Figure 5.3, which gives the inverted fracture density. For each $\boldsymbol{C}$, we can get one inverted fracture density. If we repeat this process for all incident angles, for each $\boldsymbol{C}$, we can get an array of fracture densities, which vary with the incident angles. With different CMP gathers, for each $\boldsymbol{C}$, the inverted fracture density is a function of incident angles and CMP locations, which, for example, corresponds to the left-hand colour maps in Figure 5.17.

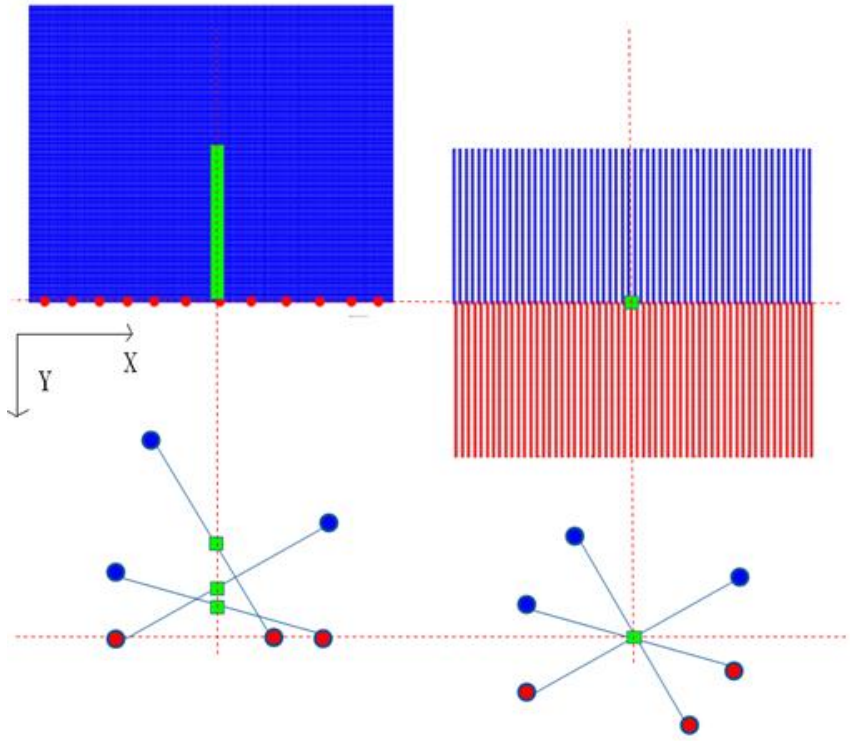

Figure 5.11: The left diagram shows the original CMPs (Red refers to the source location; blue refers to the geophone location; green refers to the CMP point), in which the azimuth range is very limited. After I merge CDPs vertically (Y direction) into one (the right diagram) I can get the azimuth range from 0 °to 180 °.

(a)

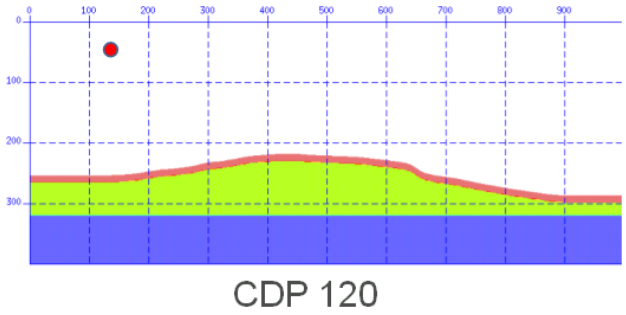

(b)

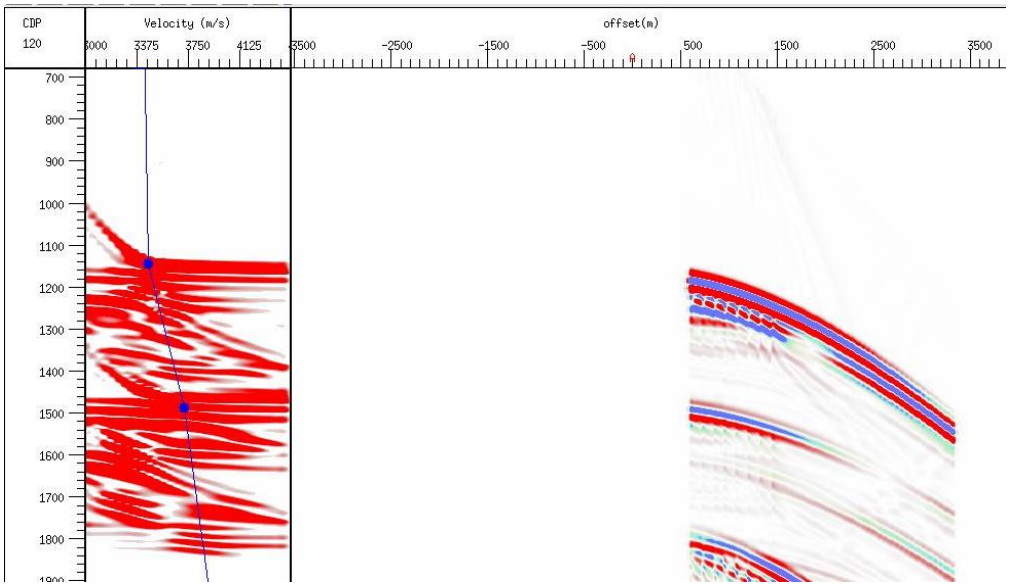

(c)

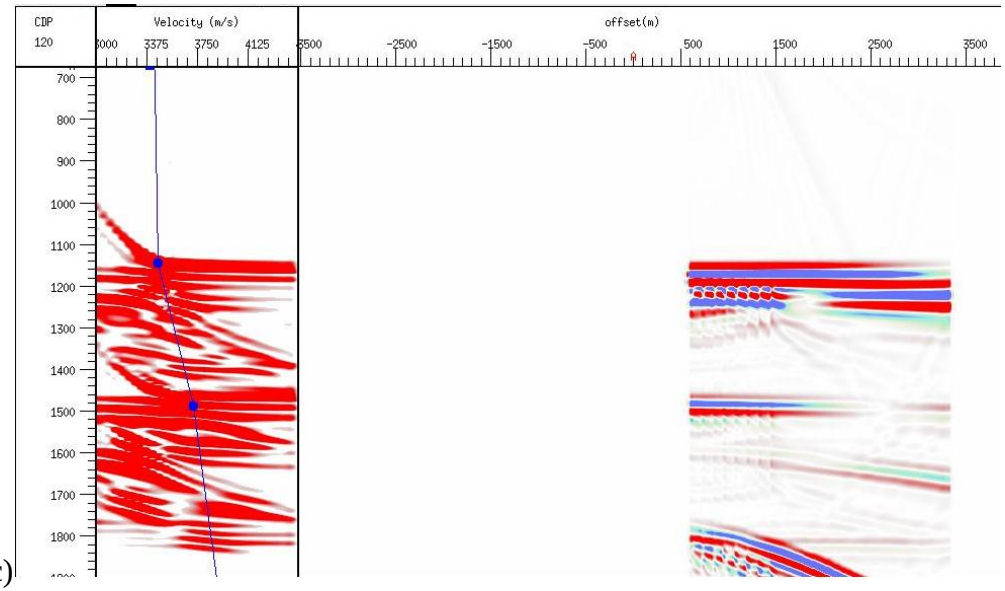

Figure 5.12: Velocity analysis at CMP 120; the CMP location is close to the left side of the model (a); the gathers before NMO and after NMO correspond to (b) and (c) respectively

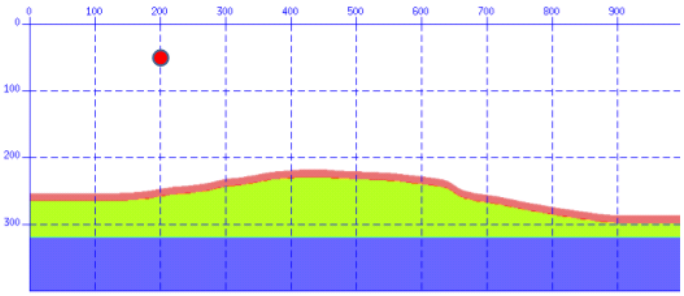

(a)

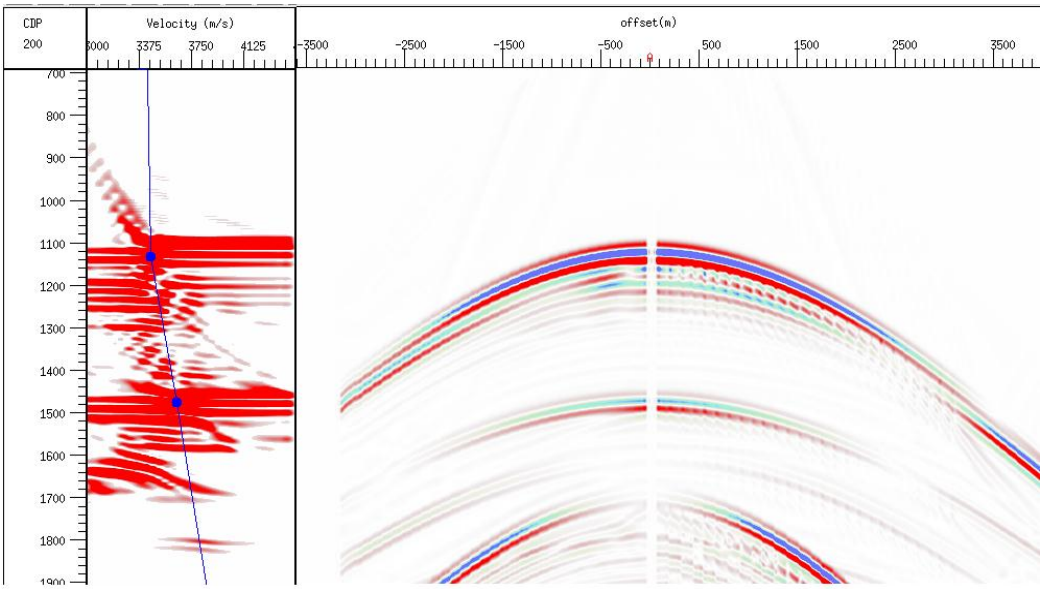

(b)

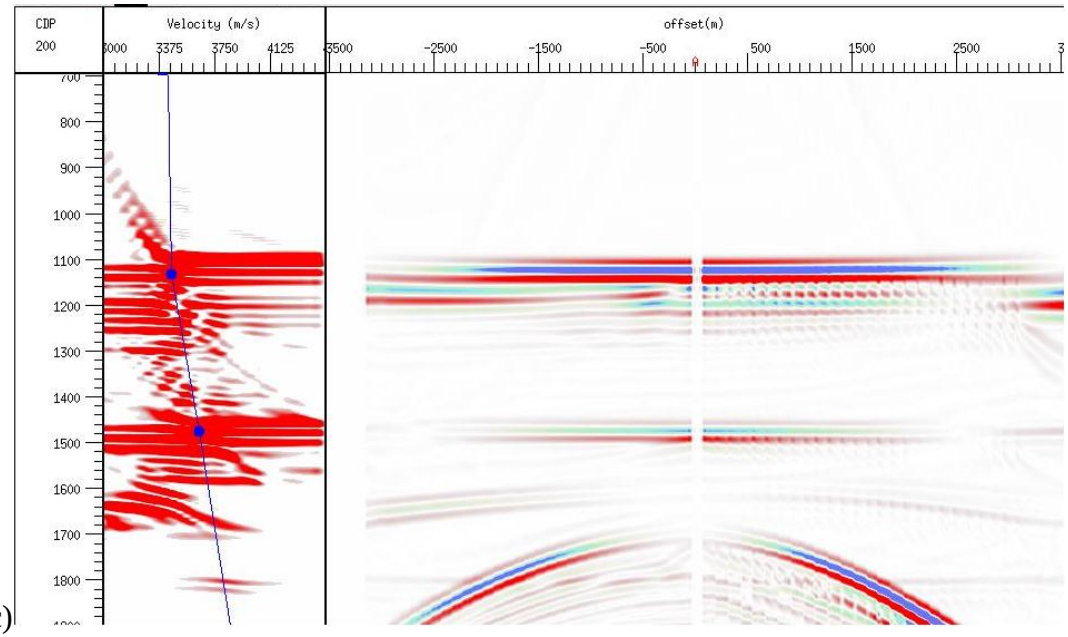

(c)

Figure 5.13: Velocity analysis at CMP 200; the CMP location is close to the left side but close to the middle of the model (a); the gathers before NMO and after NMO correspond to (b) and (c) respectively

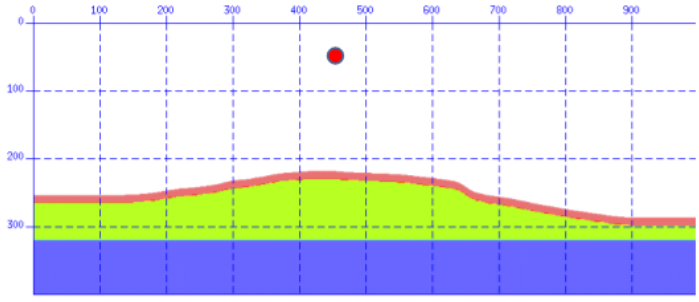

(a)

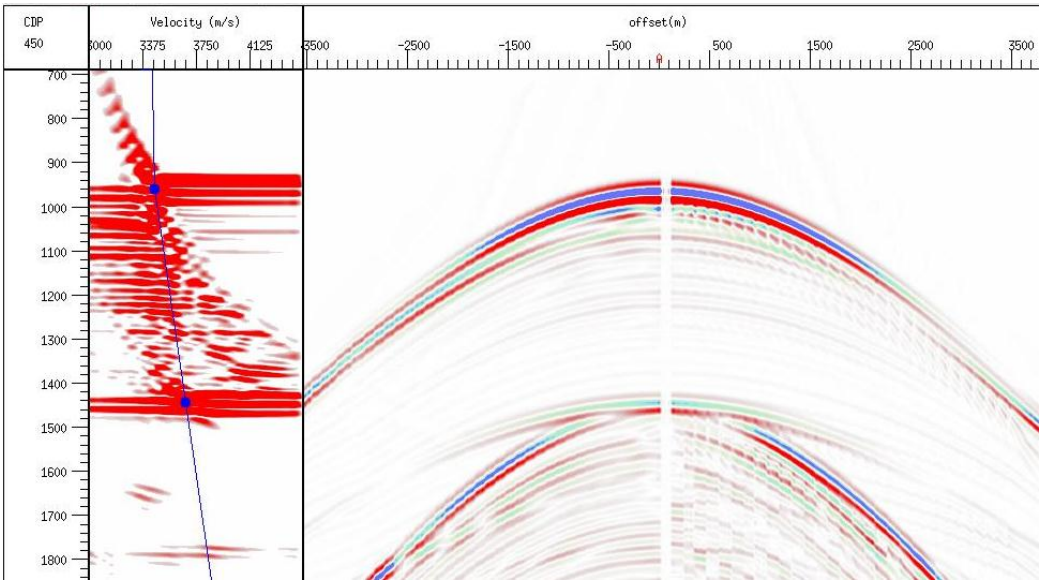

(b)

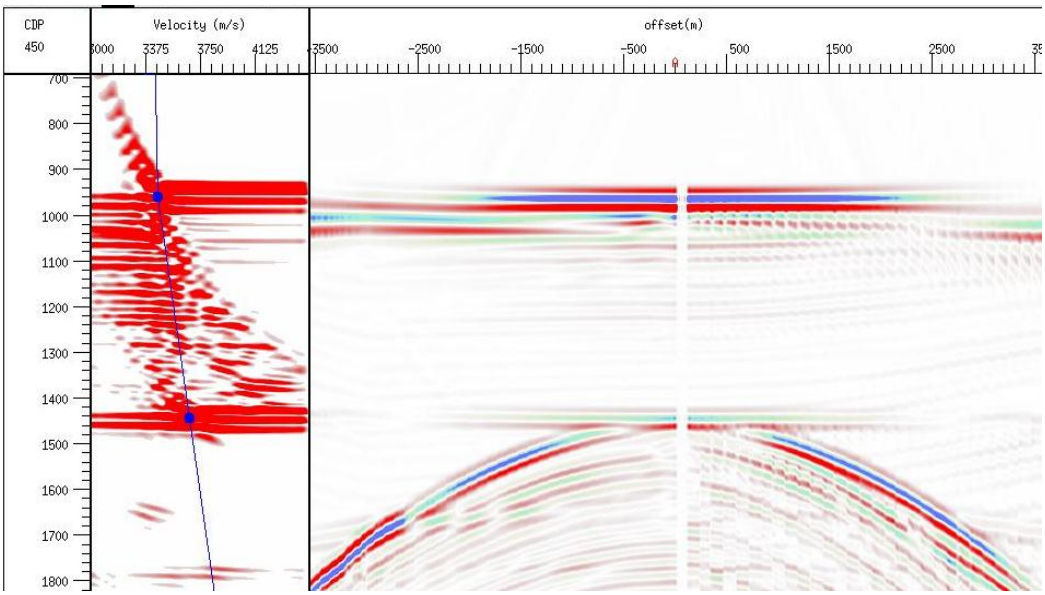

(c)

Figure 5.14: Velocity analysis at CMP 450; the CMP location is at the top of the model (a); the gathers before NMO and after NMO correspond to (b) and (c) respectively

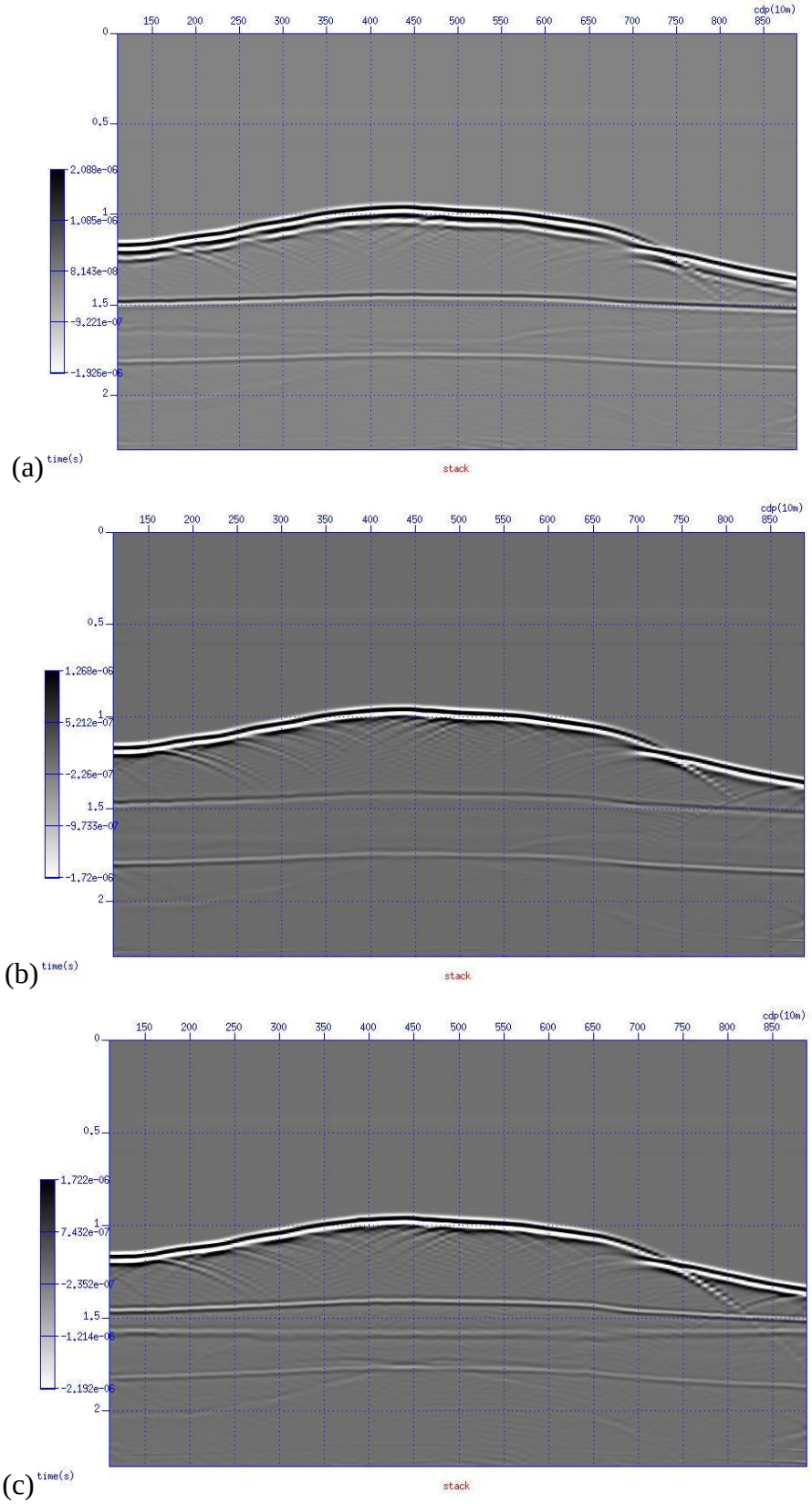

Figure 5.15: Stack sections for Model 1(a), Model 2(b) and Model 3(c)

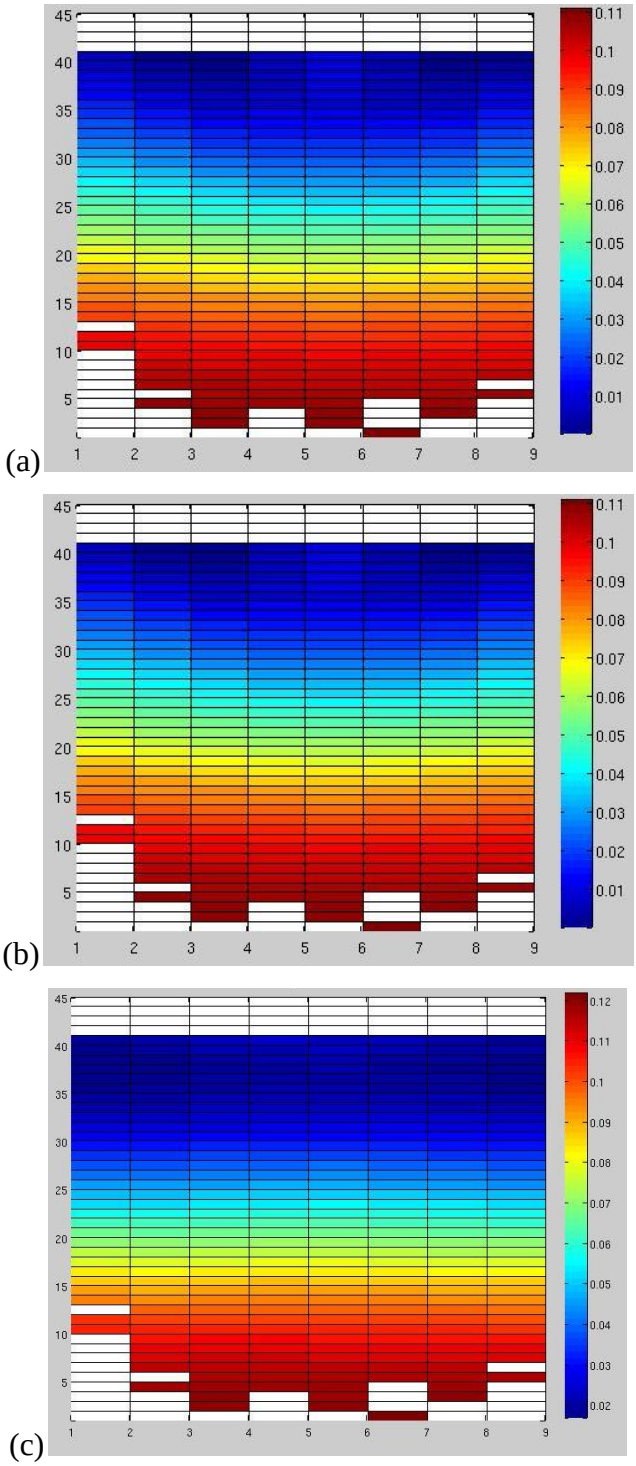

Figure 5.16: The plots above are the reflection coefficients for Model 1(a), Model 2 (b) and Model 3(c) for CMP 439, which is exactly located at the top of the anticline. The X-axis represents the azimuthal angles (from 1 to 9, which corresponds to 20 ° to 180 °) , and the Y-axis represents the incident angles from 1 ° to 45 °. Azimuthal variations in the reflection coefficients are clearly observed for Model 1 and Model 2. For Model 3, the azimuthal variation in the reflection coefficient is zero due to the isotropic signature.

5.6 Result analysis

The final results are plotted in Figure 5.17, where the left-hand plots are the inverted fracture density versus CMP locations and incident angles for the three models, and the right-hand plots are the mean fracture density (over incident angle) of the corresponding left-hand ones. Note that the dark blue colour in the left-hand colour maps of Figure 5.17 implies that no proper fracture density could be found for the inversion process. Here I mainly focus on the analysis on the mean fracture density in the right-hand plots, which only varies with the CMP locations. From Figure 5.17, we can see the most robust results are obtained using C_1 and C_2 and the results obtained using C_3 are significantly noisy.

For Model 1, the result (the first row on the right-hand plot of Figure 5.17a) indicates that the fracture density values obtained using the attribute C_1 at the top of the anticline structure are close to the pre-set fracture density value of 0.26. On the two flanks of the anticline, the inverted fracture density values are higher than 0.26 due to the dip-related effects. The results from the attribute C_2 (second row on the right-hand plot of Figure 5.17a) reveal a lower fracture density than expected. Overall I can conclude that the presence of the anticline enhances the inverted values for fracture density on its flanks but shows nearly no effect at the top of the anticline.

For Model 2, I notice that the results from three attributes (Figure 5.17b) are almost exactly the same as the results from Model 1(Figure 5.17a), which implies that there is no effect from the thickness of the thin fractured layer and consequently thin layer (tuning) effects are negligible. This point is further confirmed with the two CMP examples in Figure 5.18, where we can see the thin layer is thick enough to separate the reflections from its top interface and its bottom interface.

In Model 3, there is no fracturing and only the anticline is considered. The obtained fracture density from C_1 and C_2 (the first row and the second row on the right-hand plot of Figure 5.17c) are very close to zero at the top of the anticline but relatively large values of fracture density are obtained on the flanks of the anticline, and I

believe the values can be attributed to fake seismic anisotropy due to the presence of the dipping structure.

The results inverted from C_3 are quite noisy but they show a similar trend to the other results from C_1 and C_2 do. In addition, the SVD method, to some extent, is validated by the inversion results and proves a reliable method.

(a)

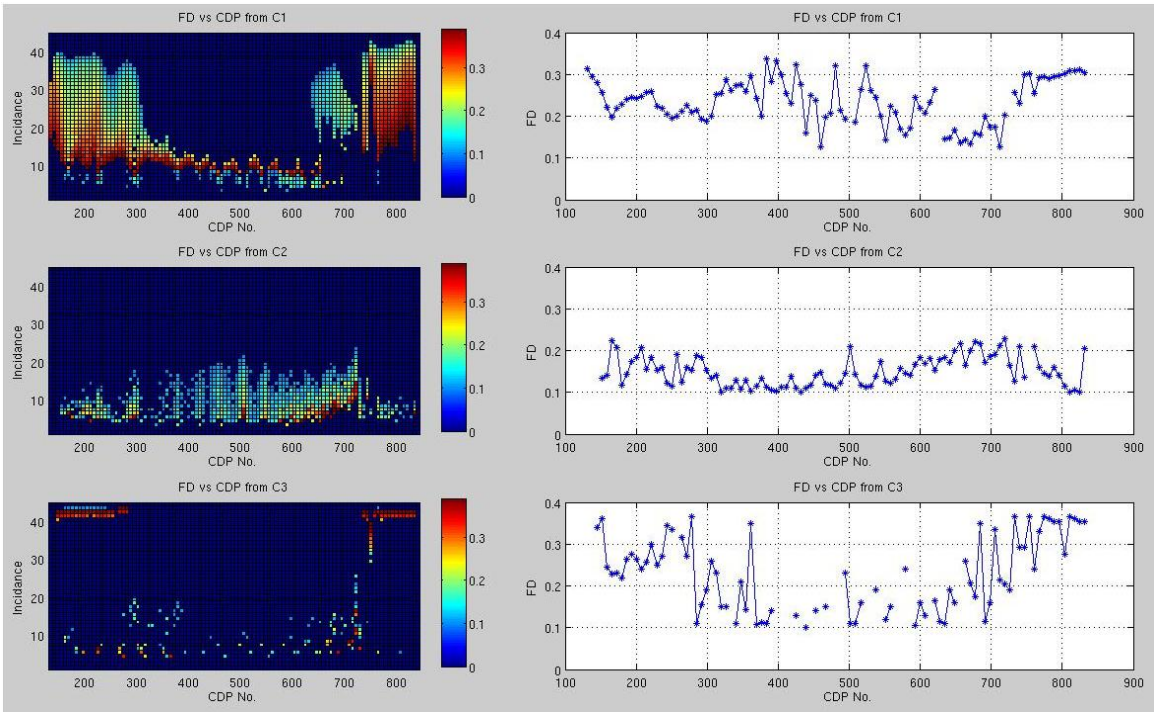

(b)

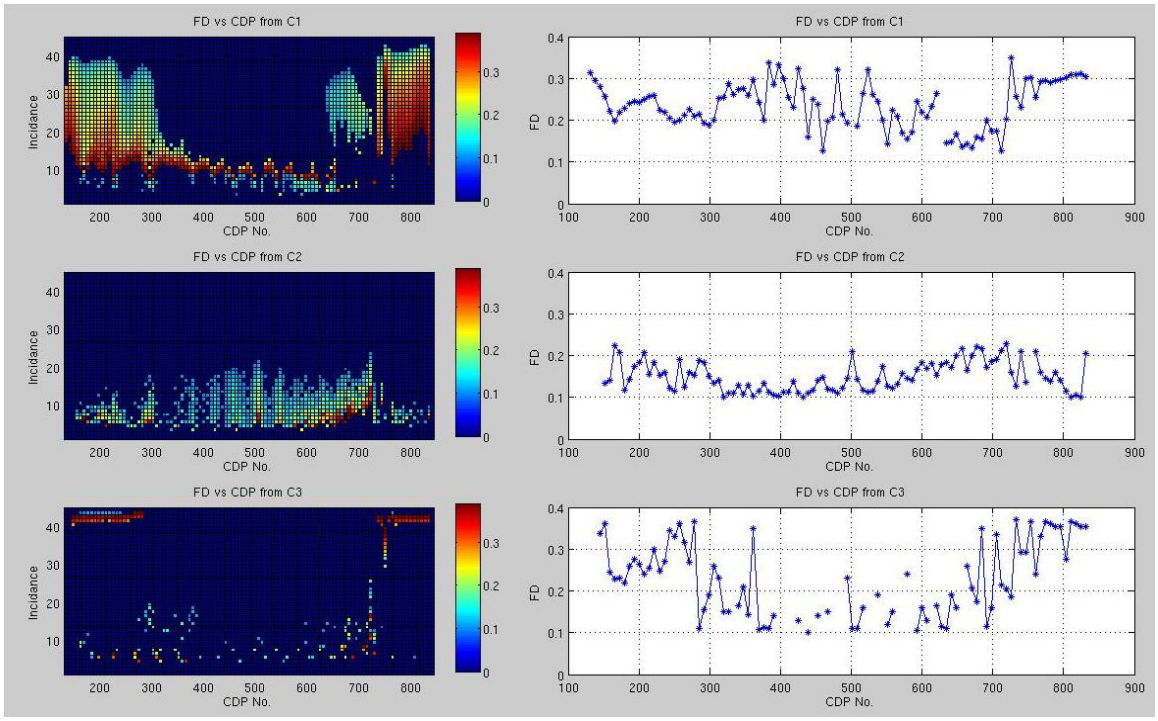

(c)

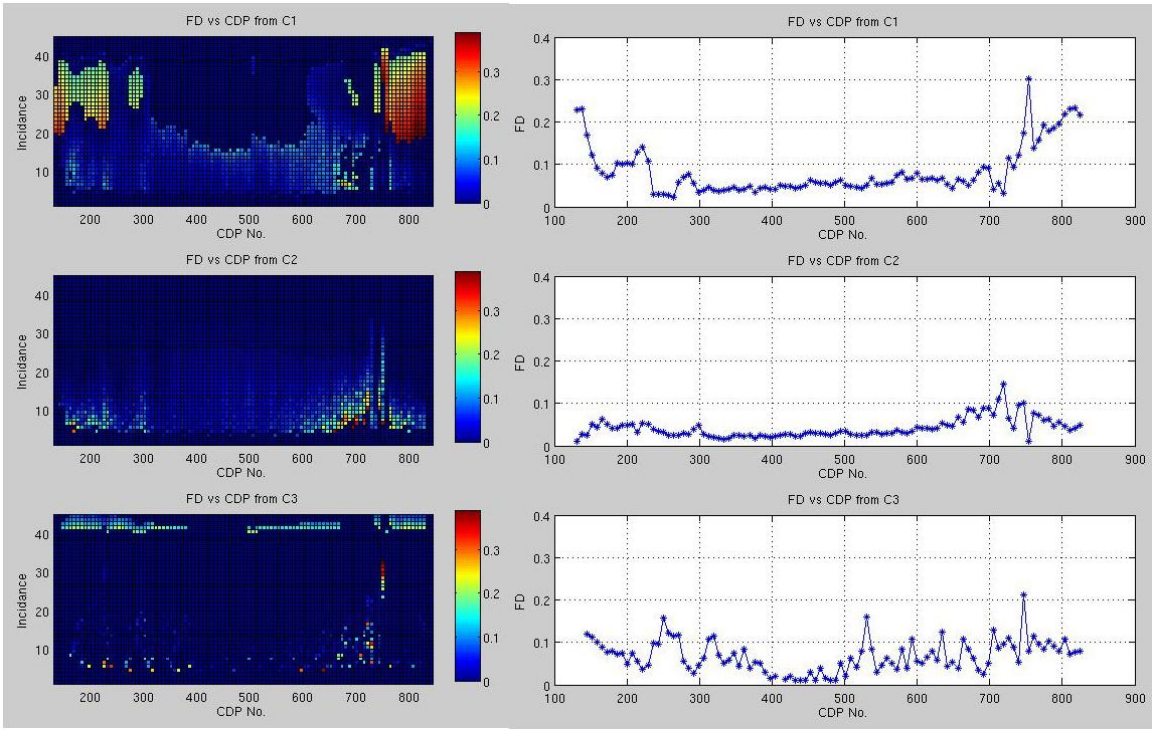

Figure 5.17: The inversion results (a), (b) and (c) correspond to Model 1, Model 2 and Model 3. The left-hand subplots are the fracture density results inverted from three attributes, which vary with incident angle and different CMP locations; the right-hand subplots are the mean fracture density from the corresponding left-hand results.

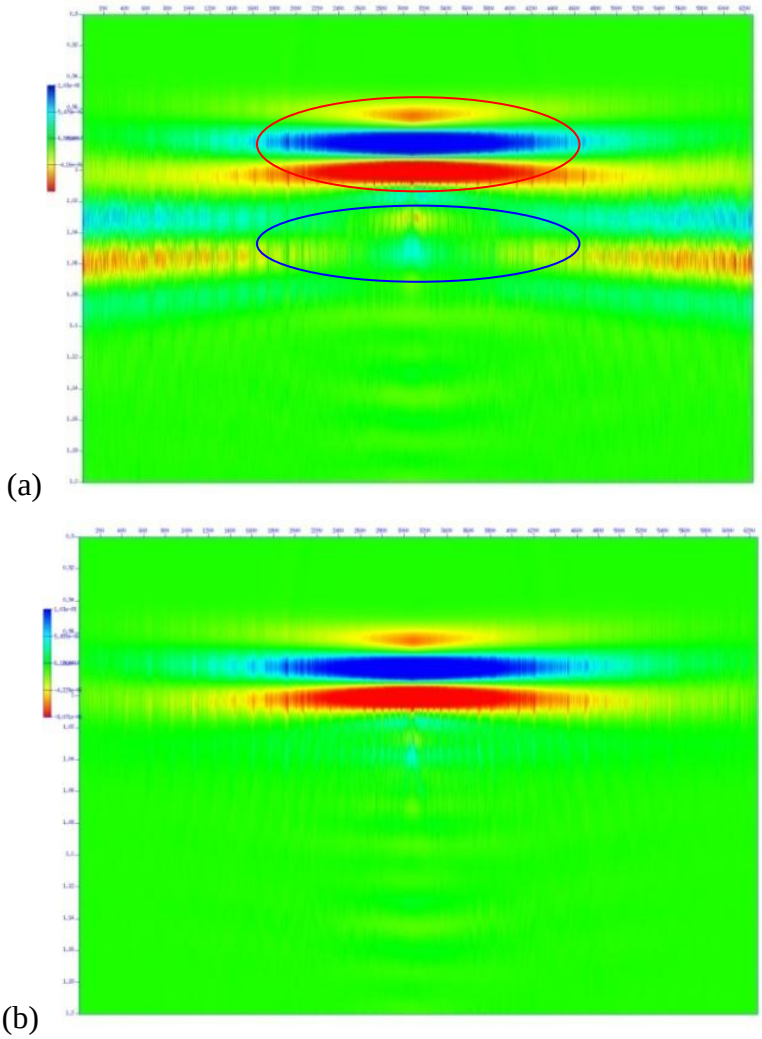

Figure 5.18: The zoom-in sections of two NMO-corrected CMP gathers from Model 1(a) and Model 2(b) at the top of the anticline. The top reflection in the red ellipse is separated from the bottom reflection in the blue ellipse, and therefore the magnitudes in the red ellipse are almost the same as those in (b).

5.7 Discussions

On the other hand, there are some points which need to be addressed:

- In field data, the rock properties for building the reflectivity matrix in the SVD method (from well logs or from seismic data) cannot represent the real case for the whole survey, which can possibly affect the inversion results. In this study, a realization of rock property distribution away from the well is not considered.

- Another problem for the field data is the possible error in the velocity model obtained from the velocity analysis on synthetic data, which needs to convert offset to incident angles, and from amplitude to reflection coefficient, because the angles are rarely correctly calculated due to the presence of geological structures or seismic anisotropy, or some other factors. Therefore, a careful velocity analysis is essential for the conversions.
- From the inversion results in Figure 5.17, we can see there is much dark blue in the left-hand plots, which means that no proper results have been inverted. In some cases, if the incident angle is fixed in the seismic attributes in Figure 5.3, there may be two inverted results. Therefore some extra procedure is required to assist in reducing the ambiguity.
- To date, Chao and Maultzsch (2010) is the only real case study with the SVD method and more case studies are required to validate the approach and to enhance our confidence.

5.8 Conclusions

This work presents a 3D numerical study of the effect of an anticline on fracture density inversion using a method based on the SVD decomposition of AVOA data, and the parameters of the numerical models are from a real case study. Finite difference modelling in 3D structured fractured media is applied to generate the synthetic data used in this study. The results indicate that the SVD method is a reliable approach for directly estimating the fracture density. The effect of the anticline on the inversion results has been assessed in this case study. The fracture density can be resolved accurately at the top of the anticline, whilst on the flanks it tends to be over-estimated. The sensitivity analysis of the inversion results also indicates that the seismic attribute C_1, related to the leading term in the SVD decomposition, is the most robust and reliable attribute for fracture density inversion.

6 Chapter 6 An integrated study of fracture prediction using P-wave field data

In this chapter, I carry out an integrated study of fracture prediction using P-wave data from Nanyishan Oil Field. The whole study area is dominated by a regional anticline and the target layer is a fractured gas reservoir. I focus on two major aspects in this study. First, I extract two P-wave post-stack attributes and examine their features in the target layer, looking for the possible fracture distribution in two prospective zones. Second, I apply the azimuthal attribute analysis approach to estimate fracture density and orientation in the whole area from the pre-stack data. The result from the post-stack data indicates the high possibility of fracture distributions in the two zones, and the prediction from azimuthal amplitudes in pre-stack data is consistent with fracture orientation from the well interpretation and the outcrop observation at the top of the anticline, but suffers from the poor offset-depth ratio and the acquisition footprint. The prediction from azimuthal traveltime is strongly influenced by the regional anticline structure and therefore is not reliable.

Nevertheless the prediction from both post-stack and pre-stack attributes provides more details of the fracture distribution in the target reservoir.

6.1 Introduction

Using P-wave seismic data to predict fracture properties is an economical means to characterize fracture reservoirs, compared to using S-waves or PS-waves (Tsvankin and Lynn, 1999). Analysis of azimuthal variation in P-wave attributes (e.g. amplitude, travel time and interval travertine) is a useful approach to predict fracture density and fracture orientation. Many such efforts have been made since the 1990s (MacBeth and Li 1999; Gray et al., 2002), and the applications have proved to be productive. In practice, a number of factors (e.g., survey acquisition, data quality, overburden layers, geological structures etc.) may affect the resulting prediction of fracture properties, and cause uncertainties in the interpretation of seismic data. Qian (2009) carries out a series of studies on some of these factors, including the offset-depth ratio in acquisition setting, data quality, overburden, each of which may show preferential effects on the results estimated from specific attributes (for example, regarding estimation with amplitude, data quality plays a major role; structure may effect estimations from travel time or interval travel time). Li (1999) and Wang (2007) have explored how to remove the overburden effect from the resulting estimation. Taking another example, I have studied the effect of an anticline on fracture inversion in Chapter 5, which tends to over-estimate the deduced fracture density on the two flanks of the anticline. In order to assess these side effects, another approach is to integrate azimuthal attribute analysis with the other geological and geophysical information, which may assist in lowering these effects and reducing the uncertainties in seismic data.

In this study, the motivation is to integrate various data (outcrops, wells, pre-stack data and post-stack data) to predict fracture distribution in the whole survey and to provide more convincing interpretations for further operation in two prospective zones. There are two major parts in this work: (1) predicting fracture distribution

with post-stack data in two prospective zones, and (2) inverting fracture parameters in the whole area with the pre-stack azimuth attributes. After that, comparison between different prediction results is made for more profound understanding of the fracture distribution in the study area.

6.2 Geological background

The study area is in the Nanyishan Oil Field (the red rectangular area in Figure 6.1a) which lies in Caidamu Basin in Northwest China, a semi-desert region. A survey confirms that a major anticline dominates the survey area (the top of the anticline is the dashed ellipse in Figure 6.1a or the SE-NW narrow area in Figure 6.1c). As we can see from Figure 6.1a, the surface appearance in the middle of the survey is like a series of squeezed tree annual rings, which is caused by geological weathering on the top of the anticline over its history.

Figure 6.1b shows the seismic data acquisition coverage map, which is used as a reference for later discussion of the acquisition. Figure 6.1c is the iso-depth colour map of the target top, indicated by the yellow rectangular area in Figure 6.1a. In the middle of the map, there are production wells. A post-stack seismic section, extracted from the yellow line in Figure 6.1a, is shown in Figure 6.1d, where we can clearly see the anticline with two reverse faults (denoted with X and Y in Figure 6.1d) at its two sides. Such geological structures come into being due to the horizontal compressional stresses in geological history. Meanwhile, intensive fracturing occurred during this process. This structural setting and the resulting fractures provide perfect conditions for fluid storage and flow.

The actual study area is around $400km^2$. The target layer in this study (in the blue ellipse of Figure 6.1d) is a fractured condensate gas reservoir which is just under the anticline at a depth of around $3km$(around 1.8s in the stack section). The top of the target layer is marked as the horizon N11 (the blue dotted line) in Figure 6.1d. Based on previous work, the lithology of the reservoir is mainly mudstone and limestone.

(a)

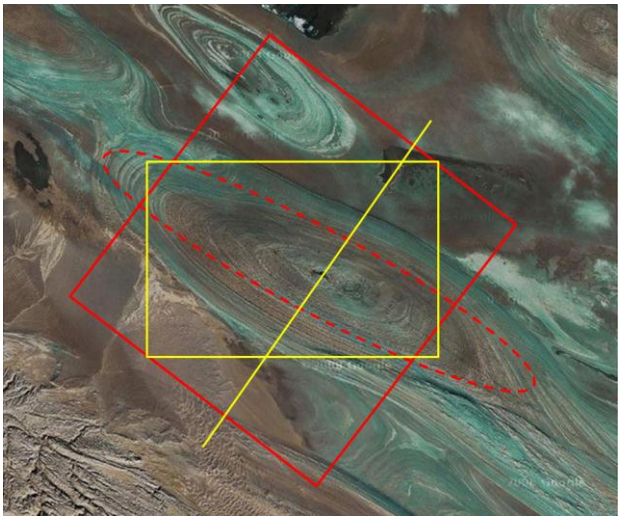

Overview of the study area in Google map:

- Red rectangle: the study area, also represents (b)
- Dashed ellipse: the anticline
- Yellow rectangle: the area (c)
- Yellow line: the section location of (d)

(b)

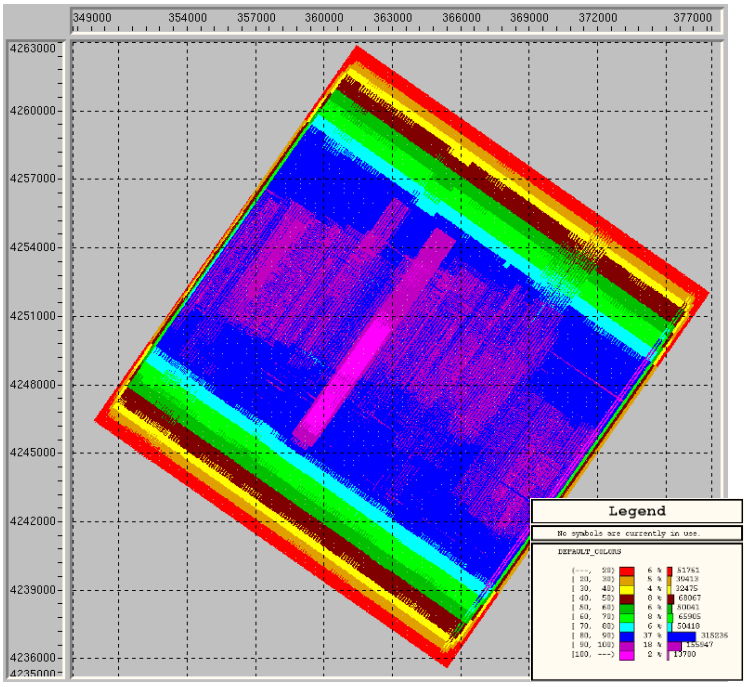

(c)

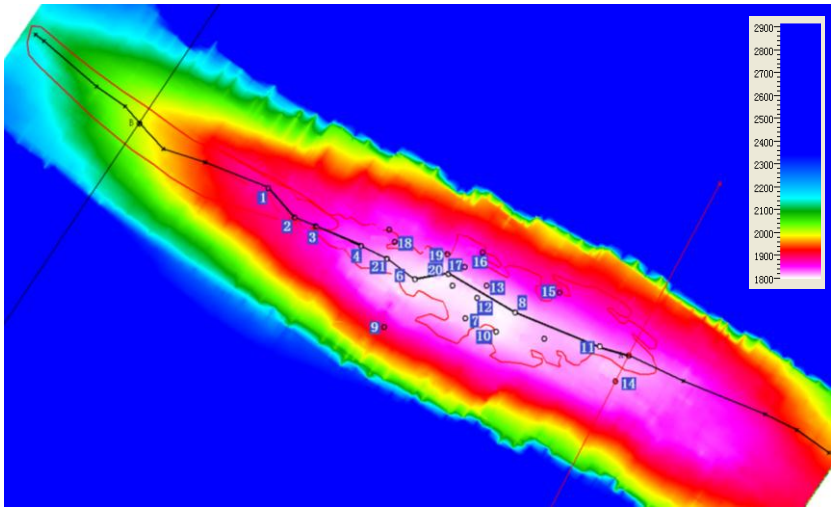

(d)

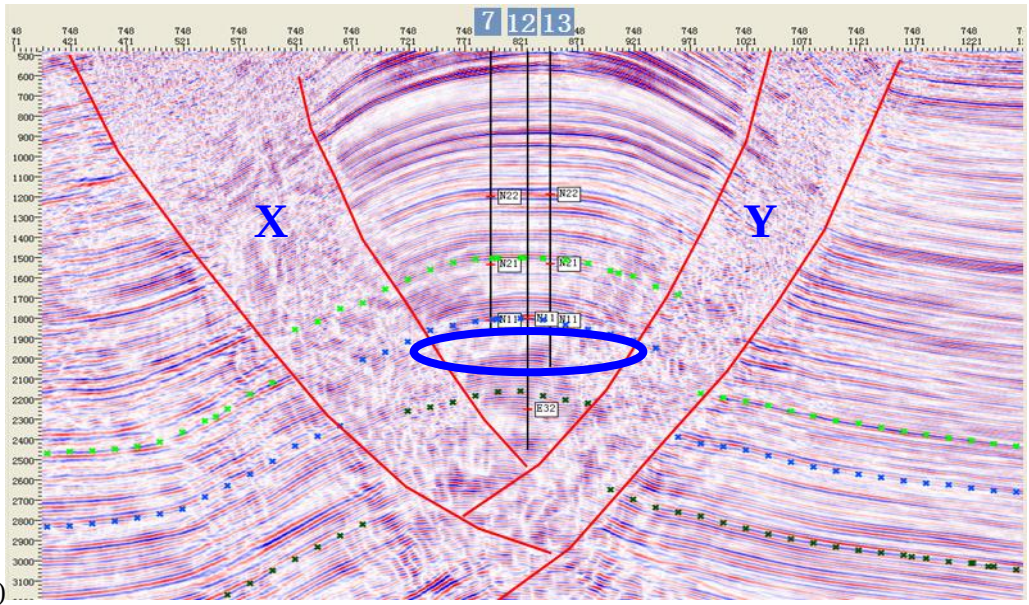

Figure 6.1: The study area (a) is in a semi-desert area. The iso-depth colour map (c) and the seismic section (d) show the anticline (the red area in c, middle area in d), the faults ('X' and 'Y' in c) and the reservoir locations (the blue ellipse in c). Well 7, 12 and 13 are also marked in the section, which can be found in (c). (b) is the geometry coverage, which is used in later discussion.

6.3 Review of the previous work

The previous work reveals that fractures are widely developed in the study area, and it includes outcrop investigation, examining core samples and microscopic rock slices, well log interpretation, and seismic data processing and interpretation. Next I will give a general review of this work.

Investigation of outcrops, core samples and microscopic rock slices, is considered as a direct and visual way to observe the overall geological phenomena in the area. The outcrop work was performed in many different locations in the study area, particularly at the top of the anticline and in the neighbouring locations of the wells. Figure 6.2a and b show two pictures of outcrops taken in the area, from which we can see that many high-angle fractures have developed. Also, the outcrop observation confirms that 70% of the fractures align parallel to or perpendicular to the anticline strike, which can be demonstrated by the rose diagrams in Figure 6.2c. These rose diagrams are obtained in a statistical way by examining the number and orientation of the fractures at the outcrop locations. The fracture development in the surface, to some extent, can reveal the fracture distribution in the subsurface.

Some cores from certain wells were examined as well. Figure 6.2d is an example of a core where a major vertical fracture is observed. Figure 6.2e shows a microscopic rock slice, from which we observe the microstructures, minerals and microcracks. It was estimated that the average aperture of the micro cracks observed is around 40 *um*, which is important for the storage and passage of fluids.

Figure 6.2f shows a cross-well section, and the black-red marks on some of the wells (denoted with vertical black lines in Figure 6.2f) indicate an interpretation of high fracture concentration. It is confirmed that there is a good correlation between the fractures and gas production at the well locations.

Figure 6.3 shows the differences in the acoustic impedance at the well locations (Well 7, 8, 10 and 11). High impedance is found in the overburden layer, low impedance in the reservoir, which allows us to infer the presence of fractures and a possible gas deposit.

The previous work proves the wide existence of fractures in the area, and these results provide a good correlation basis for later attribute analysis.

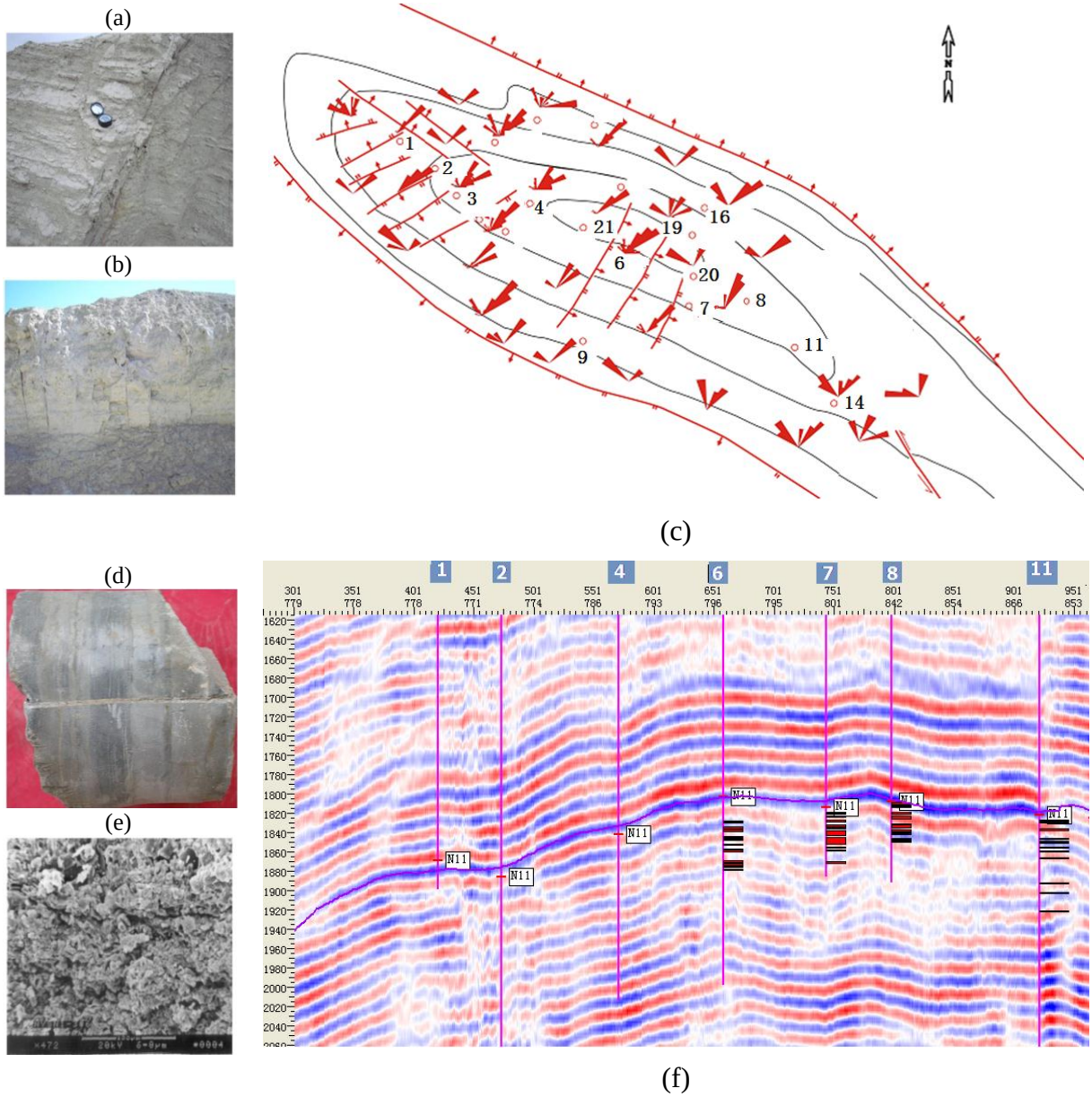

Figure 6.2: The previous work shows the evidence of fracture development in the study area. Outcrop pictures (a) and (b) show the high-angle fractures; also, the development of high angle fractures is confirmed by the outcrop investigation on the top of the anticline as shown in (c), where rose diagrams represent the fracture number and orientation. A core sample (d) and a micro rock slice (c) also show fracture existence at different scales. A cross-well seismic section along the anticline orientation (f) shows evidence of fracture development in the target reservoir. The interpretation of high fracture concentration is denoted with the black red marks on the wells. N11 marks the top of the reservoir.

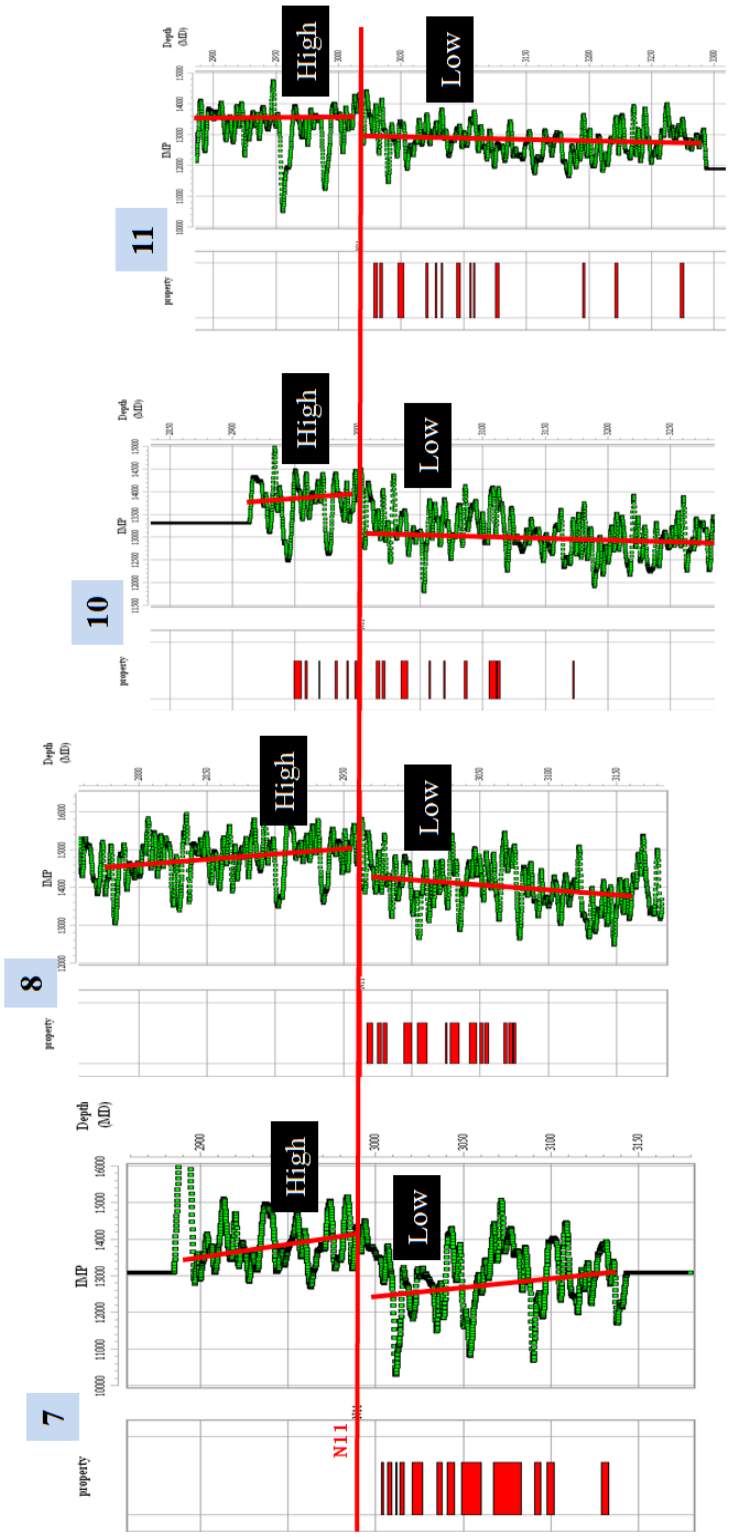

Figure 6.3: High acoustic impedance is found in the overburden layer and low impedance is found in the reservoir, at wells 7, 8, 10 and 11. Red marks are the well interpretation of fracture concentration.

6.4 Post-stack P-wave attribute analysis

6.4.1 Theoretical background

In this study, gas accumulation and fractures in the target reservoir may lower the seismic velocity and attenuate the high frequency content of the seismic waves, which therefore is more likely to result in a change in seismic energy and frequency. In this study, I extract two seismic attributes to examine such a change, reflection strength and frequency content.

One typical approach for attribute analysis, *Complex Trace Analysis*, can examine local variations in energy in seismic traces. Particularly, calculated attributes illustrated with colours, based on complex trace analysis, can convey ample seismic information to geophysical interpreters (Taner et al., 1979). Taner et al. (1979) has shown that the instantaneous seismic attribute, reflection strength, may aid the identification of lithologic changes between adjacent layers; they also point out that a fracture zone in brittle rocks is sometimes associated with low-frequency shadow. Taner (2001) concludes that reflection strength may be used to represent the acoustic impedance contrast and a major change in depositional environment. As shown in Figure 6.3, we can observe the contrast in acoustic impedance at the four well locations, and using reflection strength we may be able to laterally extend such a contrast across the seismic sections rather than confine it to the well locations.

The basic technique to determine the frequency distribution of a time series signal is the shot-time Fourier transform or windowed Fourier transform (WFT), which can describe different frequency content in a certain time window. It is a traditional technique for signal frequency analysis. However, the limitation is that the time window is a constant. A narrow window can determine the high-frequency content very nicely, but it cannot well handle the lower-frequency content. The wider window does well at lower frequency content but fails for higher-frequency content. Another frequency analysis approach, continuous wavelet transform (CWT) can

provide local frequency information, and more importantly it can extract frequency content at certain centre frequency ranges from time series signals (Moreau et al., 1997). There is no time window for CWT, and instead a group of wavelets with different centre frequencies are considered to decompose the original signal into an array of signals at these frequencies. The advantage in CWT is that any wavelet can be used. CWT has a wide application in seismic exploration, such as for spectral decomposition, denoise, data compression and migration (e.g. Ioup J. W. and Ioup G. E., 1998; Yu et al. 2004; Sinha et al. 2005; Kazemeini et al., 2007). For example, Sinha et al. (2005) and Kazemeini et al. (2007) use CWT decomposition as a direct hydrocarbon indicator.

In this study, the analysis of reflection strength and frequency content from CWT is carried out to reveal their possible link with the fracture distribution. These two attributes are calculated with the software *Geoscope*. Here I give the formula for reflection strength and CWT transform.

Assuming a seismic signal $f(t)$ and its Hilbert transform (or its quadrature) $f^*(t)$, we have a complex trace $F(t) = f(t) + jf^*(t) = A(t)e^{j\theta(t)}$ where

$$A(t) = [f^2(t) + f^{*2}(t)]^{\frac{1}{2}} = |F(t)| \tag{6.1}$$

$$\theta(t) = tan^{-1}[F(t)] = f(t) + jf^*(t) \tag{6.2}$$

$A(t)$ is amplitude envelope or reflection strength, and $\theta(t)$ is instantaneous phase (Taner et al, 1979). For a numerical solution of reflection strength, equation (6.1) can be used directly by sampling over time t.

The continuous wavelet transform (CWT) is defined as the sum over all time of the signal $f(t)$ correlated with scaled, shifted versions of the analysing wavelet function ψ (Kazemeini et al, 2007)

$$C(\sigma, \tau) = \int_{-\infty}^{+\infty} \frac{1}{\sqrt{\sigma}} \bar{\psi}\left(\frac{t-\tau}{\sigma}\right) f(t)dt \tag{6.3}$$

where σ and τ are the scale and translation parameter, respectively, and $\bar{\psi}$ is the complex conjugate of ψ. σ is a frequency-related parameter and if we fix this parameter, the CWT is a function of the translation parameter τ, which is a time-

related parameter. Scanning the parameterτ, we can get the transform signal series close to the dominant frequency that is related to σ. In this way, a seismic trace can be decomposed into a series of seismic traces at different centre frequencies.

In this study, frequency content from CWT is weighted over the energy strength at different centre frequencies and then classified into three categories, low frequency, middle frequency and high frequency, which are then coloured with Red, Green and Blue (RGB), respectively. The results for CWT at different centre frequencies can be displayed in coloured sections (as shown in Figure 6.7, 6.10, and 6.13, where red and black denote lower frequency content, and yellow and green denote higher frequency content).

6.4.2 Attribute analysis

In this section I focus on analyzing the post-stack attributes, reflection strength and frequency content in selected lines. Figure 6.4 shows the iso-depth colour map of the target top, where more than 20 wells are already drilled. Three seismic sections across the whole survey are considered: the first is the cross-well section along the major axis of the anticline (denoted as **Line 1** in Figure 6.4); the second is the section crossing Well 14 and the anticline (denoted as **Line 2**); and the third is the section at the NW of the survey and across the anticline (denoted as **Line 3**). For each section, I compare the original seismic section, the reflection strength section and the frequency section. Particularly, two zones in Figure 6.4, Zone A (where Lines 1 and 2 meet) and Zone B (where Lines 1 and 3 meet), will get more attention since they are considered as two prospective zones where there are no production wells.

Line 1

Figures 6.5, 6.6 and 6.7 are the sections of Line 1. The blue arrows point to the attribute area where the fracture concentration at the well locations is found by well interpretation and core observation (Well 2, 6, 20, 8, 11 and 14). The red arrows represent the prospective Zone A and Zone B in the subsurface.

Figure 6.5 shows the original seismic section, from which we can see the reflection is weak at the arrow marked areas whilst it is strong in the overburden layer. It is concluded that there is an energy contrast across the horizon N11. Zone A shows the same feature, which indicates the high likelihood of a fracture distribution. On the other hand, there is a difference in Zone B: the reflection above N11 is weak rather than strong, which may represent the fracture brittle area across the horizon N11. More knowledge of the two zones is needed to enhance our confidence. Next let us have a look at the features of reflection strength and frequency content.

Figure 6.6 shows the reflection strength section. Compared with Figure 6.5, it shows similar features, weak reflection under the horizon, strong above. However, the blue area under N11 from Well 6 to 11 shows more continuity than the amplitude reflection in Figure 6.5. The contrast in reflection strength cross N11 is clearer in both Zone A and B, but generally the overall features are compatible with those in Figure 6.5.

Figure 6.7 is the frequency content. As I mentioned, red and black denote lower frequency content, and yellow and green denote higher frequency content. It is widely acknowledged that fractures and gas accumulation may attenuate higher frequency content, which possibly leads to a shift to lower frequencies. The result from Figure 6.7 tends to agree with this principle, which shows a lower frequency distribution under N11 at the marked locations, including Zone A and B. Above N11, the frequency is higher, except at Zone B, where both sides of N11 show low frequency, and this confirms our analysis of reflection amplitude.

To summarize, the original section and the two attribute sections share similar features, which may implicate a fracture distribution in the prospective Zone A and B. Particularly in Zone B, the results across N11 are a little blurry, which may imply a brittle fractured region.

Line 2

Figures 6.8, 6.9 and 6.10 are the sections of Line 2, where I focus on the attribute feature at Zone A in subsurface. Obviously, these three sections show similar

features at Zone A to those of Line 1 at the corresponding location. There is a big contrast in all three sections across N11. All these features confirm the implication of fracture distribution in Zone A under the target horizon.

Line 3

Figures 6.11, 6.12 and 6.13 are the sections of Line 3, where I focus on the feature at Zone B underneath. On the contrary, in Zone B, there is no obvious contrast in the sections cross N11. The blurry results are consistent with our analysis before.

Summary

The sections from Line 1, Line 2 and Line 3 generally share the same features in amplitude reflection, reflection strength and frequency content. Analysis and comparison among all these sections, imply the high possibility of fracture distribution in the two zones. For Zone A, the distribution is just below the horizon N11, whilst for Zone B, the results imply a possible brittle fracture region across the horizon.

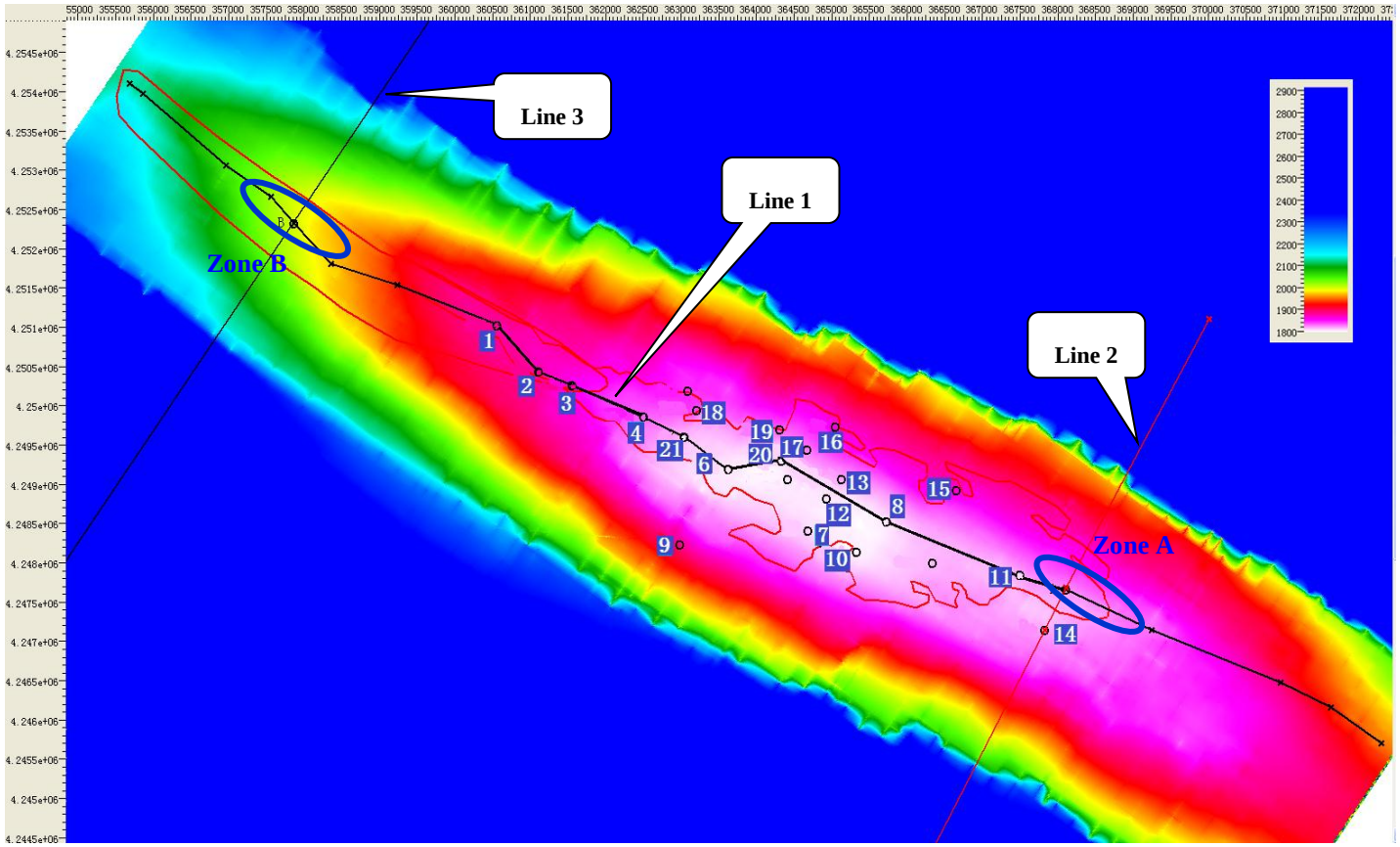

Figure 6.4: This is the iso depth colour map of the top of the target layer, which there are more than 20 wells drilled. Three lines (Line 1, Line 2 and Line 3) across the survey are extracted for further analysis for fracture prediction at the two prospective zones, Zone A and Zone B (marked with two blue ellipses). The white numbers represent the wells.

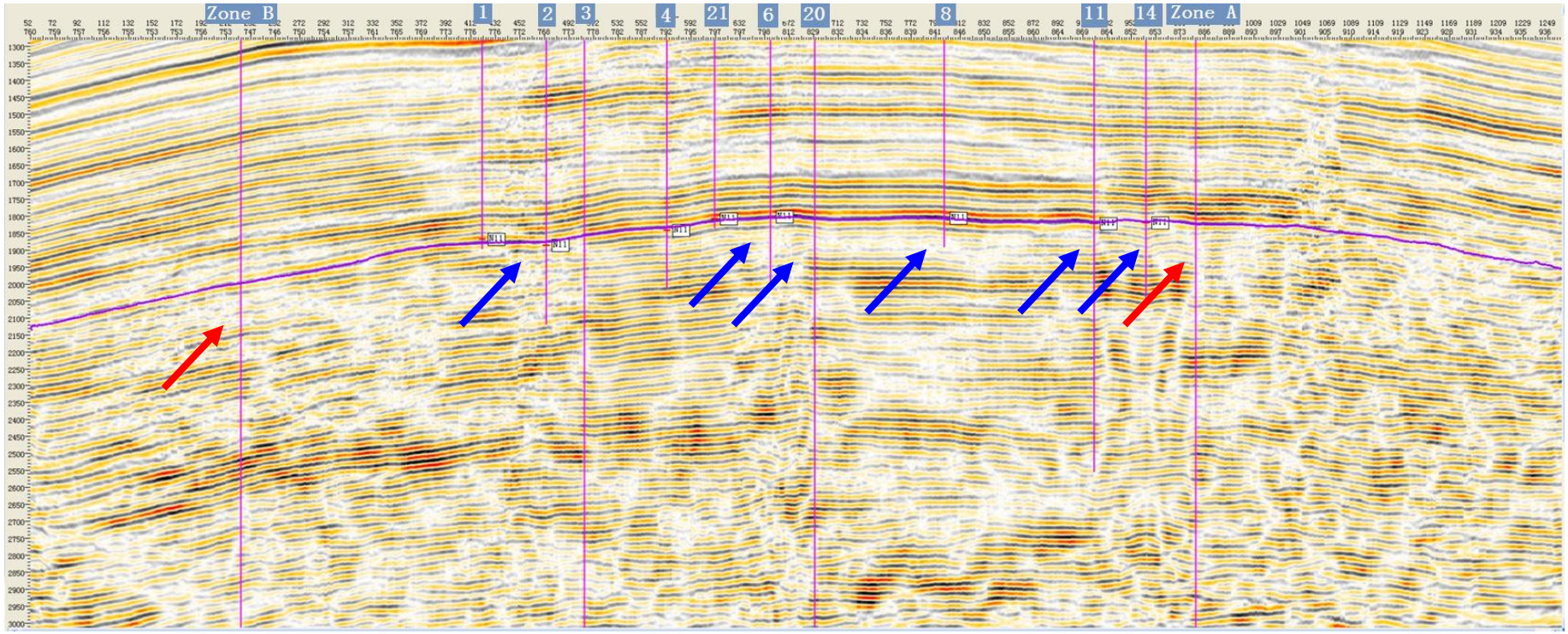

Figure 6.5: The seismic section from Line 1, where the blue arrows mark the fracture concentrations from the core observation and well interpretation. The two red arrows represent the two prospective zones, A and B.

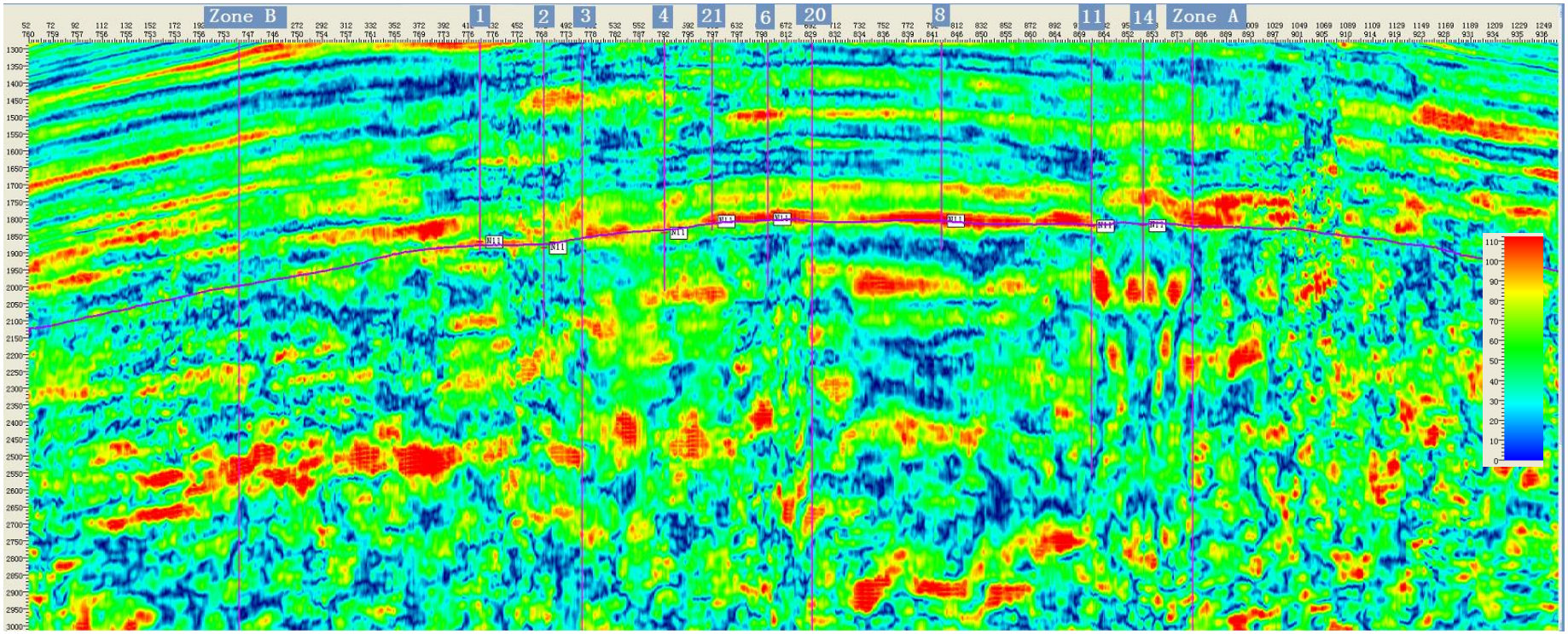

Figure 6.6: The reflection strength section from Line 1, where the blue arrows mark the fracture concentrations from the core observation and well interpretation. The two red arrows represent the two prospective zones, A and B.

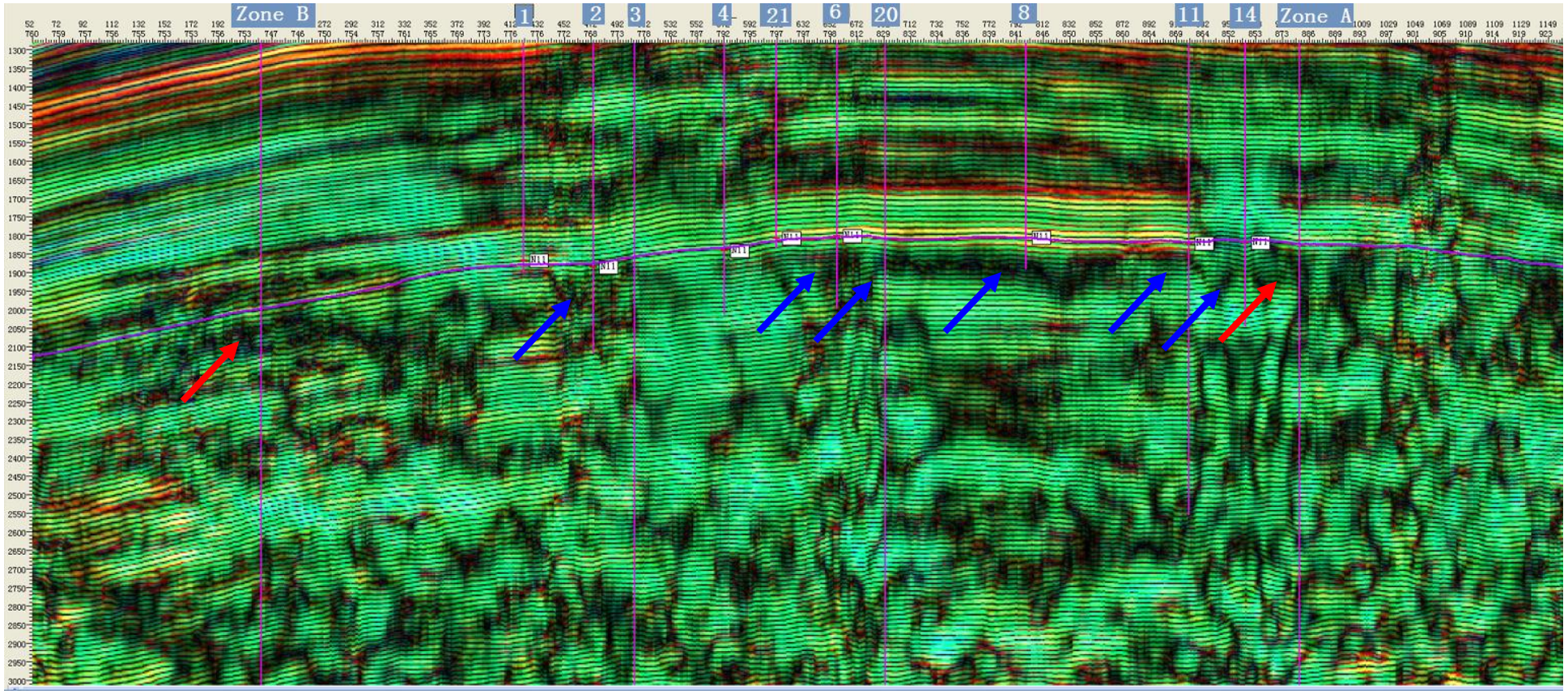

Figure 6.7: The frequency section from Line 1, where the blue arrows mark the fracture concentrations from the core observation and well interpretation. The two red arrows represent the two prospective zones, A and B.

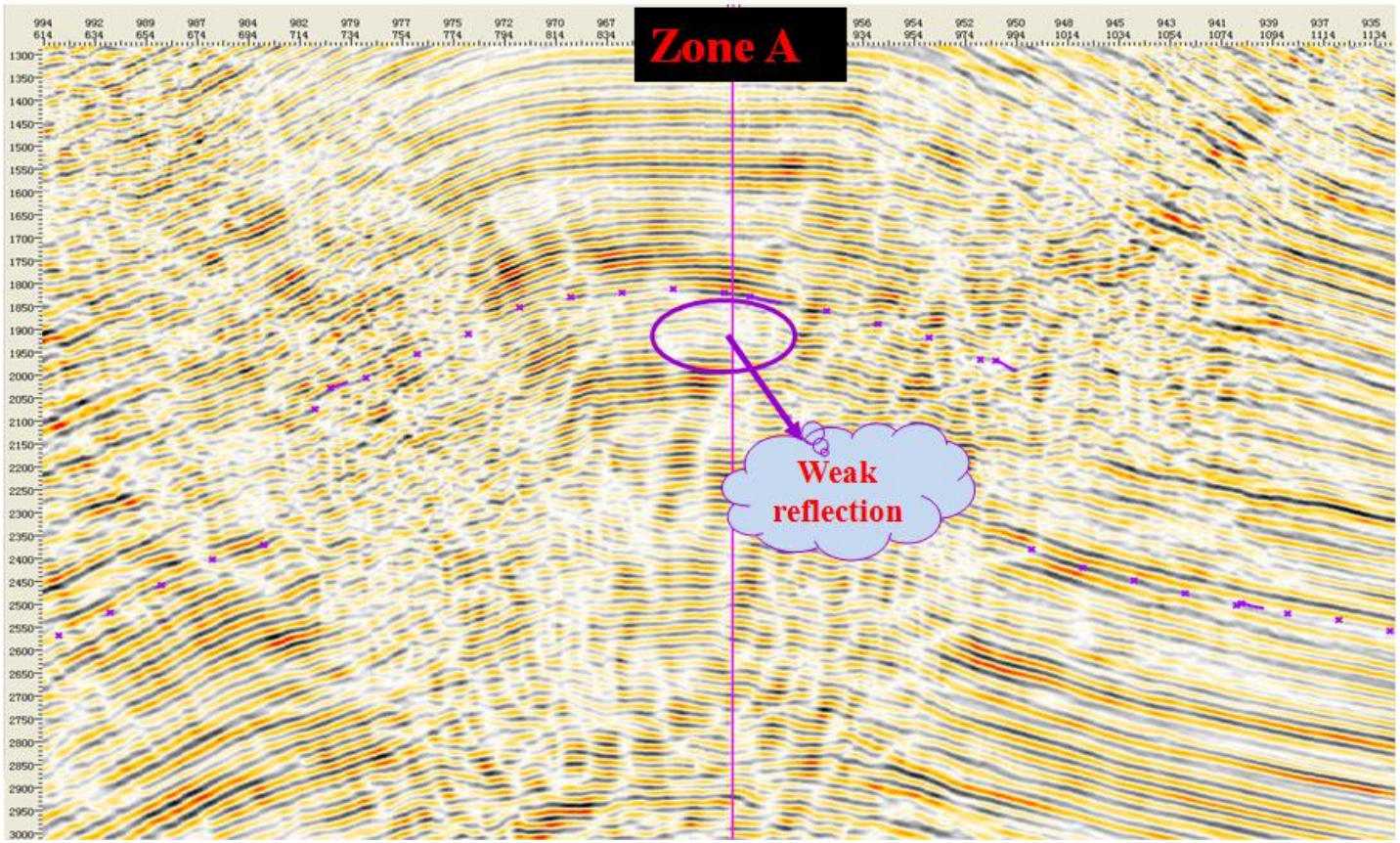

Figure 6.8: The seismic section from Line 2, where the ellipse marks the prospective region with weak reflection.

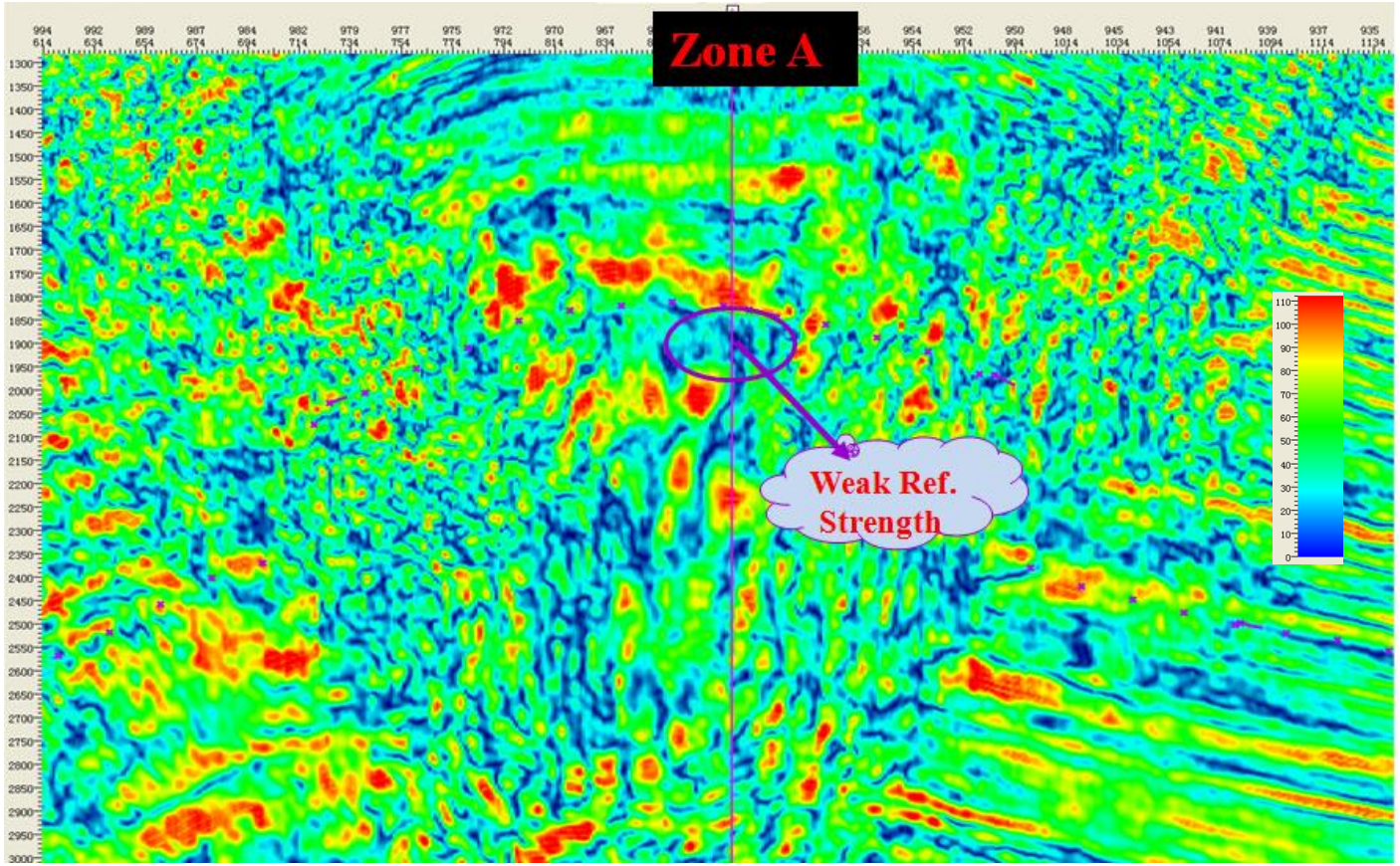

Figure 6.9: The reflection strength section from Line 2, where the ellipse marks the prospective region with weak reflection strength.

Figure 6.10: The frequency section from Line 2, where the ellipse marks the prospective region with lower frequency content.

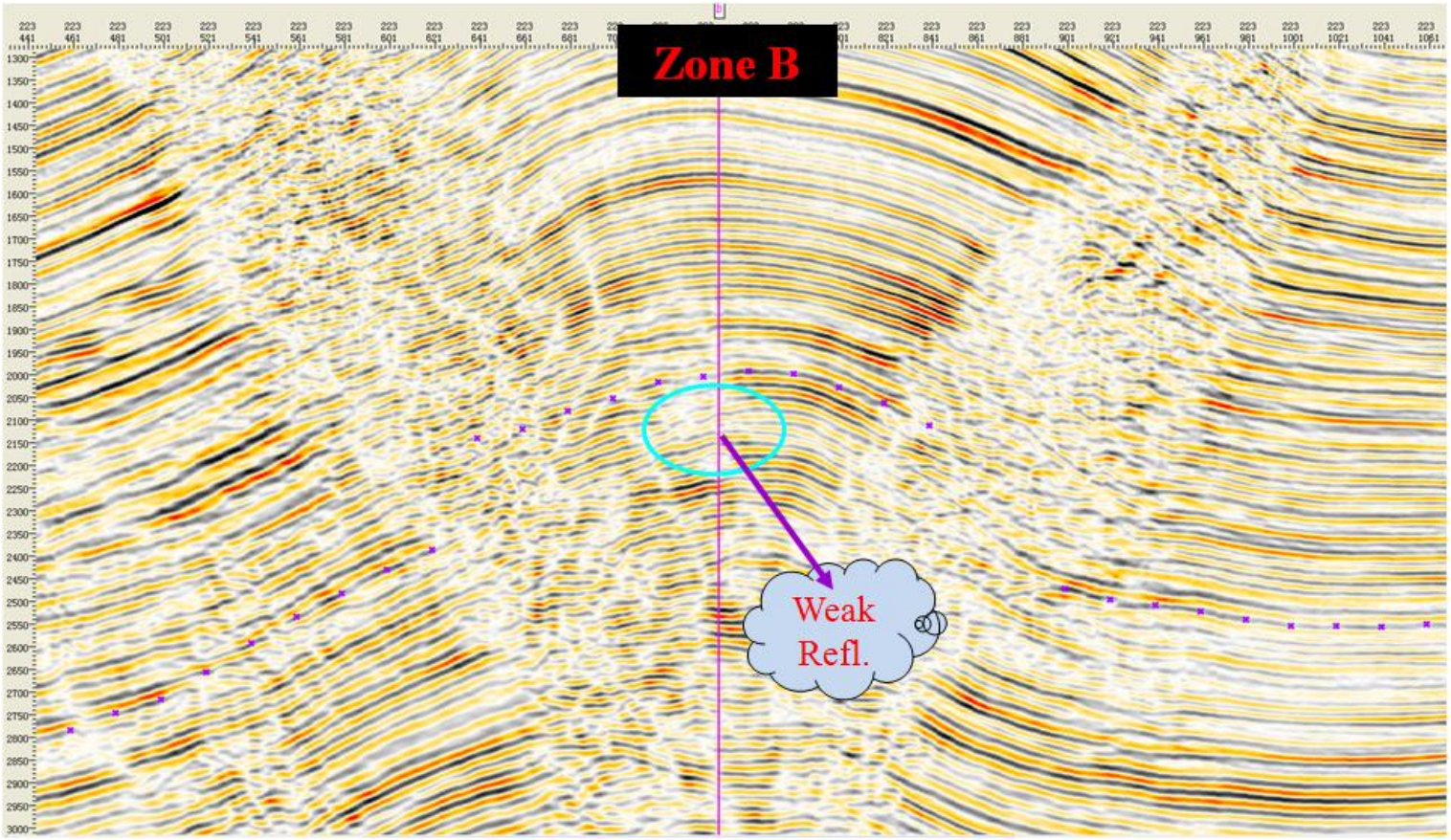

Figure 6.11: The seismic section from Line 3, where the ellipse marks the prospective region with weak reflection.

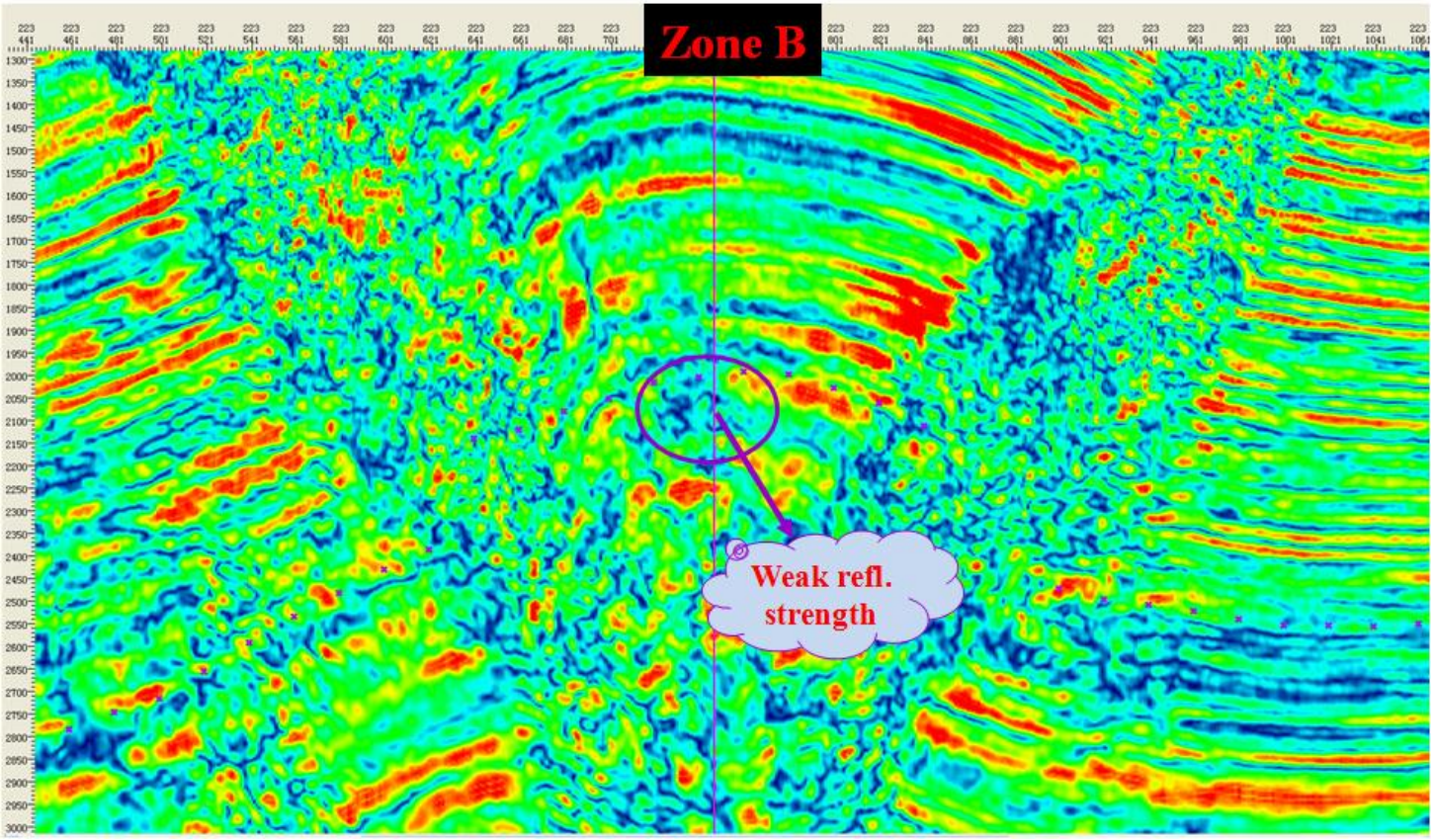

Figure 6.12: The reflection strength section from Line 3, where the ellipse marks the prospective region with weak reflection strength.

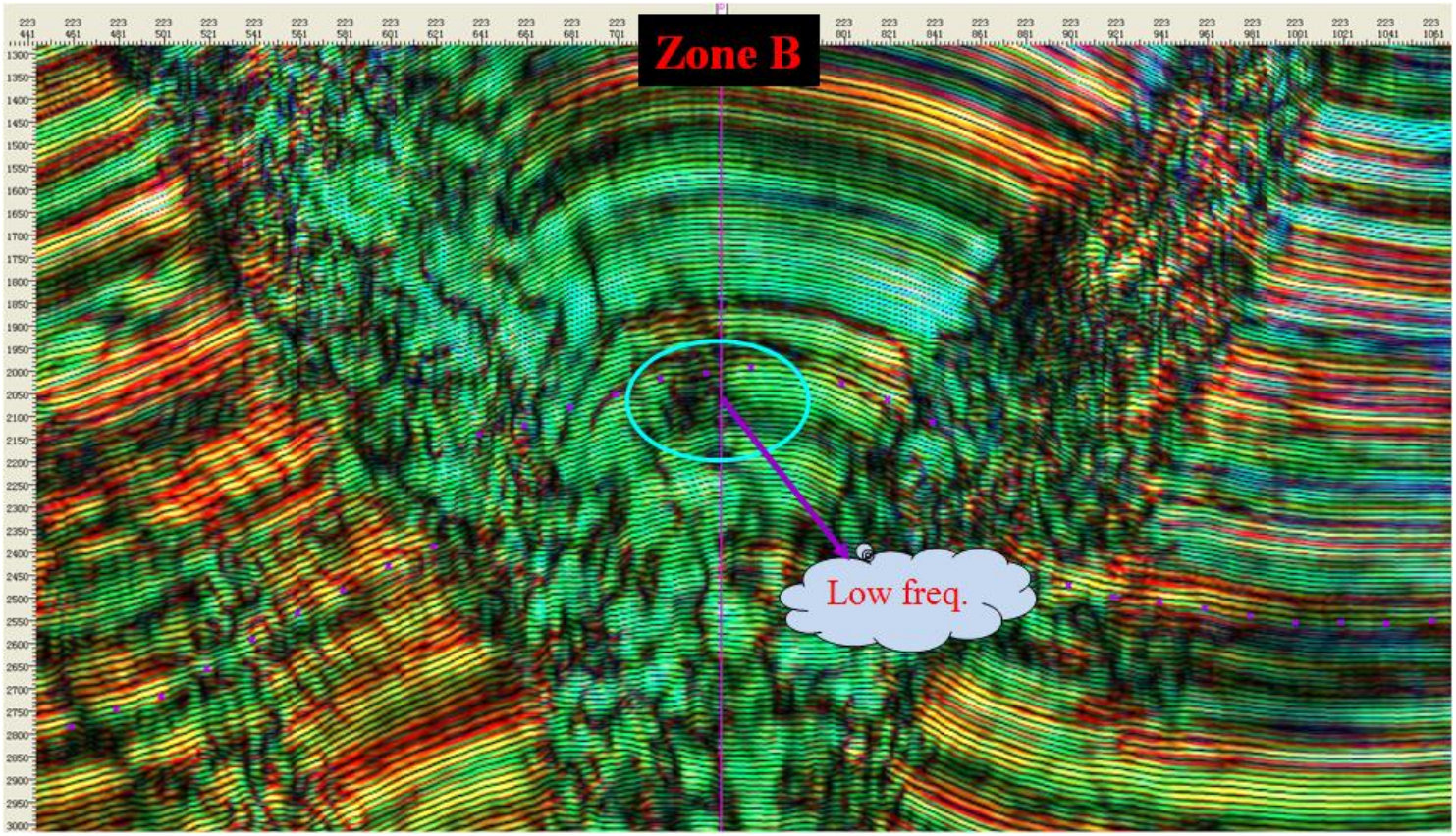

Figure 6.13: The frequency section from Line 3, where the ellipse marks the prospective region with lower frequency content.

6.5 P-wave azimuthal attribute analysis

6.5.1 Techniques for P-wave azimuthal attribute analysis

In practice, two techniques are often employed to perform azimuthal attribute analysis: full-azimuth surface fitting and narrow-azimuth stacking (Li et al. 2003; Hall and Kendall, 2003; Qian et al., 2006). The first method fits an elliptical surface of seismic attributes at all available azimuthal angles. The second method divides the full azimuthal data into different azimuthal bin gathers and the analysis is performed over all azimuthal bin gathers. The first method is applicable to amplitude and travel time, whilst the second is applicable to velocity and AVO gradient (Li et al. 2003).

In real data application, when the full azimuth surface fitting method is considered with amplitude analysis, an offset-azimuth stacking method is often included, particularly when signal-noise ratio is low or there is no sufficient offset coverage. This offset-azimuth stacking method is similar to the narrow-azimuth stacking method, but it also divides the bin gathers according to different offsets (or incident angles). Therefore each bin gather is at a certain azimuth and offset range, corresponding to a sector in Figure 6.14. Then stacking occurs at each sector, which can improve the S/N ratio. After stacking, there is one trace in each sector, which then follows the full azimuth surface fitting methods at different offset ranges. For each offset range, an estimate of fracture density and orientation can be obtained. The final estimate can be calculated by averaging the estimates at different offsets in certain ways.

There are quite a few factors that affect the fracturing. Different factors show different sensitivity to different pre-stack attributes. Seismic amplitude is most sensitive to seismic data quality. For traveltime and interval traveltime, the main factors that affect fracture estimation are the offset-depth ratio (or offset coverage) and geological structures (Qian, 2009).

Figure 6.15 shows the workflow chart for fracture prediction with pre-stack seismic attributes. Normally the conventional processing flow is applied before fracture

prediction. Note that for prediction with amplitude, amplitude should be preserved during data processing to avoid distortion. The processing proceeds until post-stack data are obtained. Then pick the top and bottom of the target fracture layer (assume there is one vertical fracture set and no overburden anisotropic layers above the target layer). The picking time is thereafter projected to the NMO-corrected super CDP gathers to extract seismic attributes, amplitude, traveltime, interval traveltime, or AVO gradient. It is necessary to examine the azimuth-offset distribution before the projection process, in order to see if offset coverage is ideal for azimuthal attribute analysis. Once azimuthal attributes are obtained, we apply those techniques discussed above for the final prediction.

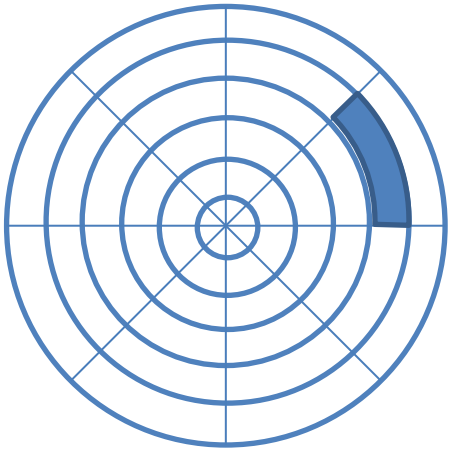

Figure 6.14: Every sector in the diagram is a bin gather in the offset azimuth stacking method.

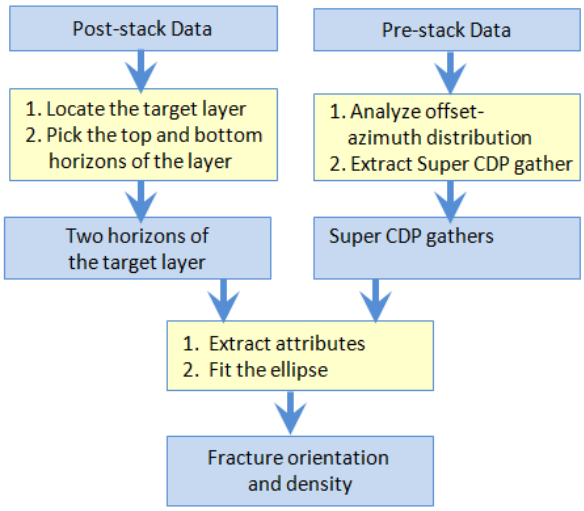

Figure 6.15: Processing chart for fracture prediction

6.5.2 Data feature

In this study, I use the offset-azimuth stacking method and the full azimuth surface fitting method to predict the fracture density and orientation with two pre-stack attributes, amplitude and traveltime. Before the prediction, let us have a look at the data quality and offset coverage across the survey. I have to mention that the survey acquisition was done by one of our sponsors in 2006-2007 and originally they didn't take the full azimuth into account for fracture prediction.

Figure 6.16 shows one typical super CDP gather before NMO correction. I extract super CDP gathers at the cell size 90m *90m and divide each gather into 6 bin gathers with an azimuthal range of 30 degrees for each in order to examine the azimuth distribution. From Figure 6.16, I find the major portion of the traces covers the azimuthal ranges 30^{o} - 60^{o} and 60^{o} - 90^{o}. Only a few traces are in the other bin gathers, which is not an ideal azimuthal coverage for fracture prediction. Also, I find the full average azimuth distribution is only in small offset range, like 0m - 1500m and the offset depth ratio is around 0.5 according to the target layer being at the depth of 3km. Qian (2009) points out that the preferred ratio is at least 0.6 for amplitude, at least 1.0 for traveltime. Obviously the ratio in this study doesn't meet the condition, particularly for fracture prediction with traveltime.

As to the data quality, from Figure 6.16a, I find it is quite noisy particularly in the time interval 1.5s-2.5s, which corresponds to the target layers. The reason for this is that the acquisition was carried out in a semi-desert area, and the loose sand in the surface degrades the signal.

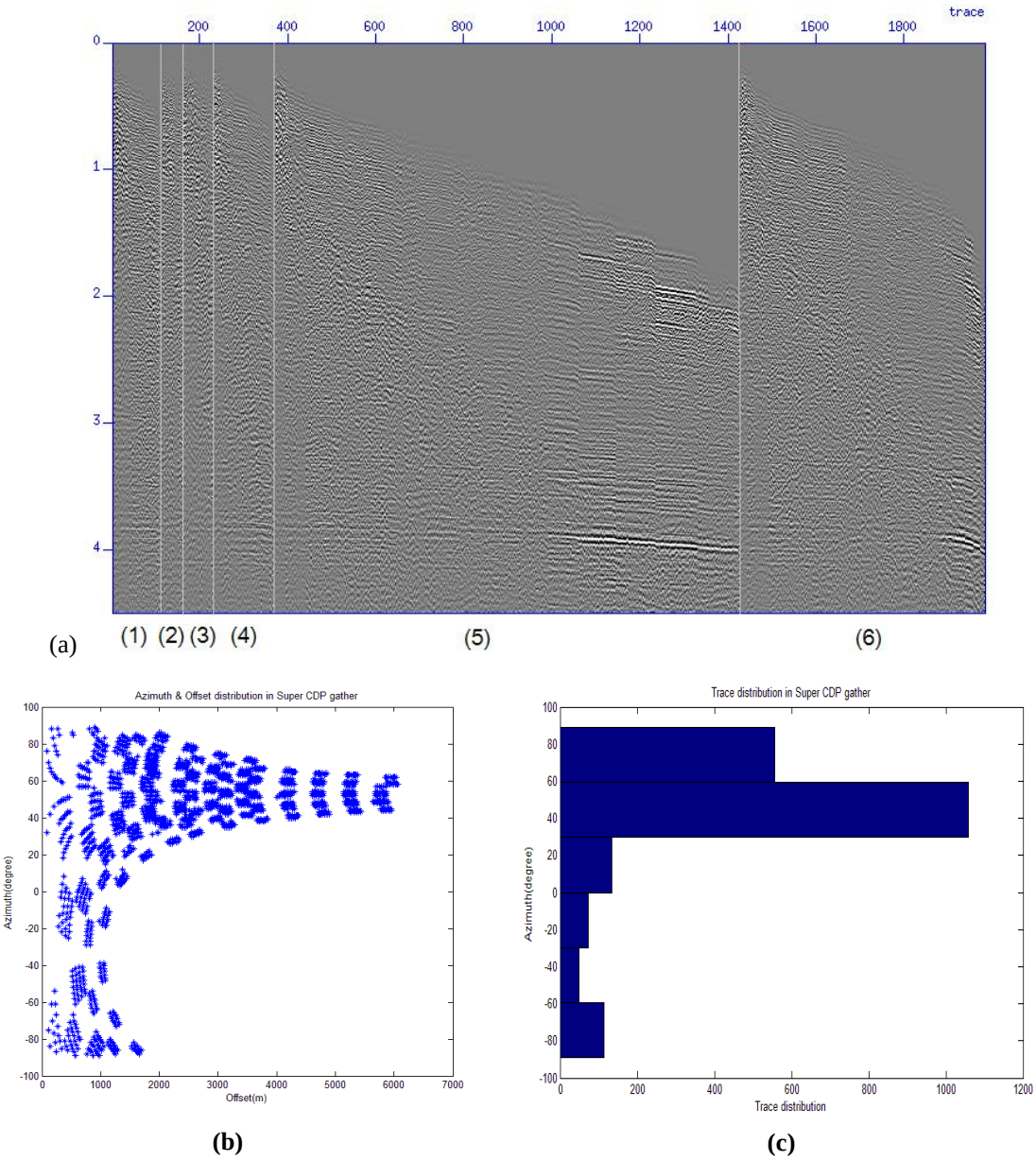

Figure 6.16: A super CDP gather (a), its azimuth-offset distribution chart (b), and its histogram of azimuth vs. trace. (1) – (6) in (a) represent azimuthal gathers: (1) -90 ^{o} - -60^{o}; (2) -60 ^{o} - -30 ^{o}; (3) -30 ^{o} - 0 ^{o}; (4) 0 ^{o} - 30 ^{o}; (5) 30 ^{o} - 60 ^{o}; (6) 60 ^{o} - 90 ^{o}. The traces in the super CDP gather are not evenly distributed over the range of azimuths.

6.5.3 Analysis and comparison of results

Considering the data features discussed in the previous section, I use the offset-azimuth stacking method and the full azimuth surface fitting method to predict

fracture parameters with amplitude; and only the full azimuth surface fitting method is applied to predict these parameters with traveltime. The prediction results include fracture density and fracture orientation across the whole survey.

Before applying the methods to the whole survey, I extract several super CDP gathers from the pre-stack seismic data close to the well and outcrop locations. Then I perform a careful parameter test (such as the bin size, the scanning time-window for amplitude and traveltime picking etc.) in order to find the optimal parameters for prediction for the whole survey. Once the optimal parameters are determined, I apply them into the calculation and obtain the results across the survey, as shown in Figures 17-20. The sub-figures (a) in Figures 17-18 give the fracture density prediction, which is superimposed with the iso-depth contours of the target top; and the sub-figures (b) give the fracture orientation prediction, where the shot arrows point to the fracture orientation predicted.

Figure 6.17 shows the prediction from azimuthal amplitude. First let us have a look at the density prediction in Figure 6.17a. The overall prediction in the whole area tends to be relatively low, from 0.04 to 0.16 for most of the area. At the top of the anticline (the long strip from SE to NW in the middle), large values up to 0.24 are obtained which agrees with the high density prediction from the well interpretation. At the two sides of the anticline, low values are inverted. Another noticeable phenomenon is that there are stripe marks across the whole area from the SW to NE, which are believed to be the effect of the acquisition footprints. The reason behind this is that the binning and stacking process mostly occurs along the same direction due to the lack of sufficient offset coverage in other directions. The strip foot print in Figure 6.1b also confirms this effect. In the two prospective zones, Zone A (the red ellipse in Figure 6.17a) and Zone B (the blue ellipse), the predicted results are relatively high, which is consistent with the results in the vicinity of the wells. Figure 6.17b shows the predicted fracture orientation, most of which uniformly points to the NE direction, either in the top of the anticline or at the two sides of the anticline. This result is compatible with the outcrop observation on the surface.

Figure 6.18 is the prediction from azimuthal traveltime. From Figure 6.18a, I obtain a relatively high fracture density across the survey, particularly, at the two sides of

the anticline. At the top of the anticline, the predictive values are lower. The overall feature in this prediction does not agree with the previous prediction or the outcrop observation. I find that the same acquisition footprint also exists in the result.

I notice there is another important feature here. From Figure 6.18a, obvious high values are aligned along the two sides of the anticline, and low values are distributed in the narrow area of the anticline top, which indicates the shape of the big anticline. The reason is, the wave raypath is distorted at the two sides of the large anticline, which affects the final traveltime picking. Therefore I conclude the anticline in the area shows a strong influence on the prediction results when traveltime is considered, and hence the prediction result is less reliable. For the fracture orientations in Figure 6.18b, there are two trends, pointing to the NE and the SE, which, however, is consistent with the fracture orientations from the outcrop observations. For the prospective zones, the predicted fracture density for both is low.

In order to get more understanding of the prediction, I extract the predicted fracture orientation from the super CDP gathers adjacent to some wells, where we already have the fracture orientation from the outcrop observations as shown in Figure 6.19. Though the outcrop observations are made from a surface survey, I believe there are still links between them and the geological conditions in the subsurface. The result in Figure 6.19 shows that the fracture orientation prediction with both seismic attributes is quite consistent with observations, which enhance our confidence in the result, particularly from the amplitude prediction.

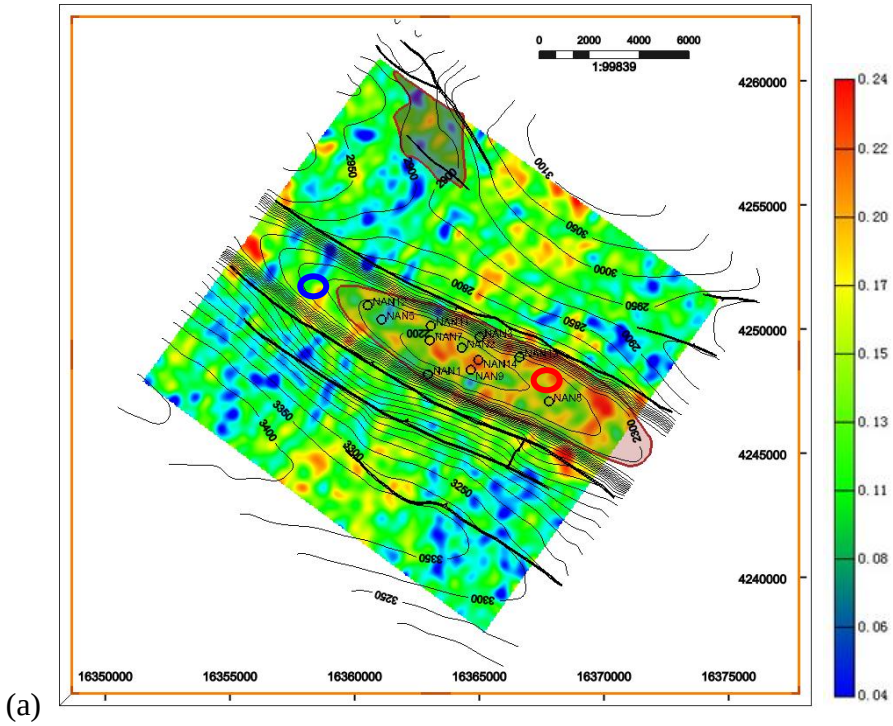

(a)

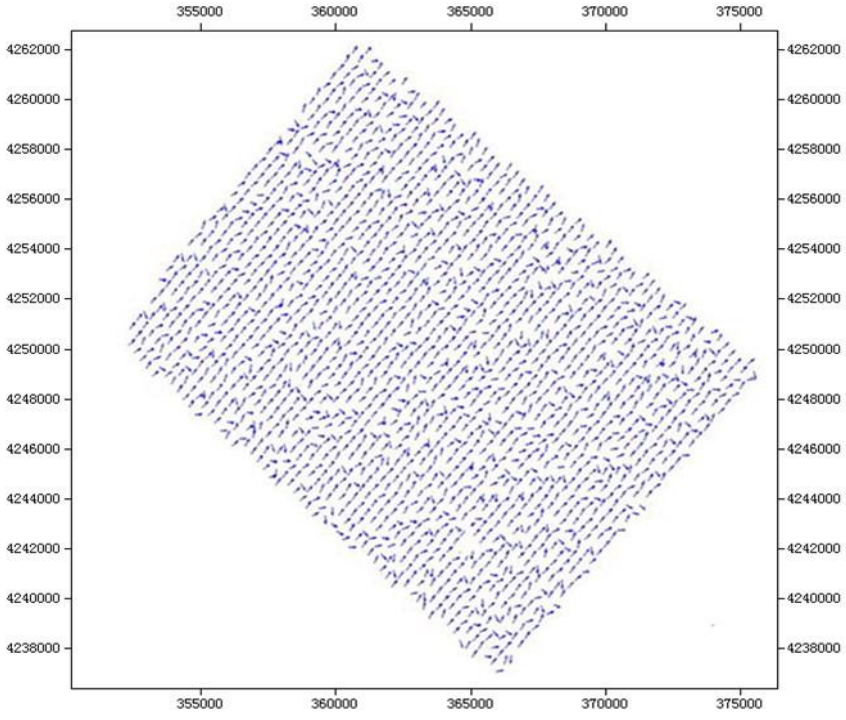

(b)

Figure 6.17: The predicted fracture density with azimuthal amplitude (a) shows a satisfactory result, which is superimposed with the iso-depth contour of the target layer top. Also the predicted fracture orientation (b) mostly points to the NE, which is consistent with the outcrop observation.

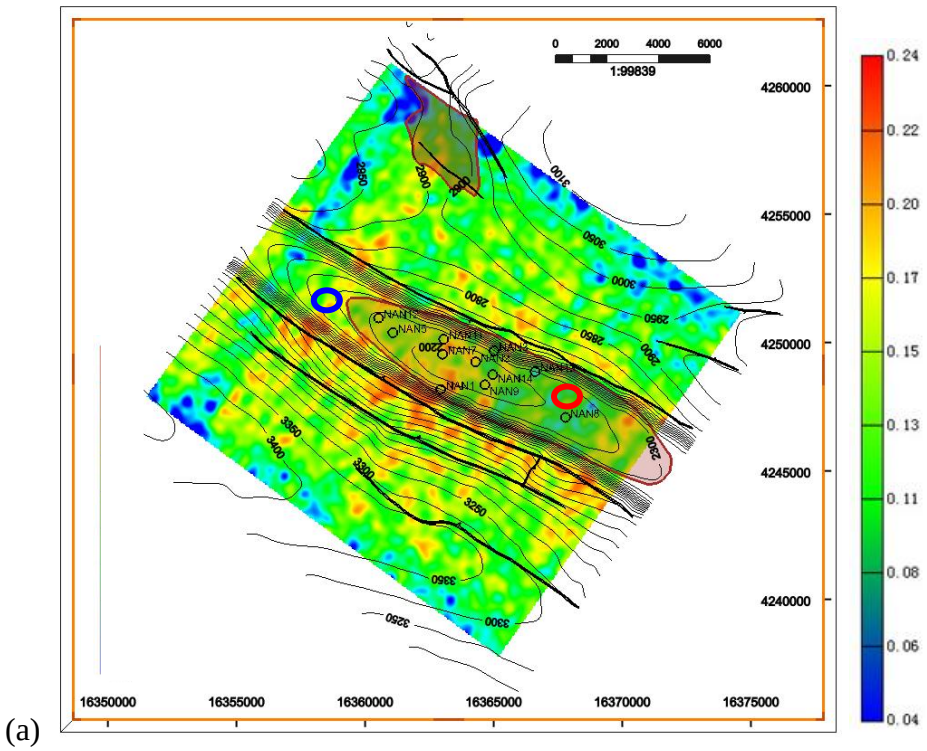

(a)

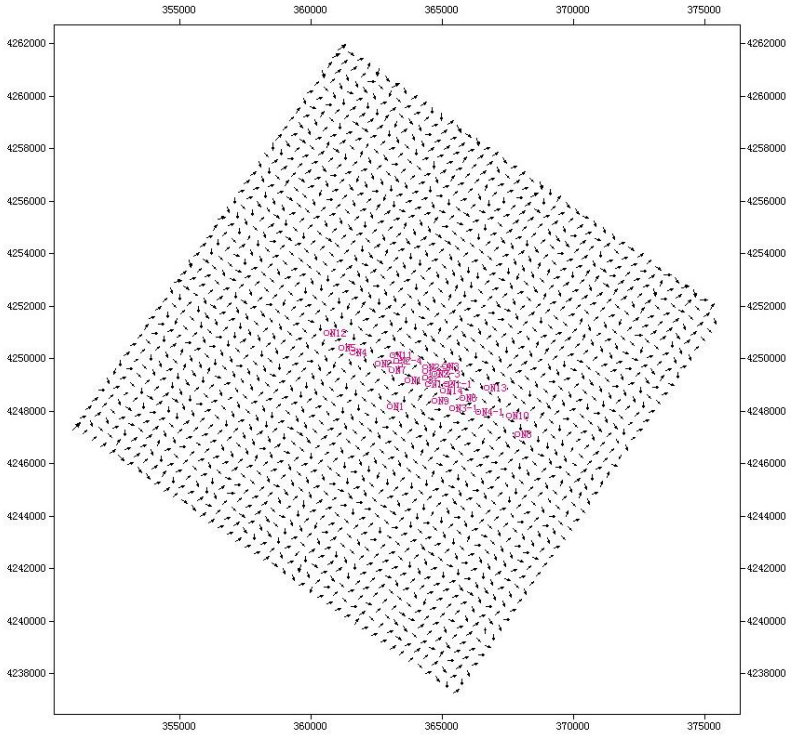

(b)

Figure 6.18: The predicted fracture density with azimuthal traveltime (a) shows a result that is strongly influenced by the large anticline structure, though the orientation prediction (b) seems to be satisfactory.

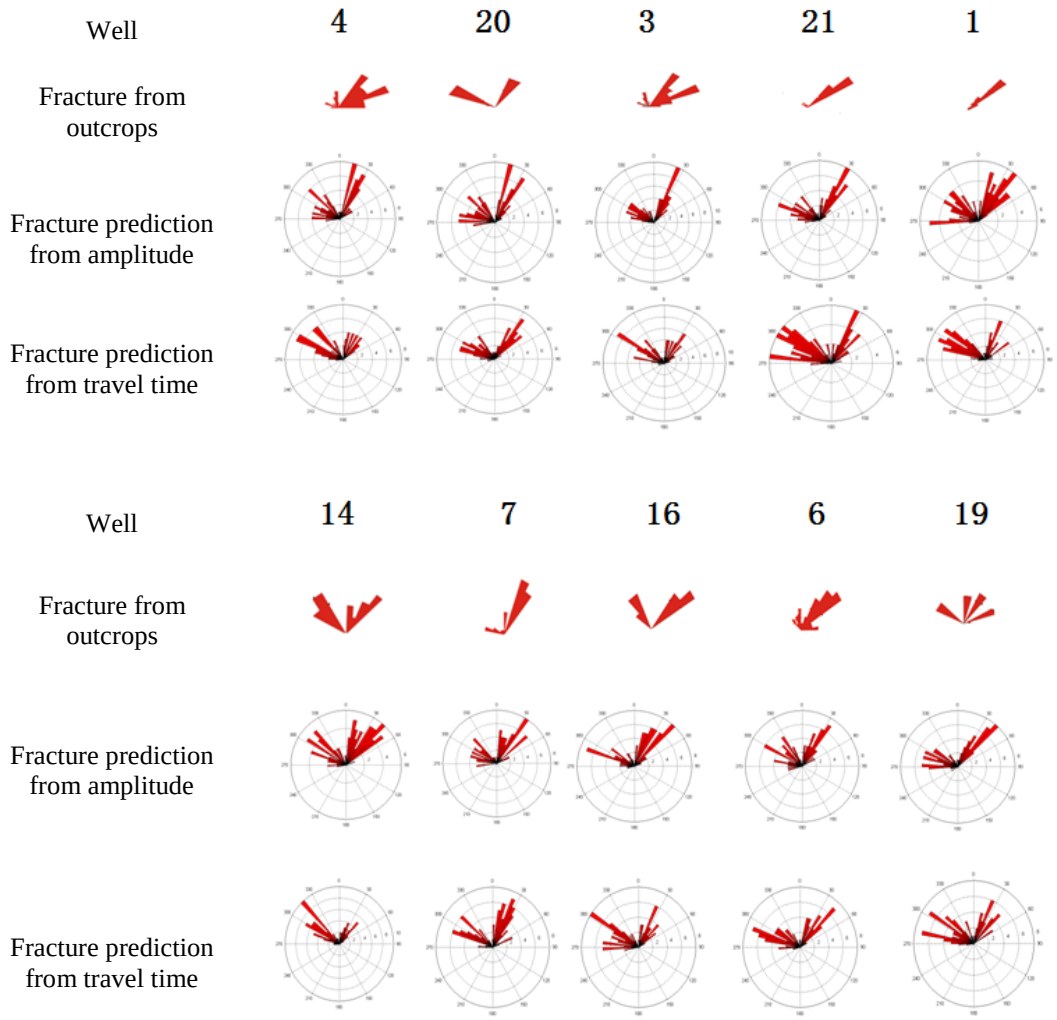

Figure 6.19: The fracture orientation prediction with the two seismic attributes shows consistency with the outcrop observations at the well locations.

6.6 Discussion on anticline effect

In Chapter 5, I have discussed the anticline effect on fracture density inversion based on the SVD method. Here I compare three cases of anticline effects in terms of different attributes, including the case in Chapter 5. Two types of anticlines are considered, Type 1 and Type 2 as shown in Figure 6.20. The case in Chapter 5 belongs to Type 1. The case in Chapter 6 belongs to Type 2. However, if we only consider the anticline top in Chapter 6, the case belongs to Type 1 as well. In order to discuss the anticlines quantitatively, I have calculated the anticline parameters as listed in Table 6.1.

First of all I consider the anticline effect on the prediction with amplitude. In Chapter 5, the data are synthetic data, which are of high quality and have full offset coverage; and the target layer is very shallow (1.2 *km*). The anticline in Chapter 5 has an average dip angle of around 9.5 degrees and the fracture orientation is fixed, and parallel to the anticline orientation. The study result in Chapter 5 shows the over-estimating effect on the two flanks of the anticline whilst there is no effect on the top of the anticline. However, in Chapter 6, the S/N ratio is low, and offset coverage is not ideal, but the dip angle (6 degree) at the top of the anticline is very small, which means the top of the anticline is relatively flat. In addition, the prediction with amplitude has less restriction to offset coverage than traveltime (offset/depth ratio should be about 0.6 for amplitude; for this study it is 0.5). Therefore I believe that the anticline in Chapter 6 shows a very small or no effect in the top area as I discussed in the case of Chapter 5. The anticline may affect the prediction at the two sides, but the effect is overshadowed by the following factors: S/N ratio, smaller offset coverage and the acquisition footprint.

From Figure 6.18a, generally, the small offset coverage and the acquisition footprint degrade the overall prediction with traveltime. On the other hand, we clearly see the effect of the anticline, particularly in the two fault zones, where large values are predicted.

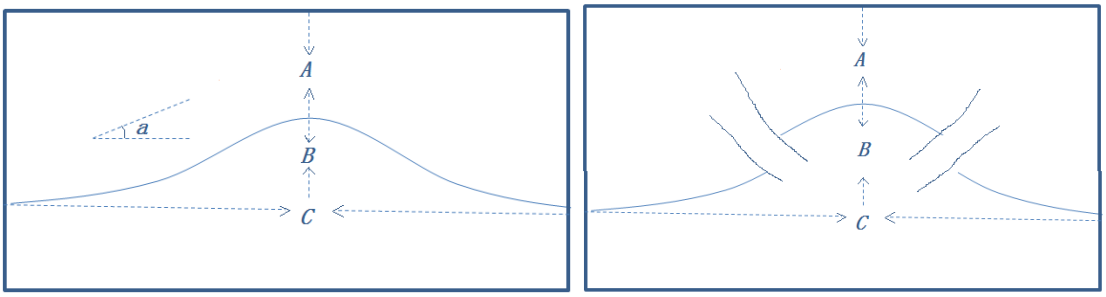

Type 1 Type 2

Figure 6.20: There are two types of anticline involved in Chapter 5 and 6. There are no faults in Type 1, which corresponds to Chapter 5; and Type 2 corresponds to Chapter 6, where there are two reverse faults at the two sides of the anticline.

	Anticline in Chapter 5 (Type 1)	Anticline in Chapter 6 (only consider the anticline top between the two faults, Type 1)	Anticline in Chapter 6 (consider the whole anticline, Type 2)
Type number	Type 1	Type 1	Type 2
Top depth (*A*)	1.2 *km*	3 *km*	3 *km*
Anticline high (*B*)	0.7 *km*	0.4 *km*	3.5 *km*
Anticline width (*C*)	7 *km*	4 *km*	16 *km*
Average dipping angle (α)	9.5^o	6^o	12.3^o
Average offset-depth ratio	>1.2	<0.5	<0.5

Table 6.1: Anticline parameters involved in Chapter 5 and 6.

6.7 General discussions

From discussions and comparison between Chapter 5 and Chapter 6 I find that, to make a good fracture prediction, several factors are very important:

- Sufficient offset coverage is the prerequisite for all azimuthal prediction; otherwise the prediction will be less reliable, or there may cause an acquisition footprint;
- Prediction with traveltime needs a larger offset-depth ratio than with amplitude; but it is less sensitive to the S/N ratio than that from amplitude;
- Geological structures show an obvious effect on prediction with traveltime.

There are still unknowns with azimuthal attribute analysis when particular cases are considered, such as dipping reflectors. The possible solution is to resort to 3D full azimuthal numerical modelling. Models with different dipping reflectors and different seismic attributes can be studied to reveal their internal effects and the sensitivity of different attributes to the reflectors. In Chapter 5, I only discuss the amplitude attribute, and from the study in this chapter, more attributes can be included for such an analysis.

6.8 Summary

In this chapter, I have carried out an integrated study of fracture prediction using P-wave seismic data from the Nanyishan Oil Field. I have used post-stack seismic attributes and pre-stack seismic attributes to predict the fracture distribution. Fracture prediction with the two post-stack attributes, reflection strength and frequency content, indicates a high fracture density distribution in the two prospective zones A and B (Figure 6.4), which is consistent with the general seismic features at the well locations. Specifically, the feature in Zone B infers a brittle fracture area across the top of the target layer. The full azimuth surface fitting method is employed with two pre-stack attributes, azimuthal amplitude and azimuthal traveltime, to predict the fracture density and orientation in the whole area. The density prediction with amplitude shows a high fracture density area at the top of the anticline, which agrees with the result from the well locations. Particularly this prediction agrees with that from the post-stack prediction in the two prospective areas. However, the presence of the anticline structure in the area strongly influences the predicted fracture density with traveltime, which therefore is not reliable. In addition, both predicted fracture density distributions reveal the effect of the acquisition footprint due to insufficient offset coverage. As for the orientation prediction for both azimuthal attributes, the result is found to coincide with the outcrop observations.

7 Chapter 7 Conclusions and future work

The aim of this PhD was to provide more insight into the seismic response of fractured media, and how this response may be used in fracture characterization, with particular reference to P-wave seismic anisotropy. In achieving these aims, I have identified problems in seismic numerical modelling in 3D fractured media, developed practical techniques to solve such problems, and implemented a new computational modelling tool. The new tool was then used to analyse the seismic response in 3D media containing discrete fractures, as well as the effect of geological structures on fracture property inversion. I have also carried out an integrated study of fracture detection with P-wave data to investigate factors that influence fracture parameter prediction. This chapter summarizes my main results as well as issues that arise from my research that need further work.

7.1 Thesis conclusions

Seismic modelling in 3D fractured media

Seismic modelling is considered to be an effective means of studying the seismic response of fractured media and the relevant inverse problems. Specifically, the pseudo-spectra method is a proven practical technique for modelling wave propagation in two-dimensional fractured media (e.g. Vlastos, 2005). However, it is not feasible to extend the technique to three dimensions for practical modelling. Instead, classic Finite Difference (FD) has shown great potential for such a purpose.

Of the three major available FD schemes, the SSG scheme has the best performance for modelling anisotropic media with orthorhombic symmetry or higher, and the RSG and DSG schemes are preferred for modelling media with other more complex symmetries. The DSG scheme has even greater potential over the RSG in the general case, with a lower computation time (38% in comparison) and memory cost (77%). These advantages have clear potential for algorithm development and modelling of complex anisotropic media, including applications such as reverse time migration and full waveform inversion. A major disadvantage of the DSG method was overcome by combining two diamond-shaped staggered grids into one, which thereby has a cubic shape. This significantly simplifies the procedure for solving the spatial derivatives during the DSG implementation. The workflow using the parameter indexing method proposed here has shown a clear advantage in accelerated computing in simulating larger 3D fractured models.

In this thesis, time constraints prevented a more in-depth analysis of more complex Earth models requiring the RSG or DSG methods, but the SSG scheme has been implemented for 3D orthorhombic media, and validated by comparison of its output with the reflectivity method.

Seismic response in Discrete Fracture Models

The synthetic seismic response of numerical discrete fracture models (DFMs) is mainly governed by the orthogonal normal and tangential fracture compliance components. Investigating the links between such behavior and given DFMs can help to diagnose the features in fracture spatial distribution and to invert fracture properties.

Considering one set of vertical aligned fractures in the DFMs, the P-wave seismic anisotropy increases systematically with decreasing vertical fracture spacing, and P-wave wavefronts show characteristic elliptical variations in the plane that is perpendicular to the fracture strike. This feature is similar to those of Hudson's model when crack density increases. Therefore, this has confirmed the link between macro discrete fractures in DFMs and micro-cracks illustrated by Liu et al. (2000), where the terms macro and micro here refer to scales at or well below the seismic wavelength. The ellipticity of the P-wave wavefront has an exponential relation with the discrete fracture spacing.

For a single set of vertically-aligned discrete fracture, the model results show that conventional analysis of azimuthal amplitude-versus-offset (AVO) data is still a valid technique for inferring fracture orientation and equivalent fracture density. These two properties can be estimated with the surface fitting method as well. However, the presence of multiple sets of vertical aligned fractures tend to cancel out the degree of P-wave seismic anisotropy which means using azimuthal P-wave AVO variation alone to directly invert the properties of multiple discrete fracture sets may be unreliable. In the case of one or more aligned vertical sets of discrete fractures in the DFMs, the spectra and the attenuation both have a strong fluctuation on top of the average trend at different azimuthal angles. This characteristic depends on the discrete fracture spacing and the number of fracture sets.

The scattered energy from the discrete vertical fracture models becomes weaker as fracture spacing increases. For more complex vertical fracture sets (e.g. with orthorhombic symmetry due to two orthogonal intersecting fracture sets) the scattered energy is cancelled out due to the interfered reflection from different discrete fracture sets.

The 3D-modelling-based studies in this thesis have enriched our understanding of the seismic response of truly 3D DFMs, and have revealed unique wave phenomena and azimuthal information in seismic attributes that relate directly to the properties of discrete fracture models. This demonstrates the feasibility of using the technique as an aid in characterizing discrete fractures in the Earth's subsurface from inversion of real data.

Effects of structure on fracture prediction

The presence of geological structure in fractured reservoirs violates the conventional assumption for fracture prediction that the Earth models are horizontally layered and the fractures vertical. This introduces a potential bias to the interpretation if realistic geological heterogeneity is taken into account. In the case of a model anticline, the fracture density inferred from single value decomposition (SVD) of the azimuthal amplitude variation, specifically its leading term C_1, is the most robust and reliable attribute for fracture density inversion. Using this method the numerical model results confirm that the fracture density is resolved accurately at the top of the anticline, whilst on the flanks it tends to be over-estimated. The over-estimation effect is not necessarily a general conclusion for all inclined geological features, and its magnitude depends on the rock physics parameters set in the SVD method in the case under study.

In practical exploration applications a velocity model of the subsurface is needed to convert offset to incident angles, and to convert amplitude to reflection coefficient. Numerical modelling here confirms that it is essential to obtain relatively accurate velocity models, because they determine the accuracy for such conversions, and hence affect the quality of the final inversion results.

Fracture prediction with P-wave azimuthal attributes

A number of factors may affect the estimation of fracture parameters based on analysis and/or modelling of P-wave data. However, by integrating all available knowledge about the fractured target it is possible to reduce the uncertainties in the interpretation significantly.

Post-stack attributes at the top of or within fractured reservoirs tend to show common features. With the calibration of well interpretation the common features can aid the interpretation of the inferred fracture spatial distribution. While it is common to use pre-stack attributes to invert for fracture information, post-stack seismic attributes can also be very effective. For example, in the real data from

Nanyishan Oil Field, the common features of weak reflection strength and lower frequency content are shown laterally across the fractured layer, which is consistent with the well interpretation results.

A number of issues arise due to data quality and the geometry of the survey. For example fracture prediction with pre-stack P-wave amplitude requires higher data quality but smaller offset-depth ratio than techniques based on inverting travel times. Large-scale geological structures can bias the inversion for fracture properties such as density at big offset-depth ratio, which particularly results in the distortion in the fracture density prediction with pre-stack travel time. Insufficient azimuthal coverage in the acquisition geometry tends to result in a strong acquisition footprint that degrades the inversion. To avoid this, full azimuth and wide offset acquisition should be considered for fracture prediction using pre-stack attributes.

To make a good prediction and to reduce uncertainties in the target layers, it is essential to correlate pre-stack and post-stack results, to calibrate seismic attributes with well interpretation, and to include geological observation as a constraint.

7.2 Future work

Fracture reservoir characterization with seismic anisotropy is a challenging topic. Many efforts have been devoted to develop equivalent medium theories to reveal the intrinsic properties of fracture networks and hence their influence on subsurface fluid flow, as well as the inversion algorithms based on such theories. In this thesis, I have discussed seismic modelling in 3D fractured media, and employed the modelling technique into the realistic applications to assess and solve problems in fractured reservoir characterization. However, there are still considerable challenges ahead.

In terms of the computation amount in the RSG and DSG schemes, I only consider computational amount of the derivative operation. Actually, to achieve the same accuracy with smaller grids in the RSG, the total computation operation includes derivative operation and other operations. Therefore the exact computation ratio is

not strictly 38% (more or less?). If the exact ratio is concerned in modelling, further work is required.

The F-K transform is applied to analyze the wavefield feature in VFMs (vertical discrete fracture models) by Grandi-Karam (2008). This method can also be used on OFMs (orthogonal discrete fracture models), which possibly reveals more features in scattering energy when multiple fracture sets are present. Other transform in 2D or 3D cases (e.g. tau-p and Continuous Wavelet Transform) can be considered in different domains as well.

Dipping reflectors strongly affect fracture property inversion. The anticline effect in Chapter 5 is a specific case, but different dipping angles and fracture strike directions could be examined more generally to enhance our understanding. A practical way to approach this problem is to design a group of isotropic models with different dipping reflectors in them, and apply the regular azimuthal attributes analysis to access the effect of the finite dip. In Chapter 6, the effect of finite dip on travel time is analysed, but it is possible to extend this to all azimuthal attributes for the effect examination, such as interval travel time and AVO gradient.

References

Aki, K. and Richards, P. G., 1980. Quantitative Seismology. University Science Books.

Anderson, D. L., 1961. Elastic wave propagation in layered anisotropic media, J. Geophys. Res. **66**, 2953-2963.

Anderson, E. M., 1942. The Dynamics of Faulting. Oliver & Boyd, London.

Angerer, E., Crampin S., Li X.-Y. and Davis T.L. 2002. Processing, modelling and predicting time-lapse effects of overpressured fluid-injection in a fractured reservoir. Geophysical Journal International, **149**, 267–280.

Auld, B.A., 1990. Acoustic Fields and Waves in Solids, vols. 1, 2. Malabar, FL: Robert E. Krieger Publication Co.

Backus, M., 1962. Long-wave elastic anisotropy produced by horizontal layering. Journal of Geophysical Research, **67**, 4427-4440.

Bansal, R. and Sen, M.K. 2008. Finite-difference modelling of S-wave splitting in anisotropic media. Geophysical Prospecting, 2008, **56**, 293–312.

Bernth, H. and Chapman C., 2011. A comparison of the dispersion relations for anisotropic elastodynamic finite-difference grids. Geophysics, **76**, WA43–WA50.

Carcione, J.M., Herman G.C. and ten Kroode A.P. 2002. Seismic modelling. Geophysics, **67**, 1304–1325.

Castagna, J. P., H. W. Swan, and D. J. Foster, 1998. Framework for AVO gradient and interpretation. Geophysics, **63**, 948-956.

Causse, E., M. Riede, A. J. van Wijngaarden, A. Buland, J. F. Dutzer, and R. Fillon, 2007. Amplitude analysis with an optimal model-based linear AVO approximation: Part I — Theory. Geophysics, **72**, C59-C69.

Cerjan, C., D. Kosloff, R. Kosloff, and M. Resef, 1985, A nonreflecting boundary condition for discrete acoustic and elastic wave equations. Geophysics, **50**, 705–708.

Chao, G. and S. Maultzsch, 2010. Pilot Fracture Characterization Study Using Seismic Attributes Derived from Singular Value Decomposition of AVOAz Data. 72nd EAGE Conference & Exhibition incorporating SPE EUROPEC 2010.

Chapman, M., 2003 Frequency dependent anisotropy due to meso-scale fractures in the presence of equant porosity. Geophysical prospecting, **51**, 369-379.

Chapman, M., Maultzsch S., Liu E. and Li X.-Y. 2003. The effect of fluid saturation in an anisotropic multi-scale equant porosity model. Journal of Applied Geophysics, **54**, 191–202.

Chapman, M., Zatsepin, S.V., Crampin, S., 2002. Derivation of a microstructural poroelastic model. Geophys. J. Int., **151**, 427– 451.

Cheng, C.H, 1993, Crack Models for a TransverselyIsotropic Medium. J. Geophys. Res., **98**, 675-684.

Chichinina,T., Sabinin, V, and Ronquillo-Jarillo, G. 2006. QVOA analysis: P-wave attenuation anisotropy for fracture characterization. Geophysics, **71**, C37–C48,

Coates, R. T., and Schoenberg, M., 1995, Finite-difference modeling of faults and fractures, Geophysics, **60**, 1514-1526.

Crampin, S., 1981. A review of wave motion in snisotropic and cracked elastic media. Wave Motion, **3**, 343-391.

Crampin, S., 1983, Shear-wave polarizations: A plea for three-component recording: 53rd Annual International Meeting, SEG, Expanded Abstracts, 425–428.

Crampin, S., 1985. Evaluation of anisotropy by shear wave splitting, Geophysics, **50**, 142-152.

Dai, H., Li X. Y., 2010. A revised two-parameter moveout equation of PS converted-waves in VTI media. 80th SEG Annual Meeting.

Daley, P., and Horn, F., 1977, R and T coefficients for transversely isotropic media: Bulletin of the Seismological Society of America, **67**, 661-675

Daley, T.M., Nihei K.T., Myer E.L., Queen J. H., Fortuna M. and Murphy J., 2002. Numerical modeling of scattering from discrete fracture zones in a San Juan Basin gas reservoir. SEG Int'l Exposition and 72nd Annual Meeting.

Dasgupta, R. and Clark, R., 1998. Estimation of Q from surface seismic reflection data. Geophysics, **63**:2120–2128

Dong, Z. and McMechan A.G. 1995. 3-Dviscoelastic anisotropic modeling of data from a multi-component, multi-azimuth seismic experiment in northeast Texas. Geophysics, **60**, 1128–1138.

Eshelby, J.D., 1957. The determination of the elastic field of an ellipsoidal inclusion, and related problem. Proceedings of the Loyal Society of London, **A241**, 376-396.

Faria, E. L., and Stoffa, P. L., 1994, Travel time computation in transversely isotropic media. Geophysics, **59**, 272-281.

Gassmann, F., 1951, Über die Elastizität poroser Medien, Vierteljahrsschrift der Naturforschenden Gesellschaft in Zürich, **96**, 1-23.

Grandi-Karem, S., 2008. Multiscale Determination of In Situ Stress and Fracture Properties in Reservoirs. PhD thesis, Massachusetts Institute of Technology.

Graves, R.W., 1996. Simulating seismic wave propagation in 3D elastic media using staggered-grid finite difference. Bulletin of the Seismological Society of America, **86**, 1091–1106.

Gray, F.D., Roberts, G. and Head, K.J., 2002, Recent Advances in Determination of Fracture Strike and Crack Density from P-Wave Seismic Data, The Leading Edge, **21**,280-285.

Grechka, V. and I. Tsvankin, 1998. Feasibility of nonhyperbolic moveout inversion in transversely isotropic media. Geophysics, **63**, 957-969.

Hall, S. A. and Kendall, J-M., 2003. Fracture characterization at Valhall: Application of P-wave amplitude variation with offset and amplitude (AVOA) analysis to a 3D ocean-bottom data set. Geophysics, **68**, 1150-1160.

Hall, S., Barkved, O., Mueller, M.C. and Kendall, J-M, 2000. An approach for P-wave AVOA in 3D-OBC data. 62nd Ann. Internat. Mtg., Expanded Abstracts.

Hokstad, K., Engell-Sorensen L., and Maao F., 2002. 3-D elastic finite difference modeling in tilted transversely isotropic media: SEG Int'l Exposition and 72nd Annual Meeting., Expanded Abstracts.

Hudson, J. A., Liu, E., and Crampin, S., 1996, The mechanical properties of materials with interconnected cracks and pores. Geophys. J. I., **124**, 105–112.

Hudson, J., 1981. Wave speeds and attenuation of elastic waves in material containing cracks. Geophys. J. Roy. Astr. Soc., **64**, 133-150.

Hudson, J.A. 1980. Overall properties of a cracked solid. Mathematical Proceedings of the Cambridge Philosophical Society, **88**, 371-384.

Igel, H., Mora P. and Bruno R. 1995. Anisotropic wave propagation through finite-difference grids. Geophysics, **60**, 1203–1216.

Ioup, J. W. and G. E. Ioup, 1998. Noise removal and compression using a wavelet transform. 1998 SEG Expanded Abstracts, SEG.

Kazemeini, K., C. Juhlin , K. Zinck-Jørgensen, and B. Norden, 2007. Application of the Continuous Wavelet Transform Decomposition to Channel Deposits and Gas Detection at Ketzin, Germany. EAGE 69th Conference & Exhibition., Expanded Abstracts.

Korneev, V. A., G. M. Goloshubin, T. M. Daley, and D. B. Silin, 2004, Seismic low-frequency effects in monitoring fluid-saturated reservoirs. Geophysics, **69**, 522–532.

Lebedev, V.I., 1964. Difference analogues of orthogonal decompositions of basic differential operators and some boundary value problems. I. USSR Computational Mathematics and Mathematical Physics, **4**, 449–465.

Levander A. R., 1988. Fourth-order Finite-Difference P-SV seismograms. Geophysics, **53**, 1425-1436.

Li, X. -Y. 1999. Fracture detection using azimuthal variation of P-wave moveout from orthogonal seismic survey lines. Geophysics, **64**, 1193-1201.

Li, X. -Y., Liu, Y. -J., Liu, E., Shen, F., Qi, L. and Shouli, Q., 2003. Fracture detection using land 3D seismic data from the Yellow River Delta, China. The Leading Edge, **22**, 680-683.

Lisitsa, V. 2007. Lebedev scheme for anisotropic elastic problems. Proceedings of 8th International Conference on Theoretical and Computational Acoustics, 331–341. ISBN 9789608975842.

Lisitsa, V., and D. Vishnevskiy, 2010. Lebedev scheme for the numerical simulation of wave propagation in 3D anisotropic elasticity. Geophysical Prospecting, **58**, 619–635.

Lisitsa, V., E. V. Lys and D. Vishnevskiy, 2009. Numerical Simulation of Waves' Propagation in Anisotropic Elastic Media by Lebedev's Grids - RAM Saving and Stable PML. EAGE 71st Conference & Exhibition., Expanded Abstracts.

Liu, E., Hudson, J. A. and Pointer, T., 2000, Equivalent medium representation of fractured rock. J. Geophysical Research, **105**, No.B2, 2981-3000.

Lubbe, R. and Worthington, M. H., 2006. A field investigation of fracture compliance. Geophysical Prospecting, **54**, 319-332.

Lubbe, R., J., Worthington M.H. and McCann C., 2007. Laboratory Estimates of Normal/Shear Fracture Compliance Ratio. EAGE 69th Conference & Exhibition.

MacBeth, C. and Li, X-Y, 1999. AVD - An emerging new marine technology for reservoir characterization. Acquisition and application. Geophysics, **64**, 1153-1159

Marion, J. B., and Thornton, S. T., 1995. Classical Dynamics of Particles and Systems (4th ed.). Saunders College Publishing. p. 424.

Markov, G.., Mukerji, T. and Dvorkin, J., 2009. The rock physics handbook. Cambridge university press.

McCollum, B. and Snell F. A., 1932. Asymmetry of sound velocity in stratified formations. Physics, **2**, 174-185

Nihei, K. T., Nakagawa, S., Myer, L. R. and Majer E. L., 2002. Finite difference modeling of seismic wave interactions with discrete, finite length fractures: SEG Int'l Exposition and 72nd Annual Meeting.

Parra, J. O., and C. L. Hackert, 2002, Wave attenuation attributes as flow unit indicators. The Leading Edge, **21**, 564–572.

Qian, Z., 2009. Analysis of Seismic Anisotropy in 3D Multi-component Seismic Data. PhD thesis, University of Edinburgh.

Qian, Z., Li X. Y., and Chapman M, 2007. Azimuthal variations of PP- and PS-wave attributes: a synthetic study. Expanded abstract of EAGE 2007.

Qian, Z., Li, X.-Y. and Chapman, M., 2008. Fracture characterization with azimuthal attribute analysis of PS-wave data: modelling and application. 70th Annual Conference, Expanded Abstracts, EAGE, P354.

Rao, Y. and Wang Y., 2009, Fracture effects in seismic attenuation images reconstructed by waveform tomography. Geophysics, **74**, R25 - R34, ISSN: 0016-8033.

Rathore, J.S., Fjaer, E., Holt, R.M. & Renlie, L., 1995. Acoustic anisotropy of a synthetic sandstone with controlled crack geometry. Geophys. Prospect., **43**, 805–829

Ruger, A., 1997, P-wave reflection coefficients for transversely isotropic models with vertical and horizontal axis of symmetry. Geophysics, **62**,713-722.

Rüger, A., 1998. Variations of P-wave reflectivity with offset and azimuth in anisotropic media. Geophysics, **63**, 935-947.

Saenger, E.H. and Bohlen T. 2004. Finite-difference modeling of viscoelastic and anisotropic wave propagation using the rotated staggered grid. Geophysics **69**, 583–591.

Saenger, E.H., Gold N. and Shapiro S.A. 2000. Modeling the propagation of elastic waves using a modified finite-difference grid. Wave Motion, **31**, 77–92.

Sayers, C. M. and Rickett, J. E., 1997, Azimuthal variation in AVO response for fractured gas sands. Geophys. Prosp., **45**,165-182.

Sayers, Colin M. and Simon Dean, 2001. Azimuth-dependent AVO in reservoirs containing non-orthogonal fracture sets. Geophysical Prospecting, **49**, 1365-2478.

Sayers, Colin M, 2007. Seismic characterization of reservoirs containing multiple fracture sets. SEG/San Antonio 2007 Annual Meeting, Expanded Abstracts.

Schoenberg, M. and Helbig, K., 1997, Orthorhombic media: Modeling elastic wave behavior in a vertically fractured earth. Geophysics, **62**, 1954-1974

Schoenberg, M. and J. Protazio; 1992, "Zoeppritz" rationalized and generalized to anisotropy. Journal of Seismic Exploration, **1**, 125–144.

Schoenberg, M. and Muir, F., 1989. A calculus for finely layered anisotropic media. Geophys., **54**, 581-589.

Schoenberg, M. and Sayers, C., 1995. Seismic anisotropy of fractured rock. Geophysics, **60**, 204-211.

Schoenberg, M.,1980. Elastic wave behaviour across linear-slip interfaces. J. Acoust. Soc. Am., **68**, 516- 1521.

Schoenberg, M and Douma, J., 1988. Elastic-wave propagation in media with parallel fractures and aligned cracks. Geophysical Prospecting, **36**, 571-590.

Sheriff, R., 2006. Encyclopedic dictionary of applied geophysics, revised 4th ed.: SEG

Shuey, R.T., 1985. A simplification of the Zoeppritz Equations. Geophysics, **50**, 609-614.

Singh, Sunil K., Hanan Abu-Habbiel, Badruzzaman Khan, Mahmood Akbar, Arnaud Etchecopar and Bernard Montaron, 2008. Mapping fracture corridors in naturally fractured reservoirs: an example from Middle East carbonates. First Break, **26**, 109-113.

Sinha, Satish, Partha S. Routh, Phil D. Anno, and John P. Castagna, 2005. Spectral decomposition of seismic data with continuous-wavelet transform. Geophysics, **70**, 19-25.

Smith, G.C. and Gidlow, P.M, 1987. Weighted stacking for rock property estimation and detection of gas. Geophys. Prosp., **35**, 993-1014.

Stockwell, J. W. Jr., 1999. The CWP/SU: Seismic Un*x package. Computer & Geosciences, **25**, 415-419

Taner, M. T., 2001, Seismic attributes. CSEG Recorder, **26**, 48–56.

Taner, M. T., F. Koehler, and R. E. Sheriff, 1979, Complex seismic trace analysis. Geophysics, **44**, 1041–1063.

Thomsen, L., 1986. Weak elastic anisotropy. Geophysics, **51**, 1954 – 1966.

Thomsen, L., 1995. Elastic anisotropy due to aligned cracks in porous rock. Geophys. Prospect., **43**, 805–829.

Thomsen, L., 2002. Understanding seismic anisotropy in exploration and exploitation. SEG distinguished instructor series, No.5.

Tonn, R., 1991. The determination of the seismic quality Q from VSP data: A comparison of different computational methods. Geophysical Prospecting, **39**, 1- 27.

Tsvankin, I., 1997, Anisotropic parameters and P-wave velocity for orthorhombic media. Geophysics, **62**, 1292-1309.

Tsvankin, I., and H. B. Lynn, 1999, Special section on azimuthal dependence of P-wave signatures – Introduction. Geophysics, **64**, 1139-1142.

Tsvankin, I., James Gaiser, Vladimir Grechka, Mirko van der Baan, and Leon Thomsen, 2010. Seismic anisotropy in exploration and reservoir characterization: An overview. Geophysics, **75**, 75A15–75A29.

Varela, I., S. Maultzsch, and X.-Y. Li. 2007. Fracture properties inversion from azimuthal AVO using singular value decomposition. Seg 77th Conference & Exhibition, **26**, 259-263

Vetri, L., Loinger, E., Gaiser, J., Grandi, A. and Lynn, H., 2003, 3D/4C Emilio: Azimuth processing and anisotropy analysis in a fractured carbonate reservoir. THE LEADING EDGE, **22**, 675-679.

Virieux, J. 1984. SH-wave propagation in heterogeneous media: Velocity-stress finite-difference method. Geophysics, **49**, 1933–1957.

Virieux, J. 1986. P-SV wave propagation in heterogeneous media: Velocity-stress finite-difference method. Geophysics, **51**, 889–901.

Vlastos, S., 2005. Seismic characterisation of fluid flow in fractured reservoirs. PhD thesis, University of Edinburgh.

Vlastos, S., E. Liu, I.G.Main, and C.Narteau, 2007,Numerical simulation of wave propagation in 2-D fractured media—Scattering attenuation at different stages of the growth of a fracture population. Geophysical Journal International, **171**, 865–880.

Vlastos, S., Liu E.,Main I.G. and Li X.Y. 2003. Numerical simulation of wave propagation in media with discrete distribution of fractures: effects of fracture sizes and spatial distributions. Geophysical Prospecting, **152**, 649–668.

Wang, L., 2007. Analysis of PP and PS multicomponent reflection data in the presence of seismic anisotropy. PhD thesis, University of Edinburgh.

Wang, Z., 2001. Fundamentals of seismic rock phsyics. Geophysics, **66**, 398-412.

Willis, M. E., Burns, D. R., Rao, R., Minsley, B., Toksöz, M. N. and Vetri, L., 2006. Spatial orientation and distribution of reservoir fractures from scattered seismic energy. Geophysics, **71**, O43-O51.

Winstertein, D.F., 1990. Velocity anisotropy terminology for geophysicists. Geophysics, **55**, 1070-1088.

Worthington, M. H., 2007a. Seismic Modeling of Fractured Reservoirs: EAGE 69th Conference & Exhibition.

Worthington, M. H., 2007b. The compliance of macrofractures. The Leading Edge, 1118-1122.

Xu, Y. and Li X. Y., 2009. Anisotropic wave propagation through finite difference staggered grids. Edinburgh Anisotropy Project Annual Meeting 2009, internal report.

Yu, Z., George A. McMechan, Phil D. Anno, and John F. Ferguson, 2004. Wavelet transform-based prestack multiscale Kirchhoff migration. Geophysics, **89**, 1505-1512.

Zoeppritz, K., 1919, Erdbebenwellen VIII B, On the reflection and penetration of seismic waves through unstable layers. Goettinger Nachr, 66−84.

Publications

Xu, Y., M. Chapman, X.Y. Li, and I.G. Main. 2010. Effects of Fracture Spacing on Seismic Wave Propagation – A 3D Numerical Simulation Study on Discrete Fracture Models. 72nd EAGE Conference & Exhibition, Expanded Abstract.

Xu Y., X.-Y. Li and H. Dai, 2010. Azimuthal AVO and seismic scattering attenuation in 3D fractured media: a numerical simulation study on the Discrete Fracture Model. SEG Denver 2010 Annual Meeting, Expanded Abstract.

Xu Y., Y. An, X.Y. and Li, Z. Cao, 2010. An Integrated Study of Fracture Detection Using P-wave Seismic Data. 72nd EAGE Conference & Exhibition, Expanded Abstract.

Xu Y., G. Chao, and X.Y. Li, 2011. The Effect of Anticlines on Seismic Fracture Characterization and Inversion Based on a 3D Numerical Study. 73rd EAGE Conference & Exhibition, Expanded Abstract.